

1984

Laser induced photocurrent transients in semiconductor liquid-junction solar cells employing n-WSe₂ and n-MoSe₂ photoanodes

Stanley G. Prybyla
Iowa State University

Follow this and additional works at: <https://lib.dr.iastate.edu/rtd>

 Part of the [Physical Chemistry Commons](#)

Recommended Citation

Prybyla, Stanley G., "Laser induced photocurrent transients in semiconductor liquid-junction solar cells employing n-WSe₂ and n-MoSe₂ photoanodes " (1984). *Retrospective Theses and Dissertations*. 9022.
<https://lib.dr.iastate.edu/rtd/9022>

This Dissertation is brought to you for free and open access by the Iowa State University Capstones, Theses and Dissertations at Iowa State University Digital Repository. It has been accepted for inclusion in Retrospective Theses and Dissertations by an authorized administrator of Iowa State University Digital Repository. For more information, please contact digirep@iastate.edu.

INFORMATION TO USERS

This reproduction was made from a copy of a document sent to us for microfilming. While the most advanced technology has been used to photograph and reproduce this document, the quality of the reproduction is heavily dependent upon the quality of the material submitted.

The following explanation of techniques is provided to help clarify markings or notations which may appear on this reproduction.

1. The sign or "target" for pages apparently lacking from the document photographed is "Missing Page(s)". If it was possible to obtain the missing page(s) or section, they are spliced into the film along with adjacent pages. This may have necessitated cutting through an image and duplicating adjacent pages to assure complete continuity.
2. When an image on the film is obliterated with a round black mark, it is an indication of either blurred copy because of movement during exposure, duplicate copy, or copyrighted materials that should not have been filmed. For blurred pages, a good image of the page can be found in the adjacent frame. If copyrighted materials were deleted, a target note will appear listing the pages in the adjacent frame.
3. When a map, drawing or chart, etc., is part of the material being photographed, a definite method of "sectioning" the material has been followed. It is customary to begin filming at the upper left hand corner of a large sheet and to continue from left to right in equal sections with small overlaps. If necessary, sectioning is continued again—beginning below the first row and continuing on until complete.
4. For illustrations that cannot be satisfactorily reproduced by xerographic means, photographic prints can be purchased at additional cost and inserted into your xerographic copy. These prints are available upon request from the Dissertations Customer Services Department.
5. Some pages in any document may have indistinct print. In all cases the best available copy has been filmed.

**University
Microfilms
International**

300 N. Zeeb Road
Ann Arbor, MI 48106

8423667

Prybyla, Stanley G.

LASER INDUCED PHOTOCURRENT TRANSIENTS IN SEMICONDUCTOR
LIQUID-JUNCTION SOLAR CELLS EMPLOYING N-TUNGSTEN-SELENIDE AND
N-MOLYBDENUM-SELENIDE PHOTOANODES

Iowa State University

PH.D. 1984

**University
Microfilms
International** 300 N. Zeeb Road, Ann Arbor, MI 48106

Laser induced photocurrent transients in semiconductor
liquid-junction solar cells employing
n-WSe₂ and n-MoSe₂ photoanodes

by

Stanley G. Prybyla

A Dissertation Submitted to the
Graduate Faculty in Partial Fulfillment of the
Requirements for the Degree of
DOCTOR OF PHILOSOPHY

Department: Chemistry
Major: Physical Chemistry

Approved:

Signature was redacted for privacy.

In Charge of Major Work

Signature was redacted for privacy.

For the Major Department

Signature was redacted for privacy.

For ~~the~~ Graduate College

Iowa State University
Ames, Iowa

1984

TABLE OF CONTENTS

CHAPTER I. INTRODUCTION	1
Ultrashort Processes and Bandwidth-Limited Picosecond Pulses	1
Dye Lasers and Mode-Locking	3
Flashlamp Pumped Mode-Locked Dye Lasers	8
Spectral Narrowing; the Dye Laser Versus the Solid State Laser	10
Spectral and Temporal Ranges of Mode-Locked Dye Lasers	12
Repetition Rates	15
Relaxation Oscillations and Spiking	18
Development of Mode-Locked Pulse Trains in Flashlamp Pumped Dye Lasers	24
Transverse Flow Dye Laser Systems	30
Photoelectrochemical Solar Energy Conversion	32
CHAPTER II. LASER DESIGN AND CONSTRUCTION	36
Motivation for Design	36
Flashlamps	36
Resonator	43
Dye Head	46
Flow Systems	58
Thermal and Acoustic Distortion Effects; Thermal Lensing	63
Polarization of Laser Output	68
Conversion of Electrical to Optical Energy	70a
Tuning Elements	71
Mode-Locking Dye Cell	73
Triplet State Quenchers; Photobleaching	75
Design of Flashlamp Driving Circuits	85
Initial Flashlamp Pulsing Systems	88
Present Flashlamp Pulser	92
Simmer and Prepulse Power Supplies	93

Laser Warm-Up and Operation	98
Pulse Switching	102
CHAPTER III. LASER CHARACTERIZATION AND PERFORMANCE	122
Operating Conditions	122
Pulse Energy	123
Mode-Locking Quality	127
Spectral Bandwidth	128
Temporal Bandwidth; Detection System	135
Factors Affecting Mode-Locking Quality and Repetition Rate	152
CHAPTER IV. LIQUID JUNCTION SOLAR CELLS	156
The Semiconductor	158
Conductance	187
The Electrolyte	189
Charge Transfer	197
PEC Photovoltaic Cells	203
A-C Techniques	207
I-V Characteristics	211
PEC Transient Studies	215
CHAPTER V. SAMPLE PREPARATION AND TECHNIQUES FOR OBSERVING PHOTOCURRENT TRANSIENTS	225
Semiconductor/Redox Couple	227
Sample Preparation	238
Electrochemical Cell	241
Electrolyte	245
Experimental Apparatus	245
CHAPTER VI. PHOTOCURRENT TRANSIENTS IN MoSe_2 AND WSe_2	253
Transient Decays	253
Current Voltage Curves	259
Peak Photoresponse	262
Charge Transfer Quantum Yield	265
Surface Imperfections	268
Calculated Biexponential Decays	272

PEC Model	276
Variation of PEC Load Resistance	284
Variation of Redox Couple Concentration	292
CHAPTER VII. DISCUSSION	297
Further Work	301
BIBLIOGRAPHY	303
ACKNOWLEDGMENTS	314

CHAPTER I. INTRODUCTION

Ultrashort Processes and Bandwidth-Limited
Picosecond Pulses

The advent of the laser has provided the experimentalist with a high intensity monochromatic source with which to investigate chemical and physical events, thereby fostering rapid advancement in spectroscopy. Lasers have been used since 1959 to study events which occur in the microsecond and nanosecond regimes. Applications of the laser have included such topics as the study of nonlinear optical effects typified by second harmonic generation and two photon absorption. The high degree of monochromaticity of the laser beam makes it useful for selective excitation of a photochemical reaction of one particular isotope of a chemical compound. Lasers also have widespread usefulness in surgery, electronic component construction, communications and holography. The microsecond and nanosecond operational times of conventional lasers have often proven to be quite satisfactory for these applications.

A limitation exists with these lasers, however, in that they cannot be used to study ultrashort processes, occurring on a picosecond time scale. The limitation is inherent in the composition of the lasing material, and is influenced by the lifetimes of the upper and lower lasing levels. This limiting factor may be surmounted by mode-locking of the

laser, whereby broadband spectral output is accompanied by trains of laser pulses with individual durations in the picosecond regime.

A relationship exists between the following pair of integrals

$$E(t) = \frac{1}{\sqrt{2\pi}} \int_{-\infty}^{\infty} e(\omega) \exp(-i\omega t) d\omega \quad e(\omega) = \frac{1}{\sqrt{2\pi}} \int_{-\infty}^{\infty} E(t) \exp(i\omega t) dt,$$

where E and e are the magnitudes of the electric field vector as a function of time t and frequency ω , respectively, such that the total energy of a pulse may be found to be proportional to either the area under the temporal or spectral intensity profiles (1). This clearly shows a symmetry

$$\int_{-\infty}^{\infty} I(t) dt = \int_{-\infty}^{\infty} E^*(t) E(t) dt$$

$$\int_{-\infty}^{\infty} i(\omega) d\omega = \int_{-\infty}^{\infty} e^*(\omega) e(\omega) d\omega$$

between the temporal and frequency descriptions of the optical pulse. In general, the relationship between $I(t)$ and $i(\omega)$ arises from the uncertainty principle

$$(\Delta\omega\Delta t)/2\pi \geq K \quad \text{or,} \quad \Delta\nu\Delta t \geq K$$

where K is a constant on the order of unity whose value depends on the intensity profile shape. The shortest pulse

possible within a given spectral bandwidth is described as being "bandwidth-limited" or "transform-limited". For Gaussian, Lorentzian, and hyperbolic secant squared pulses, the respective values of K are 0.441, 0.600, and 0.315.

Dye Lasers and Mode-Locking

Dye lasers have an oscillating bandwidth of up to 100 Å in a typical broadband cavity are favorable for mode-locking due to the fact that the transform limited pulse duration has a theoretical value on the order of tens of femtoseconds. Recent advances by Moron and Sizer (2) and Shank et al. (3) have produced ultrashort pulses of less than 100 femtosecond duration.

The resultant pulse train from a mode-locked laser may be used to study some of the fundamental chemical dynamical processes, most of which occur on a picosecond time scale. Among these processes are the free decay of vibrational excitation and orientational diffusion in liquids, phonon and exciton decay in solids, and nonradiative molecular energy transfer. At present, experimental and theoretical advances dealing with the interaction of picosecond pulses with matter lie at the forefront of the fields of laser physics and laser spectroscopy.

The difference between a mode-locked laser and an

ordinary laser consists of the addition of a source of modulation. Mode-locking may be performed either actively or passively. A passively mode-locked laser has as a source of modulation a dye cell containing a saturable absorbing dye placed within the cavity. An actively mode-locked laser can consist either of a laser containing an intracavity acoustooptic mode-locking device, or a laser which is pumped by a second laser which is already mode-locked and whose cavity length is a multiple of the first. From a frequency viewpoint, mode-locking is seen as the case where a field within the cavity consists of some number of discrete axial mode frequencies, spaced by the axial mode interval $c/2L$, each mode possessing exactly the same phase. From a temporal viewpoint, the field consists of an internal distribution of the field which circulates inside the cavity with a repetition period equal to the round-trip transit time $2L/c$. The fields lose energy due to the output coupling and gain energy due to laser amplification on each round trip (4).

The first mode-locked laser was developed in 1964, when Hargrove et al. (5) successfully mode-locked a He-Ne laser by the use of an intracavity acoustic loss modulator. In 1965, Mocker and Collins (6) developed the first laser employing a saturable dye as a passive mode-locking element by placing a cell containing the dye within a ruby laser cavity. The first mode-locked Nd:glass (7,8) and Nd:YAG (9)

lasers were developed soon thereafter, in 1966.

Chloro-aluminum phthalocyanine dye, when pumped by the Q-switched output of a ruby laser, was observed to lase with emission centered at 0.755 μm . This advance, as recorded by Sorokin and Lankard (10) in 1966, marked an important historical event in the history of the laser, specifically the advent of the dye laser. The first mode-locked organic dye laser was reported by Glenn et al. (11) in 1968 and utilized the second harmonic of a mode-locked Nd:glass laser for optical pumping. Soon thereafter, Schmidt and Schafer (12) developed the first flashlamp pumped dye laser, using R6G (Rhodamine 6G) dye as the active medium and DODCI (3,3'-diethyloxadicarbocyanine iodide) as the saturable absorber.

The dye laser serves to fill many of the experimentalist's needs as none of its predecessors could. The ability to tune over a wide range of wavelengths allows the experimentalist to expand upon the number of species suitable for study. This tunability of the dye laser is a direct consequence of the large number of closely spaced vibrational energy levels comprising the S_0 and S_1 manifolds. In contrast to a molecular gas or solid state laser, it is not generally possible to draw a detailed, accurate picture of the energy levels of a dye in solution. Even perturbation techniques, quite suitable for small molecules, are not

well adapted to large complicated dye molecules. The energy levels of a dye molecule are best given instead by a simple diagrammatic representation as shown in Figure 1.1. Each vibrational state is grouped according to the different electronic states of the molecule. The electronic states, in turn, are grouped in accordance with their electronic spin states as either singlets or triplets, ignoring the fact that realistically there exists a small mixing of singlet and triplet states due to spin-orbit interactions. The major transition of interest corresponds to stimulated emission, and occurs between the S_1 and S_0 singlet manifolds of states.

The active lasing medium can be made of high optical quality in common organic solvents and the lasing system is relatively easy to regulate thermally by the introduction of dye and water flow systems. Flowing dye systems also have the advantage of not being susceptible to damaging effects often sustained by solid state laser systems. Finally, the dye laser presents an active medium at a fraction of the cost of solid state systems. Many laser dyes are readily available for use in lasers today as both active media and modulators, and research concerned with the synthesis of new dyes is of current interest.

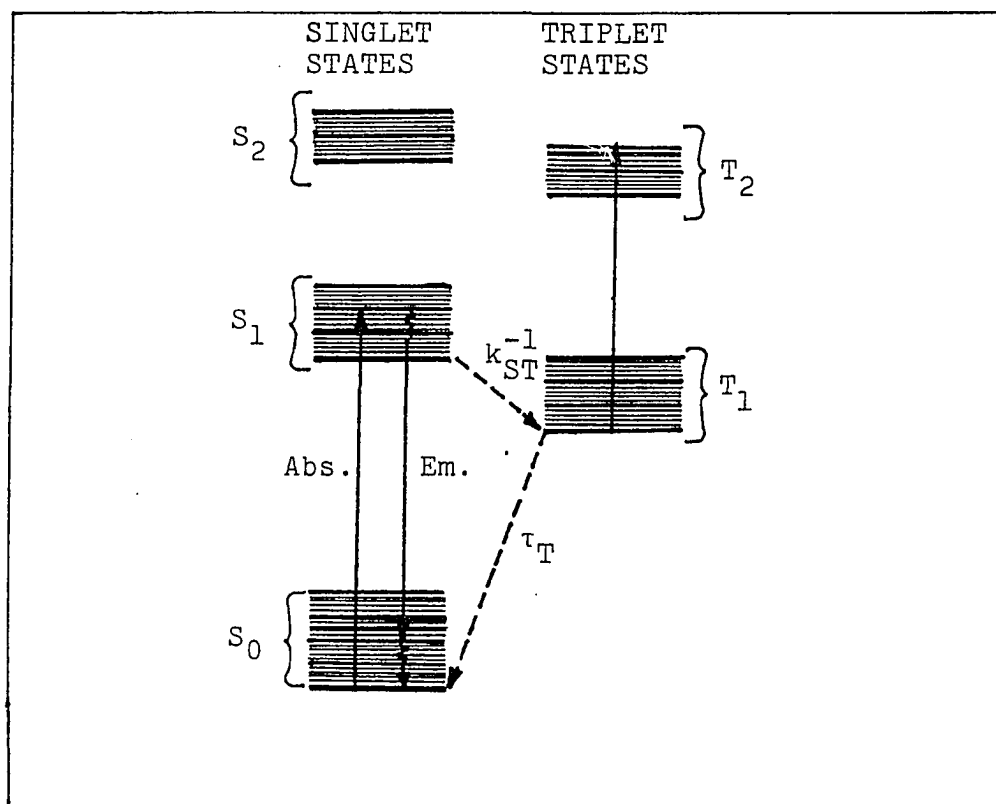


Figure 1.1. Energy levels of an organic dye molecule in solution

Flashlamp Pumped Mode-Locked Dye Lasers

In the case of a flashlamp pumped dye laser, the threshold pumping power is known to increase with increasing rise time of the pumping pulse. It was first determined by Schmidt and Schafer (13), and further investigated by Sorokin *et al.* (14), that for a system with a slowly rising pump pulse, the system is observed to have a lowered population density in the excited singlet state. Based on the assumption that there is no direct radiationless transition between the first excited singlet state and the ground state, it can be shown that this is due to a fraction of the molecules undergoing rapid intersystem crossing to the lowest triplet state T_1 . Once in the triplet state, the molecules have a long lifetime in comparison to the singlet state, which stems from the fact that the triplet-singlet phosphorescence transition is spin forbidden. A typical value of the S_1 singlet state lifetime is on the order of 5 nanoseconds for an organic lasing dye. The lifetime of the T_1 triplet state may be as long as 10 milliseconds in a carefully deoxygenated solution (oxygen present in a system tends to shorten this lifetime). A typical value of an intersystem crossing rate (k_{st}) is $2 \times 10^7 \text{ s}^{-1}$. For a flashlamp operating with a risetime greater than one millisecond, the population in the excited singlet state is

observed to reach a maximum while the pumping pulse intensity is still rising. When the ground state becomes depleted and many of the molecules are in the T_1 state, the S_1 state population falls rapidly, and lasing output is quenched. However, a fast rise-time flashlamp populates the singlet excited state in a manner such that the entire excitation-stimulated emission process is achieved on a time scale less than that of the intersystem crossing rate. Schmidt and Schafer (12) found that a 300 nanosecond risetime lamp works well to give the desired low-threshold, long-duration lasing output.

At present, xenon gas filled lamps are the most suitable light source for optical pumping due to their broad emission spectrum extending over the range from 2000-10,000 angstroms with high spectral intensity in the visible regions of overlap with the absorption curves of many dye molecules (15). If long pulse stimulated emission is a desired dye laser output characteristic, this type of lamp used in combination with a triplet state quencher is imperative (16, 17).

Spectral Narrowing: The Dye Laser
Versus the Solid State Laser

One of the most interesting features associated with dye lasers is the efficient spectral narrowing of the beam occurring when the optical feedback is made frequency selective by the insertion of a tuning element into the cavity. Nd:glass lasers show an inhomogeneous broadening of the line width of emission at 1.06 μm , associated with slight differences in the LF splittings in different sites of various Nd³⁺ ions. When interactions between neighboring sites takes place, ions emitting in only one portion of the spectrum transfer their energy to ions which emit in a slightly different region. As laser action occurs, a hole is found to be burned into the gain profile with its center at the laser frequency. In comparison, dye solutions may be either homogeneously or inhomogeneously broadened with respect to their gain profile. In both cases, a number of modes will be observed to oscillate (due to either spatial or inhomogeneous gain saturation effects, respectively). Whether a dye molecule will exhibit homogeneous broadening or not will be dependent upon solvent-molecule interactions. Inhomogeneous broadening is attributed to the different solvent cages which may form in solution, as well as different configurations adopted by the solvent molecule.

The major difference between inhomogeneously broadened solid state and dye solution lasers lies in the ability for each to fill in the holes burned by the laser transition. A solid state laser will tend to undergo nonradiative transitions at a rate slower than a dye laser due to the effective isolation of the ions from each other in the glass. The dye laser will rapidly (on the order of 10 picoseconds) undergo spectral cross relaxation, whereby the holes are filled in rapidly by neighboring transitions, thus making the gain curve show homogeneous characteristics, and subsequently allowing much more of it to be utilized. Due to the slow cross relaxation rates of solid state lasers, the insertion of a tuning element within the cavity will ultimately lead to the quenching of some of the oscillating modes and a loss in output energy. However, this is not the case in dye lasers, and much more of the energy from within the broadband gain profile will be retained. Homogeneously broadened dye-solvent solutions also undergo rapid thermalization and maintain small energy losses.

Spectral and Temporal Ranges of Mode-Locked Dye Lasers

With the use of broadband mirrors, the spectral width of the dye laser output becomes typically on the order of 100-200 Å. The use of sharply peaked reflectors produces a spectacular narrowing of the spectral width to the order of 1 Å. Gratings (18), birefringent filters (19-22), prism rings (23), and other devices (24,25) are commonly used at present with resultant spectral widths down to the order of 0.01 Å (19). This capability of broadband tunable emission may be contrasted against the spectral output of solid state lasers. At room temperature, the main laser transition at 1.064 μm is 6 Å wide for a 1% Nd:YAG laser (26) and 10-200 Å wide for Nd:glass (27) at 1.060 μm. Through the use of frequency doubling techniques such as second harmonic generation, 0.53 μm light can typically be obtained (depending upon pulse energy) from a Nd:glass laser with about 10% conversion efficiency. Frequency tripling and quadrupling can also be performed with correspondingly lower conversion efficiencies. The major problem of concern with second (and higher) harmonic generation is that the conversion efficiency is greatest at the peak of the mode-locked pulse and the process tends to flatten and broaden the pulses, in opposition to the effect of the modulator (4).

The dye laser has an overall range of tunability extending from 3400 to 11,750 Å, based on a number of dyes found to lase efficiently within this range. The ultimate limitation on this range of laser activity extends from 2500 to 17,500 Å. In the far infrared (17,500 Å), any dye capable of lasing would be subject to thermal instability at room temperature. The lower limit, in the ultraviolet, is an effect of absorption, whereby dyes containing only two conjugated double bonds tend to absorb strongly at 2200 Å, red shifting the laser output to 2500 Å.

A flashlamp pumped dye laser has been tuned and subsequently mode-locked to the point of achieving transform limited pulses by Arthurs, Bradley and Roddie (28). This laser incorporated an intracavity Fabry-Perot interferometer filter as a dispersive element which induced a laser bandwidth of 2 Å, tunable over the free spectral range of 230 Å from 6020 to 6250 Å. The active medium used was Rhodamine 6G and the mode-locking dye DODCI. Being unable to determine accurately the shape of their output pulses, Bradley and Roddie assumed a pulse shape parameter K with a value of 0.5 (corresponding to a combination of Gaussian and Lorentzian profiles). From this, one can readily determine that the spectral bandwidth of 2 Å leads to a theoretical pulse duration of approximately 3 picoseconds. The theoretical and experimental results for this experiment

agree rather well, proving that the transform limit can be approached with a flashlamp pumped dye laser. Transform limited pulses have also been obtained in cw dye laser systems, mode-locked in the same fashion, by the use of a saturable absorber. However, for this type of system, mode-locking is found to be optimum only for powers slightly above threshold, and stable over a very narrow tuning range. For best mode-locking, the cw dye laser must also be operated in a clean TEM₀₀ mode. Failure to meet these conditions can cause the picosecond pulse output to be replaced by a large number of short pulses spread over a range of up to 500 picoseconds (29). Multiple-pulse operation (more than one pulse circulating in the cavity at one time) has also been observed (30) when operating at powers above threshold. The higher average power of a flashlamp pumped dye laser is necessary if the detection of weak fluorescences with quantum efficiencies $\leq 10^{-4}$ is to be performed. Also, the repetition rate of 10-100 Hz by the flashlamp pumped dye laser is more convenient for the study of irreversible decay processes such as photo-dissociation, where the cw repetition rate of 10^2 MHz is much too high. Furthermore, the peak power in a cw mode-locked pulse is on the order of hundreds of watts, to a kilowatt, as compared to the peak powers obtainable from a similar flashlamp pumped system, extending from the kilowatt

all the way to the gigawatt range (with amplification). For studies in which single pulses are required, the flashlamp pumped dye laser is more advantageous.

Repetition Rates

The Nd:glass laser, when mode-locked, produces pulses on the order of 10 picoseconds FWHM, while the Nd:YAG laser produces 25-30 picosecond mode-locked pulses. A problem associated with the neodymium lasers stems from the fact that the pulse repetition rate is typically limited to the order of once per second to once per minute, due to the low thermal stability of the glass. The operation of this type of laser at higher pulsing rates eventually induces optical inhomogeneities in the cavity and subsequent degradation of the laser's mode-locking ability. If the pulsing rate is increased to a point where the active medium is not allowed to undergo total relaxation, permanent optical damage may occur. The flashlamp pumped, mode-locked dye laser does not experience any of these difficulties to the same degree. By flowing the dye through the cavity at a fast rate, the active region is constantly being replaced. A flowing system is more readily subjected to techniques for the removal of optical inhomogeneities caused by temperature gradients. If a large amount of power is transferred to the dye by optically pumping well above the laser threshold, thermal

lensing may occur, which can be corrected by the use of faster flow rates or the use of intracavity correcting optics. If the dye undergoes appreciable photodegradation, it can always be replaced inexpensively.

The typical experimental arrangement of a flashlamp pumped passively mode-locked dye laser is as shown in Figure 1.2. The laser dye is optically pumped by two xenon gas-filled flashlamps which are situated in a double elliptical reflector arrangement. Each of the flashlamps dissipates up to 100 joules of energy in 0.1-1.0 micro-second. The windows terminating the active region are situated at Brewster's angle with respect to the direction of beam propagation. The dye is circulated through a suitable filter and a heat exchanger for mixing and cooling. The saturable absorber dye is contained in a dye cell optically contacted with the rear cavity mirror. The dyes are in alcohol or water solution, depending upon the optical range and thermal stability requirements. A dispersion element (or other suitable tuning element) is located between the rear Brewster window and the mode-locking dye cell.

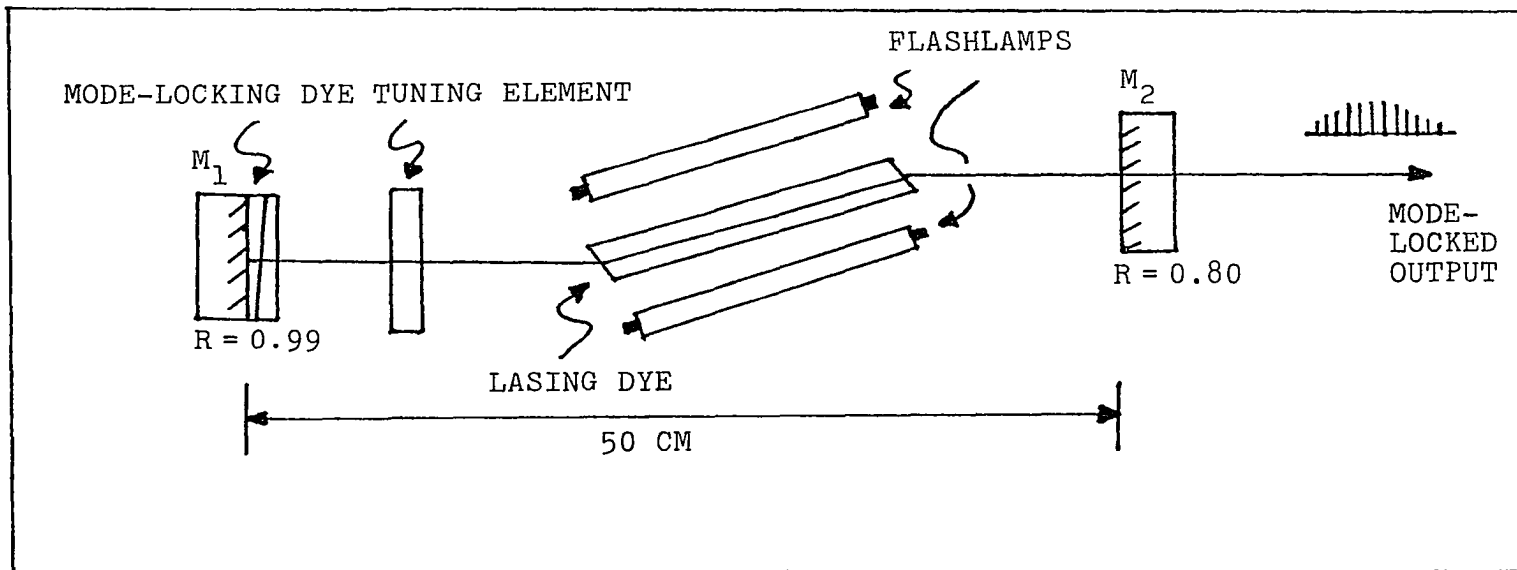


Figure 1.2. Experimental arrangement for mode-locking a flashlamp pumped dye laser

Relaxation Oscillations and Spiking

A major reason for the small impact of the flashlamp pumped mode-locked dye laser on picosecond spectroscopy to date is concerned with the dynamics of pulse narrowing within the cavity. The rate equations governing the characteristics of unmode-locked output for both the Nd:glass and the organic dye laser have been well discussed in the literature by Miyazoe and Maeda (31) and later by Lin (32). The phenomena of "relaxation oscillations" and "spiking" have been well documented in reference to solid state lasers which are subject to pulsed (flashlamp) excitation (33-36). Certain types of lasers are susceptible to spiking, and others are not, depending upon characteristics of both the active medium and the cavity configuration. To present the rate equations in a form generalized to different laser systems one must make the following basic assumptions, in accordance with Figure 1.3.

The laser is represented by a homogeneously broadened ideal four level system, with neglect of the triplet states encountered in dye systems (short pulse excitation is assumed). The lower level population N_1 , is negligible ($W^{-1} \gg t_1 \ll t_2$), where

$$\frac{1}{t_2} = \frac{1}{t_{sp}} + \left(\frac{1}{t_{21}} \right)_{NR} + (\text{transition rates to other levels})$$

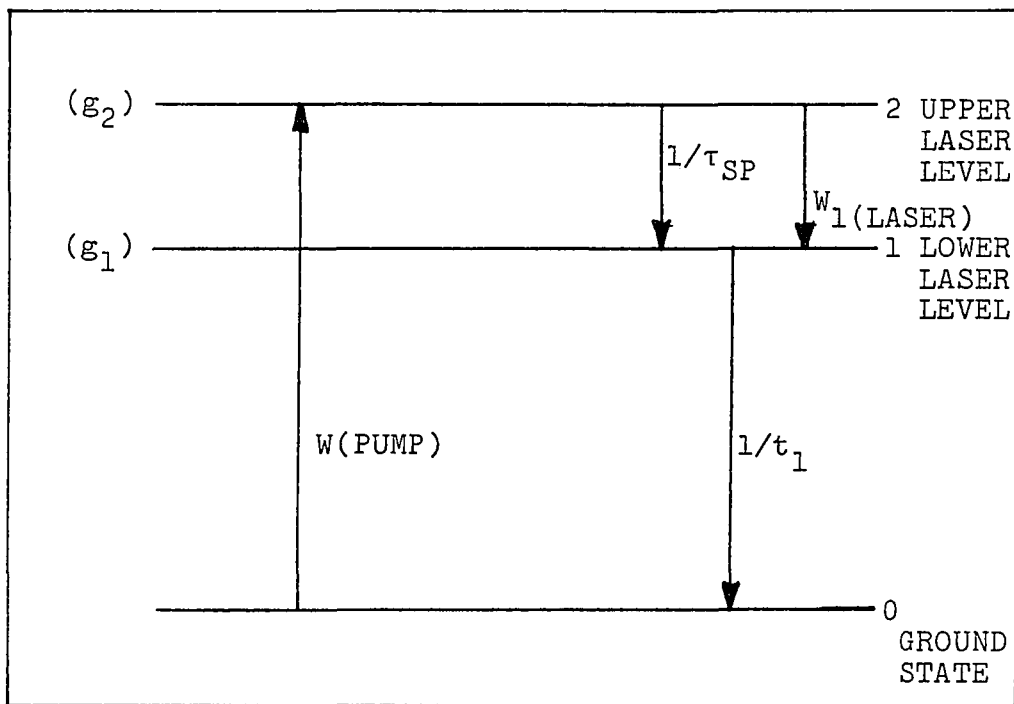


Figure 1.3. Energy levels and transition and relaxation rates of a four-level laser system

and therefore, the population density $N=N_2-N_1(g_2/g_1) \cong N_2$. The rate equations describing the population inversion and the photon density are

$$\frac{dN}{dt} = W - BNq - \frac{N}{\tau} \quad \frac{dq}{dt} = BNq - q/t_c$$

where N is the population inversion, and q is the number of photon quanta in the resonator; B is the Einstein coefficient for stimulated emission; W is the pumping rate; τ is the fluorescence lifetime; and t_c is the photon cavity decay time. If the cavity losses are assumed to be primarily transmissive, then

$$t_c = \frac{T_c}{1-R} = \frac{(n-1)\ell+L}{c(1-R)}$$

where R is the geometric mean $R = (R_1 R_2)^{1/2}$ of the cavity mirror reflectivities; T_c is the cavity transit time, $T_c = ((n-1)\ell+L)/c$ where ℓ and n are the length and refractive index of the active medium, L is the cavity spacing, and c is the speed of light. In an equilibrium situation

$\frac{dN}{dt} = \frac{dq}{dt} = 0$ and we can define the following:

$$N_0 = \frac{1}{Bt_c} \quad q_0 = \frac{W-N_0/\tau}{BN_0},$$

where N_0 is the threshold inversion above which $\frac{dq}{dt} > 0$.

The threshold pumping rate corresponding to N_0 is

$W_t = N_0/\tau = 1/Bt_c \tau$. The basic rate equations may be rewritten

as

$$\frac{dN}{dt} = W - \frac{N}{N_0} \frac{q}{t_c} - \frac{N}{\tau} \quad \frac{dq}{dt} = \frac{q}{t_c} \left(\frac{N}{N_0} - 1 \right)$$

By the use of small signal analysis (the consideration of small perturbations from equilibrium), both N and q can be envisioned as time dependent quantities.

$$N(t) = N_0 + N_1(t) \quad N_1 \ll N_0$$

$$q(t) = q_0 + q_1(t) \quad q_1 \ll q_0$$

The substitution of these quantities into the rate equations and subsequent taking of time derivatives leads to the coupled rate equations

$$\frac{d^2 N_1}{dt^2} + W_0 B t_c \frac{dN_1}{dt} + \left(W_0 B - \frac{1}{\tau t_c} \right) N_1 = 0$$

$$d^2 q_1 / dt^2 + W_0 B t_c dq_1 / dt + (W_0 B - 1/\tau t_c) q_1 = 0$$

where N_1 and q_1 are the small signal perturbations and W_0 is the assumed constant excitation. The differential equations are those describing a damped harmonic oscillator with a damping time constant t_d and an oscillation frequency ω given by

$$t_d = \frac{W_0 B t_c}{2} \quad \omega = \frac{1}{2} \left[\frac{4(W_0 B t_c - 1/\tau)}{t_c} - (W_0 B t_c)^2 \right]^{1/2}$$

Only if ω is real will an oscillatory solution be obtained,

$$\text{i.e., } \frac{4(W_0 B t_c - 1/\tau)}{t_c} - (W_0 B t_c)^2 > 0$$

$$\text{or } \frac{4\left(\frac{1}{t_c} - \frac{1}{\tau}\right)}{t_c} - \left(W_0 B t_c - \frac{2}{t_c}\right)^2 > 0$$

From this, one can see that $\tau > t_c$ is a necessary (but not sufficient) condition for spiking. By defining

$$m \equiv \left(\frac{W_0}{W_t}\right) = W_0 B t_c \tau$$

where m is the ratio of the actual pumping rate to the threshold pumping rate, the necessary and sufficient condition for spiking is

$$\frac{\tau}{t_c} > \frac{m^2}{4(m-1)}$$

Assuming that the laser in question is being pumped close to threshold ($m=1.2$), one sees that as a result $\tau > 1.8 t_c$. Parameters which correspond to our transverse flow dye laser (introduced at a later point in this Introduction) are $n=1.36$, $\lambda = 17.78$ cm, $L = 70$ cm, and $R = 0.89$ ($R_1 = 0.99$, $R_2 = 0.80$). The corresponding cavity transit time T_c is 2.54×10^{-9} seconds and the photon cavity decay time is 2.31×10^{-8} seconds. Therefore, $\tau > 4.2 \times 10^{-8}$ second is necessary and sufficient for spiking to occur. Rhodamine 6G, with a fluorescence lifetime of 7.2×10^{-9} seconds will

therefore not show any oscillatory behavior in this laser cavity. On the other hand, the parameters for a typical Nd:glass laser configuration are $n = 1.56$, $l = 20$ cm, $L = 140$ cm, and $R = (.99 \times .35)^{\frac{1}{2}} = 0.59$ (37). The corresponding cavity transit and photon decay times are $T_c = 5.04 \times 10^{-9}$ second and $t_p = 1.22 \times 10^{-8}$ second, respectively. For a pumping parameter $m = 1.2$, spiking will occur for the condition where $\tau > 2.16 \times 10^{-8}$ seconds. Typical values of τ for an Nd:glass system in a fused silica base range between 0.25 to 1.0 milliseconds (38), approximately five orders of magnitude slower than R6G. As can be seen from these rudimentary calculations, spiking is a phenomenon inherent in Nd:glass and other solid state lasers. However, the Nd:glass laser does not exhibit regular oscillations in time, but rather shows multimoding and random spiking. The explanation of this stems from the fact that the treatment given thus far has been for a homogeneously broadened ideal system, which by theoretical considerations should operate in a single mode. A Nd:glass laser, however, is an inhomogeneously broadened system, where the linewidth of the laser transition is much greater than the mode separation. The random output of the laser is due to the fact that the oscillating modes change from one spike (or set of spikes) to the next, a phenomenon known as mode hopping. Many of the treatments concerned with the mode-

locking process in the Nd:glass laser are based on the "fluctuation model", whereby the initial radiation within the cavity is regarded as consisting of a Gaussian distribution of random noise, exactly as discussed, and to which statistical treatment is readily applied (39-44).

Development of Mode-Locked Pulse Trains in Flashlamp Pumped Dye Lasers

The development of mode-locking in a Rhodamine dye laser is extremely rapid and the ultimate duration of the pulses is much shorter than the recovery time of the saturable absorber dye (45). DODCI, for example, with a relaxation time of 420 picoseconds (46), used in combination with R6G is capable of producing pulses narrowed to less than one picosecond. This is in contrast to the properties of a passively mode-locked solid state system, where the mode-locking process typically takes hundreds of cavity transits to develop (42). The final duration of the resultant pulses of the solid state system are not substantially less than the saturable absorber relaxation time, and theoretical considerations of this effect have been developed (47,48). The dye laser differs from a typical solid state laser in that it operates as a quasi-continuous system, whereby non-linear amplification (gain saturation) plays a role in pulse

development. Quasi-continuous systems contain an amplifying medium possessing relaxation times on the order of a cavity transit time, typically a few nanoseconds. The nonlinear amplification tends to sharpen the trailing edge of a propagating optical pulse. The saturable absorber tends to sharpen the leading edge, and the overall effect is that pulse shortening readily proceeds (49).

The physics of quasi-continuous systems assumes that once a profile has developed such that the pulse width is already less than the recovery time of both the amplifying and absorbing media, there must be a net round trip loss on the leading and trailing edges accompanied by a net round trip gain at the peak. Two conditions must satisfy these criteria for the case of a "slow" nonlinear absorber. First, the relaxation time of the amplifying medium T_{1a} must be of the same order as the cavity round trip time T_{rt} . Also, the cross section for absorption σ_b must be more than twice as large as the cross section for amplification σ_a . For $T_{rt}/T_{1a} \equiv \xi$, if ξ is not large, the amplifier will not recover completely between pulse transits, such that there will be net loss at the leading edge of the pulse. If ξ is too small, there is not quite enough time for the amplifier to recover and nonlinear amplification ceases to play a role in pulse sharpening. If $\sigma_b > 2\sigma_a$, the absorber will saturate before the amplifier, and the unsaturated absorption combined

with incomplete amplifier recovery diminishes the intensity of the leading edge while amplification saturation diminishes the trailing edge. Also, the peak will be favored by absorber saturation provided amplifier saturation is not complete. These criteria set both an upper and lower length on the resonator. If the resonator is of a length such that $\xi > 1$, the amplifier will fully recover. If it is too short such that $\xi < 1$, the amplifier will not undergo gain recovery. In either case, nonlinear amplification will cease to play a role in pulse shaping. A general rule of thumb stemming from this states that any mode-locked dye system can be optimally operated with a cavity length of 50 cm. In giant-pulse solid state systems, the recovery of the amplifier population inversion is so slow that once saturated, the gain never fully recovers, and the saturable absorber will be entirely responsible for pulse narrowing. These considerations were advanced by New (49,50) and later expanded upon by Haus (48,51,52) and Ausschnitt (53).

Mode-locked dye lasers produce the narrowest pulses at the very end of the pulse train, whereas mode-locked Nd:glass lasers produce the narrowest pulses toward the beginning of the train, and the pulses toward the end are broadened in time. Several problems inherent in the Nd:glass system contribute to this type of output. These phenomena, which occur at high output powers, do not affect the dye laser due

to both the inherent nature of the dye solution and the lower output powers achieved. At powers of over 1 gigawatt (peak), secondary pulses, carrying as much as 10-30% of the total energy of the output have been observed. The nonlinear index of refraction of the glass, induced at high power densities, gives rise to self-phase modulation and self-focusing effects. The self-phase modulation (also known as frequency modulation) tends to take place as the nonlinear index n_2 gives rise to a change in the refractive index of the glass matrix when subjected to a plane polarized optical field $E(t)$ corresponding to high power densities (37). The refractive index $n(t)$ is given by

$$n(t) = n_0 + n_2 \overline{E^2}(t) = n_0 + \delta n(t),$$

where the intensity is time averaged and n_2 has the value $(2 \pm 0.5) \times 10^{-22} \text{ m}^2/\text{V}^2$ in BK-7 glass. The change $\delta n(t)$ follows $\overline{E^2}(t)$ within 10^{-14} second and is equal to approximately 0.5×10^{-6} in glass at $1 \text{ gW}/\text{cm}^2$ power density. Therefore, the crests of the optical wave at the peak of the pulse travel slower than those in the wings. A frequency downshift on the leading edge and a frequency upshift on the lagging edge occurs as a result. For a pulse passing through l meters of glass with a corresponding rate of increase in refractive index $\delta n/\delta t$, the frequency shift $\Delta \nu$ resulting in

$$\Delta \nu = -(l/\lambda)(\delta n/\delta t)$$

If $\delta n/\delta t$ is equal to 0.25×10^{-6} at 1 gW/cm^2 and $l = 20 \text{ cm}$, at $\lambda = 1.064 \text{ }\mu\text{m}$ $\Delta\nu = 3.3 \text{ cm}^{-1}$ per round trip.

One study conducted by von der Linde (43) showed Nd:glass mode-locked radiation to have a duration of 5 picoseconds and spectral width of 3.3 cm^{-1} at the beginning of the pulse train, corresponding to a power density of 300 MW/cm^2 . In the latter part of the train (1 gW/cm^2 power density), the overall pulse duration was found to be 11 picoseconds with a spectral width of 67 cm^{-1} , and a corresponding time bandwidth product approximately 40 times that of the transform limit.

For a mode-locked R6G laser utilizing DODCI as the saturable absorber and operating at 6050 angstroms (45), it is observed that the peak pulse energy is reached in about 18 nanoseconds (five cavity round trips), and the risetime ranges from 18 to 40 nanoseconds (five to eleven round trips). It is also observed that after five cavity round trips, the intracavity radiation consists of a group of short pulses of total duration of about 100 picoseconds. This initial envelope is composed of a number of bandwidth limited pulses grouped together very closely with respect to time. After 20 cavity round trips, the single mode-locked pulse shows prominence above the other pulses, whose amplitudes have been reduced drastically. At this point, the duration of the central spike is on the order of

10 picoseconds. After 45 round trips (150 nanoseconds), the single mode-locked pulse is seen to have very little background amplitude present and has reached the point of bandwidth limited duration (for this case, about two picoseconds). Switching of an optimally mode-locked pulse from the flashlamp pumped dye laser becomes difficult because conventional pulse switching techniques using laser-triggered spark gap triggering (54,55) are first, wavelength sensitive, and second, are usually arranged such that a pulse early on in the train is selected. Special nanosecond switching and delaying techniques must be utilized to rectify this situation.

The mode-locked flashlamp pumped dye laser also experiences poor pulse train reproducibility from shot to shot. This can be overcome by operating the laser at a repetition rate of 10 pulses per second or higher. This has proven to be somewhat difficult to date, and all of the existing mode-locked flashlamp pumped dye lasers known employ axial dye flow. High average powers have been obtained with various nonmode-locked flashlamp pumped dye lasers (up to 100 watts broadband, with a peak power of 165 kilowatts (56-58)), employing axial flow systems. However, these systems are limited in output capabilities by the rate of dye exchange within the active region. We have recently completed the construction of a mode-locked

flashlamp pumped dye laser employing transverse dye flow. Transverse flow is attractive in that very high rates of dye exchange can easily be achieved.

Transverse Flow Dye Laser Systems

Transverse flow laser systems utilizing flashlamp pumping have been studied since 1969, when Boiteaux and DeWitte (59) developed the first transverse flow repetitive dye laser. This laser was designed to provide complete dye exchange and avoid refractive index changes resulting from temperature gradients commonly found in axial flow systems. In any dye laser, the optical pumping rate must be proportional to the reciprocal of the dye interchange time, and otherwise, dye interchange will not reach completion between shots. At high repetition rates, and correspondingly, high exchange rates, cavitation and bubble formation are often seen near the windows, causing a degradation of laser output. The Boiteaux and Witte laser readily operates at 50 Hz, being limited only by the repetition rate of the flashlamp triggering apparatus. A stable system employing transverse flow has been operated at a pulse repetition rate of 250 Hz, with 114 watts of average power output (60). With the dye flowing in a transverse fashion, the improvement upon linear coaxial flow is on the order of the ratio of gain length to the width of the dye illuminated

by the flashlamps, a number on the order of 30-40. A transverse flow flashlamp pumped laser built in 1976 by Friedman and Morton (61) readily achieves repetition rates far beyond the limits of axial flow systems. For this system, average powers obtained range from 10 watts at 15 Hz to 2 watts at 500 Hz. A reduction of flashlamp length from 30 cm to 15 cm (along with a reduction in the length of the active region, presumably) produced 2 watts of average power at 1200 Hz. Our dye laser design shares many of the features of the Friedman and Morton laser.

With the exception of the low repetition rate units manufactured by Electro-Photonics, all of the commercial mode-locked dye systems employ a second laser as a pumping source (62), and no other flashlamp pumped systems are available. A notable exception to this is a modified version of the Chromatix CMX-4, as reported by Negran and Glass (63) in 1978. This laser operates at repetition rates of up to 10 Hz to yield reliably mode-locked pulses over a broad tuning range. One of the drawbacks of this laser, however, is the fact that only a small dye cell is employed in combination with a single flashlamp. A second drawback is the fact that the system employs axial flow. The resultant output powers are low, with peak powers reaching approximately 10 kilowatts and average powers on the order of 200 milliwatts. Such a system would be better suited for

the investigation of ultrafast processes by the inclusion of a second flashlamp and a larger dye cell, as well as the employment of transverse flow for achieving higher repetition rates.

Photoelectrochemical Solar Energy Conversion

The conversion of sunlight by solar cells into electrical and chemical energy has received considerable attention in recent years. Efficiency, cost, and operating lifetime are the three main areas of concern in the preparation of solar cells. Physical studies of a particular solar cell design can help to yield the maximum return in each of these areas.

Photovoltaic cells, which convert light into electrical energy, were first realized in devices containing either p-n junctions or Schottky (metal-semiconductor) barriers. Single crystal devices of both types having high conversion efficiencies have been produced. However, the preparation of a p-n junction requires the use of difficult diffusion techniques, while a Schottky-type junction must be alloyed. The semiconductor-liquid junction solar cell (SLJSC) offers an attractive alternative to the other cell types. The cell is formed by bringing either an n-type or p-type semiconductor into contact with a redox couple containing electrolyte and attaching it to an inert counterelectrode (usually carbon or platinum) also immersed in the electrolyte. Rapid electron

exchange establishes equilibrium between the electrochemical potentials of the semiconductor and electrolyte. An extended space charge layer is formed in the semiconductor which acts as a barrier to further charge transfer. As in the solid junction cells, it is this potential gradient which is responsible for the photovoltaic effect. The electron-hole pair produced by photoabsorbption within the semiconductor are accelerated in opposite directions by the gradient. Ideally, oxidation occurs at one electrode and reduction at the other. If no degradation of either the semiconductor or the redox couple is effected, the cell is known as a regenerative solar cell.

The fate of an electron-hole pair generated in a SLJSC is dictated by the magnitude of the field at the junction, the depth at which the charges are produced, and the crystal condition in the bulk and at the interface. Losses which prevent photoproduced charge carriers from doing useful work via the external circuit are referred to as recombination processes. Recombination may manifest itself in the production of heat or light. Nonradiative recombination is by far the dominant process for losses within a semiconductor which contains imperfections. Crystal imperfections act initially as a trap, delaying the process of charge separation. Subsequent recombination may take place if energetically favorable conditions are met during the trapping period.

Lasers provide a convenient excitation source for studies involving solar cells. Using CW lasers, the efficiencies of many different semiconductor-redox couple combinations have been determined. Qualitative arguments for recombinative losses based on these studies have also been presented. The physical picture accompanying the disposal of excess charge is still incomplete, however. The dynamics of the SLJSC, particularly the charge transfer step, have not yet been characterized.

Processes occurring on a rapid time scale may best be studied by introducing an even more rapid perturbation of the system and observing a subsequent response. The dynamics of the SLJSC may best be resolved using either picosecond or nanosecond photoexcitation and observing the rise and decay of the resultant photocurrent transient. Careful analysis of artifact-free transients provides insight into the physical picture of the movement of charge through the cell.

The following chapters deal with the construction and characterization of our mode-locked transverse flow dye laser and its implementation in transient photocurrent studies of SLJSCs. Chapter II specifically deals with the laser head design, paying special attention to the electronics used to drive the flashlamps and single pulse extractor. Chapter III covers the characterization of the output of the laser. Chapter IV presents a general discussion of the semiconductor-

liquid junction solar cell, along with transient studies performed to date. Chapter V describes the experimental conditions of the transient photocurrent studies. Chapter VI shows the resultant data along with interpretations. Chapter VII includes a discussion, conclusions, and suggestions for future work.

CHAPTER II. LASER DESIGN AND CONSTRUCTION

Motivation for Design

The design and construction of a mode-locked flashlamp-pumped transverse flow dye laser (Fig. 2.1) was motivated by the previous design of a nonmode-locked transverse flow laser by Friedman and Morton (61). As previously mentioned in the Introduction, high repetition rate operation is the major advantage of this laser configuration. Mode-locked operation (64,65) of the transverse flow dye laser should provide stable, high repetition picosecond train output.

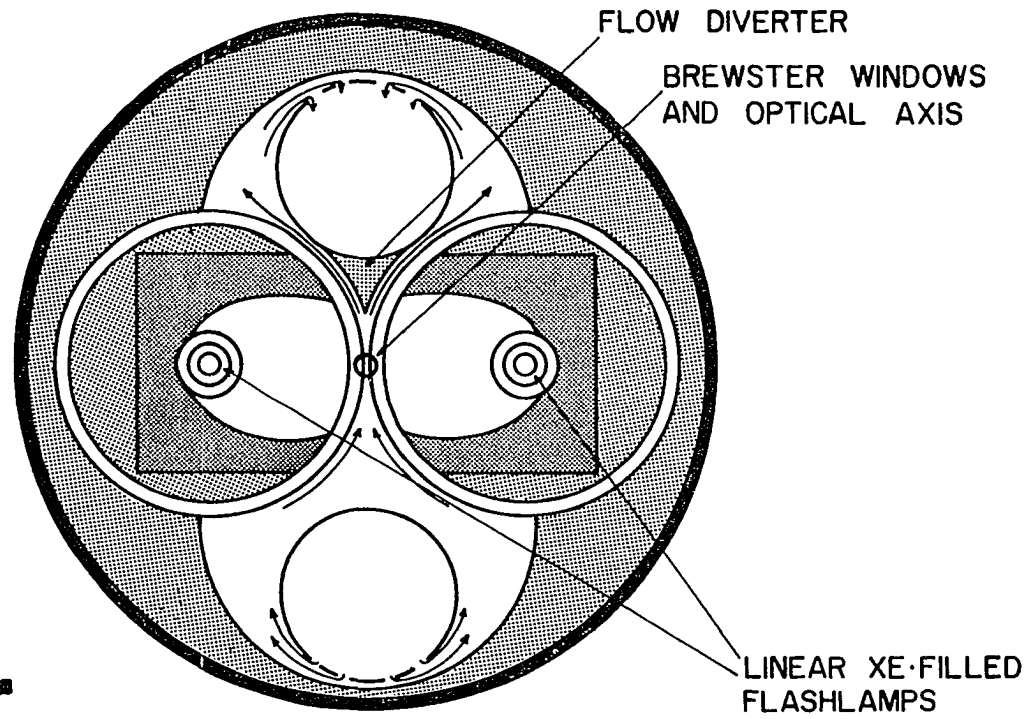
In preparation for the construction of a design of novel origin, the problems which are to be encountered should be given due consideration beforehand. The first variable to undergo consideration is that of the optical pumping source, in this case, the flashlamps.





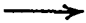
Flashlamps

One general feature of the dye laser is that the upper laser level has a lifetime approximately five orders of magnitude smaller than that of a solid state laser (66). The laser dye will only store energy for a few nanoseconds. This leads to the practical consequence that since the flashlamp pulses have durations of approximately one micro-

Figure 2.1. Cross section of transverse flow dye laser (end view)

TRANSVERSE CROSS SECTION



- SS 304 
- PYREX 
- NYLON 
- ALUMINUM 
- DYE FLOW 

second or longer, the single pass gain in a solid state laser depends on the total light energy supplied by the flashlamps, while the gain in a dye laser is extremely sensitive to flashlamp pulse risetime. For example, a ruby laser has a rather small saturation intensity I_s (a few kw/cm^2), but a rather high stored energy (a few J/cm^3). A dye laser has a large saturation intensity I_s (a few hundred kw/cm^2), but very poor energy storage capability ($1 \text{ mJ}/\text{cm}^3$). Thus, a solid state laser can best serve as an energy amplifier while a dye laser can best serve as an intensity amplifier in which weak signals have to be amplified to moderate power levels.

The existence of a triplet-level system in parallel with a singlet-level system in laser dyes requires that a high-brightness short-duration optical pumping source be used for excitation. If the leading edge of the flashlamp pulse rises linearly in time, attaining a maximum value at time τ_m , laser action is possible only if $\tau_m < \tau_\ell$, where τ_ℓ is defined as

$$\tau_\ell = (2/k_{S,T})(\epsilon_{SS}/\epsilon_{TT}). \quad (2.1)$$

$k_{S,T}$ is the first excited singlet state to triplet state intersystem crossing rate, ϵ_{TT} is the triplet-state molar absorptivity, measured at the lasing frequency, and ϵ_{SS} is the singlet-singlet molar absorptivity, measured at the peak of the absorption band (which is the mirror of the laser

emission band). If nonradiative emission from the first excited singlet state S' to the ground state S are neglected, the critical time, τ_{λ} , can be written as

$$\tau_{\lambda} = [2\tau/(1-\phi)][\epsilon_{SS'}/\epsilon_{TT'}], \quad (2.2)$$

where ϕ is the fluorescence quantum efficiency and τ is the observed fluorescence lifetime:

$$\tau^{-1} = \tau_F^{-1} + k_{S,T}. \quad (2.3)$$

τ_F is the true radiative lifetime of state S' . Assuming that equation (2.2) is applicable to the xanthene dyes (e.g., R6G, RhB), and that values of $\phi = 0.9$, $\epsilon_{SS'}/\epsilon_{TT'} = 10$, and $\tau = 5 \times 10^{-9}$ seconds are appropriate, a critical time of $\tau_{\lambda} = 1 \times 10^{-6}$ seconds is obtained. Specialized flashlamps capable of delivering submicrosecond pulses of 10 to 100 joules are commonly used. Various efficiencies of electrical energy conversion to photon energy have been reported in the literature with an average of 10% being acceptable (14,67, 68).

Nonuniform heating of the dye solution warrants careful consideration. Close coupled linear flashlamps (e.g., aluminum foil close wrap) have been observed to cause the active medium to become prism or lenslike, focussing or defocussing the laser beam (69). A spiral flashlamp of the type normally used in solid state lasers was also observed to cause optical inhomogeneities and did not exhibit very

good conversion efficiencies (due to very long output pulse durations) (70). A coaxial pumping lamp is hindered by the fact that it produces a spatially inhomogeneous plasma and subsequent nonuniform pumping (7). This type of excitation tends to disperse energy into higher order transverse modes in a fashion randomized in time. High overall angular divergence accompanies this effect. This angular divergence problem may be explained by the influence of an ultrasonic wave (shock wave) which propagates through the active medium. The variation in refractive index due to pressure increase is even greater than that due to heating effects (71).

The type of lamp which is most ideally suited for dye laser optical pumping is the linear flashlamp, which may be readily isolated from the dye and contained within an elliptical cavity (72) which focusses the lamp radiation onto the active region. The lamp is normally filled with xenon gas because of its wide range of high spectral intensities in comparison to the next best lamp fill, argon (73). The original lamps chosen for this project were modified N-701C water cooled linear quartz flashlamps with a 3 mm bore, purchased from Xenon Corporation. The lamps had a longer quartz envelope than the stock version, extending the distance between electrodes from 3.5 to 6.0 inches. The external dimensions of the lamp are 7 mm O.D. about the gas fill region, and 9 mm O.D. about the electrodes. Problems

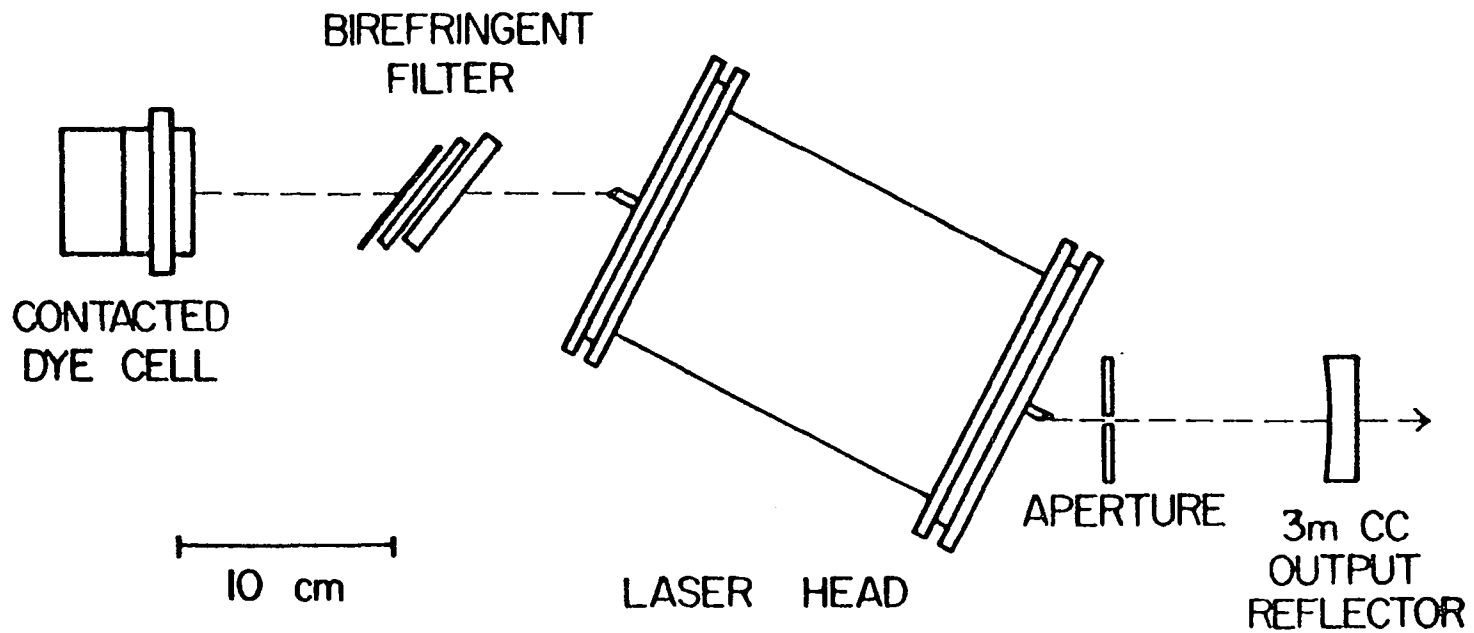
encountered with these lamps included explosion (caused by increasing the pumping power to, or beyond the explosion limit), cracking, and channeling of the lamps. Three types of ILC Technology lamps were also used in the laser. The first type utilized was the L-3690, with a 7 mm O.D. and a 3 mm bore, along with a 50 torr Xe fill. The second type utilized was the L-3628 with a 3 mm bore and 5 mm O.D., with 7 mm about the electrodes. This lamp contained a 200 torr fill of xenon. The third type utilized was the L-3689 with a 4 mm bore, 6 mm O.D., and a 50 torr fill. The L-3690 lamps have provided moderate to good operational lifetimes. The L-3628 lamps are thin-walled and prone to explosion at high input powers, and are therefore unsuitable; the L-3689 lamps tend to show barium deposits from the electrodes along the inner walls of the lamps. It appears that the electric discharge tends to follow the path of the deposit, thereby degrading the output properties of the lamp. The best lamps to date to be used in this laser cavity are EG&G FX-139C-6 flashlamps, 29 centimeters maximum length, with a 350 torr xenon fill and a 6 inch arc length. Degradation of these lamps occurs very slowly, and they can provide good mode-locked output for extended periods of time.

Resonator

The resonant cavity design consists of a dye head and two dielectric mirrors (Figure 2.2). Each of the cavity mirrors is mounted in an Oriel #1170 2 inch precision mirror mount fitted with an adapter to accommodate the one inch diameter mirrors used in the system. The rear mirror mount may be translated perpendicular to the beam axis by means of a Newport Research Corporation #420 precision translation stage fitted with a 1.00 inch travel micrometer. The dye laser cavity is 65 cm (± 1 cm) long, with the dye head (as measured from the front to the rear Brewster window) occupying 26.4 cm of the total cavity length. The head is angled within the cavity at 21.1 (± 0.1) degrees such that the beam will be incident upon the windows at Brewster's angle (55.55 degrees for fused silica). The entire resonator is mounted on a rail system employing three 1.25 inch diameter stainless steel rods four feet in length. The stainless steel rods are in an inverted triangular configuration, with three one inch thick aluminum plates holding them rigidly in this fashion. The aluminum plates are securely fastened to a Newport Research Corporation RS-48-8 4'x8'x1' optical table. This configuration reduces the effects of room shock and vibration on the laser cavity.

Figure 2.2. Dye head, dielectric mirrors, and contacted mode-locking dye cell

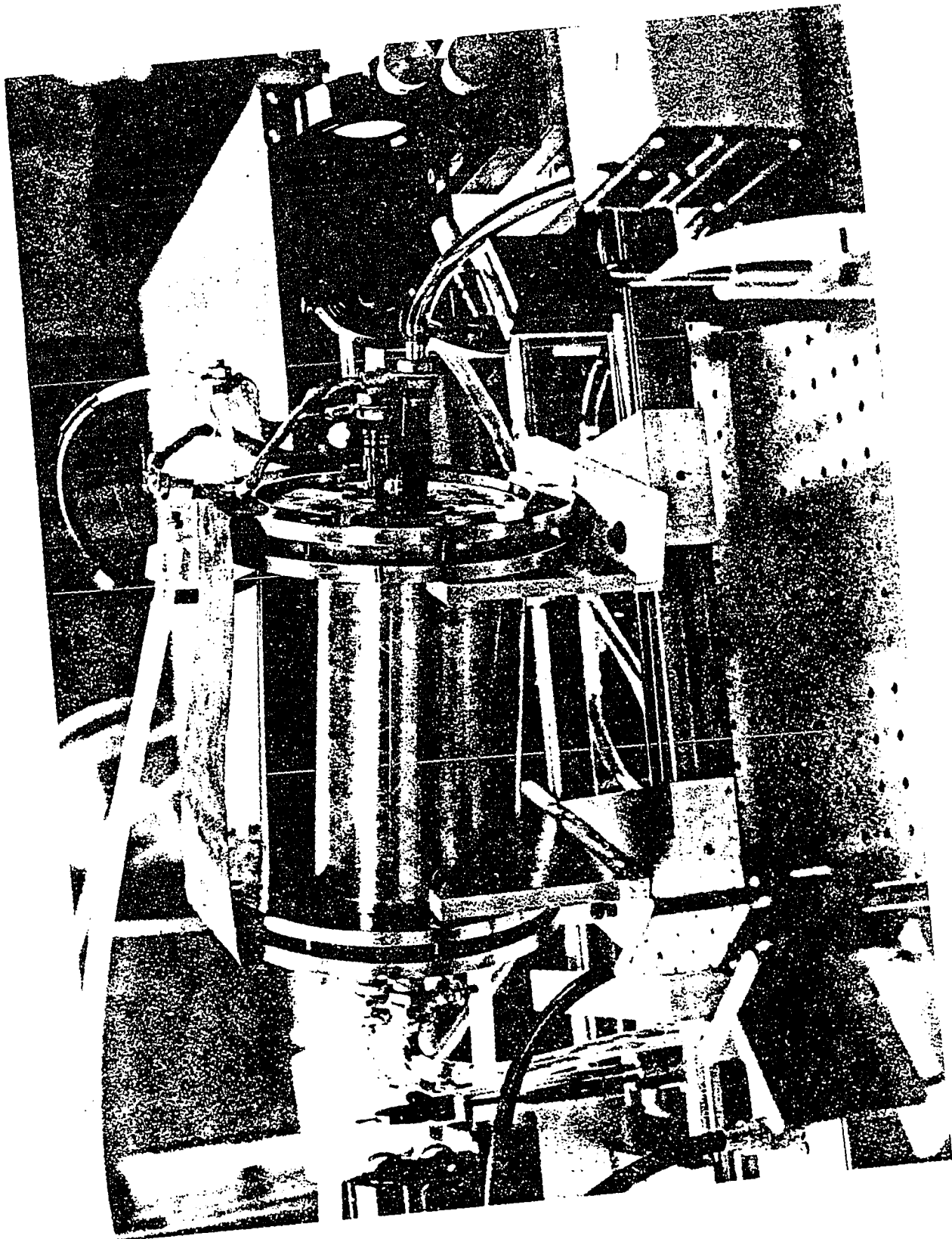
MODE-LOCKED TRANSVERSE-FLOW DYE CAVITY



Dye Head

The dye head consists of a cylindrical stainless steel canister with a press fit nylon core (an assembled view of the dye head may be seen in Figure 2.3). The core is 5.875 inches in diameter and 7.75 inches long. A section from the center resembling a cloverleaf pattern has been removed along the entire length of the core as shown in Figure 2.1. The two horizontal lobes of the "cloverleaf" are fitted with 70 mm O.D., 64 mm I.D. Pyrex tubes 8.0 inches in length. Specially designed sleeves which hold the elliptical reflectors are contained within the tubes. The foci of each ellipse are located 1.50 inches apart and the major and minor axes measure 2.00 and 1.32 inches, respectively, as depicted in Figure 2.4. The reflectors were cut from brass stock and overcoated with silver. Aluminum, in turn, was vacuum deposited on top of the silver to ensure higher reflectance below 370 nanometers. The reflectance of silver is approximately 96% from 370 to 1100 nanometers, while the reflectance of aluminum averages approximately 90% over this range. From 370 nanometers to 320 nanometers, however, the silver reflectance decays from 95% to 5%, while the aluminum reflectance remains above 90% (74). The reflectivities of both metals are shown in Figure 2.5, along with a typical xenon flashlamp output spectrum. It is readily seen that there is high output

Figure 2.3. Dye head and mode-locking dye cell. The optically contacted cell is to the right of the picture



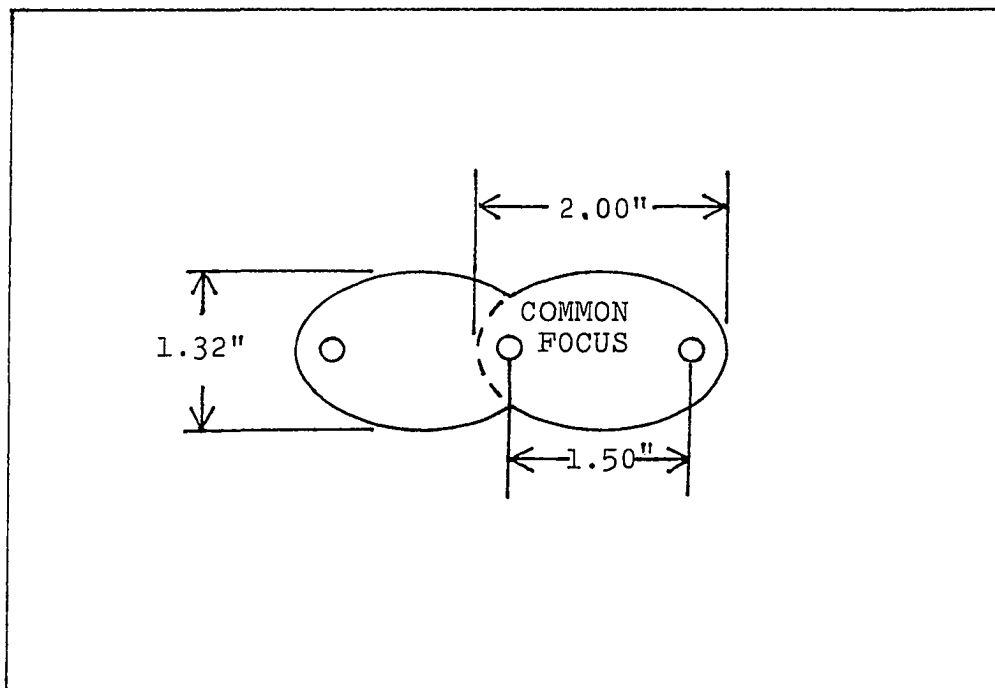


Figure 2.4. Elliptical cavity schematic

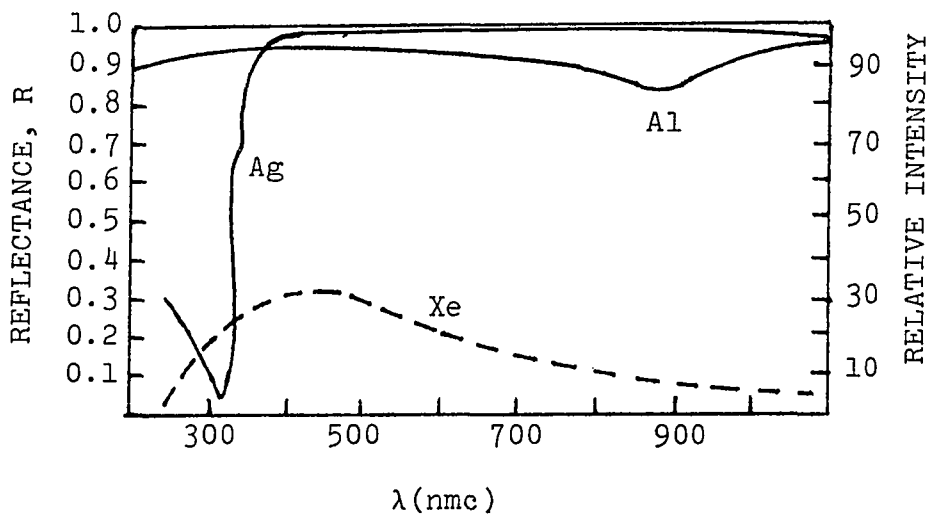


Figure 2.5. Reflectance versus wavelength for silver and aluminum and typical xenon flashlamp output spectrum (only continuum portion of xenon spectrum shown)

intensity from the lamp occurring between 300 and 400 nanometers (15), which may be better utilized by employing aluminum as the reflective surface.

The dye flow through the head proceeds upwards through the dye channel formed by the two glass envelopes. Cavitation problems are eliminated by the placement of a cusped nylon flow diverter directly below the dye outlet manifold. Both the inlet (bottom) dye manifold and the outlet (top) manifold are constructed of stainless steel. The end plates of the canister are constructed of glass-filled Teflon with milled slots replacing many of the normally drilled holes, such that the width of the active region may be easily adjusted between the lower limit of 2 mm and the upper limit of 5 mm. Originally, the end plates were constructed in such a way that many o-rings were necessary for totally sealing the fluid flows within the head. Two sets of end plates were used, the inner being constructed of Lexan (polycarbonate sheet; Plexiglass) with outer plates of stainless steel being used to hold the inner plates in position and to seal the head. This configuration did not prove suitable because the inner plates were affected by the dye solvent, showing cracking, some dissolution and discoloration. By changing to the glass-filled Teflon end plates, which are largely unaffected by the dye solvent, this problem was eliminated. Many of the o-rings used for

sealing were also eliminated, making the head sealing less complicated. The Teflon end plates are secured to the head by a stainless steel ring which bolts through to the flange on the canister, as shown in the horizontal and vertical cross sections in Figures 2.6 and 2.7.

The flashlamps were originally cooled by passing water directly through the entire elliptical reflector cavity on each side. Problems associated with this method included oxidation of the reflector material and insufficient flow rates due to the large cavity cross sectional area which caused warming of the dye within the active region. This system has since been modified so that the lamps are contained in cooling jackets of Pyrex glass whose inside diameter is just slightly greater than the O.D. of the lamp. The medium between the lamp coolant tubes and the glass envelopes which channel the dye flow is simply ambient air. Holes in the endplates in between the lamp and the window allow the reflector area to maintain the ambient operational temperature of approximately 25 degrees centigrade.

Four nylon multiple-slip-ring plates serve to make all of the seals between dye, water and air. Their design may be seen in Figure 2.6. When tightened from the outside of the endplates, the slip rings press outward on the o-rings and seal the large glass envelopes in place.

Figure 2.6. Horizontal cross section of transverse flow dye laser

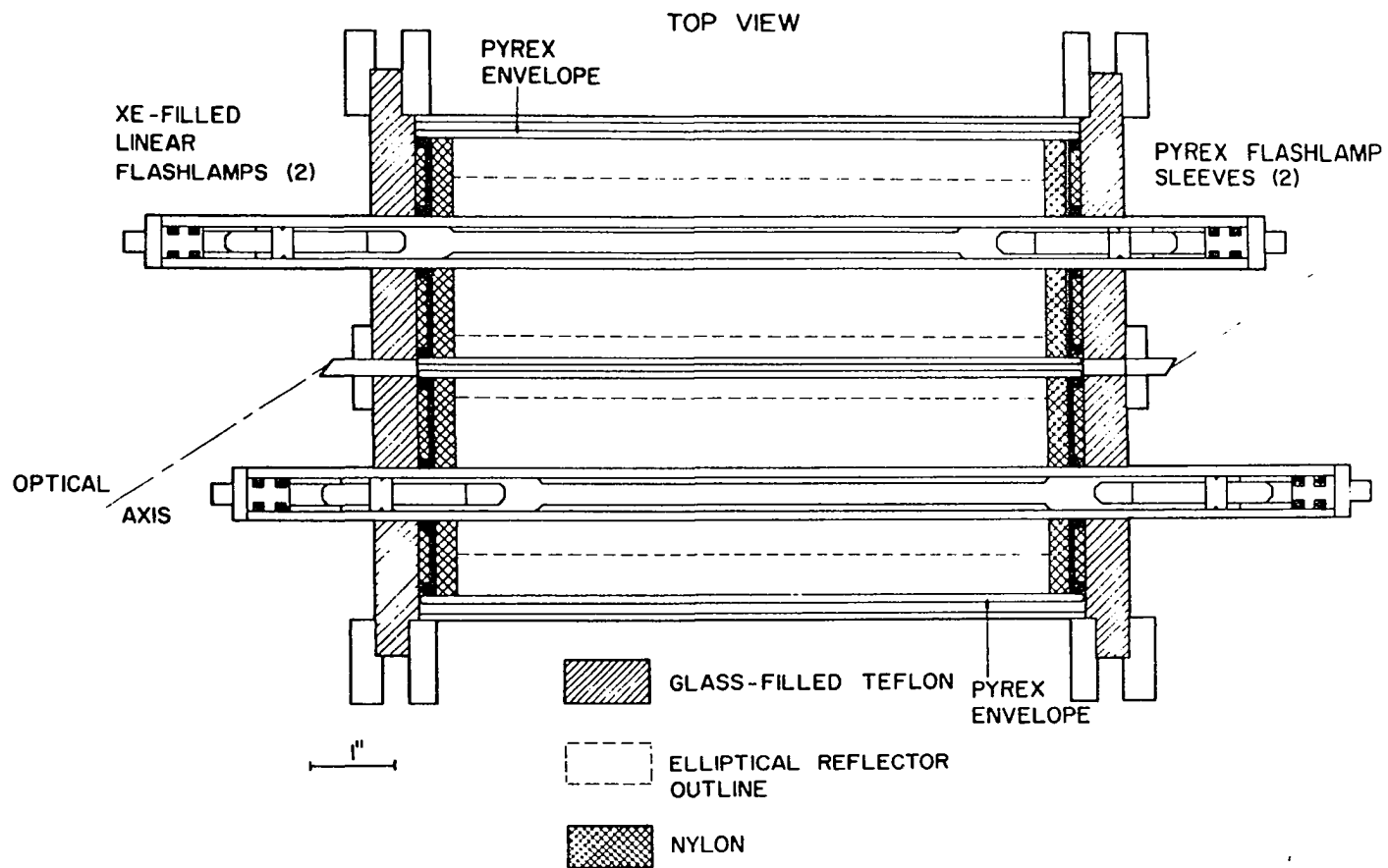
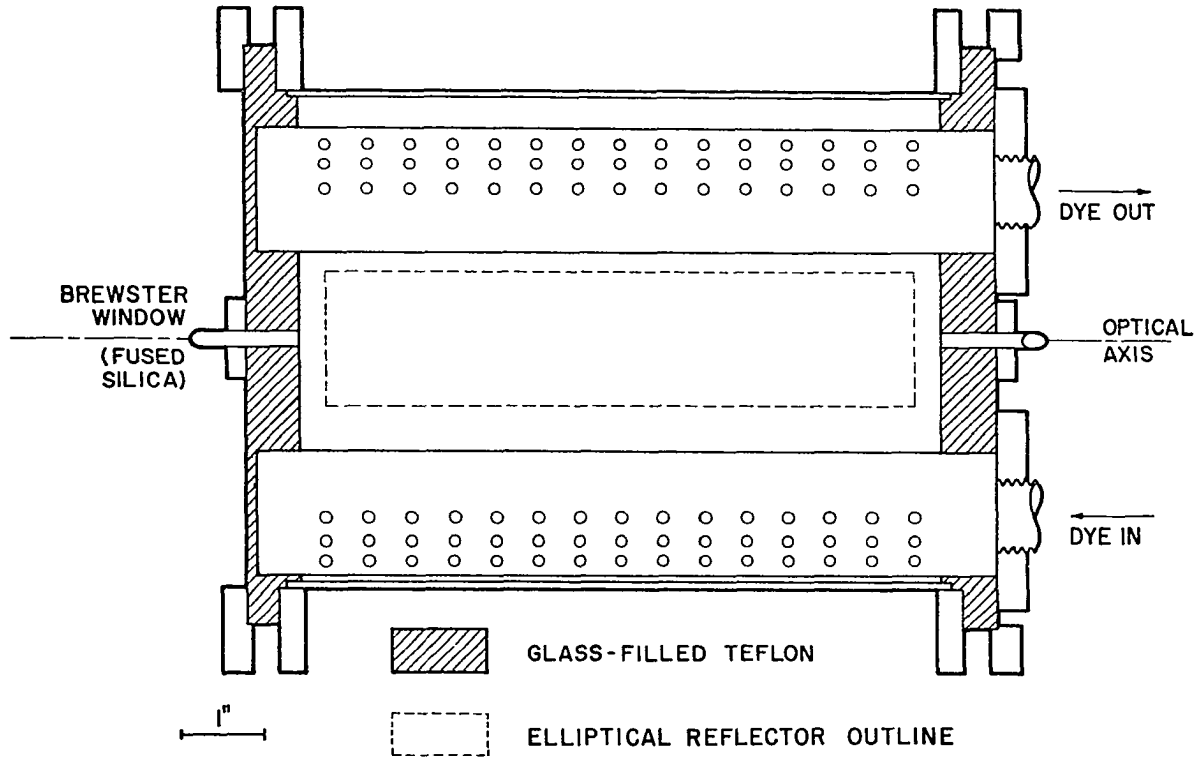


Figure 2.7. Vertical cross section of transverse flow dye laser

SIDE VIEW



Several problems have arisen from the choice of glass-filled Teflon as the material for construction of the end plates. Glass-filled Teflon does not have the optimum rigidity for this type of a system. Stainless steel studs used for securing the dye manifolds and Brewster end windows have tended to pull away from their tapped holes. The plates also tend not to sit perfectly flat, causing some stress on the internal parts of the head (glass envelope breakage has proven to be a problem). Also, the holes for the Brewster end windows are flexible enough to allow the windows to be a few arc minutes off from the beam axis, causing some alignment problems. Finally, the end plates have shown some discoloration caused by the use of the Rhodamine dyes. This could possibly cause problems upon switching to a dye which does not belong to the Rhodamine family (e.g., a coumarin dye). A more rigid material which is unaffected by dye-solvent mixtures, such as nylon, would be a superior end plate material.

One point to note is that the only materials used within the head are glass-filled Teflon, stainless steel, glass, and nylon. The few o-rings within the head have a very small amount of surface area directly in contact with the dye, and upon inspection seem totally unaffected by it (R6G or Rhodamine 590 in ethanol).

Flow Systems

A schematic of the flow systems incorporated in this laser is shown in Figure 2.8. The dye is pumped by means of a Gorman-Rupp #7146 centrifugal pump head coupled in line with an Eastern Industries 1/5 horsepower 6000 rmp pump motor. By using this type of arrangement in combination with a variac for pump speed control, high dye velocity within the head can be maintained. From the pump head the dye flows through a BCF 03008-002 American Standard heat exchanger with 2.4 square feet of internal surface area, and then through an ABLAK3J Pall Trinity Micro Corporation filter cartridge encased in a PTMC polypropylene filter housing. This type of filter will remove 100% of 0.65 μm or larger material from solution. The main concern of placing this filter in such a position is to remove any small bubbles produced by the pump head which would cause optical inhomogeneities to appear within the resonator. The dye flow continues from the filter to the bottom manifold of the laser head, a stainless steel tube running the length of the active region with a grid consisting of a number of 1/8 inch diameter holes drilled along the bottom surface. Several smaller holes have also been drilled along the upper surface of the manifold to remove any bubbles which appear when the dye head initially fills with dye solution. After travelling through the active region, the dye exits via a grid of

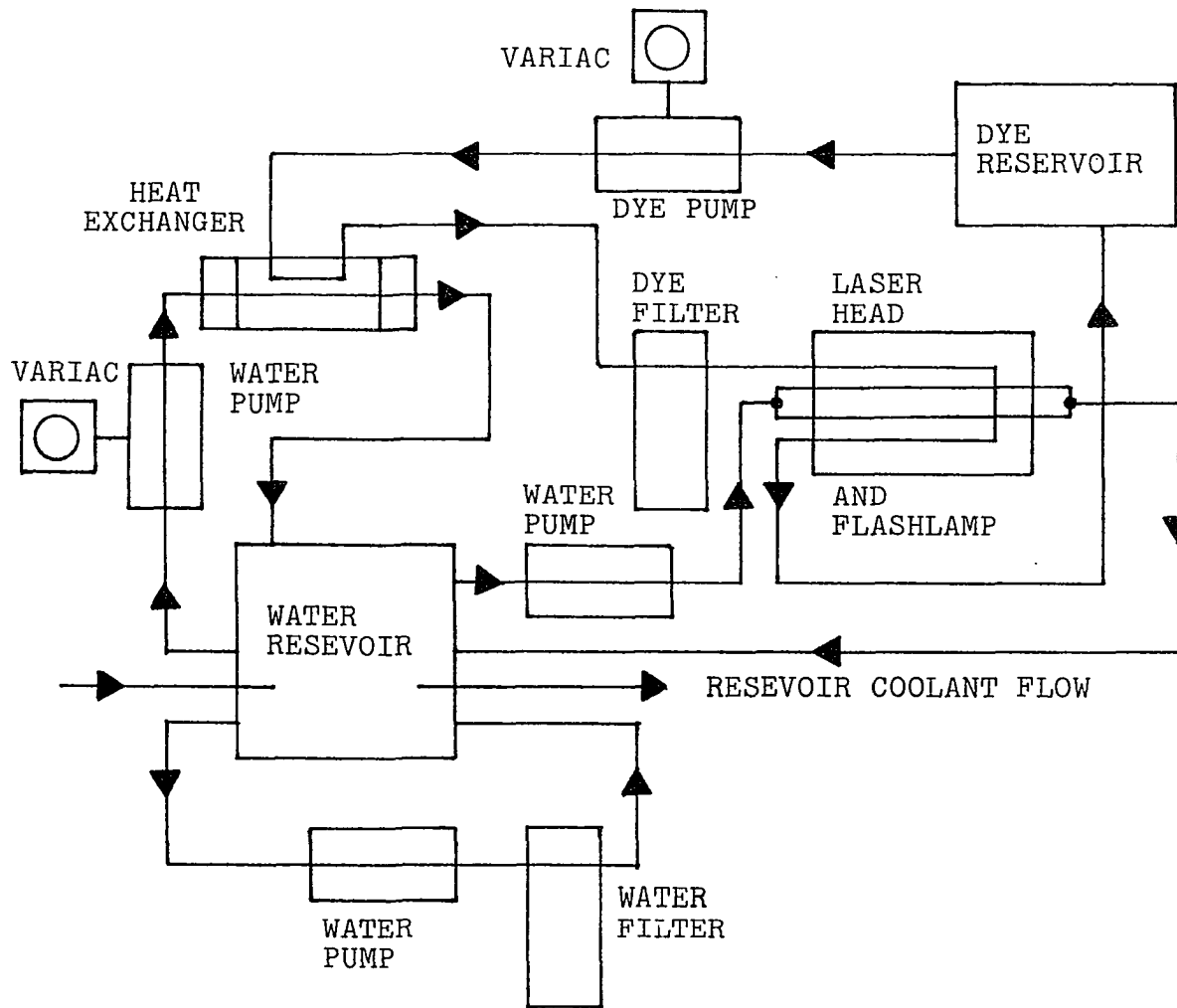


Figure 2.8. Dye and coolant flow systems

holes on the upper half of the exit manifold. Both entrance and exit manifolds are attached to the flow system through the front of the head. No sharp edges are met by the dye up to the active region and all flow lines consist of 1/2 inch polyethylene tubing. The dye exits the head and returns to a pumping reservoir. The reservoir volume is generally maintained such that there are approximately four liters of dye solution within the entire system at all times.

The coolant system employs deionized water to cool both the flashlamps and dye solution. A 20 liter water reservoir holds the deionized water, which is distributed by several pumps. Within the reservoir lies a cooling coil consisting of several turns of stainless steel tubing. A Gorman-Rupp #7136 centrifugal pump is coupled to 1/2 inch I.D. polyethylene tubing. The latter is attached to a T-joint from which two 3/8 inch I.D. Tygon tubes extend to the electrodes of the flashlamps which are located in the front of the head. The parallel flow system cools both lamps and the coolant flows out through the rear of the head. A similar parallel arrangement with a T-joint returns the water to the reservoir. A March Manufacturing Company model AC-2CP-MD magnetic drive pump provides water flow to a Crystalabs Deem-A-Flow water deionizer model DF-500 containing a DNF-525 ion exchange resin filter cartridge. A

Crystalabs Ionlite II is connected to the filter outlet to assure that the water remains deionized to within 25 ppm. The water return from the ion exchange filter goes back to the reservoir. By using the filter in a parallel fashion, as described, it does not provide a "bottleneck" to rapid coolant flow. A modified pump of the same type used for pumping the dye solution is used for flowing water through the tubes of the heat exchanger. The heat exchanger is nickel coated to avoid corrosion of the brass of which it is constructed and to avert subsequent deterioration of the coolant. A Statco variac provides the rate control of water flow through the heat exchanger.

The dye flow system is approximately linear in flow rate with respect to variac setting (see Figure 2.9). The flow in liters/min is equal to $0.22 \times [\text{the variac setting (in \% of 120 volts full setting)} - 5.83]$ (indicating that the pump will not operate at lower variac settings). Generally, the system is run at a setting of 50, giving a flow rate of slightly better than 5 liters/minute. The volume of the active region is $0.5 \text{ cm} \times 4 \text{ cm} \times 17.8 \text{ cm} = 3.56 \text{ cm}^3 = 3.56 \times 10^{-3}$ liters. At a setting of 50, this corresponds to slightly better than 23 dye exchanges per second. A setting of 70 corresponds to a dye exchange rate of 9.5 liters/minute. This will yield 44 dye exchanges per second. The flashlamp coolant flows through the head at a

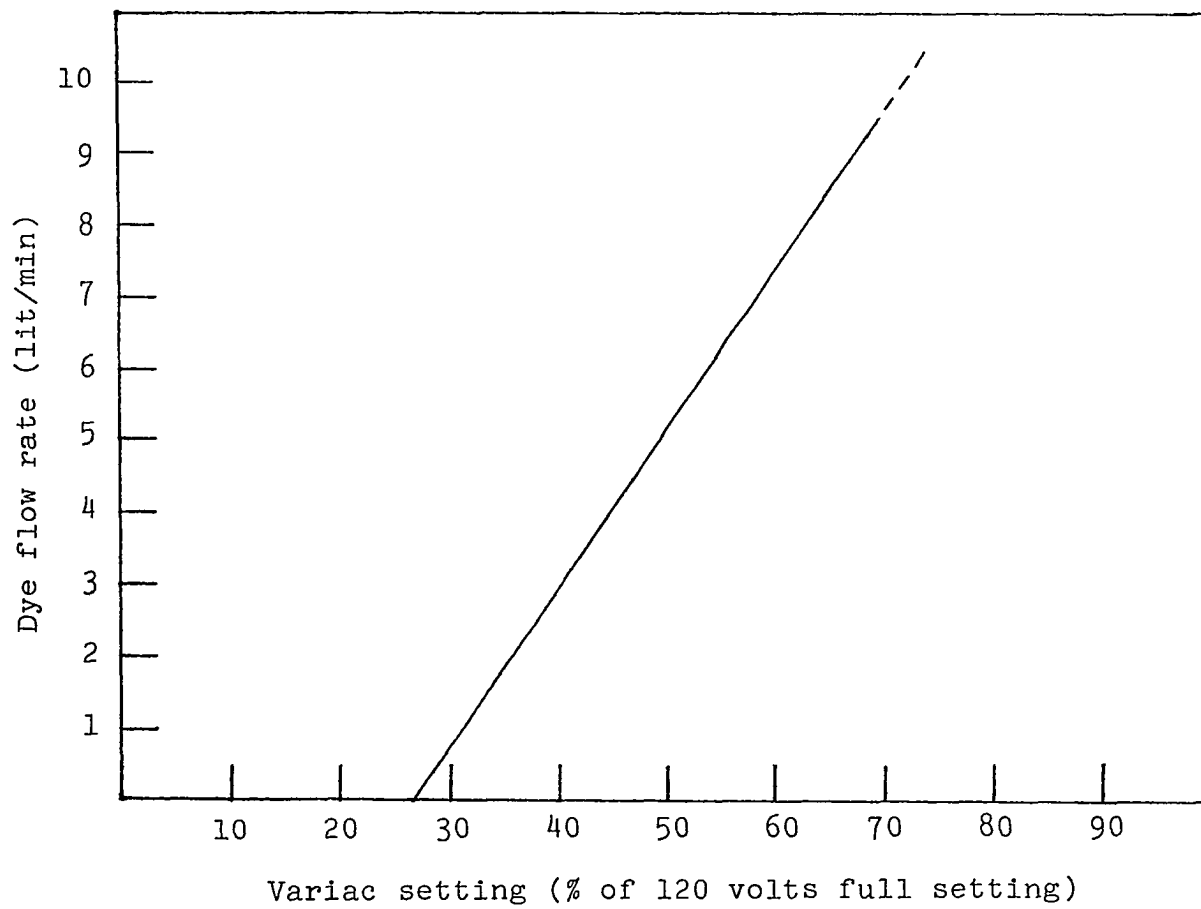


Figure 2.9. Dye flow rate versus variac setting

rate of 5.2 (± 0.2) liters/minute. A variac setting of 50 will pass 4 liters/minute of coolant through the heat exchanger while a variac setting of 60 will pass 9 liters/minute. For variac settings below 40, the pump will not turn. The inability to achieve slower flow rates can cause problems in the system, as is to be shown.

Thermal and Acoustic Distortion Effects;

Thermal Lensing

Since the dye solutions used in this type of laser have very fast fluorescence decay times on the order of 2 to 10 nanoseconds, the optical pump power density must be quite high, on the order of kilowatts/cm³, in order to prevent excessive fluorescence losses and achieve gain. The insertion of a tuning element into the cavity tends to condense the output linewidth with very little energy loss and much increased spectral brightness. The resultant higher power operation creates a problem in that the liquid medium tends to thermally distort. Upon optical excitation, heat is generated by the optical pumping source, which in time changes the temperature of the dye solution due to the temperature dependence of the index of refraction of the solvent. Beam quality will become degraded and if enough optical inhomogeneity is incurred, laser action will

terminate completely (75). For a temperature difference ΔT transverse to the direction of lasing, the optical path length difference ΔL is

$$\Delta L = \ell \left(\frac{dn}{dT} \right) \Delta T$$

where ℓ is the length of the liquid solution (active region). Under the assumption that an optical path length greater than $\lambda/2$ is unacceptable,

$$\ell \Delta T < \lambda/2 \left(\frac{dn}{dT} \right)$$

where λ represents the output wavelength, in angstroms. Values of $\ell \Delta T$ for different solvents may be found in reference 73 (where $\lambda = 6000 \text{ \AA}$). Water has a very low value of dn/dT ($-8 \times 10^{-5} \text{ } ^\circ\text{K}^{-1}$) yielding a high value of $\ell \Delta T$ (0.375°K cm). For the 7 inch long active region employed in this laser, the temperature transverse to the lasing direction must be maintained to 0.021°K . If the case is such that the dye has a low fluorescence quantum yield in water, a different solvent must be used. Such is the case for R6G in ethanol, the dye-solvent combination commonly used in our laser ($dn/dT = -40 \times 10^{-5} \text{ } ^\circ\text{K}^{-1}$). The temperature must be realistically maintained to within less than 0.004°K .

Index of refraction gradients also occur during the pumping pulse. The maximum temperature rise during a single pump pulse is

$$\Delta T = E / (A \ell \rho C_p)$$

where E is the heat energy deposited by the optical pump pulse, A is the cross sectional area of the dye cell, ρ is the density of the solvent and C_p is its specific heat. The optical path length difference Δn is defined by

$$\Delta n \ell / \lambda = \frac{E}{A \rho C_p \lambda} \left(\frac{dn}{dT} \right)$$

For this system, in a mode-locking situation at 6000 Å, E is approximately 50 joules, ρC_p is 1.9 joule $\text{cm}^{-3} \text{K}^{-1}$, A is 0.20 cm^2 , and therefore $\Delta n \ell / \lambda = 877$. If the optical pumping is uniform along the length of the active region, this change in refractive index will not deflect the beam. If the requirement that $\Delta n \ell < \lambda / 2$ is once again imposed, the pump distribution must be uniform to within 0.06%.

If the excitation pulse is very short, on the order of a microsecond, the change in the index of refraction cannot follow the excitation pulse and changes come about as an acoustic effect instead. The sound waves produced by temperature differences in the dye solution are driven by the resultant pressure gradients. This effect is detected as a time dependent beam divergence and premature termination of the laser pulse (76).

Thermal lensing takes place if a sufficient difference exists between the two fluids on opposite sides of the 70 mm Pyrex envelopes. In this laser system, the second fluid is

ambient air. Drake and Morse (77) conducted an experiment whereby the effects of coolant-dye temperature gradations were studied. They found that for a 10^{-4} molar solution of R6G in EtOH with oxygen as a triplet quencher, there are two distinct regions of laser operation.

T_d = dye temperature

T_c = coolant temperature

$\Delta T = T_d - T_c$

When ΔT is positive, a divergent thermal lens forms creating an unstable resonator with a resultant loss in laser output of 25% per degree of temperature difference. However, for a system in which ΔT is negative, the thermal lens is convergent, creating a stable resonator for which the loss in laser output is only 10% per degree of temperature difference. By keeping the dye slightly cooler than the ambient temperature, our system should be most stable. Overcooling of the coolant solution, when running at one hertz, has been discovered as a problem in our system. Output power was observed to increase with simple thermalization of the dye solution with the surrounding air, bypassing the heat exchanger as a functional component in the system. The problem actually centers around the particular pump being used, which has a threshold flow rate for operation. Replacement of this pump with one which will

pump at a slower rate should rectify the situation.

In their transverse flow laser paper (61), Friedman and Morton discuss the effects of temperature differences within their system. The problem of thermal lensing appears to be solely related to average output power and not single pulse phenomena. At a dye flow rate of 5.7 liters/minute with 100 joule/pulse input, thermal lensing effects were seen to degrade laser output only for repetition rates greater than 20 Hz. Slower flow rates imposed much lower limits on allowable repetition rates. The focal lengths of the resultant lenses formed have been calculated. For a 100 joule pumping pulse at 20 Hz, a lens with a focal length of 7 meters is formed which reduces to 2.5 meters at 30 Hz. To correct for this problem, a cylindrical lens was inserted into the cavity. As well as countering self-focussing effects, the tuned bandwidth of the output was also reduced by a factor of 14 for 30 hertz, 100 joule operation. Our laser has no need for a lens correction due to 1) separation of the two flow systems within the dye head by an air gap, and 2) the capability of much higher flow rates through the heat exchanger than obtained by Friedman and Morton.

Polarization of Laser Output

If an electromagnetic wave travelling through a medium is incident upon a second medium, the angle of transmittance as a function of the angle of incidence, with respect to the normal of a tangent plane is given by

$$n_i \sin \theta_i = n_t \sin \theta_t$$

where θ_i and n_i are the incident angle and refractive indices, respectively, and θ_t and n_t are the analogous transmitted quantities. The coefficients of reflection r_{\perp} and r_{\parallel} (where \perp and \parallel correspond to the plane of incidence) and the coefficients of transmission t_{\perp} and t_{\parallel} are defined as

$$r_{\perp} = -\sin(\theta_i - \theta_t) \sin(\theta_i + \theta_t)$$

$$t_{\perp} = 2(\cos \theta_i)(\sin \theta_t) / \sin(\theta_i + \theta_t)$$

$$r_{\parallel} = -\tan(\theta_i - \theta_t) / \tan(\theta_i + \theta_t)$$

$$t_{\parallel} = 2(\cos \theta_i)(\sin \theta_t) / [\sin(\theta_i + \theta_t) \cos(\theta_i - \theta_t)]$$

The above equations are known as the Fresnel equations. The reflectance is defined as the fraction of incident light which is reflected and is denoted by R_{\perp} and R_{\parallel}

$$R_{\perp} = \sin^2(\theta_i - \theta_t) / \sin^2(\theta_i + \theta_t) = (r_{\perp})^2$$

$$R_{\parallel} = \tan^2(\theta_i - \theta_t) / \tan^2(\theta_i + \theta_t) = (r_{\parallel})^2$$

$$T_{\perp} = 1 - R_{\perp}$$

$$T_{\parallel} = 1 - R_{\parallel} .$$

Observation shows that R_{\perp} can never be zero, while R_{\parallel} may become zero when the denominator is infinite, i.e., when $(\theta_i + \theta_t)$ is equal to 90 degrees. The reflectance for linear light with \vec{E} parallel to the plane of incidence vanishes, and the entire beam is transmitted. Therefore, due to the finite reflectance of the perpendicular component of the beam at each interface, a randomly polarized beam will eventually become polarized in the parallel sense. The resultant polarized beam will encounter no reflection losses at any of the Brewster angle interfaces. From Snell's law, and the fact that $\theta_t = 90 - \theta_i = 90 - \theta_B$, where θ_B is referred to as the polarization angle or Brewster's angle. It follows that

$$n_i \sin \theta_B = n_T \sin \theta_B$$

$$\tan \theta_B = n_T/n_i$$

$$\theta_B = \arctan(n_T/n_i)$$

For BK-7 borosilicate crown glass, the refractive index at 6000 Å is equal to 1.516 and the corresponding θ_B is equal to 56.59 degrees. For fused silica (SiO_2), the refractive index at 6000 Å is 1.458, yielding a Brewster's angle of 55.55 degrees. Brewster windows of flatness $\lambda/4$, 30 arc

minutes accuracy on the Brewster angle, Brewster cut on one end and normal cut on the opposite end were acquired. The windows are 3/16 inch in diameter and 1 1/4 inch long (as measured along the long side). The BK-7 windows were purchased from Melles-Griot, and the fused silica windows were purchased from The Optical Shop (formerly Karl Lambrecht Incorporated). The fused silica windows are more suitable for this laser due to the closer index matching of the SiO_2 with the dye solution. Also, the optical crown glass has a cutoff (10% transmission) at 3100 angstroms (78), while the fused silica has a cutoff at 1200 angstroms (62) for 10 mm thickness samples. The accessibility of the lower wavelengths could be eventually useful for shorter wavelength output or intracavity frequency doubled output.

Conversion of Electrical to Optical Energy

The elliptical reflector dimensions have been given earlier. The light from a source within an ellipsoidal cavity set at the first focus is focussed onto the second focus, and the energy density of the source is reproduced. Many factors affect the actual amount of energy which is transmitted to the dye solution. Tiny inhomogeneities inherent in the surface, corrosion effects, and the reflectivity of the surface material serve to determine the actual amount of light

being focussed. Also, the flashlamp radiates isotropically, causing approximately 64 degrees of back radiation to strike the lamp envelope and be scattered, along with approximately 50 degrees of forward transmitted radiation which misses the front of the reflector entirely and is therefore not reflected into the active region. This sets the geometric optical efficiency at 68%. Also, ray diagrams show that the glass envelopes tend to act as a negative lens, lengthening the second focus. To counter this effect it is best to set the second focus (theoretical focus) just on the outside of the dye envelope, rather than at the center of the active region. This was done by milling some of the material off of the back of the reflectors and setting them back 3/16 inch. The resultant focussing of the light from both flashlamps falls in the center of the active region. The actual cross section of the illuminated area has not been calculated. However, if the cross sectional area under illumination is greater than that of the flashlamp ($.013 \text{ cm}^2$) but still less than the cross sectional area of the active region (0.20 cm^2), the only effect would be that the power density would be somewhat lower and resultant optical inhomogeneities would not be as severe.

Tuning Elements

Two tuning elements have been tested for interchangeable use with this system. The first employs a dispersive element (specifically a number of dispersive elements) in the form of a multiple prism tuning ring. Single prism tuning generally has not been used due to the much higher dispersive properties of a simple grating system as compared to the use of a single prism. A number of prisms may be used to obtain the necessary dispersion. The advantage of this type of system is that light can be made to enter and exit at near Brewster's angle with subsequent reflection losses much smaller than the corresponding grating losses. The prism ring for this laser consists of six 60 degree equilateral prisms, 3 cm on a side, set on a template such that the angle between two successive prisms whose bases are touching is 111 degrees. To tune the laser, the rear cavity mirror is rotated about a central axis such that only a certain narrow range of wavelengths are reflected back upon their path to the rear mirror. A system of this type has achieved moderate success in other laser systems, whereby up to 56% of the initial broadband energy output was maintained with a prism ring tuner inserted into the cavity (23). Friedman and Morton use such a tuner in conjunction with a beam expanding telescope to tune their transverse flow dye laser. A 4x (approximate) beam expanding

telescope inserted within our cavity provided unmode-locked tunability over the range of 5781-6142 Å, with a bandpass average of 1.9 Å. The laser would not mode lock satisfactorily with the prism ring used as a tuning element, however, and a spatially nondispersive element (birefringent filter) had to be substituted in its place. The reason for poor performance when using the prism ring as a tuning element is concerned with the fact that the cavity length must be maintained at greater than 80 cm, a length so great that mode-locking becomes a difficult (or impossible) task.

Tilted plates of a suitable birefringent material such as crystalline SiO₂ may be used as a narrowband selection device. To eliminate reflection losses, the plates are oriented at Brewster's angle with respect to the beam path. Wavelength selection comes about due to the two different axes of retardation of the material corresponding to incident light polarized along these axes. If the wavelength of the incident light corresponds to an integral number of full-wave retardations in the plates, the laser will operate as though the birefringent filter were absent. At any other wavelength, the laser mode polarization is shifted by the plate and losses are suffered at the Brewster surfaces. Rotation of the plates in a plane parallel to their surfaces changes the angle between the optic axis and laser axis and hence changes the principle indices of refraction of the plate. This causes

the shifting of the intensity maximum of wavelength transmission. The best commercially available configuration consists of a 3-plate filter with air spaces in between the parallel plates. The birefringent filter employed in our system is a Coherent Radiation G38371 3-plate filter with a tuning range of 5675 to 6480 angstroms. The width of the aperture is approximately 6 mm, and to the best of our ability, we have determined the ratio of plate thicknesses to be $1:4 \pm 1:15 \pm 1$. The tuning range of the birefringent filter has proved to be 5858 Å to 6100 Å when used in an unmode-locked configuration with Rhodamine 6G.

Mode-Locking Dye Cell

The mode-locking optically contacted dye cell is depicted in Figure 2.10. It may also be seen assembled in its proper position within the cavity, in Figure 2.3 (the cell is white in color, and located on the right side of the photograph). The cell is constructed of Teflon, and uses a double set of O-rings to hold both the rear cavity mirror (99.9% reflecting, $R = \text{infinite}$) and an uncoated optical flat in place. The length of the dye cell is set to either 200 μm or 2.0 mm by the insertion of Teflon shim stock spacers. The cell is constructed so that it readily fits into the rear Oriel mount. The dye cell utilizes constant flow of dye in the

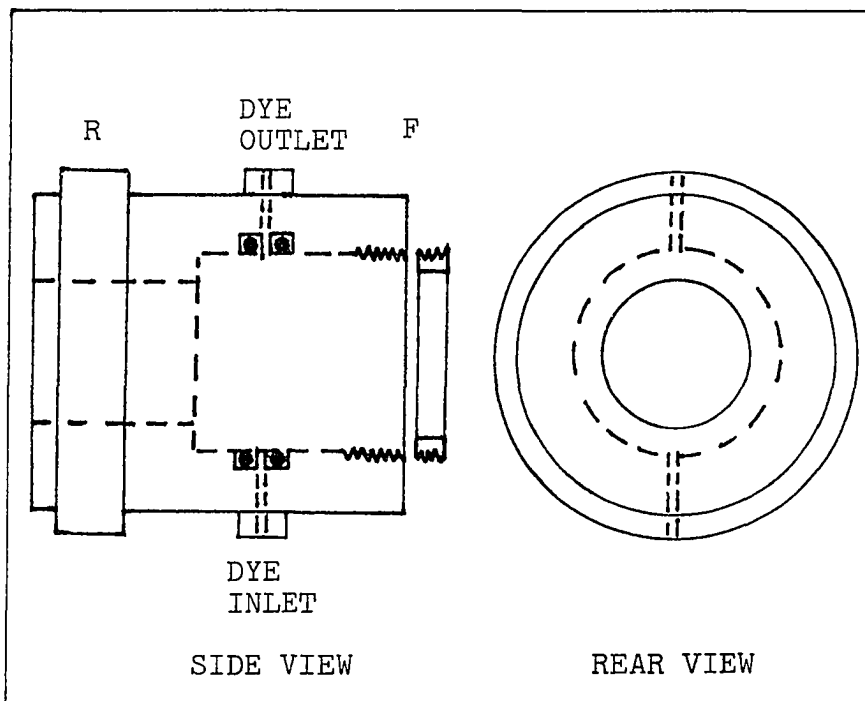


Figure 2.10. Optically contacted mode-locking dye cell

vertical direction, from bottom to top, to avoid air bubble formation within the cell. A Dayton 1/15 horsepower right angle gearmotor with a full load speed of 21 rpm, equipped with variable speed control, is used in conjunction with a Masterflex peristaltic pump head to supply dye to the cell. A 200 ml reservoir is attached to the pump head to assure thorough dye mixing and accurate measurement of concentration. One of the problems associated with the mode-locking dye flow system involves the fact that only tygon tubing is suitable for this system due to flexibility requirements. However, the tubing tends to discolor and plasticize upon exposure to the dye (at least in the case of DODCI). Gooch latex tubing is used for all connections outside of the pump head, and appears to be unaffected by the dye.

Triplet State Quenchers; Photobleaching

One of the limits of the lasing performance of a particular dye is established by the triplet state of the dye in question. Lasing may be quenched in a few microseconds by absorption between triplet levels of dye molecules accumulating in the lowest triplet state (23). The addition of a triplet state quencher may be needed to prevent the accumulation of molecules in the triplet state and thereby enhance the output lasing energy. Oxygen is an effective triplet state quencher for the xanthene (R6G inclusive) and coumarin

dyes (79). The effects of oxygen on the polymethine dyes show the opposite effect, a quenching of laser output with additional dissolved oxygen present in the system (80,81). Chemical additives are also available for use with all of the different lasing dyes (16).

All triplet state quenchers are characterized by having an even number of electrons and corresponding distinct singlet and triplet manifolds. An effective triplet state quencher may have either singlet or triplet ground states. The metastable levels of TSQS (triplet state quenchers) may also be triplet or singlet states, respectively. This is in contrast to lasing dyes, which almost always have singlet ground states and triplet metastable states. The effectiveness of a TSQ is determined by comparison of the energies of the lowest metastable states of the lasing dye and the TSQ. If the TSQ is to be effective, it must be able to decrease the triplet state molecular population by collisional deexcitation in solution. With oxygen as a triplet state quencher, fluorescent quenching also occurs, and encounters in solution tend to increase the triplet state population of dye molecules. Competition between these effects determine the usefulness of O_2 as a triplet quencher. For R6G the best triplet state quenchers appear to be cyclooctatetraene, oxygen, and N-aminohomopiperidine at concentrations of 2.5×10^{-2} molar, 1.0 atmosphere, and 4.0×10^{-3} molar, respectively.

It is known that photobleaching may place a limitation on the life of a laser dye. The mechanism of photobleaching is not well understood, and is sensitive to variables such as solvent nature, temperature, and chemical additives. Photobleaching has been shown to depend upon the triplet state population (82). Two possibilities may be utilized in order to reduce the effects of photobleaching. The first involves the addition of a TSQ; the second involves lowering the temperature for dye systems which have strongly temperature dependent singlet-triplet intersystem crossing rates. The best solvent to use (yielding the lowest quantum yield of photobleaching with R6G) is ethanol (83). Also, a Pyrex shield filters out ultraviolet radiation generated by the flashlamps, and greatly reduces the photobleaching effects (84). Our laser utilizes ethanol as the dye solvent, and the tubes which form the dye channel are made of Pyrex, thereby minimizing photobleaching.

Rhodamine 6G (structure shown in Figure 2.11) is the most efficient dye known at present. High output energies and efficiencies have been reported for R6G-ethanol solutions. The chemistry of R6G has also been very well characterized by a number of authors (70,85-89). R6G is used in ethanol solution in this laser due to the high overall efficiency and fluorescence quantum yield of this combination. The additional effect of minimized photobleaching benefits the

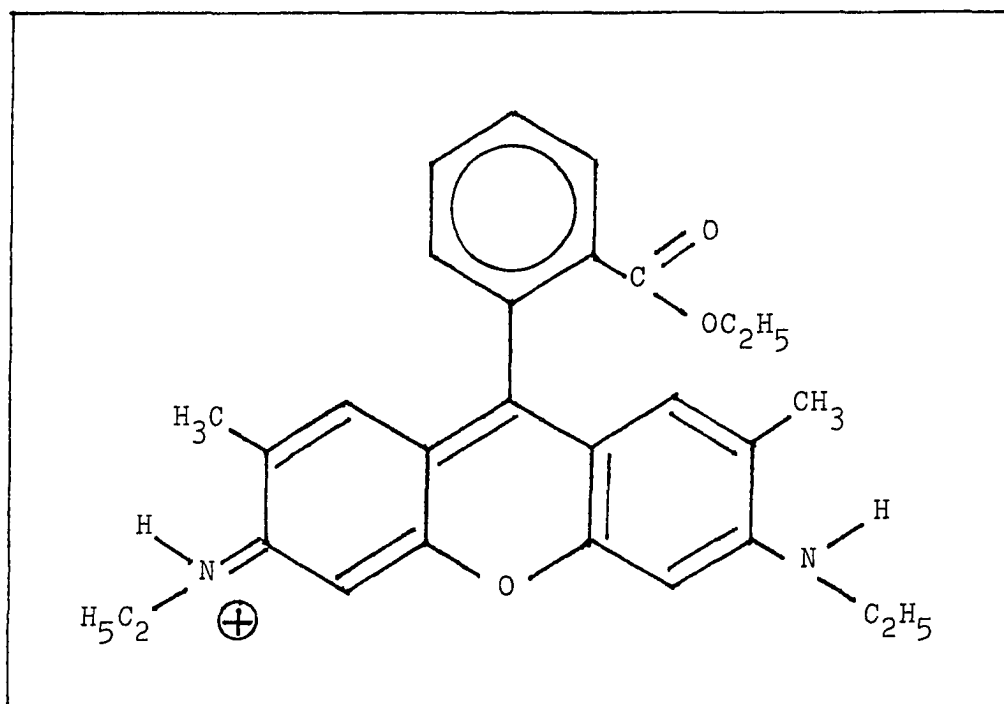


Figure 2.11. Rhodamine 6G (Rhodamine 590)

operation of this laser. Thermal effects are tolerable with the ethanolic solution. The tradeoffs between using water as a solvent and utilizing its good thermal characteristics as opposed to the inferior quantum yield of fluorescence make it a poor choice, and it is therefore not used. A stock solution of 4 liters of Eastman [R6G]Cl⁻ or Exciton Rhodamine 590 is maintained in the dye reservoir at a concentration of 2.0×10^{-4} molar (all of the recent experiments with this system have been performed with the superior quality Exciton dye). The triplet quencher cyclooctatetraene is used in this solution at a concentration of 2.0×10^{-4} molar. With regards to the DODCI, ethanol is also used as a solvent with concentrations of 1.5×10^{-4} molar, and 2.3×10^{-5} molar found to be optimum for mode-locking with use of the 200 μ m and 2 mm cells, respectively.

The design of flashlamp driving circuits is a topic which has undergone detailed discussion (90-92). The driving circuit must be able to withstand severe power conditions to allow for lamp risetimes as short as 100 nanoseconds. The design must take into account flashlamp explosion parameters, capacitor voltage limits and other criteria. The total circuit inductance of a circuit of this type is usually considerably less than one microhenry. The contributions to circuit inductance include the inductance of the lamps, the thyatron (or spark gap) inductance, and the inductance of all

connections and cables for the circuit depicted in Figure 2.12

$$C = \left[\frac{2E_o \alpha^4 T^2}{K_o^4} \right]^{1/3} \quad (2.4)$$

$$L = \frac{T^2}{C} \quad (2.5)$$

$$V = \left[\frac{2E_o}{C} \right]^{1/2} \quad (2.6)$$

where

C = capacitance (farads)

L = inductance (henries)

V = voltage (volts)

E_o = energy input to lamp (joules)

T = \sqrt{LC} and is approximately equal to
one-third of the pulse width

α = circuit damping parameter (0.8 for
a critically damped pulse)

K_o = flashlamp impedance parameter (ohms-amps^{1/2})

the value of K_o may be found on the data sheets supplied with each specific lamp type (e.g., from ILC Corporation) or it may be approximated by

$$K_o = k\ell/d \quad (2.7)$$

where ℓ is the lamp arc length (cm), d is the lamp bore diameter (cm) and k is a parameter depending on the gas type and fill pressure. The flashlamp lifetime may be taken into consideration by knowledge of the explosion energy Exp:

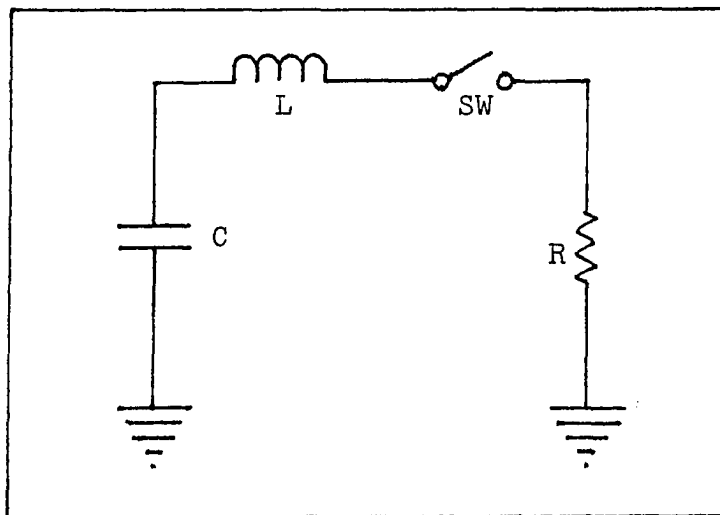


Figure 2.12. Flashlamp discharge circuit

$$\begin{aligned} \text{Exp} &= E_1 \ell d T^{1/2} \\ K_e &= \text{Exp}/T^{1/2} \quad (\text{watts sec}^{1/2}) \end{aligned} \quad (2.8)$$

where

Exp = single shot explosion energy (joules)

ℓ = arc length of lamp (cm)

d = bore diameter of lamp (cm)

$T = \sqrt{LC}$

E_1 = explosion energy parameter
(joules $\text{cm}^{-2} \text{sec}^{-1/2}$)

K_e = single shot explosion energy
constant (joules $\text{sec}^{-1/2}$)

for an FX-139C-6 flashlamp from EG&G Incorporated, with a 3.5 mm bore and a 15.2 cm arc length, values of optimum capacitance, voltage, and inductance may be readily obtained through the use of equations 2.4 - 2.6. First, a value for the flashlamp impedance parameter must be found. Based on the value of $k = 1.2 \text{ ohms-amperes}^{+1/2}$ (90), equation 2.7 yields

$$K_o = 52.2 \text{ ohms-amperes}^{+1/2}$$

The explosion energy (Exp) of the lamp in question is approximately 72 joules. Utilizing equation 2.8, in conjunction with the desired value of T (1.0×10^{-6} seconds, for this example), a value for K_e is obtained.

$$K_e = 7.2 \times 10^4$$

The energy E_0 may be determined from the flashlamp lifetime, where

$$[\text{life (flashes)} = (E_0/\text{Exp})^{-8.5}]$$

and the lifetime of a lamp is defined as the number of pulses to 70% of the original light output. Assuming a lifetime of 10^5 is desired for the system, $E_0 = 0.26 \text{ Exp}$. Therefore, $E_0 = 18.6$ joules (for 10^5 shot life). Utilizing a value of $\alpha = 0.8$ (critical damping) (90), one obtains

$$C = 1.3 \text{ microfarads}$$

$$L = 0.77 \text{ microhenry}$$

$$V = 5.35 \text{ kilovolts}$$

These values are seen to be in accordance with the aforementioned criteria of low capacitance and inductance in order to achieve the desired rapid current impulse. The inductance parameter, however, is dependent upon the capacitor design, the connecting lines and the flashlamps themselves. This condition determines that the only variables available for determining the characteristics of a system are the size of the capacitor (capacitance) and the peak voltage stored by the power supply.

Two additional factors may be calculated from the above information which are also of interest. The first is the maximum current value achieved at the peak of the pulse, and

is given by

$$J = \left[\frac{CV^2}{L} \right]^{1/2}$$

where the parameters C, V, and L are as before. The steepness of the current rise is then given by

$$\Delta J / \Delta T$$

where ΔJ and ΔT are the changes in both current and time, respectively, and have thus far been denoted J and T. For the system under discussion, the resultant values are

$$J = 6.95 \times 10^3 \text{ amp}$$

$$\Delta J / \Delta T = 6.95 \times 10^9 \text{ amp/sec}$$

The pertinent parameters upon which risetime of the pulse, peak current amplitude, and current rise are dependent may now be discussed. First, one must assume that the inductance of the system is somewhat controlled by the nature of the components which are used in the system, and is to a degree not a true independent variable in the system. The risetime of the pulse is seen to depend upon the capacitance and inductance of the components. In order to achieve faster risetimes, one must lower the capacitance of the storage capacitor. The maximum current is dictated by the capacitance and voltage and is inversely proportional to the inductance of the system. Therefore, maximum current may be increased

by either raising the capacitance or the voltage. The current rise is a function of voltage, and is inversely proportional to inductance. Higher voltages will give steeper current rise.

Design of Flashlamp Driving Circuits

Practical problems become of concern when designing a pulse system. It is quite obvious that to achieve favorable characteristics for the flashlamp pumping of a dye laser, a high voltage low capacitance system is optimum. For the small capacitances required to yield pulses of microsecond and submicrosecond duration, high dc charging voltages must be applied. Large components with high dc ratings must be employed and much care must be taken to assure that all components are properly insulated. By increasing the value of the storage capacitor, the amount of power to the flashlamps will be greater, but only at the expense of rapid pulse risetime. A compromise must be made involving component size, component cost, and the ability to keep the system as simple as possible structurally.

A low inductance capacitor used in a pulse system for flashlamp pumping usually has a value in the range of 0.05 - 0.9 μ farads. The generation of a short duration pulse to the flashlamps is seen to require relatively low capacitance values and high anode voltages. One technique with which

this can be achieved is overvoltage triggering. This technique is especially applicable when the lamp hold-off voltage is exceeded by the required anode voltage, as is the case at present. A thyatron or ignitron is generally used for switching this system, represented schematically in Figure 2.13. The ignitron shall not be discussed here for its development has taken a very slow pace over the past ten years (the interested reader may turn to references 93 and 94 of this thesis for information concerned with the workings of ignitrons). Thyratrons have provided the simplest, most inexpensive means of rapid capacitor switching in recent years. Particularly, the hot cathode (versus the cold cathode) thyatron has been most useful (93) due to its precision in starting. Heated thyratrons have brought forth three basic types characterized by different fill gases, namely, mercury vapor, xenon (or another inert gas), and hydrogen. The thyatron is so constructed that it consists of a discharge chamber in which are arranged a cathode, an anode, one or several grids, and in which the anode either contains an inert gas or a metal vapor. This gas fill distinguishes the tube from the more common vacuum tubes. Under the influence of a supplied anode voltage, the electrons which are emitted from the cathode assume high velocities sufficient to ionize the gas atoms in their path. The resultant ions are responsible for a considerable amount of

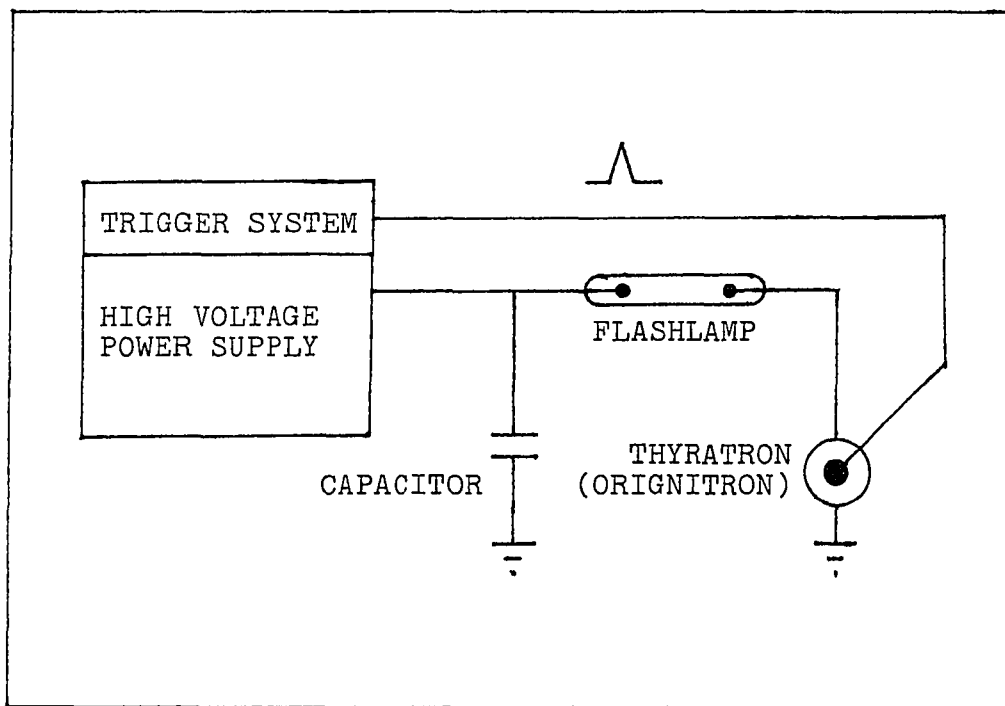


Figure 2.13. Schematic of overvoltage triggered flashlamp pulser

charge conveyance within the tube. The anode current becomes larger by several orders of magnitude than in any type of corresponding high vacuum tube. With the addition of a grid placed between anode and cathode, the anode current may be made to flow spontaneously at certain applied potentials to this grid. The resultant firing of the tube passes an arc between cathode and anode, whereby the voltage drop is primarily independent of the current value, and rather, is dependent upon the type of fill gas and its pressure.

The use of hydrogen as a fill gas for thyratrons has some definite advantages. The primary advantage is that the high fall of cathode potential can occur without damage to the oxide cathode. In other types of thyratrons, this is not always the case. For example, the respective destruction voltages for mercury ion filling and hydrogen filling are 30 volts and 600 volts, giving the hydrogen filled thyatron the advantage by a factor of 20. Also, the deionization time in the case of a hydrogen filled thyatron is about one-tenth of that of mercury, argon, or xenon filled thyratrons.

Initial Flashlamp Pulsing Systems

The first pulser employed in the transverse-flow dye laser system was a model 481 Micropulser produced by Xenon Corporation. This 300 watt system has the capability to provide 25 joules of energy to the flashlamps by the hydrogen

thyatron switching of a 0.5 μf energy storage capacitor at 10 kilovolts output. The maximum pulse repetition rate for this system is therefore 12 pulses per second. The rise time of the pulse is on the order of 600 nanoseconds. The system originally was designed to keep the flashlamps at high potential and drop the potential across the lamps to ground upon discharging the capacitor, as is schematically shown in Figure 2.14. The system was then modified such that the lamps remained at ground until such time that the capacitor was discharged, thereby sending a negative pulse through the lamps (see Figure 2.15). This system succeeded in igniting the flashlamps, but not enough power was output to the dye solution to achieve lasing (the system lases presently at less energy than 25 joules applied to the lamps; however, during the first trials, high energies were required to overcome deterioration of the lamps from repeated testing, slight misalignments in the cavity, and thermal effects in the dye solution).

The second pulser employed was a model 457 pulser from Xenon Corporation, also employing a 10 kilovolt system, this time with a .2 microfarad capacitor, and a special modification package such that the power range was extended to 1000 watts in order that the system could be operated at rates up to 100 pulses per second. The system was further modified, as was the first, to produce negative pulses. This system

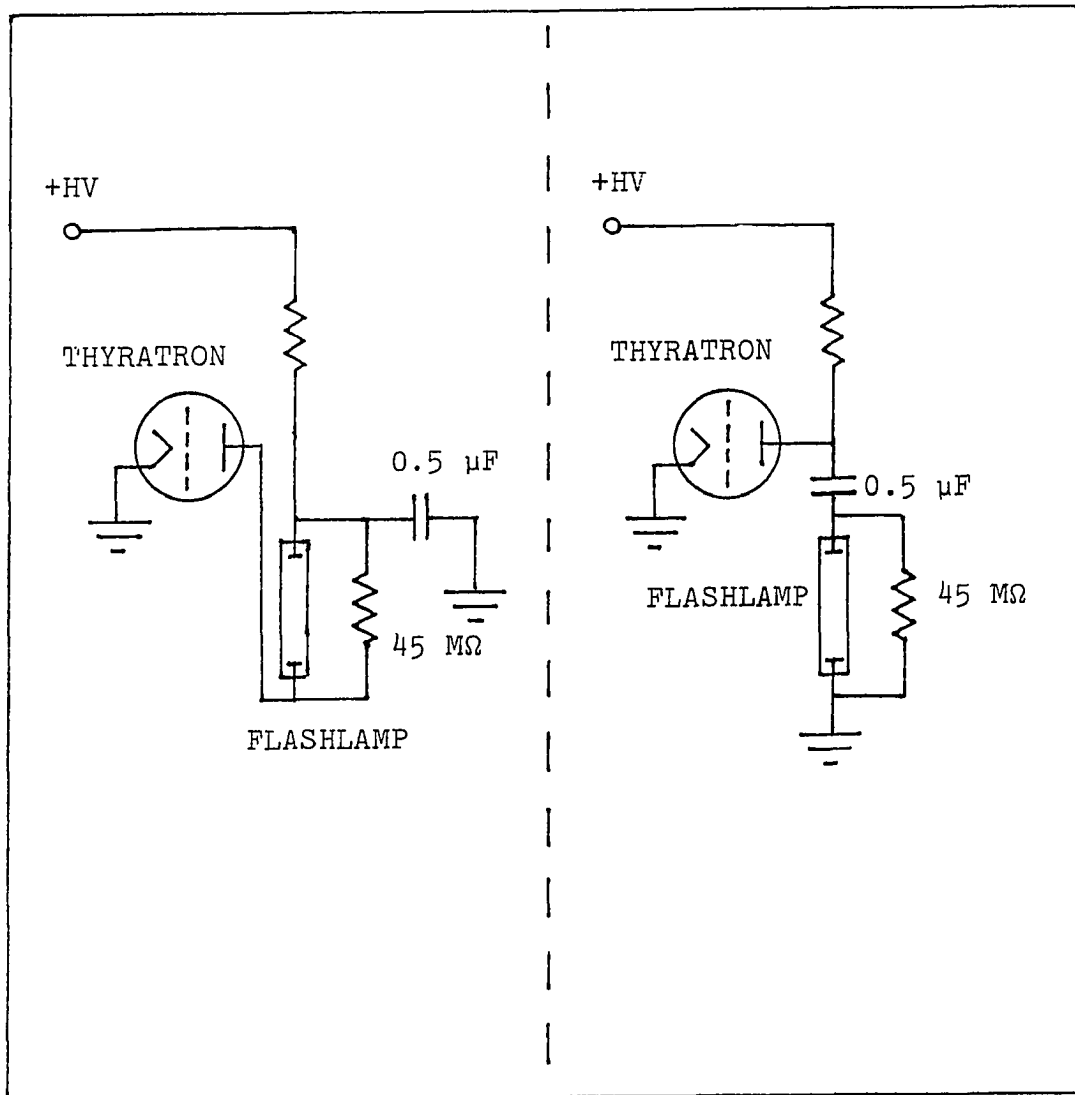


Figure 2.14. Xenon Corporation Model 481 Micropulser

Figure 2.15. Modified discharge circuit of Model 481 Micropulser

produced a peak energy output of 10 joules, which was insufficient to promote the lasing of the dye solution. The .2 microfarad capacitor (oil filled metal canister) also failed and the .5 microfarad capacitor from the previous system was used as a replacement. The lamps would not cause the dye solution to lase, and only some superradiance was observed when the .2 microfarad capacitor was used. The flashlamps were tested in both a parallel and a series configuration, but neither served to produce laser output. By removing one of the flashlamps entirely from the system, lasing was first observed, due to the better conversion efficiency of electrical energy to photon energy when the total stored energy was dumped into a single flashlamp. The lasing was only observed, however, at the maximum output energy of the system, 10 joules per pulse. The resultant lasing output was seen to occur for 60-70% of the pumping pulses, and had a risetime of approximately 300 nanoseconds with a corresponding full width-half-max of 600-800 nanoseconds. With the proper alignment of the cavity, the .5 microfarad capacitor could be used to pump both flashlamps such that the laser operated at about 25% above threshold at 10 kilovolts. The first mode-locking of this laser was achieved by using a 15 kilovolt, 5 milliamp power supply in conjunction with the Xenon 457 power supply charging circuit.

Present Flashlamp Pulser

The power supply currently in use is a custom-built supply designed by George Holland and constructed by the Instrumentation Shop at the Ames Laboratory. The charging circuit consists primarily of a 30 kilovolt, 65 milliamp transformer which is connected to a full-wave bridge rectifier. The rectifier produces dc output, which in turn is current limited by the addition of sufficient ballast resistance, such that the peak current never exceeds 3 amperes. This in turn serves to protect the rectifying diodes, which are rated at 100 milliamps. Furthermore, the power resistors are of the wire wound variety, which utilize inductance effects to counter voltage spiking which may damage the diodes. Control of the voltage which reaches the transformer is accomplished with the use of a 3.5 kilovolt-amp variac equipped with a 50 ohm bypassable load resistance which limits the initial line surge upon turn-on of the unit. The discharge capacitor is a 0.6 microfarad, 35 kilovolt, low inductance capacitor. The negative lead from the discharge capacitor is connected to the cathode of the first flashlamp, which in turn is in a series configuration with the second flashlamp. The negative lead of the capacitor is also connected to ground through a 50 megohm resistor. The positive lead of the capacitor is connected to an EG&G HY-32

hydrogen thyratron which is fired by an EG&G TM-27 variable rate trigger module. A schematic of this power supply is shown in Figure 2.16.

Simmer and Prepulse Power Supplies

The most serious problem concerned with using the transverse-flow flashlamp-pumped dye laser configuration as described thus far involves the rapid deterioration of the flashlamps. The sudden shock of a high current discharge through the lamps tends to erode the inner bore of the lamps and deposit the electrode material along the walls. Both of these effects cause a lessening of light output, either due to the provision of paths of least resistance within the lamp resulting in a lowering of the intensity of the emission of the gas itself, or to the simple blockage of the emission by the deteriorated inner bore. These problems are potentially much larger in our system than in most because of its unusually high average power output. A variety of techniques have been tested in order to combat this phenomenon, and many of these have been quite successful. One popular technique employs a dc power supply which is connected to the flashlamps and maintains a constant, low current discharge through the lamps. This type of arrangement is known as a "simmer"

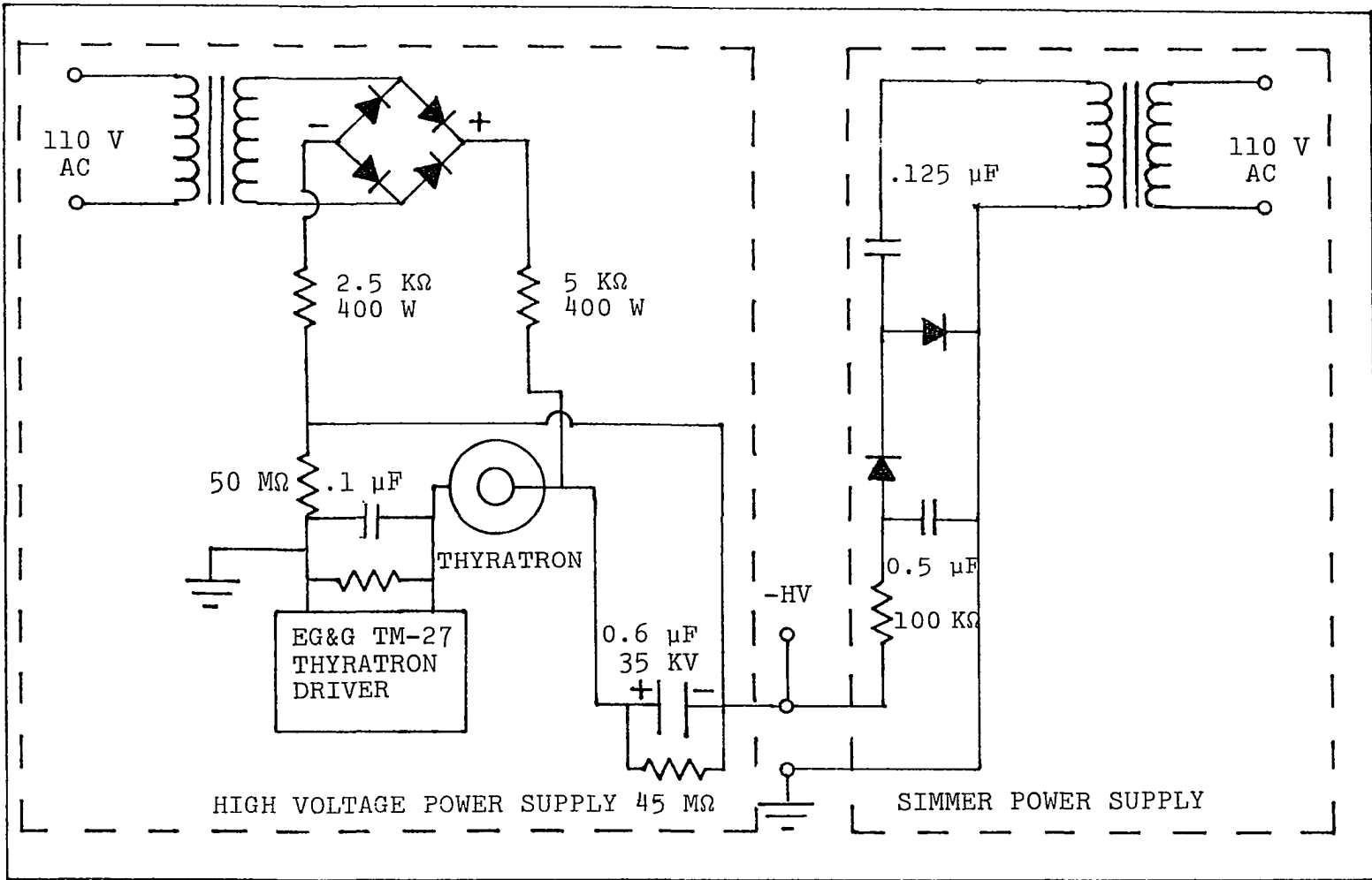


Figure 2.16. Schematic of 30 kilovolt high repetition rate power supply and simmer power supply

power supply, and the lamps are said to be operating in the "simmer" mode (56,58,95,96). A second technique involves the use of a "prepulse" power supply which supplies a high voltage, low energy pulse to the lamps, thereby assuring the ionization of the fill gas immediately prior to the high energy discharge of the main power supply (61,97). Both techniques, used jointly with the main pulser, appear to provide improved lamp lifetimes along with the best increases in flashlamp output intensities (98-101).

Several types of "simmer" and "prepulse" power supplies were constructed before arriving at a reliable design suitable for constant use with the existing system. The first prototype was a simmer supply consisting of a center tap transformer with a full wave rectification system. A 5 kilovolt transformer used in combination with a .125 microfarad oil bath capacitor and two 50 kilovolt diodes were used, with 20 thousand ohms of ballast resistance. The lamps would not preionize using this system and it was consequently abandoned. Another system utilized a 10 kilovolt transformer, a 2.67 microfarad capacitor (consisting of three 8 microfarad 1000 volt capacitors in series), and a bridge rectifier (each branch consisting of 5 rectifier type, silicon, 600 volt PIV, 750 microamp diodes placed in series). A 20 kilohm ballast resistor was also utilized with this system. At 3000 volts dc output, the supply should have provided 150 milliamps to

the load, assuming a very low resistance for the lamps themselves in comparison to the ballast resistor. This supply would not preionize the lamps either, and was subsequently modified. Prior to modification, the highest dc output which could be achieved was 3000 volts due to the limitations imposed by both the rectifying diodes and the capacitors. Each branch of the bridge rectifier now consisted of a single 50 kilovolt, 50 milliamp rectifier diode, and the capacitor was changed to a 0.05 microfarad, 35 kilovolt model. To this was added 400 kilohms of ballast resistance. This simmer supply would preionize one flashlamp (at a breakdown voltage of 7000 volts) but would not cause both lamps, placed either in series or parallel, to break down. This was probably because the combination of the two lamps would raise the initial breakdown voltage, such that more than a 10 kilovolt system would be required.

A pulsed preionizer was constructed using an EG&G KN-22 krytron tube (4 element cold-cathode, gas-filled switch tube designed to operate in an arc discharge mode), in conjunction with an EG&G TR130 miniature pulse transformer and a Motorola #2N4443 silicon controlled rectifier. The SCR fired a 30 volt pulse from a 1 microfarad capacitor into the trigger transformer which in turn was connected to the krytron tube. The krytron, in turn, would then fire a second 1 microfarad 2.5 kilovolt capacitor charged to approximately one kilovolt

into an EG&G TS-146A type number 76-01 30:1 ratio series injection trigger transformer, which would itself fire a pulse to the flashlamps. The main disadvantage of this system lay in the fact that it tended to fire the main pulsed power supply. An attempt was made to use optical isolation to prevent the triggering of the main power supply thyatron, but this also failed. Biasing of the thyatron grid was also tested yielding no positive results. Being unable to trigger the two system individually, we abandoned the prepulse approach entirely.

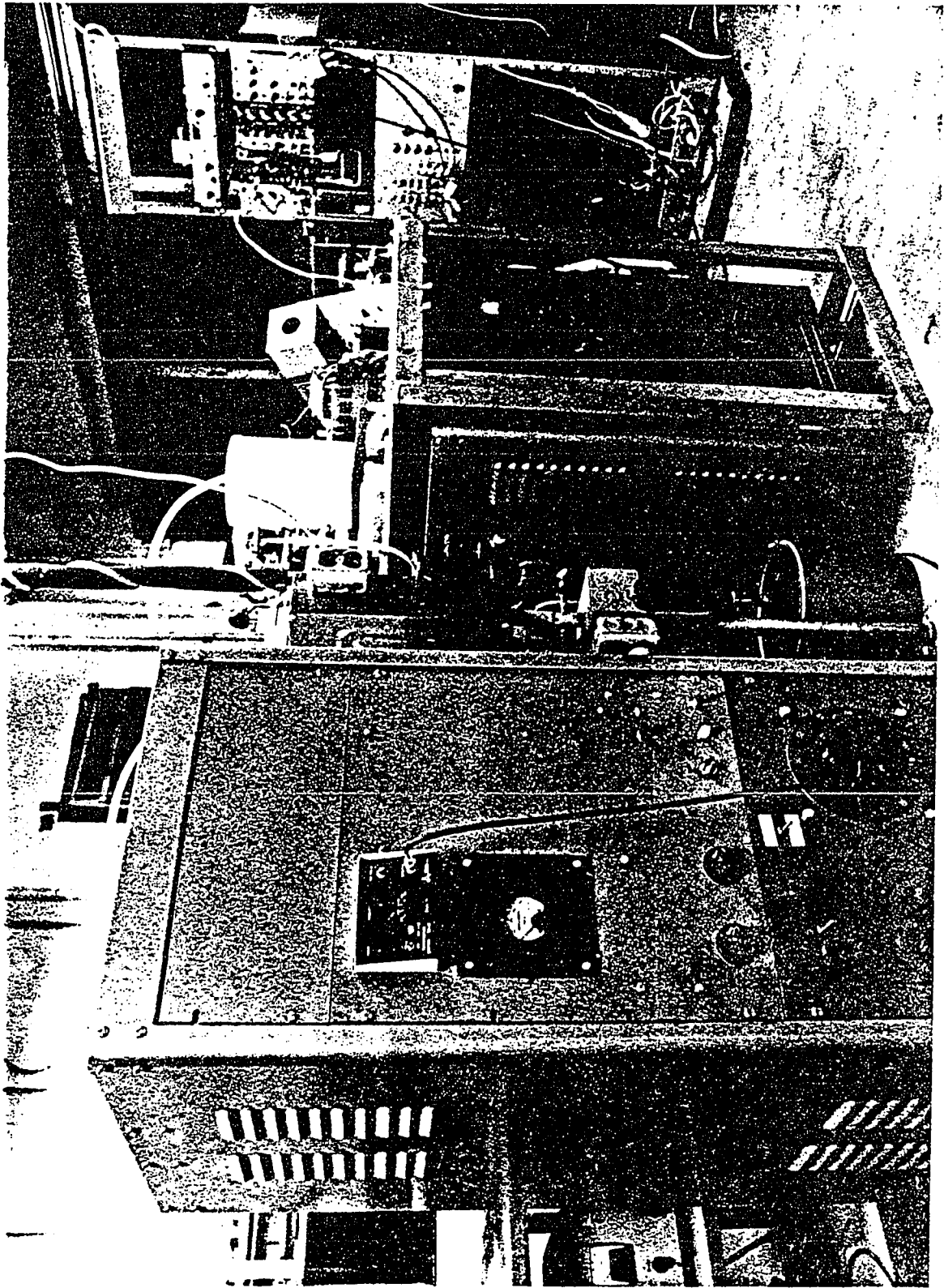
Stable preionization of the lamps was achieved with the system which is in current use, a simmer-mode voltage doubling dc power supply. The supply is very simple and employs as its main components: a 15 kilovolt oil bath transformer (origin unknown), two 50 kilovolt, 50 milliamperere rectifying diodes, a .125 microfarad, 40 kilovolt oil-filled capacitor, and a 0.5 microfarad capacitor (consisting of 3 2.0 microfarad 5000 volt capacitors and two 1.0 microfarad 5000 volt capacitors placed in a series-parallel configuration). A 100 kilohm, 225 watt ballast resistor is used for current control with the system. The simmer supply provides a constant streamer discharge through both of the lamps, with a voltage drop of 750 volts across the lamp and a corresponding current flow of 50 milliamperes. The flashlamp breakdown voltage is approximately 8000 volts. A schematic

of this simmer supply is shown along with that of the main power supply in Figure 2.16. Figure 2.17 shows both power supplies attached to the laser system.

Laser Warm-Up and Operation

In order to benefit future operators of this particular system, at this point a stepwise procedure is included for the operation of the laser system. Prior to turning on the main power supply, one checks to see that the switch next to the variac is in the "start" position and that the thyatron driver switch is on (the thyatron driver switch is always left in this position). It should also be noted that the range pps knob should be either on "1-20" or in the "external" position. The pulse rate knob should be turned to the lowest value (all the way counterclockwise). At this point the main power supply may be turned on by flipping the toggle switch to the "on" position. The instrument will require a 10 minute warmup period after which the amber "ready" light will come on indicating that the system can now be operated. During the warmup period, the dye and water pumps should be started. The system should not be operated without starting the pumps because some damage to the system will occur. First, the pump that provides water to the flashlamps is started. This is followed by starting the pump which runs water through the deionizing filter. The variac which is

Figure 2.17. Flashlamp pulser and simmer power supply.
The pulser is on the left



used to control water flow through the heat exchanger is next started, followed by the variac which controls dye flow. The dye control variac must be turned up cautiously, all the while noting the progress of dye flow into the head. Broken dye channel tubes have been a problem with this system, and the subsequent flooding of the reflector cavities should be avoided. This variac should be maintained at a setting of 30 when the laser is not being operated. When it has been ascertained that all of the flow systems are running properly, the simmer power supply should be started. This power supply requires essentially no warmup time and may be immediately adjusted. The simmer supply variac should be adjusted such that the lamps are observed to break down and a stable filamentary discharge is seen. Advancing the variac by five units will assure a steady current flow throughout the operational period of the laser. When the amber light indicates that the main power supply is ready for use, the "high voltage on" button should be depressed, at which time a red light will come on. This red light serves as an indication that the thyatron is ready for firing. Prior to firing the power supply, the dye flow should be increased to a setting of 50 on the variac. The main power supply variac control switch should now be switched from "start" to "operate". The flash-lamps will begin to fire as the variac setting is increased and the laser action should first appear at 9-10 kilovolts.

The system is shut down by first turning the main power supply off. The variac on this power supply is turned to zero, the thyatron driver range pps switch to the "external" position, and the single shot switch is depressed once to release all of the residual energy in the discharge capacitor. The high voltage "off" button should then be depressed, and a resultant extinguishing of the red indicator light should be noted. The variac switch should then be returned to the "start" position and the main power supply switch turned off. At this point, the simmer power supply variac should be turned to zero and the main power switch turned off. All of the circulation pumps should then be turned off. When mode-locking the system, the same procedure should be followed with the addition that the mode-locking dye pump should be started during the warmup period of the main power supply. The dye pump motor speed should be adjusted so that dye is seen to freely circulate within the cell. The first lasing will now appear at a higher threshold, approximately 11 kilovolts, and mode-locking will take place at 12-13 kilovolts.

Pulse Switching

When a mode-locked dye laser is capable of producing stable trains of mode-locked pulses, a suitable means of switching out single pulses must be devised. The most common technique employed for pulse switching involves the use of a

Pockels cell (102). The electro-optic effect involves the phase changes which polarized light undergoes upon passage through a uniaxial crystal material which is under the stress of an electric field. The phase change which occurs when a potential is applied parallel to the crystal optic axis (in the same direction as the incident light) is a linear function of applied voltage. This is in contrast to the Kerr effect in which the electric field is applied transverse to the direction of light propagation. For the Pockels cell, the equation which defines the retardation (with respect to orthogonal polarizations of the incident light) is given as

$$\Delta = n_o^3 r_{63} V_z / \lambda$$

where Δ = number of wavelengths retarded

n_o = ordinary index of refraction of the crystal

r_{63} = electro-optic constant in microns/volt $\times 10^{-16}$

V_z = longitudinally-applied voltage in volts

λ = wavelength of light used in μm

This equation shows that for a given crystal, different wavelengths of light will require specific voltages to obtain a given retardation, specifically 1/2 wave, which will yield a rotation of the plane of polarization by 90 degrees.

A number of crystals are commonly available for use as longitudinal modulators. The most readily available in high optical quality are ADP (ammonium dihydrogen phosphate), KDP

(potassium dihydrogen phosphate), and KD*P (potassium dideuterium phosphate). The choice of which of these crystals is to be used is made mainly on the basis of application. ADP was once the standard material used, but has since been replaced by KDP, due to the fact that the ADP has a large piezoelectric constant and tends to generate ringing oscillations in the transmitted light beam, an effect not generally seen in KDP or KD*P. If very low operating voltages must be used, the advantage of using KD*P is that it requires 50% less applied voltage to obtain the same degree of retardation as achieved using a similar crystal of KDP.

The most simple setup for the modulation of a light beam is depicted in Figure 2.18. The pulse train, highly polarized in the horizontal plane by repeated passages through Brewster angled glass-air interfaces, passes through the input polarizer, which is transparent to horizontally polarized light. Upon reaching the appropriately oriented Pockels cell, the light undergoes complete transmission and impinges upon the second polarizer (analyzer) which has an orthogonal polarization with respect to the first polarizer. The vertical polarizer will not pass the horizontally polarized light, and rejects it. This rejected light may or may not be rerouted to a spark-gap trigger which is used to supply a potential to the Pockels cell. Regardless of the means of triggering, when the Pockels cell reaches the half-wave

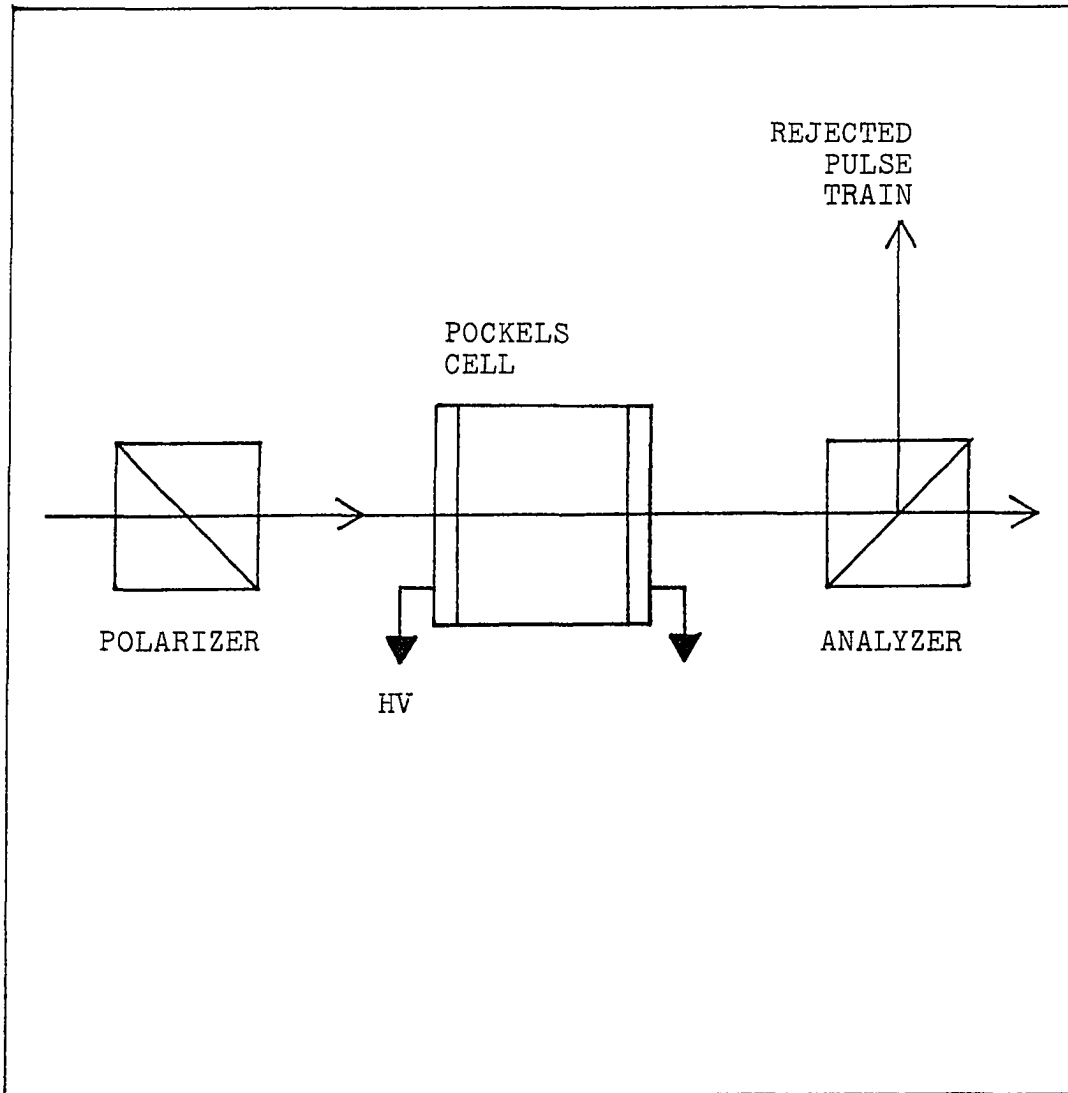


Figure 2.18. Pockels cell electro-optic amplitude modulator

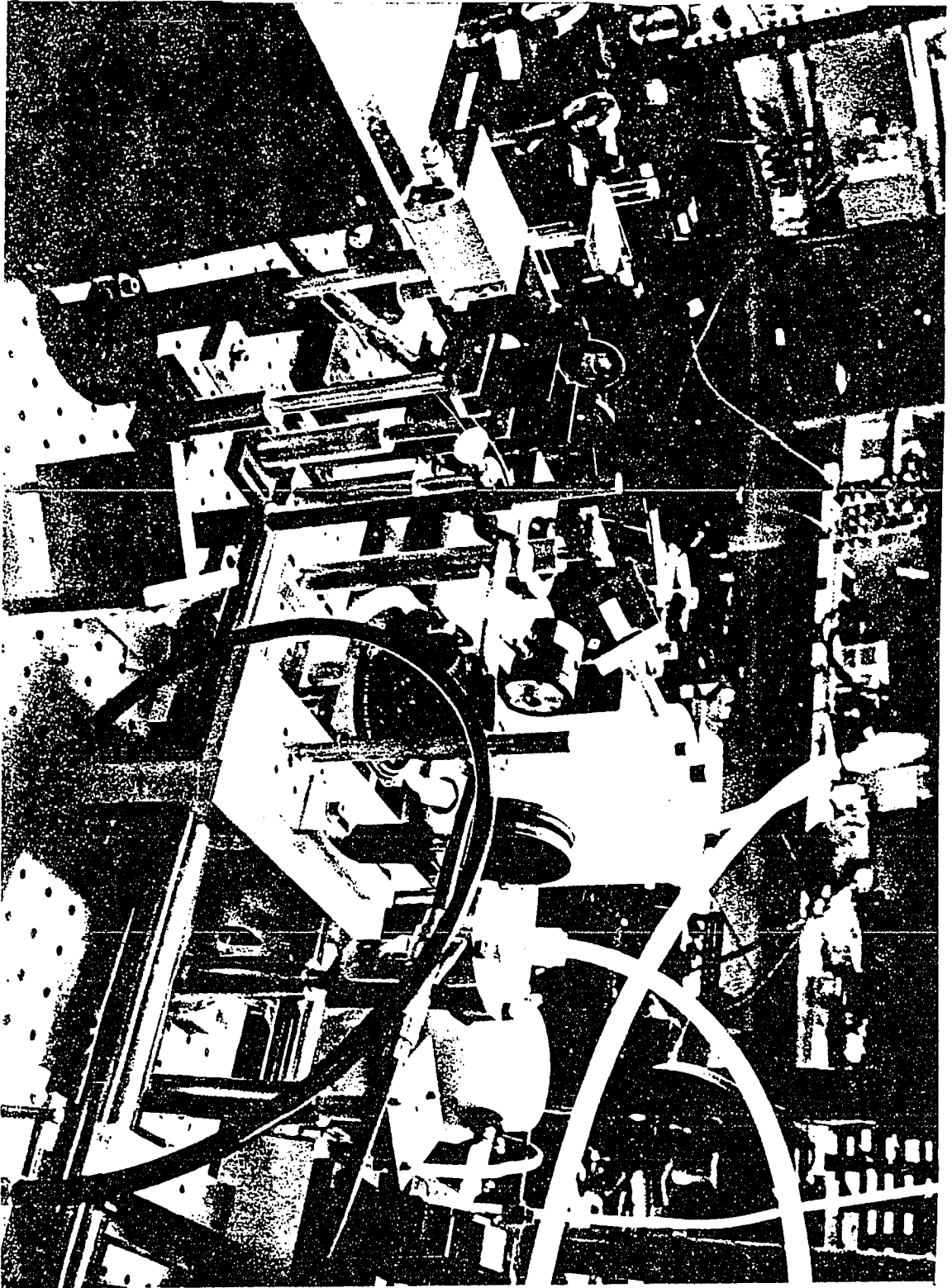
retardation voltage, the picosecond pulse passing through the cell at that time will have its initial plane of polarization rotated by 90 degrees. This will allow the passage of a single picosecond pulse through the analyzer. After a pulse has passed through the system, various means are employed such that the rest of the pulse train is also rejected.

The Pockels cell in use with the mode-locked transverse flow dye laser is a Lasermetrics model 1040-6FW employing a KD*P crystal with cylindrical band-electrodes (ring electrodes) instead of the more traditional endplate electrode construction (103). This particular cell is shown in its proper position within the cavity in Figure 2.19. The cell has a linear aperture of 6.35 millimeters and employs Lasermetrics FC-43 index matching fluid to reduce the reflectance of the internal optical surfaces. The polarization contrast ratio for this particular cell is greater than 700 to 1. For KD*P at 0.633 microns, $n_o = 1.52$ and $r_{63} = 23.6 \times 10^{-12}$ volts/meter, and a corresponding half-wave voltage of 3.8 kilovolts may be obtained. For any given wavelength setting the approximate half-wave voltage V_z may be obtained by

$$V_z = 3.8\lambda/0.633 \text{ kilovolts,}$$

where λ is the wavelength in μm . The Pockels cell is supported by a W. W. Boes Company Astro Compass MK II gimbal

Figure 2.19. Pockels cell positioned to modulate laser output. The output mirror is to the far right



mount, and utilizes two glan-foucalt polarizers (104).

A method must be employed such that the potential applied to the Pockels cell takes the form of a rapidly rising pulse, with a FWHM less than the separation between two picosecond pulses in the mode-locked train (approximately 5 nanoseconds for a 65 centimeter cavity length). Two techniques are commonly used to achieve this goal. The first, laser-induced spark-gap triggering (55,105,106) is more conventional, and is commonly used for switching neodymium laser systems. The second, electronic switching, employs a variety of fully electronic switching techniques (107,108) and is very much in its early stages of development at the present time.

The first triggering technique used involved a laser-triggered spark-gap. A schematic of the spark gap arrangement is shown in Figure 2.20. A 15 kilovolt, 5 milliamp dc power supply is connected through a 70 megohm current limiting resistor to the spark gap, using RG-8A/U coaxial cable. The electrodes of the spark gap consist of two modified Champion automobile N-12Y spark plugs. The construction of the spark gap chamber is exclusively of aluminum. Dry bottled nitrogen is used to pressurize the gap. The gas undergoes ionization and becomes conductive upon being struck by the incident laser beam, which passes into the chamber through a quartz window. When the spark gap has broken down, a high voltage pulse is passed on to the

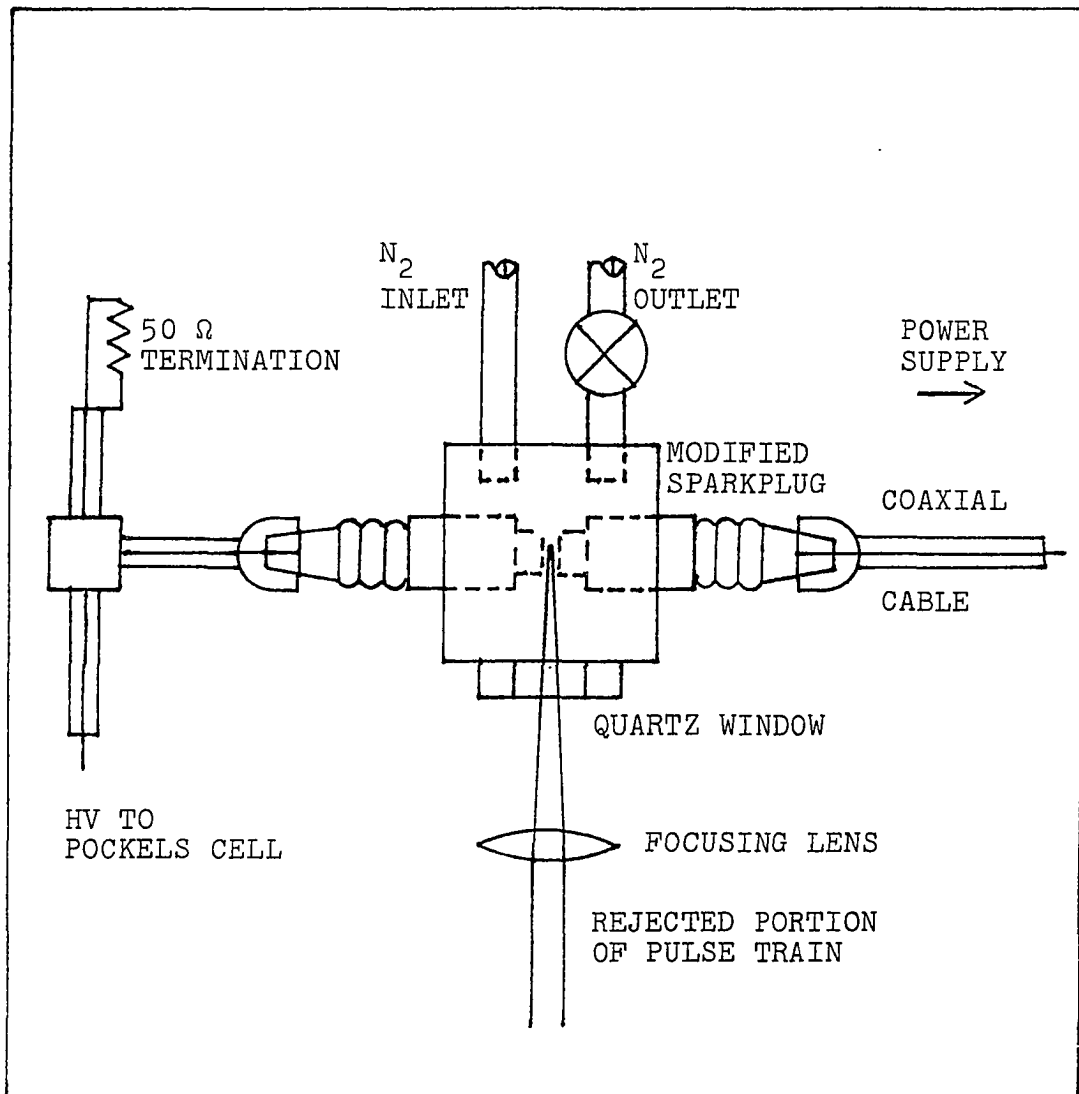


Figure 2.20. Spark gap pulse switching system

Pockels cell, causing a rotation of the plane of polarization within the cell. The grounded side of the Pockels cell is connected to a 50 ohm resistor and a small potentiometer such impedance matching may be used to minimize reflections of the high voltage pulse which has passed through the cell. Further modifications of the spark gap system include the addition of a tee box and a box for the 50 ohm termination. The inclusion of these boxes serves to keep the radio frequency emission from disturbing the pulsing characteristics of the spark gap system. This system was run by attaining a nitrogen pressure of 25 pounds per square inch, setting the spark gap voltage to 7 kilovolts, and running the mode-locked laser at a power supply setting of 13 kilovolts. With these parameters set as such, a 7-8 nanosecond pulse (FWHM) was observed, and single pulses could now be switched from the pulse train. However, pulse switching by this technique proved to be very erratic with pulses being switched either singly or in pairs very early on in the train. By observing the switching of a pulse with an oscilloscope, one could readily see that the RF still being generated by the firing of the gap was obscuring the interpretation of how well the switching was taking place. Furthermore, the delay of pulse switching within the train was accomplished by a complex optimization of high voltage and nitrogen pressure. By no means could the switching be made to take place reliably at the portion of

the train where mode-locking is optimum. Consequently, the use of the spark gap as a switch was terminated, and a move to total electronic switching was initiated.

One method by which total electronic triggering can be obtained is through the use of an avalanche transistor circuit (107). In order to use a krytron tube as a fast high voltage switch, it must first be triggered with an equally fast rising pulse of up to a kilovolt. By using suitable transistors (e.g., 2N5551 transistors) in the avalanche mode, this fast risetime may be obtained. In the regular mode of operation, 2N5551 transistors have a risetime of approximately 20 nanoseconds. However, if the collector-base voltage is increased to exceed the zener voltage of the transistor (approximately 280 ± 20 volts dc for the 2N5551) the risetime will rapidly decrease to about 2 nanoseconds. A number of these transistors can be cascaded in series to get positive high voltage pulses, or in parallel to get negative high voltage pulses. An attempt to use fifteen of these transistors in a series configuration in conjunction with a stripline circuit board produced a pulse with a risetime of 8-10 nanoseconds, far too long for our purposes, and the avalanche circuit was not used to trigger the Pockels cell. Another technique for fast pulse production involves the use of a krytron-switched blumlein structure for the production of short high-voltage pulses (108). An attempt was made to construct one of these

systems; however, the desired high voltages were not achieved.

The system which is currently in use serves to reliably switch pulses from any portion of the pulse train, and functions particularly well in switching pulses from the optimum mode-locking portion of the pulse train, in sharp comparison to spark gap pulse selection. A schematic of the entire system which is used to trigger the Pockels cell is shown in Figure 2.21. As shown in the schematic, the first portion of the pulse train passes through the Pockels cell which is at ground potential. Upon reaching the analyzer (P2), the initial pulses are redirected such that they propagate at a right angle to the original direction of beam propagation. A negative pulse photodiode detector, in response to the initial pulses, serves two purposes. First, the photodiode sends the signal to a Tektronix 7704A oscilloscope, which in turn displays the pulse train. Through the use of a tee connector, the signal from the photodiode is also sent to one channel of an Ortec model 924 quad discriminator. The discriminator, upon receiving a sufficient signal which exceeds the discriminator output level, outputs a single 2 nanosecond risetime 0.7 volt square pulse. The rapidly rising edge of the pulse serves two functions. First, the pulse is used to trigger the oscilloscope, and second, through the use of a tee joint, the pulse triggers an Ortec GD150/N delay gate. The delay gate provides adjustable

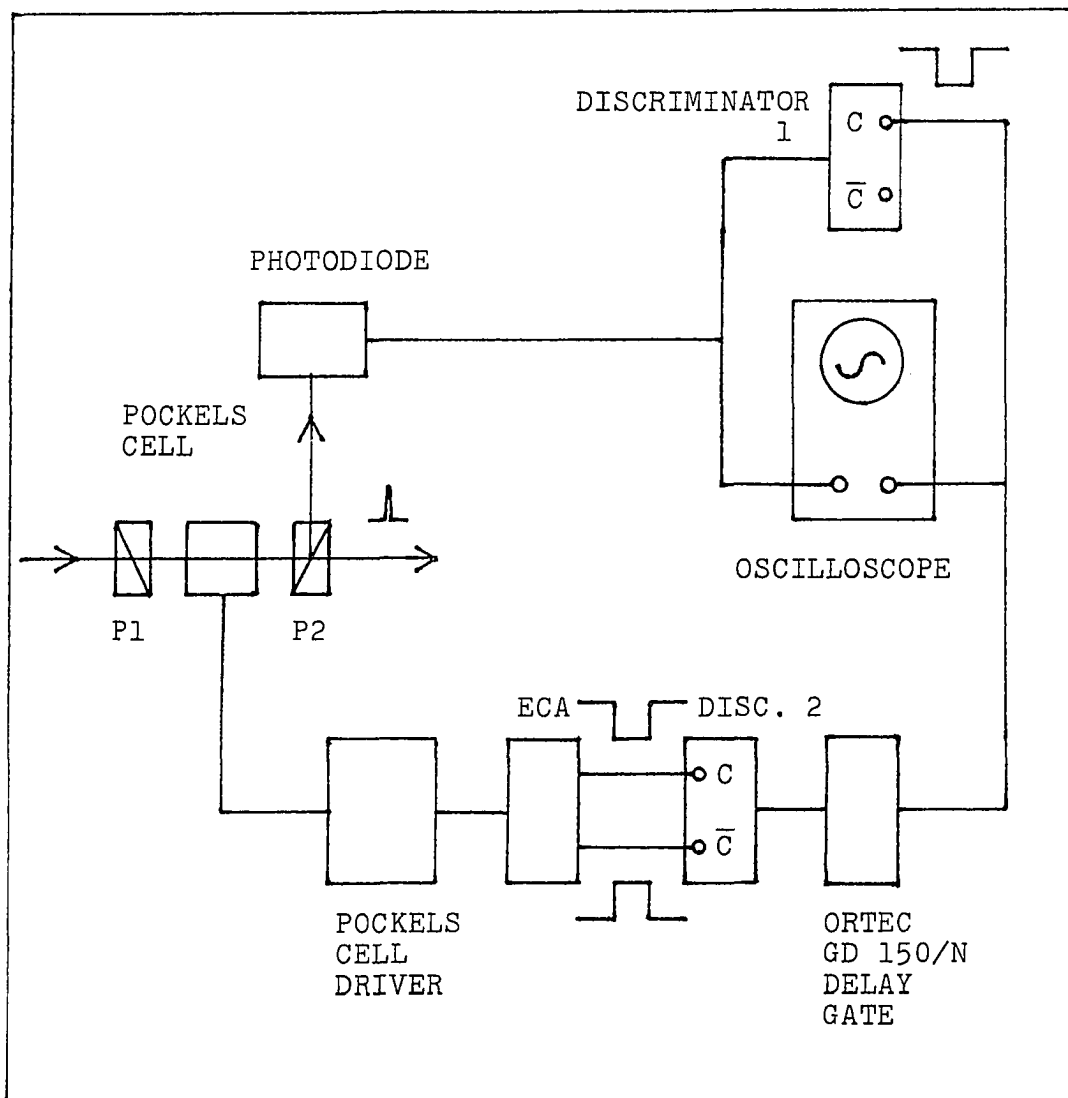


Figure 2.21. Schematic of Pockels cell triggering system

pulse widths from 0.1-100.0 microseconds, as well as providing 0.1 to 100.0 microseconds of variable delay with respect to the incoming pulse. The low (0.7 volt) output of the delay gate is connected to a second discriminator, which outputs both a 0.7 volt and a -0.7 volt output to an emitter coupled amplifier. The emitter coupled amplifier, shown in Figure 2.22, utilizes both the input pulses to provide an output pulse of 3 volts with a 3 nanosecond risetime. The +3 volts is necessary for triggering the Pockels cell driver circuit, depicted in Figure 2.23. The driver circuit consists of three 2N5551 transistors, coupled in a series avalanche mode configuration, which is used to trigger a KN-22 krytron, and in turn, a second KN-22 krytron. The first transistor is triggered in the conventional way, with the second and third transistors being triggered by over-voltage. Approximately 8 kilovolts (empirically adjusted to provide optimum operation of the Pockels cell) is switched by the second krytron, which sends the signal to a stub of RG8-A/U cable 15 inches long. The stub of cable, acting as a capacitor, stores the voltage, V , and outputs $V/2$ to the cable leading to the Pockels cell. The time delay of 1.27 nanoseconds per foot (for foam polyethylene dielectric material) assists shaping of the pulse. The aforementioned electronics (delay, amplifier, and pulse shaping circuit) are all mounted in a Nim module bin which, along with the

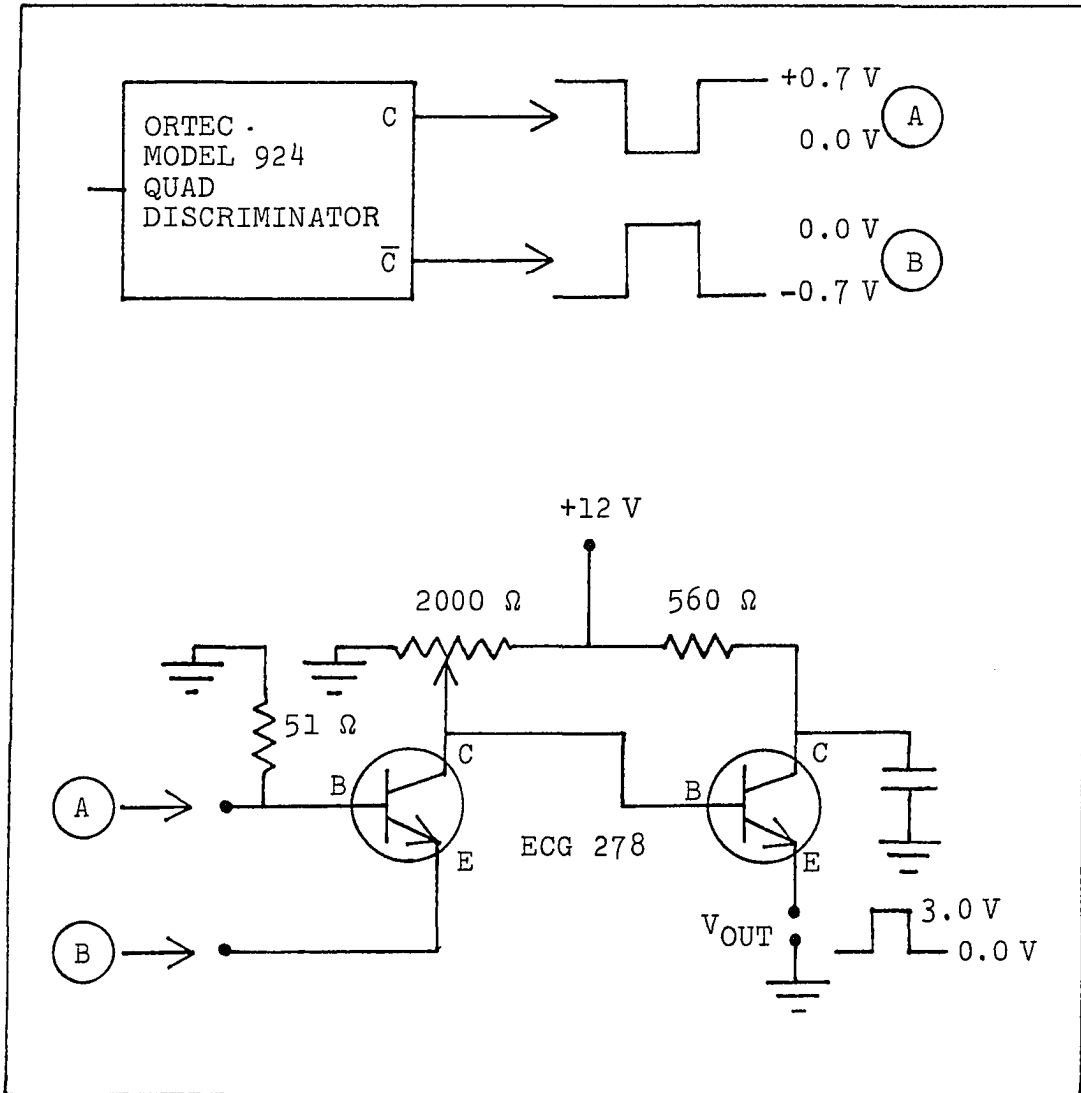


Figure 2.22. Emitter coupled amplifier

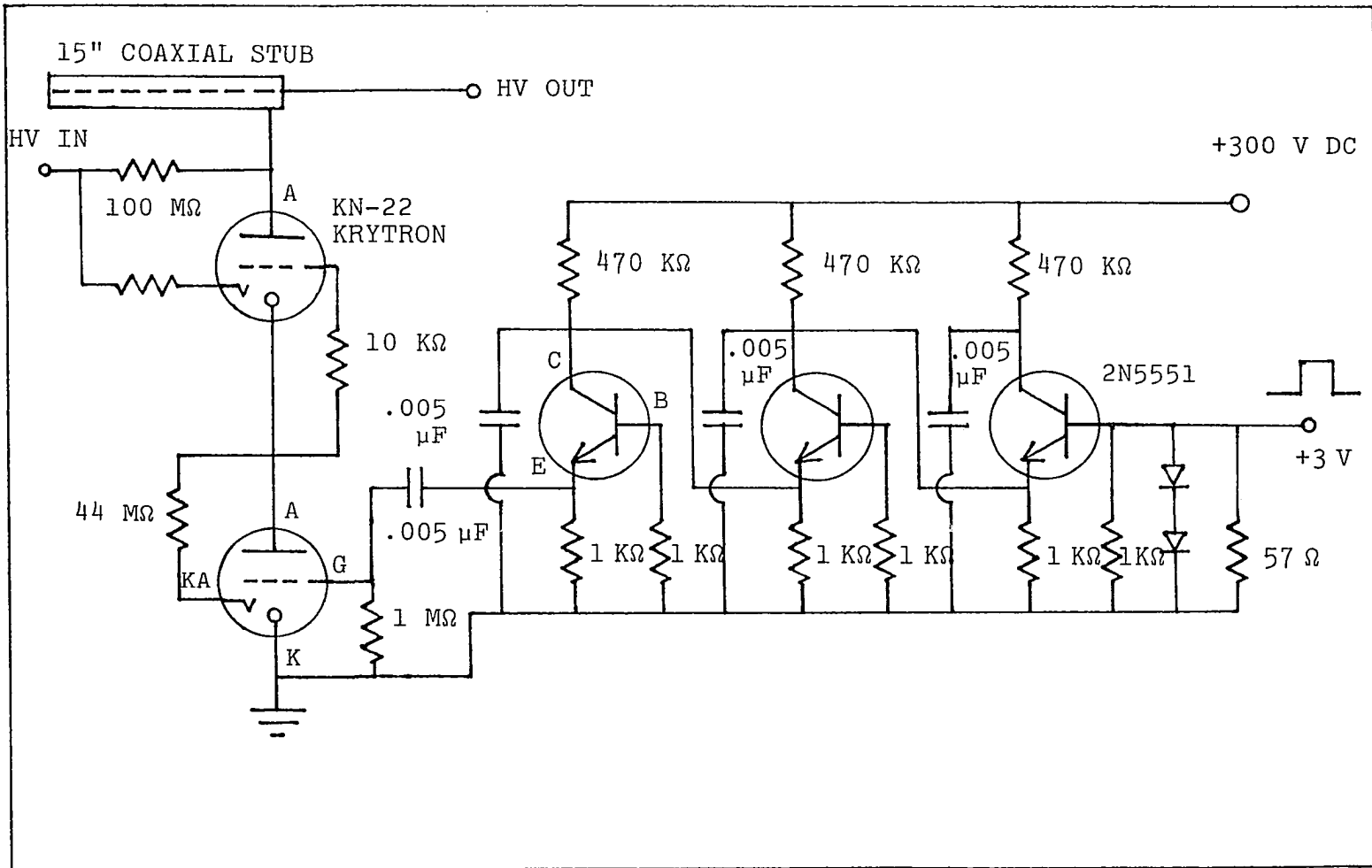
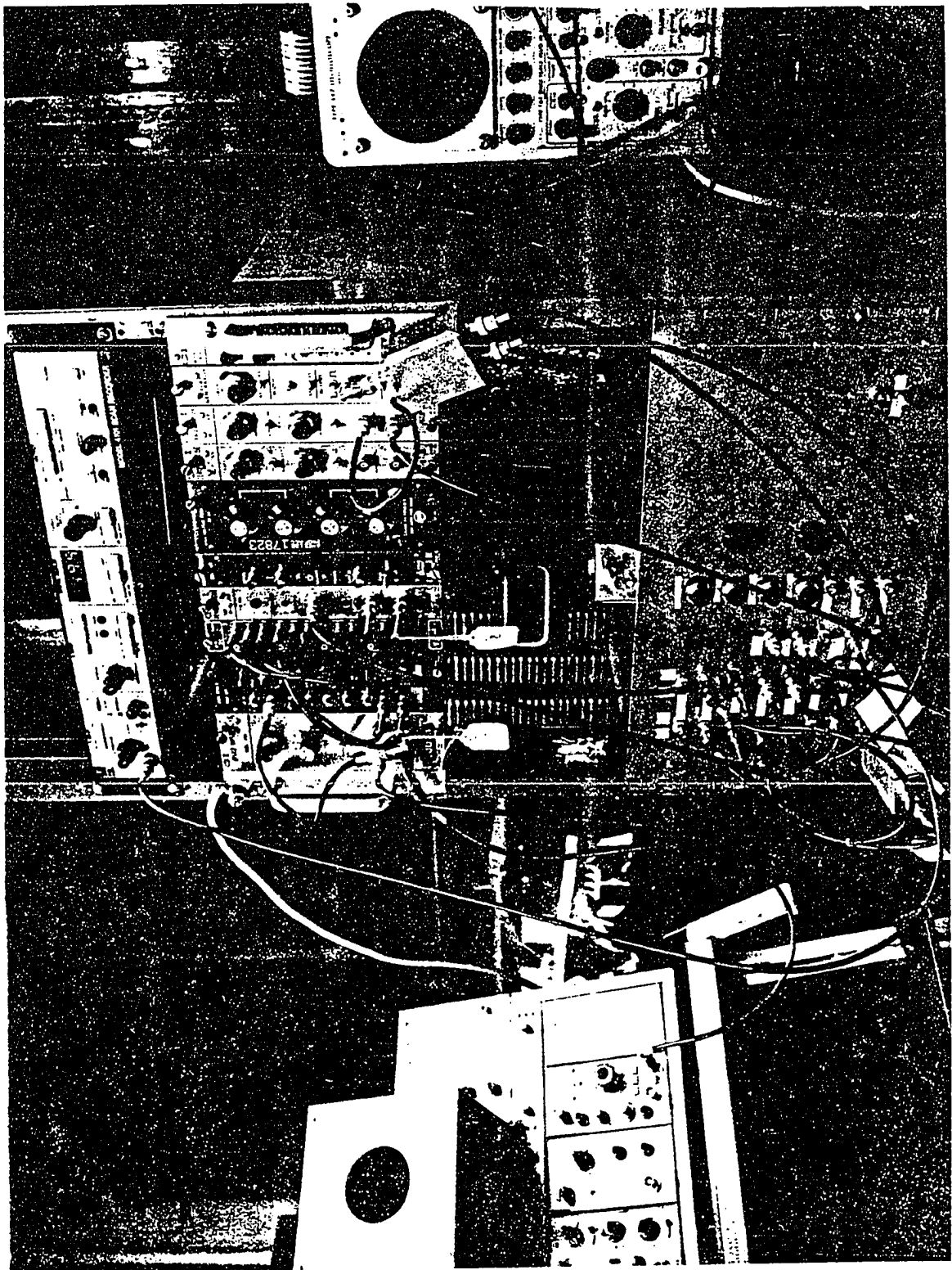


Figure 2.23. Pockels cell driver circuit

Tektronix 7704 oscilloscope, may be seen in Figure 2.24. A timing diagram for the associated electronics is shown in Figure 2.25. A 5 nanosecond risetime pulse with a FWHM of 8-10 nanoseconds has been observed from this arrangement.

Figure 2.24. Pockels cell driving circuitry and fast oscilloscope used for output monitoring



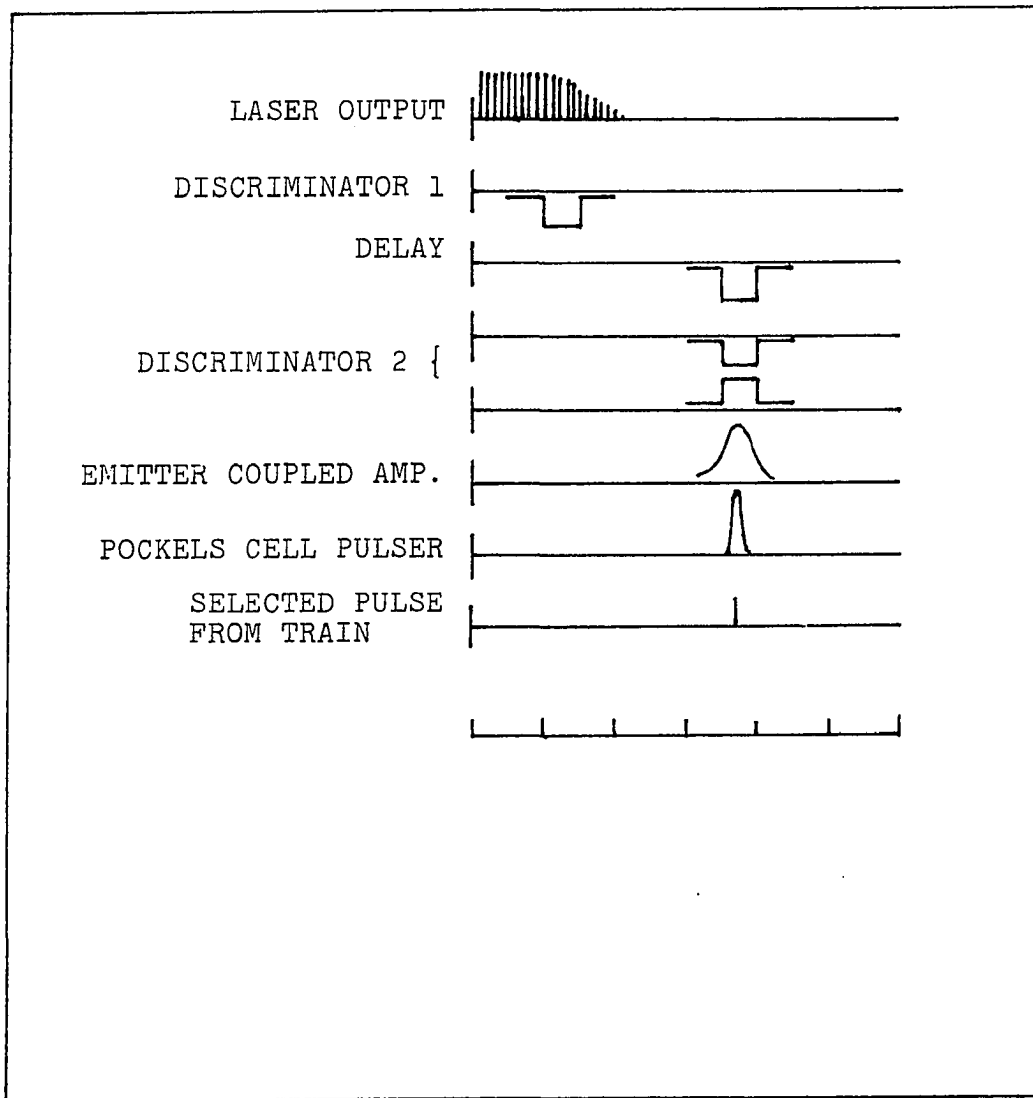


Figure 2.25. Timing diagram for Pockels cell pulser system

CHAPTER III. LASER CHARACTERIZATION AND PERFORMANCE

Operating Conditions

The transverse flow dye laser may be operated in one of three modes. When mode-locking dye is used in the contacted flow through dye cell, a train of mode-locked pulses is output by the laser. If the mode-locking dye is replaced with absolute ethanol, long pulse output lasting 1-2 microseconds is obtained. By using the Pochels cell and crossed polarizers as a light gate, a portion of the microsecond pulse lasting several nanoseconds may be switched out.

In order to determine the output characteristics of the transverse flow dye laser system, the following operating conditions were used.

Cavity length: 65 (± 1) cm

Dye solvent: absolute (100%) ethanol

Rhodamine 590 (Exciton) concentration: 2.0×10^{-4} molar

Front mirror reflectivity at 6070\AA and normal incidence:

80%

Rear mirror reflectivity at 6070\AA and normal incidence:

99.9%

Front mirror radius of curvature: 3 meters

Rear mirror radius of curvature: infinite (flat)

Mode-locked output:

DODCI (Eastman Kodak Co.) concentration (in 200 μm

cell): 1.3×10^{-4} molar

Switched nanosecond output:

Absolute ethanol in 200 μm cell

Pulse Energy

A calibrated Hewlett-Packard 5082-4220 PIN photodiode was used to monitor both the pulsewidth and the energy of the nanosecond output. When reverse biased in a low inductance configuration, the 5082-4220 photodiode exhibits rise and decay times of less than one nanosecond. The use of a wide entrance aperture in combination with a diffuser plate assure homogeneity of the signal reaching the small photodiode active region.

The energy monitoring photodiode was calibrated using a DL-200 Molelectron tunable dye laser, for which single pulse energies are readily obtained. The DL-200 system utilizes a grating tuned nitrogen laser pumped dye cell and operates at 25 pulses per second. During the calibration, the vertically polarized output component (while using Rhodamine 590 dye) was observed. A glass slide beamsplitter was placed at a 45 degree angle with respect to the output beam axis. The off-axis reflected portion of the beam was sent to the photodiode, while the transmitted laser output was sent to a model 3600 D1 laser power meter (ballistic thermopile, serial #1098)

with a response of 90.2 microvolts per milliwatt. A Keithly Instruments model 155 null detector microvoltmeter was used to monitor the thermopile output voltage. Output from the photodiode was connected to a Tektronic 457 oscilloscope with a 50Ω input. Neutral density filters were placed before the photodiode to assure linear response.

The output from the Molelectron laser was determined to have a pulsewidth of 10 nanoseconds FWHM, and a corresponding single pulse energy of 191 nanojoules. Under the assumption that both laser systems output approximately gaussian nanosecond laser pulses, the photodiode was calibrated. When used to monitor a 5 nanosecond FWHM pulse, the amplitude response of the photodiode corresponds to 47.75 nanojoule/millivolt.

Switched nanosecond output from the transverse flow dye laser exhibits a 5 nanosecond FWHM pulsewidth, as determined using a Hewlett-Packard 183D oscilloscope. With the beamsplitter and appropriate neutral density filters in place, the single pulse energy is determined to be 4300 nanojoules per pulse while operating the flashlamp pulser at 13 kilovolts. This corresponds to the amount of energy which would be transmitted through the beamsplitter to the sample. Any desired attenuation of the laser output at this point is readily accomplished by the placement of calibrated neutral density filters in the beam.

A second glass slide beamsplitter diverts a portion of the laser output into a Jarrell-Ash 1/4 meter monochromator equipped with an RCA 1P28 phototube. The phototube output is connected to an Evans model 4130 gated integrator which outputs a DC signal to a digital voltmeter. During an experiment, the digital voltmeter provides an estimate of pulse-to-pulse fluctuations and long-term stability.

The suppression of a microsecond laser pulse background intensity during optical gating is seen to be better than 1500:1. Pulse-to-pulse fluctuations never exceed more than 5%. Long-term output stability is achieved by slight adjustment of the rear laser cavity mirror and the flashlamp power supply.

The pulse energies of both the entire mode-locked pulse train and extracted single pulses were characterized using the Scientech 360001 laser power meter and Keithly Instruments model 155 microvoltmeter. Since the overall cavity length is 65 cm, with 5.99 cm occupied by the laser windows, 20.32 cm occupied by the dye solution, and the rest by free space, and since the respective refractive indices of air, silicon dioxide, and ethanol average 1.00, 1.46 and 1.36, respectively, one finds that the 65 cm cavity spacing has a path length of 75 cm. Therefore, the resultant mode spacing within the cavity is five nanoseconds. By monitoring the length of a mode-locked pulse train by oscilloscope, and

knowing the pulse separation within the train, the average single pulse energy may be determined from data obtained from the thermopile.

The data were obtained by examining the full laser output train in three different configurations. First, the full laser train was viewed without any attenuation; secondly, the train was viewed as attenuated with an ND 0.3 neutral density filter, and lastly, the beam was completely blocked in order to get a zero signal for the detection system. The following results were obtained;

Energy in (joules)	Train length (μ seconds)	Average energy (joules)	Single pulse energy (joules)
63.0	1.0	$.53 \times 10^{-3}$	2.6×10^{-6}
67.5	1.2	$.79 \times 10^{-3}$	3.3×10^{-6}
77.0	1.4	1.27×10^{-3}	4.5×10^{-6}
87.0	2.0	1.77×10^{-3}	4.9×10^{-6}
97.0	2.0	2.49×10^{-3}	6.9×10^{-6}

The lasing and mode-locking characteristics appeared stable at input powers up to 100 joules. No measurements were taken at above 97 joules due to the limiting characteristics of some components of the laser power supply, and finite lifetime and explosion limits for the flashlamps.

Mode-Locking Quality

The mode-locked organic dye laser system of D. J. Bradley (28,45,109,110) utilizes a 5.5 mm diameter x 21 cm quartz axial dye flow cell in conjunction with a single flashlamp in a cavity configuration which is 54 centimeters long. The front and rear cavity mirrors are 65% and 100% reflecting, respectively, with a contacted mode-locking dye cell 2 mm long containing a 1.0×10^{-4} molar solution of DODCI in ethanol. The concentration of Rhodamine 6G in ethanol is maintained at 1.5×10^{-4} molar. With interferometric tuning (28), the system readily produces pulses with an output gain bandwidth of 2.0 angstroms. At the lasing threshold, pulse trains are observed to be 200 nanoseconds (55 pulses) long with respective energies per pulse of 2×10^{-3} millijoules at 6250 angstroms, and 5×10^{-3} millijoules at 6050 angstroms. One hundred percent modulation of the pulse envelope is observed with this system. One point to note, however, is that up to 1000 joules of electrical energy is used to operate the flashlamp.

Negran and Glass (63) employ a modified Chromatix CMX-4 dye laser to produce mode-locked trains. A Fabry-Perot tuning element is used in this system. By using an unspecified concentration of Rhodamine 6G in combination with an ethanolic solution of DODCI which is slightly greater

than 50% transmitting through 5 millimeters, picosecond pulse trains were observed, but with a significant (>100 nanoseconds) nonmode-locked portion at the beginning of the train, mode-locking begins 300 nanoseconds after the laser is fired. The portion of the train which is totally mode-locked has a total duration of 800 nanoseconds. Output energies with this system of up to 10 microjoules per pulse and 10 millijoules total average energy have been observed.

The mode-locking quality of our transverse flow dye laser is comparable to the Bradley laser in terms of the entire pulse envelope being mode-locked. It is superior to that of the Negrán and Glass laser in that their laser does not mode-lock along the entirety of the output pulse. In consideration of the high optical pumping energies used in the Bradley laser and the single flashlamp, low pumping energies used in the Negrán and Glass laser, our output appears to be quite acceptable. A photograph of a mode-locked pulse train taken from the Tektronix 7704 oscilloscope is seen in Figure 3.1.

Spectral Bandwidth

The spectral bandwidth of our birefringent filter-tuned mode-locked output was measured using a Heath 0.35 meter monochromator. The grating in this monochromator has a

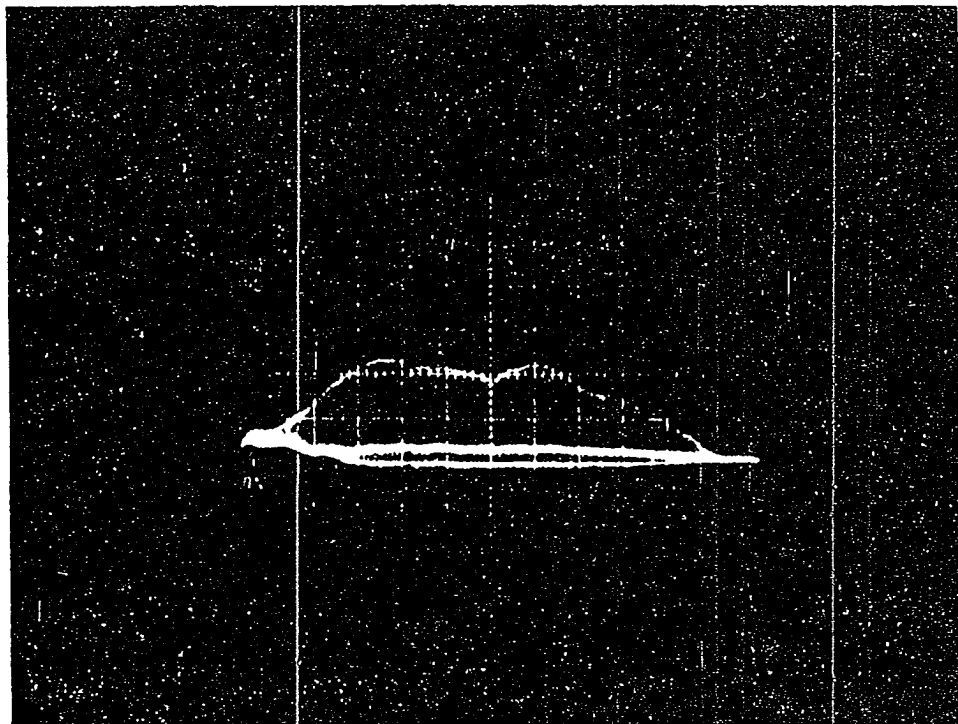


Figure 3.1. Mode-locked train from Rhodamine 590/DODCI;
laser operating at 607 nm; time scale 100 nanoseconds/
division

groove density ($1/d$, where d is the groove spacing) of 11,800 grooves/cm, and a 35 cm focal length f . The bandpass of a monochromator may be found as a function of the entrance slit width by using the relationship for linear dispersion

$$d\lambda/d\ell = d/nf$$

where n is the order of interference, λ is the wavelength of light passed by the monochromator, and ℓ is the approximate entrance slit width. For this particular instrument, $d\lambda/d\ell = 24.2$ angstroms/millimeter, which means that a slit setting of 8.26 μm will have a bandpass of 0.2 \AA , and a setting of 82.6 μm will have a bandpass of 2.0 \AA . A resolution of 0.5 \AA at 5000 \AA is readily obtainable with this monochromator.

A second monochromator (Jarrell-Ash 0.25 meter) is used to obtain a normalization monitor signal. Some of the laser light is directed into this monochromator with a 3% beam-splitter. One millimeter slit widths are used on this monochromator. Slits this wide correspond to a larger bandpass than that due to the laser, and are used to monitor the intensity of the laser output. The intensity measurement is used in turn to normalize the signal from the Heath monochromator. The Jarrell-Ash monochromator is adjusted to the wavelength of maximum intensity for the laser output, while the Heath monochromator is scanned through the entire tuning range with a synchronous stepping motor. The Heath monochromator is coupled with an EMI 9558 photomultiplier with

S-20 spectral response, while the Jarrell-Ash monochromator is coupled with an RCA 1P28 photomultiplier. Each photomultiplier signal is input to Evans model 4130 gated integrators triggered by a delay gate signal; a more comprehensive review of the electronics involved in data collection will be reviewed later. The output signals generated by the gated integrators are in turn input to an Evans model 4122 ratiometer, which outputs an A/B normalized signal to a Princeton Applied Research model 4101 scan recorder. The scan recorder memory can be read out into a Mosley model 135 X-Y recorder which produces hardcopy recordings of the laser's spectral output.

With the laser output tuned to approximately 6070 angstroms, and the slits of the Heath monochromator set to $40 \mu\text{m}$ (1.0 \AA bandpass), the output bandwidth for the entire pulse train was determined to be approximately 3.4 \AA FWHM (prior to deconvolution). Using $80 \mu\text{m}$ slit widths, pulses from the front (approximately 100 nanoseconds into the train), middle (500 nanoseconds), and end (850 nanoseconds) were determined to have observed bandwidths of 2.2 \AA , 2.8 \AA and 3.0 \AA , respectively. The true spectral output of the laser must be obtained by deconvolution of the apparent bandwidths.

The observed spectral distribution $f(x)$ can be calculated from the convolution integral of the actual spectral

distribution $\phi(x)$ and the apparatus function (slit function) $a(x)$

$$f(x') = \int_{-\infty}^{\infty} a(x'-x)\phi(x)dx,$$

where the apparatus function, observed spectral distribution and actual spectral distribution are all normalized to unity.

$$\int_{-\infty}^{\infty} a(x)dx = \int_{-\infty}^{\infty} f(x)dx = \int_{-\infty}^{\infty} \phi(x)dx = 1$$

The true spectral distribution may be represented in the form of a superposition of harmonic distributions, i.e., as a fourier integral:

$$\phi(x) = \frac{1}{2\pi} \int_{-\infty}^{\infty} \Phi(\omega)\exp(i\omega x)d\omega$$

The observed spectral distribution can then be represented by

$$f(x) = \frac{1}{2\pi} \int_{-\infty}^{\infty} A(\omega)\Phi(\omega)\exp(i\omega x)d\omega$$

where $A(\omega) = \int_{-\infty}^{\infty} a(x)\exp(-i\omega x)dx$

is the fourier transform of the apparatus function. The fourier transform of the observed spectral distribution is

$$F(\omega) = \int_{-\infty}^{\infty} f(x)\exp(-i\omega x)dx.$$

Therefore, the amplitude of the harmonic component of the observed spectral distribution is

$$F(\omega) = A(\omega)\Phi(\omega)$$

and the true spectral distribution may be found from the fourier transform of $\phi(\omega)$.

$$\phi(x) = \frac{1}{2\pi} \int_{-\infty}^{\infty} \frac{F(\omega)}{A(\omega)} \exp(i\omega x) d\omega$$

This equation offers the most general solution to the problem at hand. It must be remembered, however, that the direct use of this equation requires a complex integration over each value of x such that a single line profile $\phi(x)$ requires many integrations. Exact solutions are obtained by computer. However, if a functional form for both the slit function and the observed distribution are assumed, numerical solutions may be obtained (111,112). In order to use a numerical technique, one must first know the slit function of the monochromator. In the case of a grating monochromator, the spectral line is the image of the slit taken at the appropriate wavelength. Narrowing of the slit decreases the line width linearly to a certain point, after which the line width ceases to decrease. This is known as the diffraction limit and may be obtained from

$$w = \lambda f/a$$

where w is the diffraction-limited slit width, λ is the wavelength at peak intensity, f is the focal length of the monochromator, and a is the width of the aperture of the diffracting element (grating). In the case of the Heath

monochromator, with a 35 cm focal length, monitoring laser output at approximately 6070 angstroms (the Heath monochromator employs a 2" diffraction grating), the diffraction-limited slit width is 4.18 μm . A slit width of 80 μm is now seen to correspond to approximately 20 times the diffraction limit. An 80 μm slit width (as calculated from the dispersion relation for the grating) also corresponds to a 2.0 \AA bandpass. Taking into account the diffraction limit, the slit function is seen to be 2.1 \AA wide (FWHM). Based on the assumption that both the slit function and the observed spectral distribution are gaussian functions,

$$f(x) = c \exp(-x^2/\beta^2)$$

$$a(x) = d \exp(-x^2/\beta'^2)$$

The true spectral distribution may be found from

$$\beta^2 = (\beta')^2 + (\beta'')^2$$

where β'' corresponds to the gaussian function

$$\phi(x) = b \exp(-x^2/\beta''^2)$$

The following results are obtained using this approximation:

<u>Observed spectral width (\AA)</u>	<u>True spectral width (\AA)</u>
2.2 (100 ns)	0.7
2.8 (500 ns)	1.9
3.0 (850 ns)	2.1

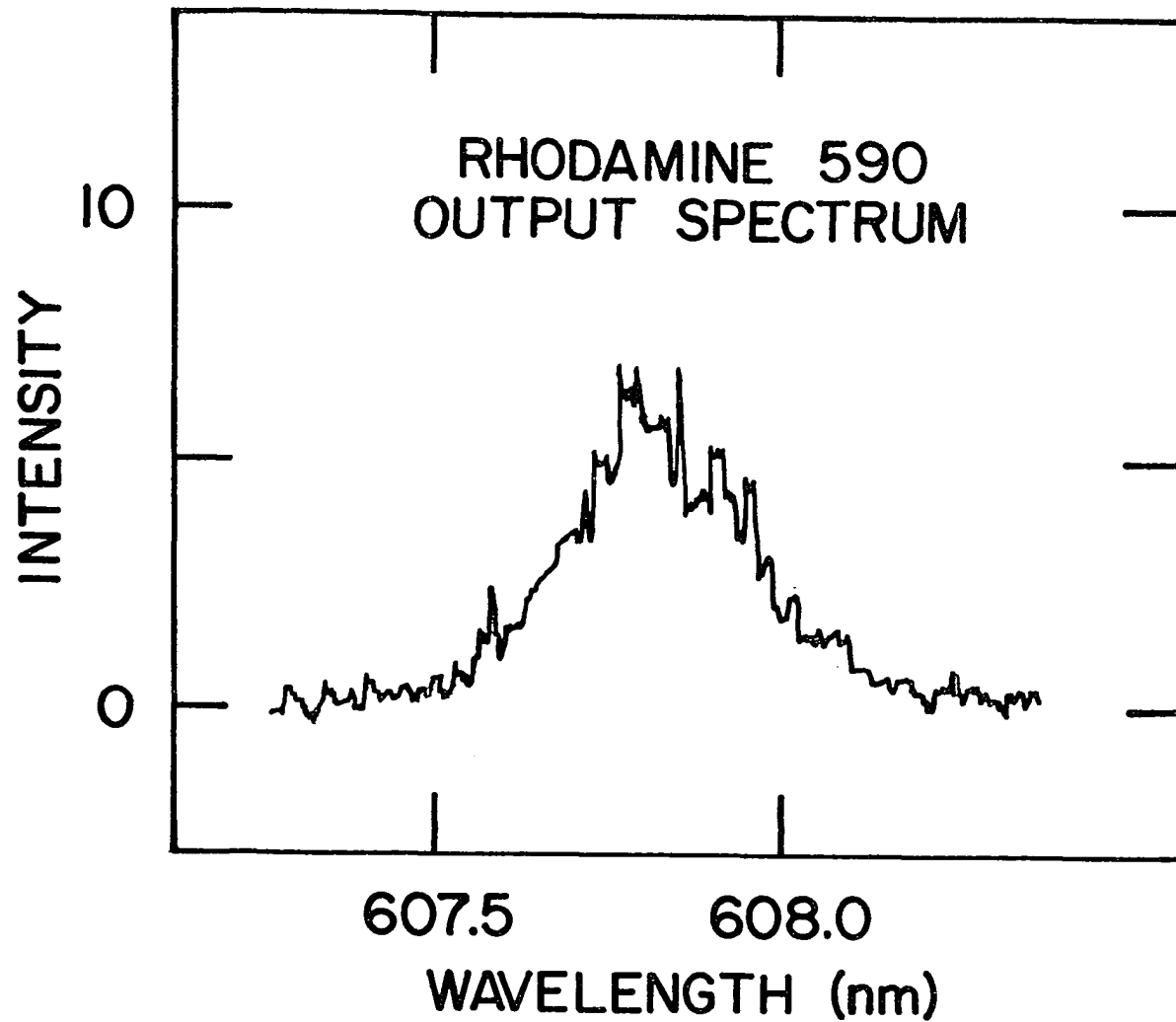
A sample output spectrum of a late pulse may be seen in Figure 3.2.

Temporal Bandwidth; Detection System

The direct measurement of the individual picosecond pulsewidths is limited by the resolution time of the measuring instrument. Oscilloscopes and fast photodiodes are limited to risetimes in the range of 50-100 picoseconds. Neither real time oscilloscopes nor sampling oscilloscopes permit the observance of single picosecond pulse durations. The only technique which employs direct measurement involves the use of a "Picochron" ultrafast streak camera (113), which is capable of resolution to 0.5 picoseconds. However, the streak camera system is first, highly expensive, and secondly, is susceptible to large quantum fluctuations (noise) due to the small amount of signal per mode resolution element which it receives.

Several indirect methods exist for picosecond pulsewidth measurements down to the order of 10^{-13} seconds or better. One of these techniques is based on the fact that a linear interferometer will measure the autocorrelation function of the amplitude of a pulse. Linear optical pulsewidth measurement techniques (114) are limited by the fact that the measured quantity is the coherence lifetime of the optical

Figure 3.2. Output spectrum of single pulse 850 nanoseconds
from start of pulse train; Rhodamine 590/DODCI



pulse. The coherence lifetime of the optical pulse is only equal to the actual lifetime of the pulse, however, for the case where the entire spectrum of the pulse is due to the short duration of the pulse envelope. In other words, the pulse being measured must be transform limited to provide credibility to the measurement. Otherwise, the measurement merely provides a lower limit to the duration of the pulse. To obtain a true measurement of the duration of a mode-locked pulse, one must rely on nonlinear techniques. A nonlinear technique employing type I second harmonic generation is used to measure the pulsewidths of our transverse flow mode-locked dye laser. A diagram of the Michelson interferometer auto-correlation setup is depicted in Figure 3.3. A single pulse impinges upon a beam splitter angled at approximately 45 degrees with respect to the beam path and the pulse amplitude $E(t)$ is split into two pulses, each with amplitude $E(t)/\sqrt{2}$. The beams traverse their respective paths L1 and L2 and are recombined at the second harmonic crystal. The two mirrors M1 and M2 reflect the beams back upon themselves, with M1 rigidly fixed and M2 translatable along the beam path. In our system, the beamsplitter, both mirrors, and the frequency doubling crystal are mounted on Oriel #1450 2-inch diameter precision mirror mounts for full adjustability. M2 is also mounted on an Oriel 1" travel translation stage driven by a Superior Electric Co. M061-FC08 Slo-Syn synchron-

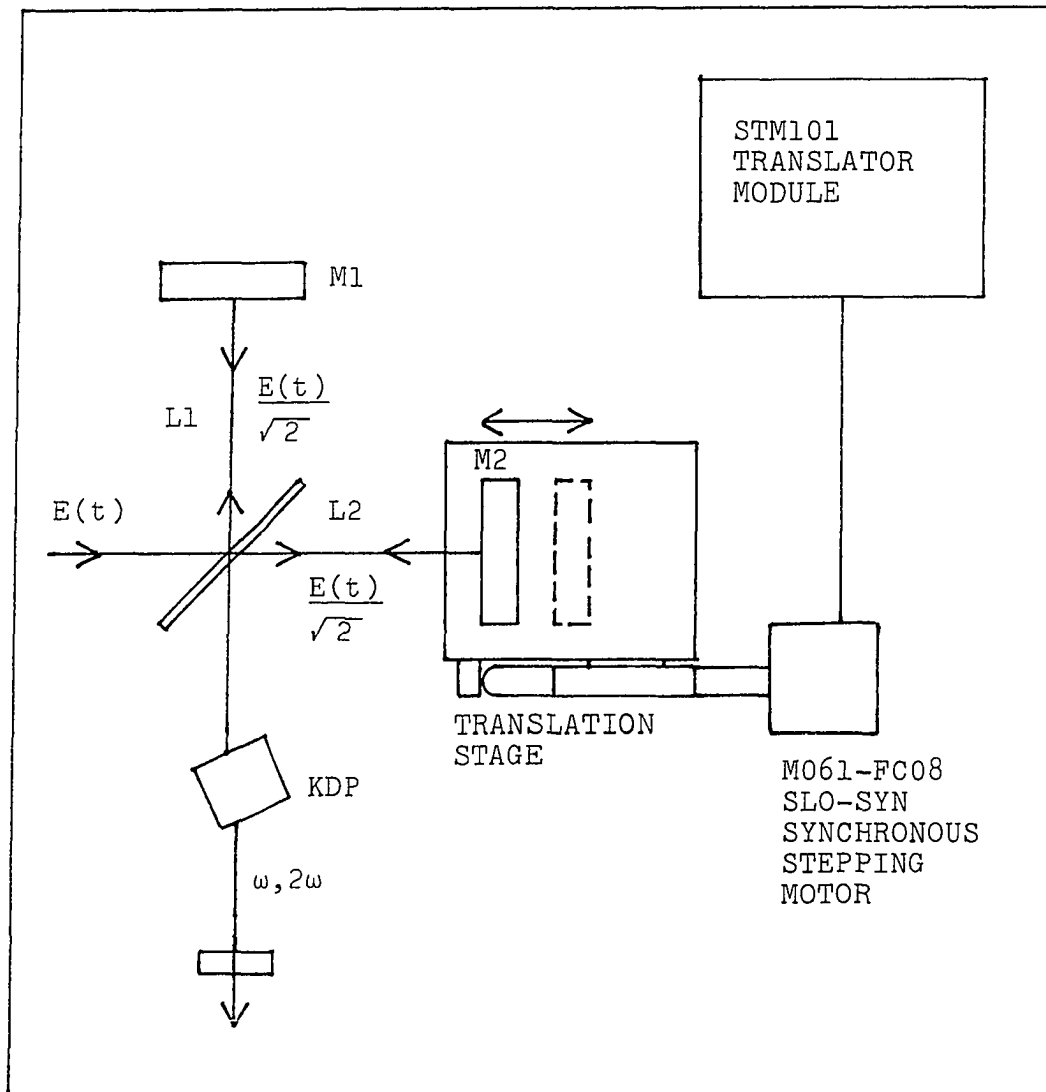


Figure 3.3. Schematic of Michelson interferometer used in autocorrelation pulsewidth measurement

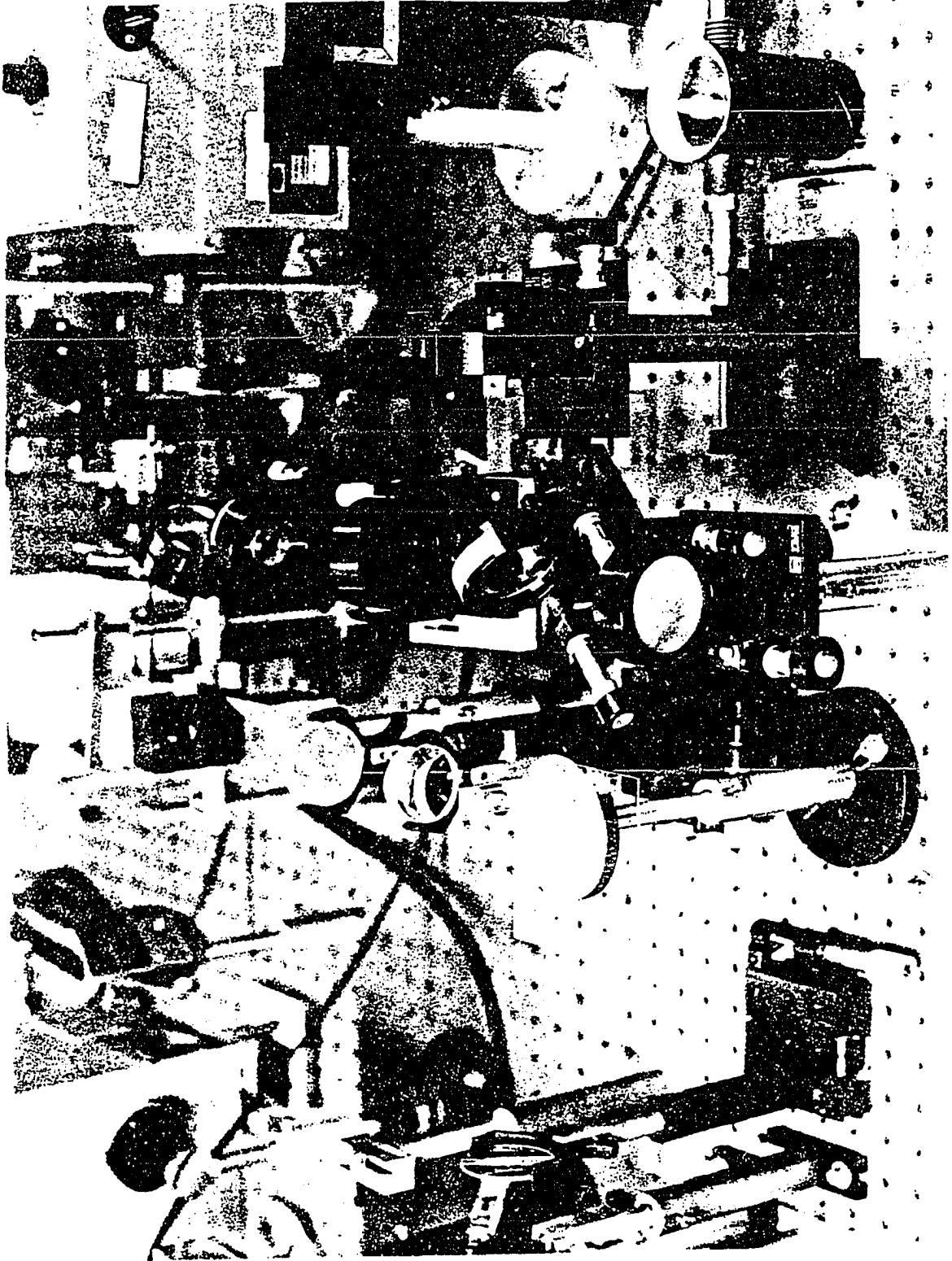
ous stepping motor. The latter is actuated by an STM101 translator module, which contains the logic elements for bidirectional operation. The single step increment for this motor is 1.8 degrees, and the unit may be continuously operated at step rates of 1 Hz and greater. A single step jog circuit allows the unit to be initialized to a particular position. The SHG (second harmonic generation) crystal is composed of KDP (potassium dihydrogen phosphate) and was purchased from Lasermetrics, Inc. The crystal dimensions are 14 x 14 x 12.5 millimeters, and an index matching fluid (Lasermetrics FC-104) is used to keep the crystal from contacting moisture. The crystal is cut in such a fashion that the incident beam makes a 67 degree angle with respect to the optic (z) axis and a 45 degree angle with respect to the x crystal axis. The interferometer and frequency doubling crystal are shown in Figure 3.4.

As the two output pulses $E_1(t)$ and $E_2(t)$ pass from the interferometer to the nonlinear optical crystal, the second harmonic output from the crystal will be

$$2\omega E(t) = [E_1(t) + E_2(t-\tau)]^2$$

(neglecting the second harmonic generation efficiency constant of the crystal, which would add another term to this expression) (112). For this expression, τ is the delay time incurred by the movement of the translatable mirror and is

Figure 3.4. Michelson interferometer and frequency doubling
KDP crystal



equal to $2d/c$, where d is the differential displacement of the mirror, and c is the speed of light. The resultant output signal $S(\tau)$ from a detector which has a slow response time with respect to ω and t is

$$S(\tau) = \int_{-\infty}^{\infty} 2\omega E(t)^2 dt = 2\omega_W(1 + 2G(\tau)),$$

where $2\omega_W$ is the second harmonic pulse energy and $G(\tau)$ is the autocorrelation function of the pulse intensity.

$$2\omega_W = \int_{-\infty}^{\infty} E^4(t) dt$$

$$G(\tau) = \frac{\int_{-\infty}^{\infty} E^2(t)E^2(t-\tau) dt}{\int_{-\infty}^{\infty} E^4(t) dt}$$

In the case where there is total overlap of the nondelayed and delayed portion of the pulse ($\tau = 0$), $S(\tau)/2\omega_W = 3$. If no overlap exists between the two portions of the pulse (τ large), $S(\tau)/2\omega_W = 1$. Through the measurement of the variation of $S(\tau)/2\omega_W$ as a function of τ , one can obtain the time duration over which the energy of the pulse is distributed. What should be ideally seen for the case of a completely mode-locked pulse is a peak to background contrast ratio of 3:1 (30,115). For a laser with incomplete mode-locking or improper spatial correlation of the two pulses within the harmonic crystal, contrast ratios of 3:2:1 (a spike with relative intensity of 3 superimposed upon a peak with

relative intensity 2, with a background of intensity 1), or 2:1 (115-118) are seen. In any case, the width of the auto-correlation trace at FWQM provides a good approximation of the pulse width (63). For a determination of the actual pulse width, a pulse shape (Gaussian, Lorentzian, sech^2 , etc.) must first be assumed. Multiplicative factors for obtaining the actual pulsewidths for each type of pulse are listed in reference 1.

The detection system used for interpretation of the output from the second harmonic generating crystal is shown in Figure 3.5. The output from the second harmonic crystal is directed into the entrance slit of a Jarrell-Ash model #82410 quarter meter monochromator. By using a 3% beamsplitter placed in the fundamental beam prior to the interferometer, a direct signal from the laser can be used for normalization. This fundamental signal is first sent through an appropriate neutral density filter to reduce its intensity, and is then sent into a second Jarrell-Ash quarter meter monochromator. The laser is frequency tuned to an optimum mode-locking wavelength (approximately 6070 angstroms for Rhodamine 590), to which the normalization monochromator is also tuned. The monochromator viewing the second harmonic signal is adjusted to half of that wavelength (for this case, approximately 3035 Å). The monochromator slit widths are adjusted to a wide setting so the entirety of an extremely small signal may

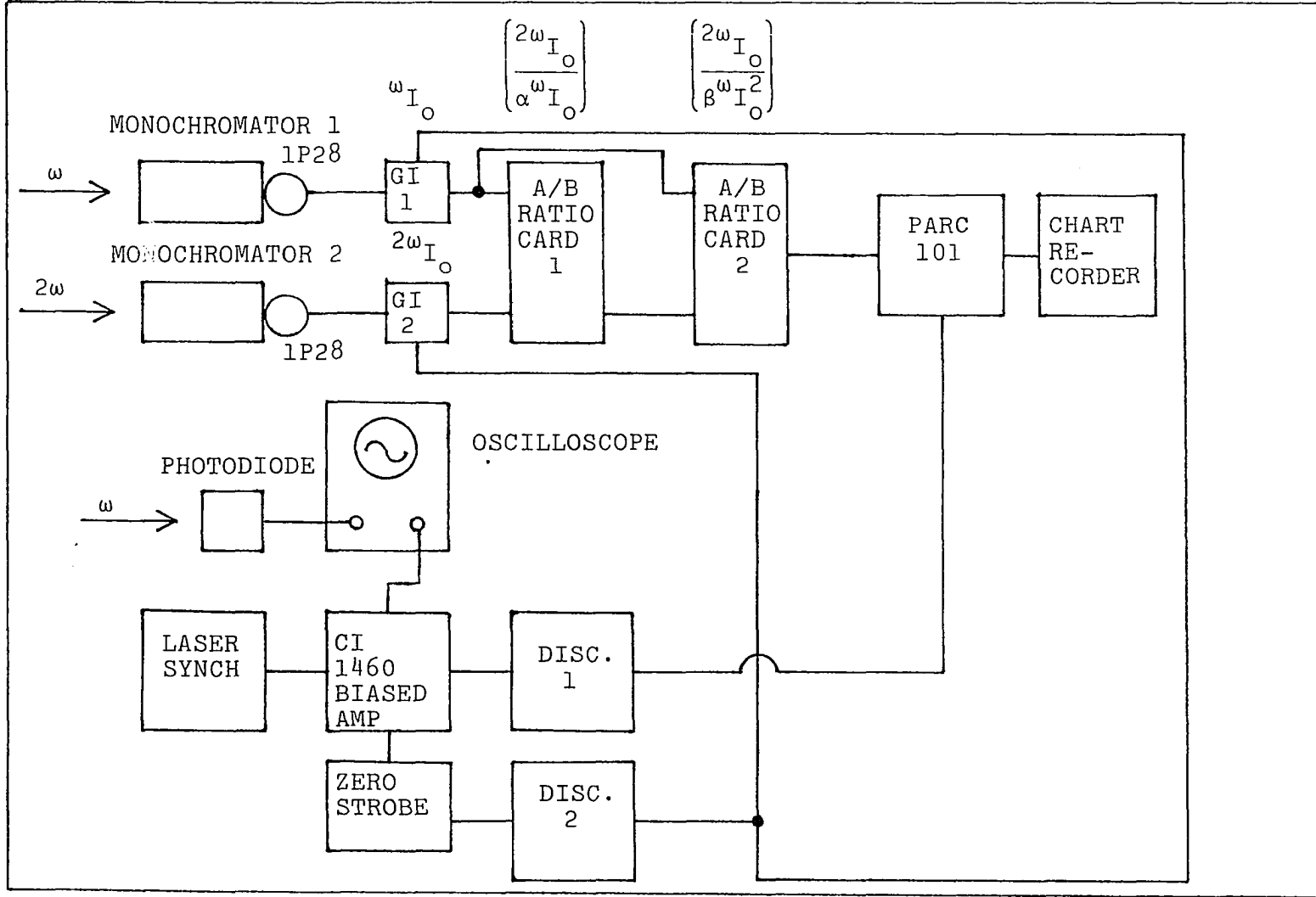


Figure 3.5. Autocorrelation detection system

be detected with a high background to noise ratio. Both signals are received by RCA 1P28 phototubes and subsequently sent to a set of Evans gated integrator cards (a timing correlation diagram for all of the signals generated by the components of the detection system may be seen in Figure 3.6). The gated integrators are triggered by -5 volt square timing pulses which come from a Nuclear Physics delay generator. In order to operate the delay generator, the laser sync pulse out is first input to a Canberra Industries (Sturup Nuclear Division) model 1460 biased amplifier. The biased amplifier serves to only amplify a portion of the sync pulse which exceeds a fixed voltage, while rejecting the rest of the pulse, in order to yield an output pulse with a very fast risetime. This output pulse, in turn, is introduced to a Canberra Industries model 1420 zero strobe. The zero strobe is used as a discriminator which rejects electronic noise which might cause spurious triggering in the data collection. The noise-free amplified fast risetime output pulse from the zero strobe is used to trigger the Nuclear Physics delay generator. The output signal from the delay generator is split and ac coupled (using .1 microfarad capacitors) prior to transmission to the gated integrators. This timing pulse which is received by the gated integrators initiates data collection (in the form of dc signals) from the phototubes. Gated integrator #1 (GI_1) integrates the fundamental signal

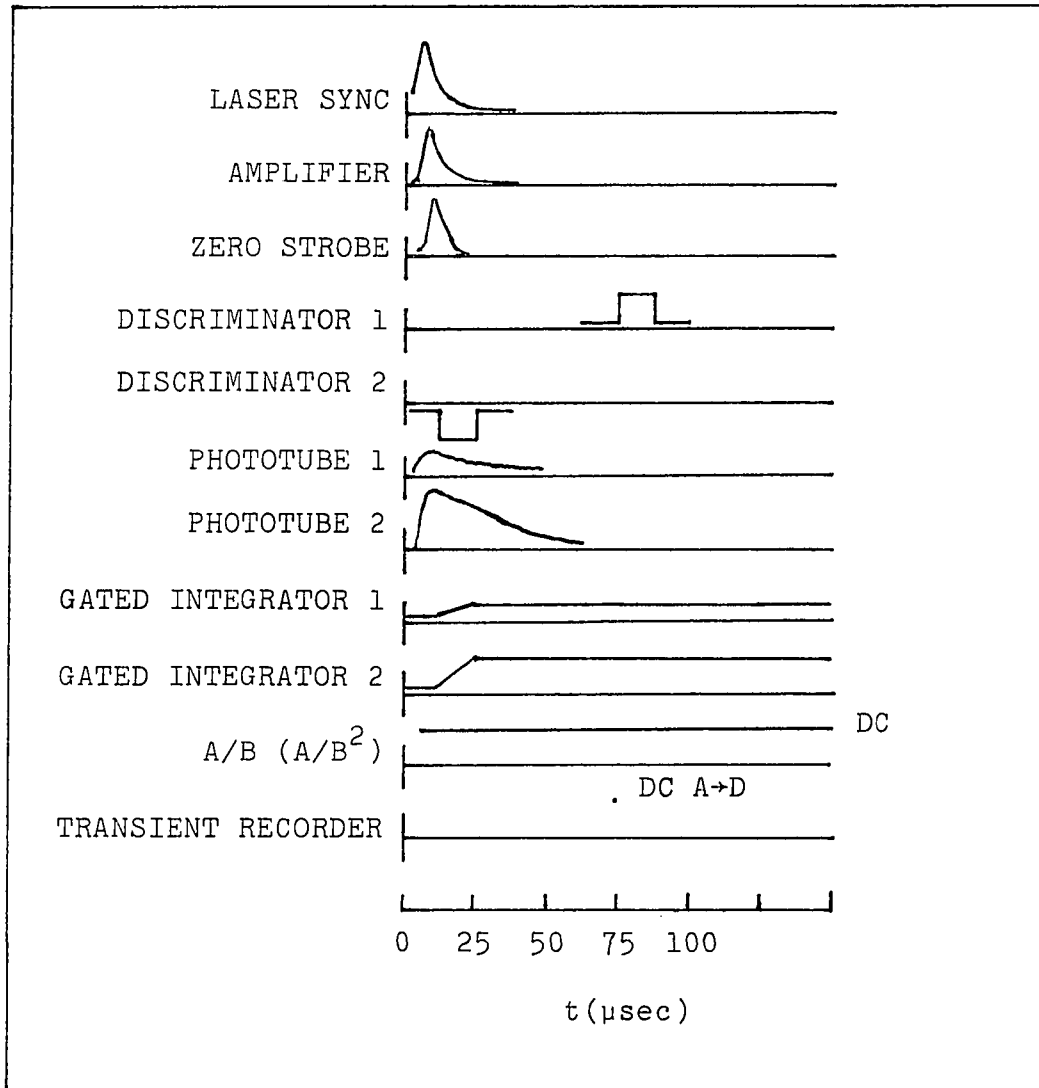


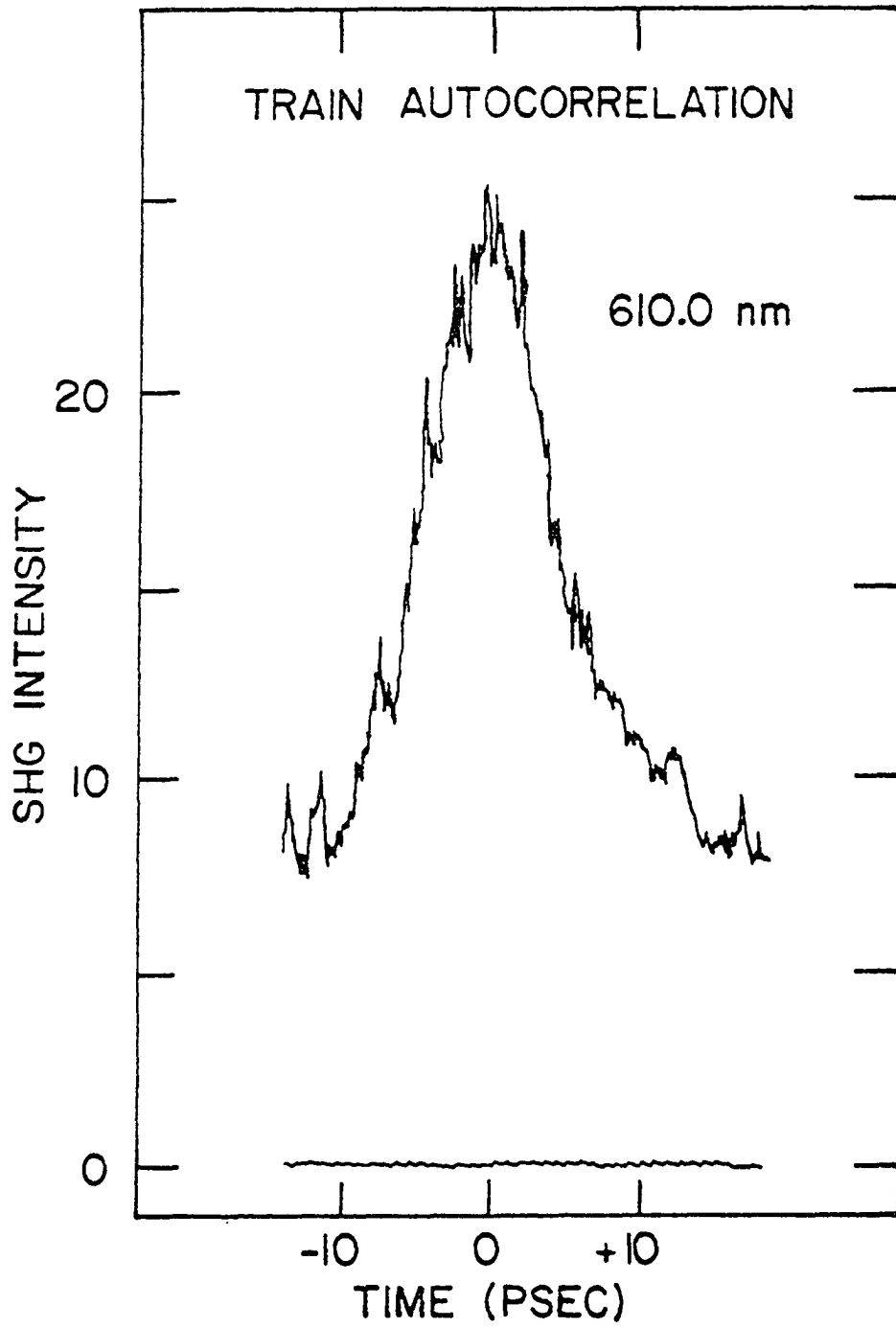
Figure 3.6. Timing diagram for autocorrelation detection system

(ωI_0), while gated integrator #2 (GI_2) integrates the second harmonic ($2\omega I_0$) signal. Both of the integrator signals are sent into an Evans model 4122 ratiometer, which inputs the two dc voltages, v_x and v_y , and outputs the ratio of the two, v_x/v_y (the ratiometer module also offers the option of absolute value $|v_x/v_y|$ and log functions $\log(v_x/v_y)$). The output signal v_x/v_y , with v_y resultant from the fundamental beam, is input to a second ratio card as the v_x input. The fundamental signal, v_y , is once again taken directly from the integrator, and input as v_y into the second card. The output is then (v_x/v_y^2) , yielding an A/B^2 normalized signal of the second harmonic generation output. A second output from the sync pulse-triggered biased amplifier is input to an EG&G model GD150/N delay gate, which outputs a +5 volt square wave timing pulse, delayed with respect to the -5 volt output pulse of the first delay generator. This pulse is input to the Princeton Applied Research model 4101 scan recorder. The dc signal output by the second ratio card, which is also input to the scan recorder, does not require a precisely delayed timing pulse to initiate signal collection. Therefore, the trigger pulse is delayed only to the extent that it occurs anytime after the second ratio card is ready to output data. The scan recorder inputs data into a 1024 word memory, each half of which is individually accessible. The output can consist of the first 512 locations of memory

(y_1), the second 512 locations of memory (y_2), both halves of memory (y_1, y_2), or the sum, difference, or ratio (point by point) of y_1 and y_2 . When an oscilloscope display is used, y_1 may be displayed above y_2 with an adjustable vertical displacement. Outputs from the recorder are connected to the horizontal and vertical inputs of a Tektronix type 547 oscilloscope, as well as to the inputs of a Mosley model 135 X-Y chart recorder.

Autocorrelation measurements were made and permanent recordings of the second harmonic traces were made with the x-y plotter. Under the assumption that the actual pulse shapes for mode-locked pulses produced by this system are unknown, only the autocorrelation values are presented here. All autocorrelation measurements were performed with the laser mode-locked at 607 nm and operating at a repetition rate of 1 hertz. First, a full pulse train autocorrelation measurement was performed, utilizing 200 mode-locked shots from the laser. This measurement yielded the result that the average pulsewidth within the train is approximately 13 picoseconds (Figure 3.7). The desired autocorrelation ratio of 3:1 appears to have been obtained. However, the measurement produced a very noisy signal, and the exact shape of the autocorrelation signal is not ascertainable. A single pulse autocorrelation measurement 850 nanoseconds into the train yielded a pulsewidth of 3.9 picoseconds.

Figure 3.7. Autocorrelation trace for entire mode-locked pulse train; Rhodamine 590/DODCI



When mode-locked with DODCI and Rhodamine 590 (or Rhodamine 6G), the laser is tunable over a range of approximately 150 Å, with the optimum mode-locking observed at 6050-6070 Å. Plans for mode-locking with other dyes include: mode-locking Fluorol 7GA with DQOCI (1,3'-diethyl-4,2'-quinolyloxadicarbocyanine iodide) in the range of 5500-5800 angstroms (119); mode-locking Coumarin 314 with PIC (1,1'-diethyl-2,2'-cyanine iodide) in the range of 5040-5200 angstroms (120); mode-locking of Cresyl-Violet (+ Rhodamine 590) with DOTCI (3,3'-diethyl-2,2'-oxatricarbocyanine iodide) in the range of 6450-6800 angstroms (110). Mode-locking of Rhodamine B with DODCI in the range of 6150-6450 angstroms (110); mode-locking of Rhodamine 590 with DQOCI in the range of 5750-6000 angstroms.

Factors Affecting Mode-Locking Quality and Repetition Rate

Some of the factors which affect the quality of mode-locking with the transverse flow laser have been previously discussed in Chapter II of this thesis. More empirical evidence has led to the discovery of other factors affecting mode-locking. The cavity length, for example, did not produce the best mode-locked output for cavity lengths of 50 to 55 centimeters, as theoretical considerations had previously pointed out. Instead, the best mode-locking was found to

occur for a 65 centimeter cavity. It was also determined that for cavity lengths of 80 centimeters or greater, mode-locking was very poor. This stands in agreement with theoretical considerations (49).

One factor which may affect mode-locking and has not been investigated yet is dye quality. It is known that the Exciton Rhodamine 590 is superior to Eastman Rhodamine 6G, but the reasons for this are not documented. It has been shown that different lots of Eastman Rhodamine 6G[Cl⁻] contained dyes of different molecular structure (77). All dyes which are not of 100% purity contain either other dyes, organic impurities, or inorganic salts. The comparison of dye samples purified by column chromatography with raw samples can lead to the determination of the amount of impurity present. Dye quality verification for all dyes used with this laser could present a topic for future work. Dye lifetimes as affected by photodegradation should also be looked at more carefully.

One point to note is the lack of sensitivity of the quality of mode-locking to the concentration of mode-locking dye in the contacted dye cell. With the 200 μm cell in use, the dye concentration can be varied from $1.3\text{-}1.7 \times 10^{-4}$ molar without any significant differences in output occurring. Through the use of a circulating system instead of a standing system for the saturable absorber dye, it is possible that we are diminishing the presence of products of photoreaction

which could contribute to the concentration dependence for mode-locking. Of course, this ability to vary the concentration may be a characteristic of the R6G-DODCI system, and we may find that such is not the case for other dye combinations.

The transverse flow dye laser is at present limited with respect to repetition rate, and is generally operated at one hertz. This is quite satisfactory for many applications, but the ability to achieve higher repetition rates would facilitate rapid data collection and allow better signal to noise ratios to be obtained. The pulsed power supply does not present a problem because it is capable of repetition rates of up to a kilohertz. At present, the laser may be operated satisfactorily at 5 or 10 hertz, with a corresponding higher lasing threshold (greater than 100 joules/pulse train). The main consideration in achieving higher repetition rates with this system lies in the limiting of the area of dye which is illuminated within the active region. The height of the region which is illuminated by the pump light is not 2-3 mm (as dictated by the separation of the glass envelopes), but rather on the order of 2-3 cm. To correct for this situation, the outside of the glass envelopes could be silvered, with the exception of thin strips approximately 4 mm high running the length of the active region. An alternative solution involves the insertion of 6" long cylindrical lenses between

the flashlamps in the active region in order to refocus the pump light into the lasing region.

The flashlamps have been thoroughly discussed in Chapter II with the exception of numerical examples representative of flashlamp lifetimes for different lamps, with and without the simmer power supply. Two lamp types, both of similar configurations, have provided the best operational lifetimes. With the aid of the simmer power supply, the best lamps by far have been the EG&G FX-139C-6 flashlamps, with a 50 torr xenon fill and a 6 inch arc length. These lamps have lasted (to approximately 70% of original light output) for 200,000 shots with this laser system. The next best lamp (used with the simmer supply) is the ILC L-3689 flashlamp, providing operational times on the order of 50,000 shots. The EG&G flashlamps have not been utilized without the simmer power supply, but at one time the ILC lamps were, with resultant lifetimes of 10,000 (or fewer) shots.

CHAPTER IV. LIQUID JUNCTION SOLAR CELLS

The semiconductor liquid-junction solar cell (SLJSC), more generally called a photoelectrochemical cell (PEC), utilizes a junction interface which is simpler than that of either p-n junctions or Schottky barrier solar cells. The SLJSC junction requires no elaborate preparation and is simply formed by immersion of the semiconductor into a liquid electrolyte containing one or more redox couples. A counter-electrode, typically an inert, nonphotosensitive metallic electrode, is also in contact with the electrolyte. The cell circuit is completed internally by ionic conduction in the electrolyte.

Two modes of operation exist for the PEC. In the photovoltaic mode, light energy is directly converted into electrical energy, while in the photoelectrolysis (photoelectrosynthetic) mode, the conversion is into chemical energy. The photoelectrolysis cell normally operates under short circuit conditions, so that a photovoltage is not produced. For photoelectrolysis, two redox couples are used, each contributing a half-cell reaction. The energy which is stored via chemical product formation is ideally equal to the difference in electrochemical potential between the two couples. One of the major goals for a cell of this type is the efficient

production of H_2 via the photoelectrolysis of water (121-123). The production of methane gas, chlorine gas, and ammonia are also presently under study (124-126). Electrochemical photovoltaic cells, of primary importance to this study, employ a single redox couple in solution. If an n-type semiconductor is utilized, the reduced species in solution is oxidized by a hole produced at the photoanode. The resultant oxidized species migrates to the counterelectrode, where it is in turn reduced by electrons which have passed through the external circuit. The oxidized species is reduced by a conduction band electron at the photocathode of a PEC employing a p-type semiconductor. For either type of PEC, the energy gained by the majority carrier in the system is converted to work as the carrier flows through the external circuit (via a load or device for extracting work). The ideal photovoltaic PEC is "regenerative," i.e., the composition of the semiconductor and electrolyte does not change over a period of time.

The present photovoltaic PECs show a highest efficiency for solar illumination of 12% for a device employing n-GaAs/0.8M Se^{2-} , 0.1M Se_2^{2-} , 1M OH^- /C. This cell consists of a single crystal GaAs photoanode in contact with an aqueous electrolyte containing Se^{2-}/Se_2^{2-} redox couple and incorporates a carbon counterelectrode (127). N-type material is generally used in photovoltaic PECs because p-type photo-

cathodes have typically shown efficiencies of $\leq 5\%$ and have been unstable toward cathodic dissolution. To date, only single crystal p-InP used with a V^{2+}/V^{3+} redox couple has shown promise among p-type materials with an efficiency of 9.4% (128). The exceptional stability and efficiency of this system is attributable to fast kinetics and favorable energy level structure associated with the V^{2+}/V^{3+} couple as well as low surface recombination rates associated with a thin oxide layer on the p-InP.

The Semiconductor

In order to gain a fundamental understanding of the operation of a PEC, one must first explore the nature of the semiconductor. As isolated atoms are brought together to form a crystalline solid, the wavefunctions of the individual atoms begin to overlap. All spin-paired electrons acquire energies slightly different from energies found in the isolated atoms, and the Pauli exclusion principle is satisfied. Instead of occupying discrete energy levels, bands of states are found, where the energy distribution of the states shows a strong dependence on the interatomic distances within the crystal. Two bands may be distinguished as being most important in semiconductors. The lower band (valence band) contains as many states as electrons and, therefore, cannot by itself

supply free electrons for current flow. The upper band (conduction band) contains only empty states at 0°K. If an electron is promoted into the conduction band, it is capable of acquiring a net drift under the influence of an electric field. Between the valence and conduction band exists a region referred to as the energy gap or bandgap, where no electronic energy levels exist. The extent of the bandgap determines whether the solid is a metal, a semiconductor, or an insulator. In a metal, the upper band is populated with electrons far above the energy gap with an electron concentration of $\sim 10^{23} \text{ cm}^{-3}$. A typical semiconductor bandgap is less than 3 eV, with thermal populations of less than 10^{20} cm^{-3} . The bandgap of an insulator is greater than 3 eV, with negligible electron populations in the conduction band. The divisions between metal, semiconductor, and insulator are not clear cut, but logical divisions are commonly used.

The allowed electron energy states in a crystal can be obtained, in principle, by solving the Schrodinger equation involving all of the electrons in the solid. This task is made tangible by the introduction of several simplifying approximations. First, the crystal is assumed to consist of an ideal periodic structure of atoms at rest in their lattice sites. The interactions of electrons with thermal vibrations of the nuclei and lattice imperfections are treated as per-

turbations and not considered for the initial solution. Only valence electrons are considered. The potential consists of a periodic term due to the nuclei and inner core electrons and a constant term due to the charge distribution of all the other valence electrons.

The one-dimensional model by Kronig and Penney (129) best exhibits the features of band structure and electron propagation in a crystal. This model utilizes the Bloch theorem (130), whereby the corresponding wavefunctions for a periodic potential in one dimension (Bloch functions) are of the form

$$\psi(x) = U_k(x)e^{ikx}, \quad [4-1]$$

where $U_k(x)$ exhibits the periodicity of the potential such that

$$U_k(x+a) = U_k(x), \quad [4-2]$$

with "a" corresponding to the distance between two lattice points. The wave number, k , is related to the deBroglie wavelength of the electron by

$$|k| = 2\pi/\lambda. \quad [4-3]$$

After much manipulation, the solutions obtained exhibit allowed energy ranges (bands) of electron states separated

by forbidden zones. The energy $E(k)$ is a periodic function of period $2\pi/a$. This allows the restriction of k to the interval $2\pi/a$, usually expressed by

$$-\pi/a \leq k \leq \pi/a. \quad [4-4]$$

This region of pertinent k values, when extended to three dimensions, is known as the first Brillouin zone.

Of the allowed energy bands, the two most important are those corresponding to the highest occupied electron states (valence band) and the lowest unoccupied electron states (conduction band). We frequently need to know only the form of the energy bands near the maximum or minimum value of energy, as it is only states near these that contribute to the phenomena under consideration. Figure 4-1 illustrates the conduction band minimum and valence band maximum utilizing parabolic band shapes whose extrema exist at the center of the first Brillouin zone.

In three dimensions, it is rather difficult to represent the energy bands pictorially. It is customary to draw several diagrams of E as a function of k along the principle directions of the crystal. If the bands exhibit extrema at the center of the Brillouin zone and the parabolic dependence is the same for each principle axis, the resultant constant energy surfaces are spherical. This represents a special

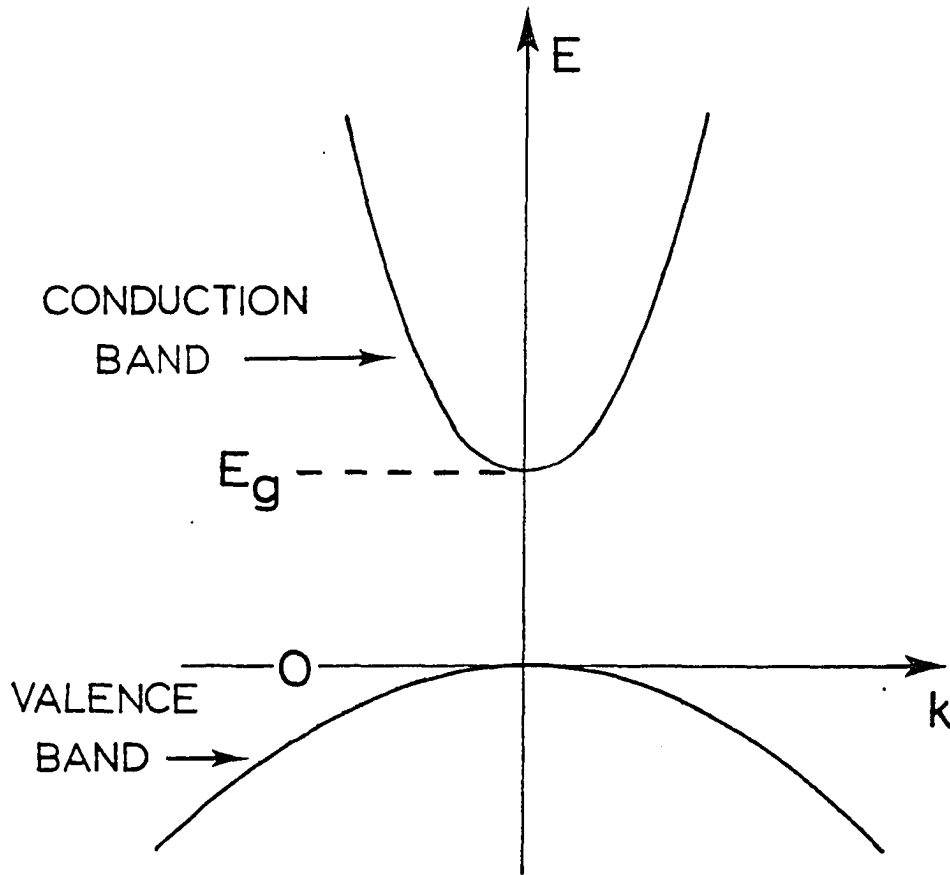


Figure 4-1. Parabolic conduction and valence bands with extremum at the center of the Brillouin zone. Electron energy vs. wave vector is depicted for one dimension.

case of the more general ellipsoidal constant energy surface found for nonequivalent parabolic dependence along the principles axes.

Due to the interaction of nearest neighbors, next-nearest neighbors, and all higher order neighbors, the conduction band minimum may not occur at the Brillouin zone center. Figure 4-2 illustrates this for one dimension. Symmetry considerations dictate the presence of a second minima along this symmetry axis, and two minima along the other equivalent symmetry axes. The constant energy surface corresponding to the depicted minima consists of eight ellipsoids of revolution, two about each axis.

Absorptive transitions in a semiconductor involve the promotion of an electron from the valence band to the conduction band with the net result of electron-hole pair formation. In general, absorption may be expressed in terms of the relationship

$$\frac{I(x, \nu)}{I(x_0)} = e^{-\alpha(\nu)(x-x_0)} \quad [4-5]$$

where α is the absorption coefficient (a function of wavelength) and x represents the distance from the crystal surface located at x_0 . The absorption coefficient is related to another useful quantity, the extinction coefficient \hat{K} , which is in turn defined via the complex index of refraction \hat{N}_c for

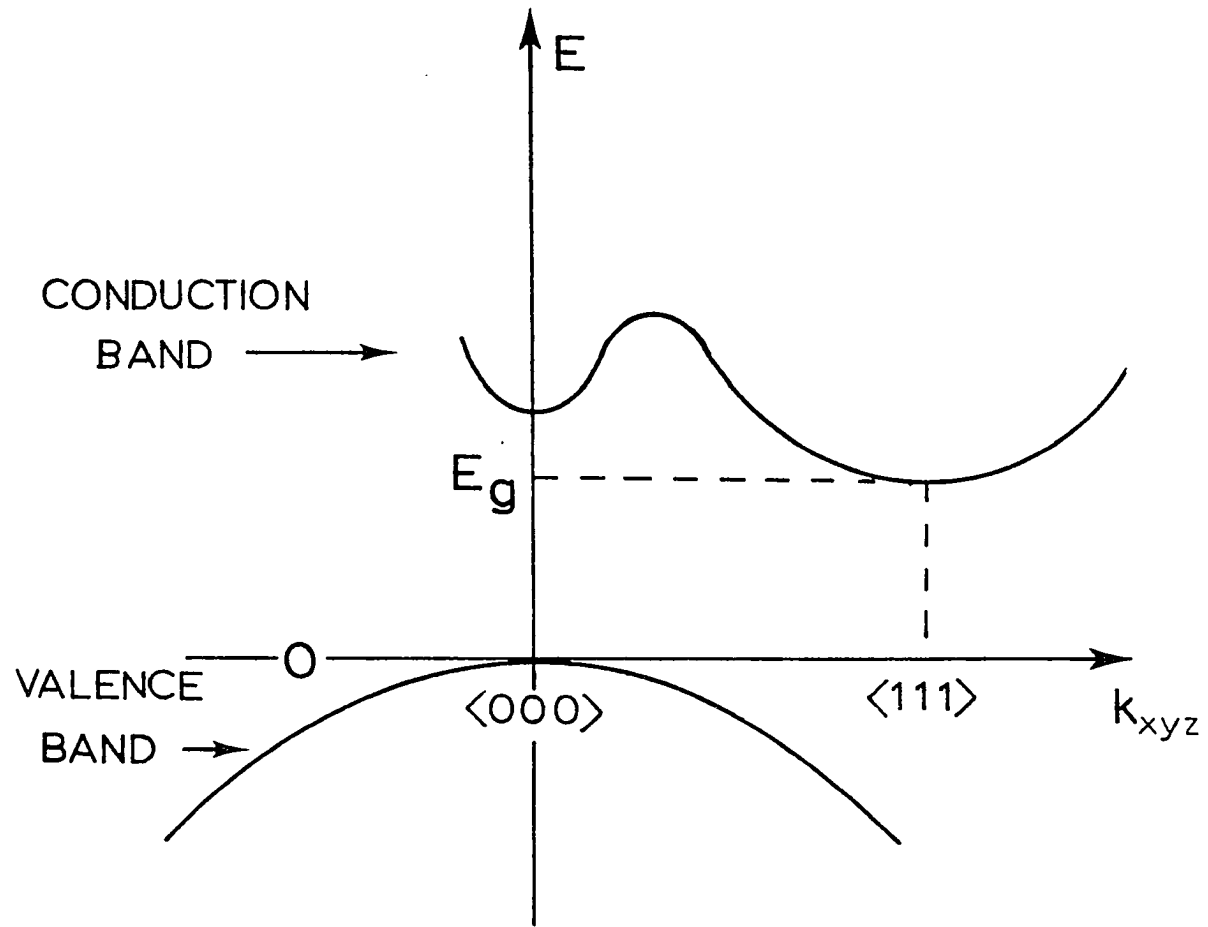


Figure 4-2. Energy vs. wave vector diagram for a semiconductor with a minimum bandgap not corresponding to the Brillouin zone center. The symmetry axes depicted lie along the body diagonal of a cubic crystal

an absorbing material.

$$\hat{N}_c = \hat{N} - i\hat{K} \quad [4-6]$$

If light incident on a crystal is described as a plane wave of frequency ω propagating in the x direction with velocity v , the associated field strength may be written as

$$E = E_0 \exp [i\omega(t - x/v)]. \quad [4-7]$$

The velocity within the semiconductor is related to the vacuum velocity, c , by

$$v = \frac{c}{\hat{N}_c} \quad [4-8]$$

Therefore,

$$\frac{1}{v} = \frac{\hat{N}}{c} - \frac{i\hat{K}}{c}, \quad [4-9]$$

and substitution into equation [4-7] yields

$$E = E_0 \exp(i\omega t) \exp \left[\frac{-i\omega x \hat{N}}{c} \right] \exp \left[\frac{-\omega x \hat{K}}{c} \right] \quad [4-10]$$

where the last term expressed the attenuation of the incident light as it passes into the semiconductor. Comparison of equations [4-5] and [4-10] yields

$$\alpha = \frac{2\omega \hat{K}}{c} = \frac{4\pi v \hat{K}}{c}. \quad [4-11]$$

From this stems another important relationship relating the absorption coefficient to the amount of light reflected from a surface at normal incidence (131).

$$R = \frac{(\hat{N}+1)^2 + \left(\frac{\alpha c}{4\pi\nu}\right)^2}{(\hat{N}-1)^2 + \left(\frac{\alpha c}{4\pi\nu}\right)^2} \quad [4-12]$$

Band-to-band transitions are subject to selection rules, whereby the momentum of the promoted electron is conserved. This requirement may be met by an additional transition involving a phonon (the momentum of a photon h/λ is small in comparison to the crystal momentum h/a , with "a" a lattice constant). The absorption coefficient α is proportional to the probability P_{if} for the transition from the initial state to the final state, the density of electrons in the initial state N_i , and the density of the empty states N_f , summed for all possible transitions between states separated by an energy difference $h\nu$.

$$\alpha(h\nu) = A \sum_{if} P_{if} N_i N_f \quad [4-13]$$

In a direct absorption transition where all momentum-conserving (vertical) transitions are allowed, the transition probability P_{if} is independent of photon energy (Figure 4-3). Each initial state at E_i is associated with a final state E_f such that

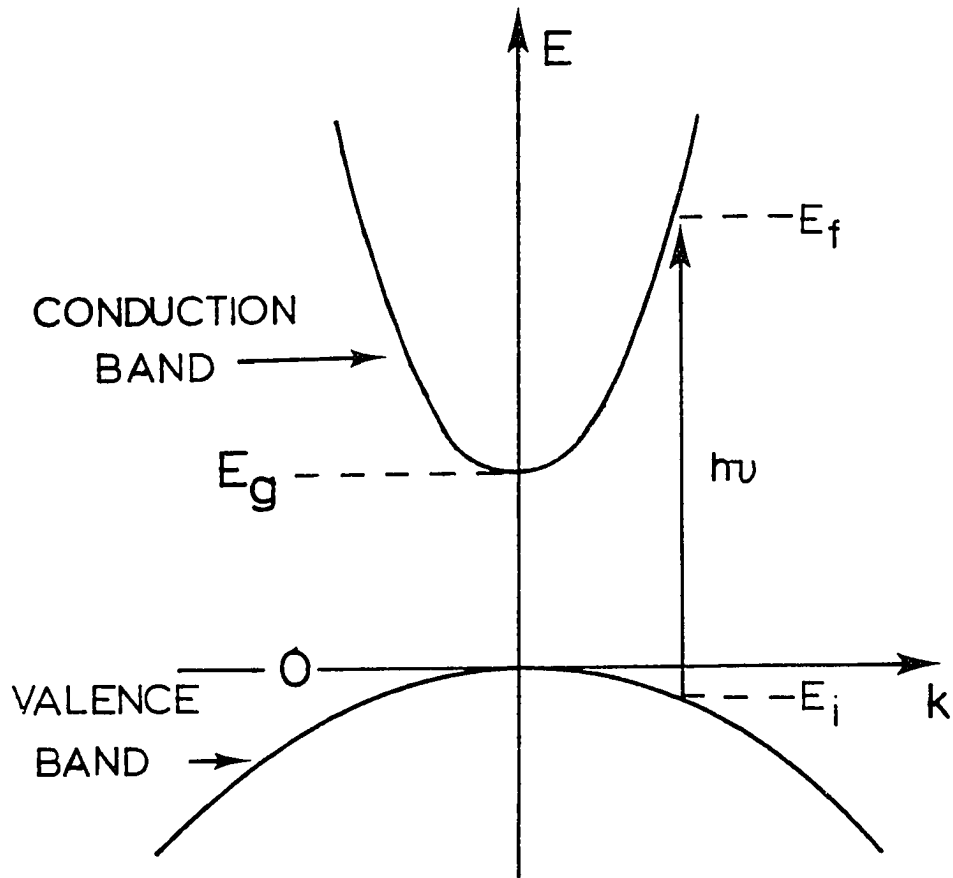


Figure 4-3. Absorption of a photon with $h\nu > E_g$ via a direct transition

$$E_f = h\nu - E_i. \quad [4-14]$$

The absorption coefficient for this type of transition turns out to be

$$\alpha(h\nu) = A^*(h\nu - E_g)^{\frac{1}{2}} \quad [4-15]$$

Where A^* is given by (132)

$$A^* = q^2 \frac{\left(\frac{2m_n^* m_e^*}{m_n^* + m_e^*} \right)}{\hat{n} \text{ch}^2 m_e^*} \quad [4-16]$$

In this expression, q is the charge on an electron, \hat{n} is the real part of the refractive index, and m_e^* and m_n^* are effective electron and hole masses, respectively. Each of the effective masses m_{ij}^* is in general a tensorial quantity whose character is defined by the symmetry of the energy surfaces. The effective mass components are defined as

$$\frac{1}{m_{ij}^*} = \frac{1}{h^2} \frac{\partial^2 E}{\partial k_i \partial k_j}. \quad [4-17]$$

Direct transitions are first order processes and, hence, correspond to large absorption constants.

If the valence band and conduction band extrema occur at different points in momentum space, the transition from the top of the valence band to the bottom of the conduction band requires both a change in energy and wavevector \mathbf{k} . A two-step process is required because the excitation photon cannot

provide a sufficient change in lattice momentum. Momentum is conserved in the transition via a phonon interaction where a phonon (in simplest terms) corresponds to a quantum of lattice vibration. Each phonon available for interaction has a characteristic energy E_p which is either emitted or absorbed (Figure 4-4). The two processes are defined by

$$h\nu_e = E_f - E_i + E_p \quad (\text{phonon emission}) \quad [4-18]$$

$$h\nu_a = E_f - E_i + E_p \quad (\text{phonon absorption}) \quad [4-19]$$

The absorption coefficient for transitions involving single phonon absorption and emission involves an electron-phonon interaction constant, which may be evaluated in terms of the relaxation times involved in lattice scattering. Transitions are regarded as taking place through a virtual state which may be regarded as short lived. Momentum, but not energy, is conserved in the transition to the virtual state. Energy is conserved in the overall transition which may proceed along one of the two paths denoted in Figure 4-5.

The absorption coefficients corresponding to this type of transition are

$$\alpha_a(h\nu) = \frac{A(h\nu - E_g - E_p)^2}{\exp\left(\frac{E_p}{kT}\right) - 1} \quad \text{for } h\nu > E_g - E_p \quad [4-20]$$

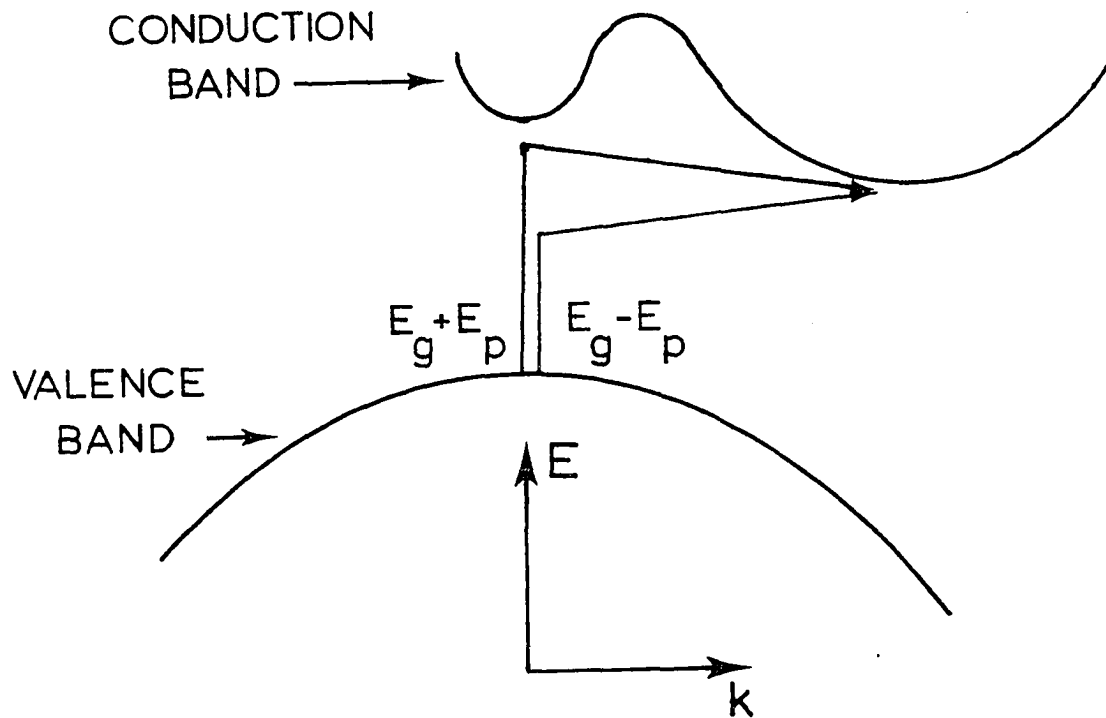


Figure 4-4. Absorption of a photon via an indirect transition with the corresponding absorption or emission of a phonon

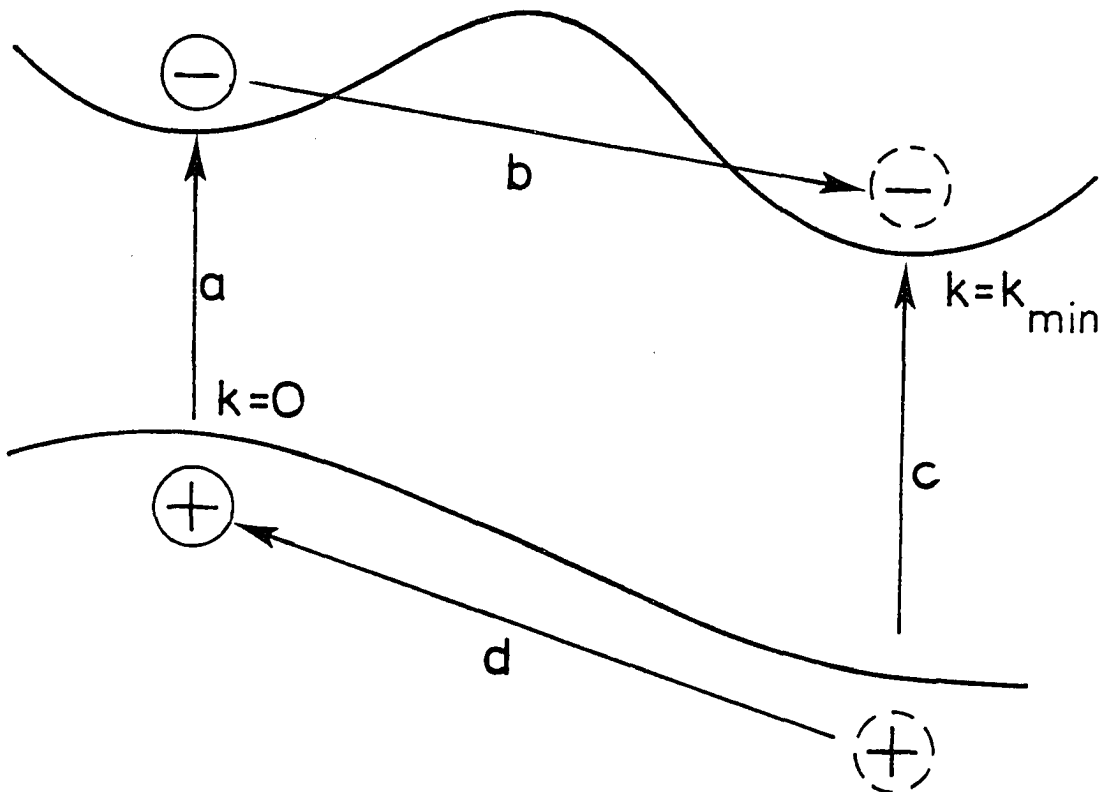


Figure 4-5. Electronic transition with emission or absorption of a phonon (via path 1 or 2)

Path 1: (a) Excitation of an electron without change of wave vector k from near the top of the valence band ($k=0$) leaving a hole with $k=0$. The electron goes into a $k=0$ state in the conduction band. (b) The electron then undergoes a transition to a state with minimum conduction band energy accompanied by the emission of a phonon with momentum equal to k_{\min} .

Path 2: (c) Vertical excitation of an electron from deep in the valence band to a state having $k=k_{\min}$ leaving a positive hole deep in the valence band. (d) The positive hole then undergoes a transition to a state with minimum valence band (hole) energy with the absorption of a phonon with momentum equal to k_{\min} .

$$\alpha_e(h\nu) = \frac{A(h\nu - E_g + E_p)^2}{1 - \exp\left(\frac{-E_p}{kT}\right)} \quad h\nu > E_g + E_p \quad [4-21]$$

where $\alpha_a(h\nu)$ and $\alpha_e(h\nu)$ correspond to phonon absorption and emission, respectively. Both processes are possible if $h\nu > E_g + E_p$ and for this case, $\alpha(h\nu) = \alpha_a(h\nu) + \alpha_e(h\nu)$. Indirect transitions are second order processes, and the absorption coefficient is thus smaller than for direct transitions.

Direct and indirect transitions can be differentiated by plotting α versus incident photon energy $\hbar\omega$. If a plot of α^2 versus $\hbar\omega$ produces a linear plot, the transition is direct; a plot of $\alpha^{1/2}$ versus $\hbar\omega$ will produce two linear sections for an indirect transition (Figure 4-6).

Impurities and imperfections in a semiconductor give rise to localized energy levels. An electron or hole occupying one of these states no longer has a corresponding wavefunction extending through the crystal, but rather possesses a localized wavefunction existing in the bandgap region. Impurity levels are generally separated into "donor" and "acceptor" levels. Donors are electron donors which yield electrons to the conduction band. Acceptors are electron acceptors which create a hole in the valence band. If the solid is dominated by donors, it is denoted n-type; if the solid is dominated by acceptors, it is denoted p-type. The

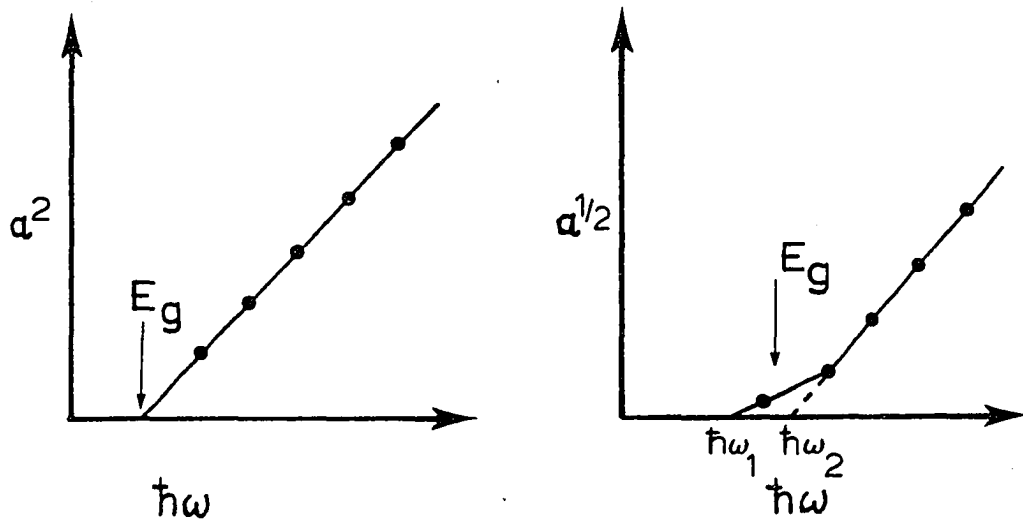


Figure 4-6. Variation of absorption coefficient with respect to energy of exciting photons

(a) Electronic excitation of direct bandgap semiconductor. (Absorption coefficient)² vs. excitation energy plotted. (b) Phonon assisted electronic excitation of indirect bandgap semiconductor. (Absorption coefficient)^{1/2} vs. excitation energy plotted. $\hbar\omega_1 = E_g - E_p$;

$$\hbar\omega_2 = E_g + E_p$$

dominating carrier is the majority carrier and the other, the minority carrier. The electron and hole densities at thermal equilibrium are given by (133) as

$$n = N_c \exp [-(E_c - E_F)/kT], \quad [4-22]$$

$$p = N_v \exp [-(E_F - E_v)/kT], \quad [4-23]$$

and

$$\begin{aligned} n_i^2 &= np = N_c N_v \exp [-(E_c - E_v)/kT] \\ &= N_c N_v \exp (-E_g/kT) \end{aligned} \quad [4-24]$$

where N_c and N_v are the effective densities of states at the band edges in the conduction and valence bands, E_c and E_v are the energies of the conduction and valence bands, E_F is the Fermi level of the semiconductor (energy for which the probability for occupation of a state by an electron is 0.50), and n_i corresponds to the intrinsic (undoped, nondegenerate) carrier density. Another important parameter is the Fermi distribution function f , which defines the Fermi energy E_F and the probability of electron occupation not within the bandgap, but rather within the bands themselves.

$$f = \frac{1}{[1 + \exp(E - E_F)/kT]} \quad [4-25]$$

The Fermi energy is E_F , k is the Boltzmann constant and T is the temperature in degrees Kelvin. The Fermi energy applies to the occupation of energy levels at thermodynamic equilib-

rium. More important to the present discussion, however, is the case where thermodynamic equilibrium is disrupted by the absorption of photons having energy greater than the bandgap.

Defects in a semiconductor single crystal may consist of vacancies, substitutional impurities, interstitial impurities, or dislocations. The semiconductor surface itself may be considered as a defect due to the break in the continuous crystalline structure and the presence of unsaturated bonds. If a semiconductor in a PEC is illuminated, a nonequilibrium distribution of charge carriers is created. There exists a propensity for the charge carriers to lose their acquired energy and return to an equilibrium distribution. The preferred method of charge carrier deactivation is via work performed in the external circuit. An alternative process which the electron-hole pairs may undergo is known as recombination, whereby the energy is lost within the semiconductor crystal in the form of thermal excitation (phonon emission). Defects are intimately involved with recombinative processes. Each recombination process has a rate associated with it, and several types operating in parallel have a rate which is the sum of the individual rates. Important recombination processes include: radiative recombination, auger recombination, recombination through traps, and recombination at surfaces.

Radiative recombination

Radiative recombination is the reverse of the absorption process described earlier. An electron relaxing from the conduction band to the valence band does so with the emission of a photon (of bandgap energy). Direct bandgap semiconductors, such as GaAs or InP, will exhibit rapid radiative transitions, whereas indirect bandgap semiconductor exhibits slow emission due to the two-step process involving the assistance of a phonon. The emission of radiation from a semiconductor is termed luminescence. The van Roosbroeck-Shockley relation (134) is used to describe the relationship between emission and optical excitation. The rate of emission at a frequency ν in an interval $d\nu$ is given by

$$R(\nu)d\nu = P(\nu)\rho(\nu)d\nu \quad [4-26]$$

where $\rho(\nu)d\nu$ is the density of photons of frequency ν in the interval $d\nu$ and $P(\nu)$ is the probability per unit time of absorbing a photon of energy $h\nu$. The photon density is obtained using Planck's Law,

$$\rho(\nu)d\nu = \frac{8\pi\nu^2\hat{n}^3}{c^3} = \frac{1 d\nu}{[\exp(\frac{h\nu}{kT})-1]} \quad [4-27]$$

where \hat{n} is the real part of the refractive index and all other symbols have their usual meaning. The relationship between the absorption probability and the mean lifetime of a photon

in the semiconductor is

$$P(\nu) = \frac{1}{\tau(\nu)}. \quad [4-28]$$

Calculation of the mean lifetime can be performed from knowledge of the mean free path $1/\alpha(\nu)$ of a photon moving with velocity $v = c/\hat{n}$ within the semiconductor.

$$\tau(\nu) = \frac{1}{\alpha(\nu)v}, \quad [4-29]$$

yielding

$$P(\nu) = \alpha(\nu) \frac{c}{\hat{n}}. \quad [4-30]$$

Utilizing equation [4-11], along with [4-26] and [4-27], we then have

$$R(\nu)d\nu = \frac{32\pi^2 K(\nu) \hat{n}^2 v^3 d\nu}{c^3 [\exp(h\nu/kT) - 1]} \quad [4-31]$$

Integration over all photon frequencies yields the total number R of recombinations per unit volume per second.

$$R = \frac{8\pi \hat{n}^2 (kT)^3}{c^2 h^3} \int_0^\infty \frac{\alpha(\nu) u^2 du}{e^u - 1} \quad [4-32]$$

where

$$u = \frac{\alpha(\nu)c}{4\pi K(\nu)} \frac{h}{kT}. \quad [4-33]$$

The van Roosbroeck-Schockley relation is valid for transitions between any sets of states, and not just band-to-band transitions.

The derivation thus far applies only to the system in a state of thermal equilibrium. The total radiative-recombination rate R_c is a function of electron and hole concentrations n and p , and also of the intrinsic carrier concentration n_i .

$$R_c = \frac{np}{n_i^2} R \quad [4-34]$$

If equilibrium conditions are disrupted by photon absorption, n and p become $n = n_o + \Delta n$ and $p = p_o + \Delta p$, where n_o and p_o are equilibrium concentrations of electrons and holes. Disequilibrium produces the net recombination rate

$$\Delta R_c = \left[\frac{\Delta n + \Delta p}{n_o p_o} \right] R_c \quad [4-35]$$

The radiative lifetime of excess carriers (assuming $\Delta n = \Delta p$) is then found to be

$$\tau = \frac{\Delta n}{\Delta R_c} = \frac{1}{R_c} \left(\frac{n_o p_o}{n_o + p_o} \right) \quad [4-36]$$

Radiative recombination is best observed for direct bandgap compounds with few recombination centers (traps) located in the bandgap, for the capture cross-sections for direct recom-

binations are typically orders of magnitude smaller than the cross-sections for recombination at a center.

Recombination through traps

The presence of dopants or general impurities (inclusive of lattice defects) will introduce energy levels into the forbidden bandgap. These impurities, particularly those introducing energy levels near the middle of the bandgap, degrade the properties of a semiconductor device through increased recombination. Trapping is a fundamental process for energy storage in almost all solids. When trapped, an excited electron or hole is prohibited from moving freely through the crystal and remains localized until the proper amount of energy (thermal, optical, etc.) is supplied to remove it. A trapping center (trap) is distinguished by its thermal equilibrium exchange with the nearest band. If a trap does not release the captured carrier, but rather allows a carrier of opposite charge to recombine with it, the trap is termed a recombination center. Shockley-Read-Hall theory (135-137) best describes recombination in semiconductors through the mechanism of trapping.

The rate of recombination through a trapping center depends upon the occupancy of the center, which is in turn related to the two capture cross-sections characterizing the

center; the cross-section for electron capture (by an unoccupied center), σ_n , and the cross-section for hole capture (by an occupied center), σ_p . The processes of electron and hole capture, as well as electron and hole emission, are depicted in Figure 4-7.

For a single recombination center with electron ionization energy E_R , the net rate of electron capture may be written as

$$R_{cn} = n(N_R - n_R)v_{th}\sigma_n - n_R v_{th} n_1 \sigma_n \quad [4-37]$$

where N_R is the density of recombination centers, n_R is the density of occupied recombination centers, σ_n is the capture cross-section of an unoccupied recombination center for a free electron, v_{th} is the carrier thermal velocity, equal to $\sqrt{3kT/m^*}$, and n is the electron density in the conduction band. The quantity n_1 represents the density of free electrons when $E_F = E_R$, and is written as

$$n_1 = N_c \exp(-E_R/kT) \quad [4-38]$$

where N_c is the effective density of states in the conduction band. In terms of the Fermi level, the occupancy of the centers, n_R , can be expressed as

$$n_R = N_R f_R = N_R \frac{1}{1 + \exp[(E_F - E_R)/kT]} \quad [4-39]$$

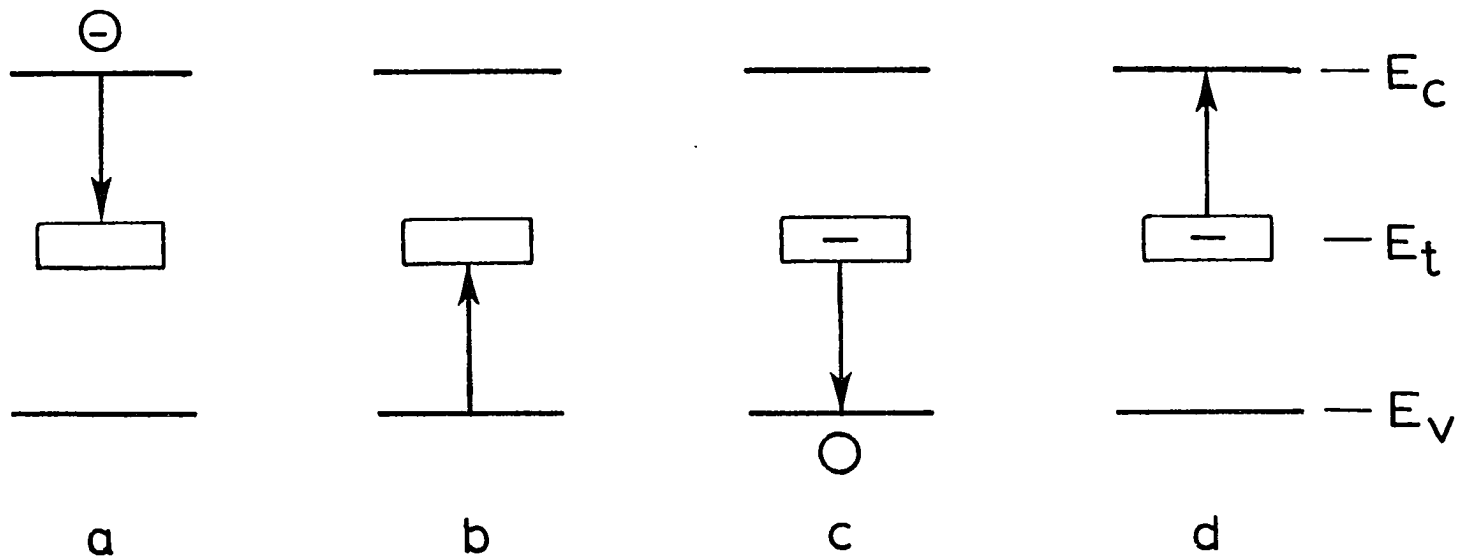


Figure 4-7. The basic processes of carrier generation and recombination through traps (a) Electron capture, (b) hole emission, (c) hole capture, (d) electron emission

Equation [4-37] may now be rewritten as

$$R_{cn} = nN_R(1-f_R)v_{th} \sigma_n - N_R f_R n_1 v_{th} \sigma_n \quad [4-40]$$

and, similarly, a net rate of electron hole capture may be written

$$R_{cp} = pN_R f_R v_{th} \sigma_p - N_R(1-f_R)p_1 v_{th} \sigma_p, \quad [4-41]$$

where

$$p_1 = N_v \exp[-(E_{BG}-E_R)/kT] \quad [4-42]$$

is defined in terms of the bandgap energy, E_{BG} , and the effective density of states in the valence band.

Under steady state conditions, where electron-hole pairs are being generated at a constant rate R , the net rate of electron capture is equal to the net rate of hole capture ($R = R_{cp} + R_{cn}$). By equating [4-40] and [4-41], the following expression for f_R is found:

$$f_R = \frac{\sigma_n n + \sigma_p p_1}{[\sigma_n(n+n_1) + \sigma_p(p+p_1)]} \quad [4-43]$$

Substitution of [4-43] back into [4-40] yields

$$R = N_R v_{th} \left[\frac{\sigma_n \sigma_p (np - n_1 p_1)}{\sigma_n(n+n_1) + \sigma_p(p+p_1)} \right] \quad [4-44]$$

The product $n_1 p_1$ is independent of E_R and is equal to n_i^2 , where n_i is the density of free electrons or holes in an intrinsic sample for which $n=p$.

Therefore,

$$R = N_R v_{th} \sigma_n \sigma_p \left[\frac{(np - n_i^2)}{\sigma_n (n + n_1) + \sigma_p (p + p_1)} \right] \quad [4-45]$$

If the simplifying condition $\sigma_p = \sigma_n$ is imposed, it may be determined that the maximum rate of recombination occurs for the center lying at midgap.

Under nonequilibrium conditions, $n = \Delta n + n_0$ and $p = \Delta p + p_0$, where n_0 and p_0 are the equilibrium carrier concentrations, the recombination process may be characterized for an n-type semiconductor as

$$R = \frac{p - p_0}{\tau_p} = \frac{\Delta p}{\tau_p} \quad [4-46]$$

where τ_p is the minority carrier lifetime. If $n \gg n_0$, $n \gg n_i$, $n \gg p$, and $\Delta p \gg p_0$, [4-45] reduces to

$$R = \sigma_p v_{th} N_t \Delta p \quad [4-47]$$

The combination of equations [4-46] and [4-47] yield the minority carrier (hole) lifetime

$$\tau_p = \frac{1}{\sigma_p v_{th} N_t} \quad [4-48]$$

A similar treatment yields the electron lifetime for a p-type semiconductor as

$$\tau_n = \frac{1}{\sigma_n v_{th} N_t} \quad [4-49]$$

Photoproduced carrier lifetimes with regard to specific initial conditions may be found in ref. 137.

Surface recombination

At the surface of a semiconductor (semiconductor electrolyte liquid-junction) exist localized energy levels, different from those in the bulk of the semiconductor, which provide reduced energy pathways for either charge transfer or electron-hole recombination. These energy levels are termed "surface states." The localized energy levels may arise simply because the periodicity of the lattice is broken, in which case they are called "intrinsic states." Electrons in surface atom orbitals which do not overlap neighboring orbitals comprise what are known as "dangling bonds" and are a prime example of an intrinsic state. More generally, surface states arise from impurities located at the semiconductor surface, adsorbates, or even nearby ions in solution which give rise to localized surface energy levels. A band diagram depicting surface states is seen in Figure 4-8.

The filling of these levels may be treated in a manner analogous to that of bulk recombination to arrive at an expression for recombination at the surface which is similar in form to [4-45] (138).

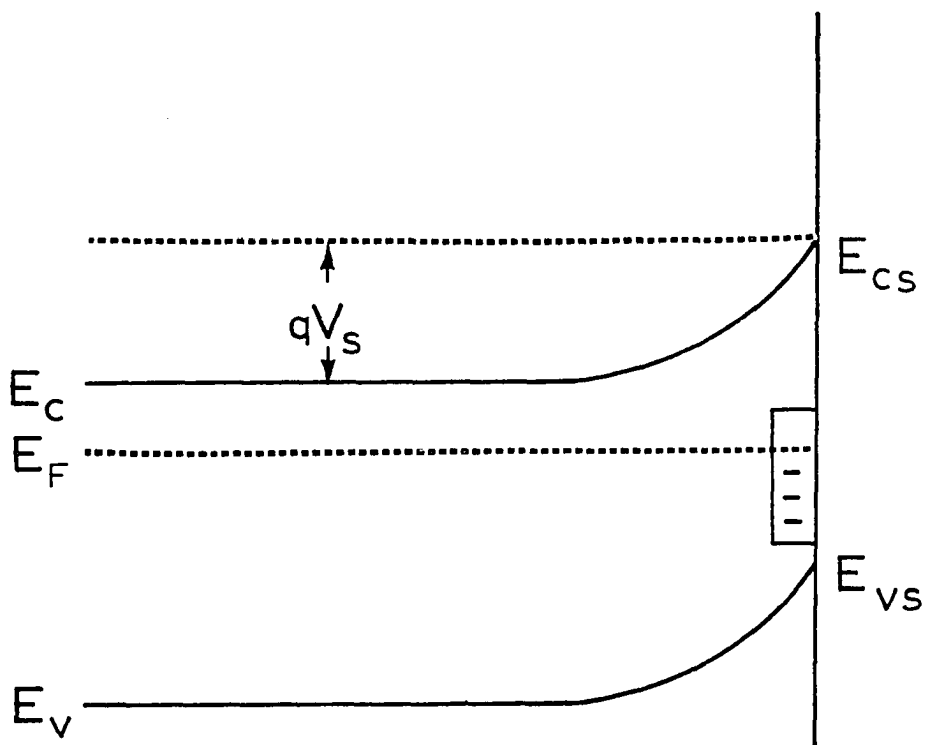


Figure 4-8. Energy band diagram of semiconductor immersed in redox couple containing electrolyte solution. Valence and conduction band edge energies are depicted for the bulk (E_V , E_C) and surface (E_{VS} , E_{CS}) of the semiconductor along with the Fermi energy E_F and magnitude of band bending qV_S . Partial filling of surface states is also shown

$$R = N_{ss} v_{th} (\sigma_n)_{ss} (\sigma_p)_{ss} \left[\frac{(n_{ss} p_{ss} - n_i^2)}{(\sigma_n)_{ss} (n_{ss} + n_1) + (\sigma_p)_{ss} (p_{ss} + p_1)} \right] \quad [4-50]$$

where

$$n_1 = N_c \exp(-E_{ss}/kT) \quad [4-51]$$

$$p_1 = N_v \exp[-(E_{BG} - E_{ss})/kT] \quad [4-52]$$

and $(\sigma_n)_{ss}$ and $(\sigma_p)_{ss}$ are the capture cross-sections at the surface for free electrons and holes, respectively, and n_{ss} and p_{ss} are the surface densities of electrons and holes (N_{ss} being the total density of available states). Under the assumption that the surface density of carriers is at equilibrium with the bulk density, we can relate the surface density of either carrier to the size of the surface barrier, V_s .

$$n_{ss} = n_b \exp(-qV_s/kT) \quad [4-53]$$

$$p_{ss} = p_b \exp(+qV_s/kT) \quad [4-54]$$

where n_b and p_b are the bulk densities of electrons and holes. Surface states existing at an energy level near the Fermi level under flatband conditions provide the best pathways for recombination, the rate of which will be optimized for moderate surface barriers V_s .

Conductance

The electronic conductance of a completely occupied or completely empty energy band is zero because none of the electrons can gain energy by moving to a higher energy level in the band. If the band is partially filled, electrons may move to higher energy levels, with a corresponding increase in energy and velocity in response to an applied electric field. Holes analogously increase energy by moving to a lower level in the band. The relationship between the average velocity v of carriers and the applied electric field is

$$v = \pm \mu \left(\frac{d\phi}{dx} \right) \quad [4-55]$$

where ϕ is the electrical potential and μ (a proportionality constant) is known as the "mobility." The electronic conductivity of a solid, σ , is given by

$$\sigma = nq\mu_n + pq\mu_p \quad [4-56]$$

where n and p are the densities of free electrons and holes, q is the electronic charge, and μ_n and μ_p are the electron and hole mobilities. Conductance G and resistance R are given by

$$G = R^{-1} = \sigma A/L \quad [4-57]$$

where A is the cross-sectional area of the sample and L is the

sample length in the direction of current flow. Another important parameter associated with mobility is the carrier diffusion coefficient (D_n and D_p for electrons and holes, respectively). The relationship between D_n and μ_n for conditions of thermal equilibrium of a nondegenerate semiconductor is

$$D_n = \left(\frac{kT}{q}\right)\mu_n \quad [4-58]$$

Similarly,

$$D_p = \left(\frac{kT}{q}\right)\mu_p . \quad [4-59]$$

These equations are known as the Einstein relationships. At 300°C, $kT/q=0.0259$ V, and values of D are readily obtainable from mobilities. Mobilities may be determined using

$$\rho = \frac{1}{\mu_n q} \quad [4-60]$$

for the case of a semiconductor where $n \gg p$. The resistivity ρ is usually determined by a point technique such as described by Runyan (139), and the carrier density n is commonly revealed through the determination of the Hall coefficient R_H (140).

The Electrolyte

Ions in solution interact with both the solvent molecules and with other ions or molecules in solution. Interactions between nearest neighbor ions are termed "inner sphere", while interactions between ions which are farther removed are termed "outer sphere." Of great importance is the inner sphere complex formation where an ion and neighboring ions (molecules) in the solution (at the semiconductor surface) form a group which can be almost considered a compound.

The electronic energy levels of an ion (or molecule) in solution reflect the tendency of that species to give up or accept an electron when the species approaches the electrode. The simplest type of transfer involves a one-electron reaction by a species with two stable oxidation states. Figure 4-9 illustrates the relationship between the solution energy levels and energy levels of the semiconductor. This model is oversimplified in that the energy levels for both the reducing agent and the oxidizing agent are the same, e.g., Fe^{2+} and Fe^{3+} have the same energy level, with Fe^{2+} corresponding to the occupied level and Fe^{3+} to the empty level. This model dictates that an electron could transfer between the ion and semiconductor, then transfer back isoenergetically. However, because of differences in the solvation energies of the oxidized and reduced ions in solution, the electron

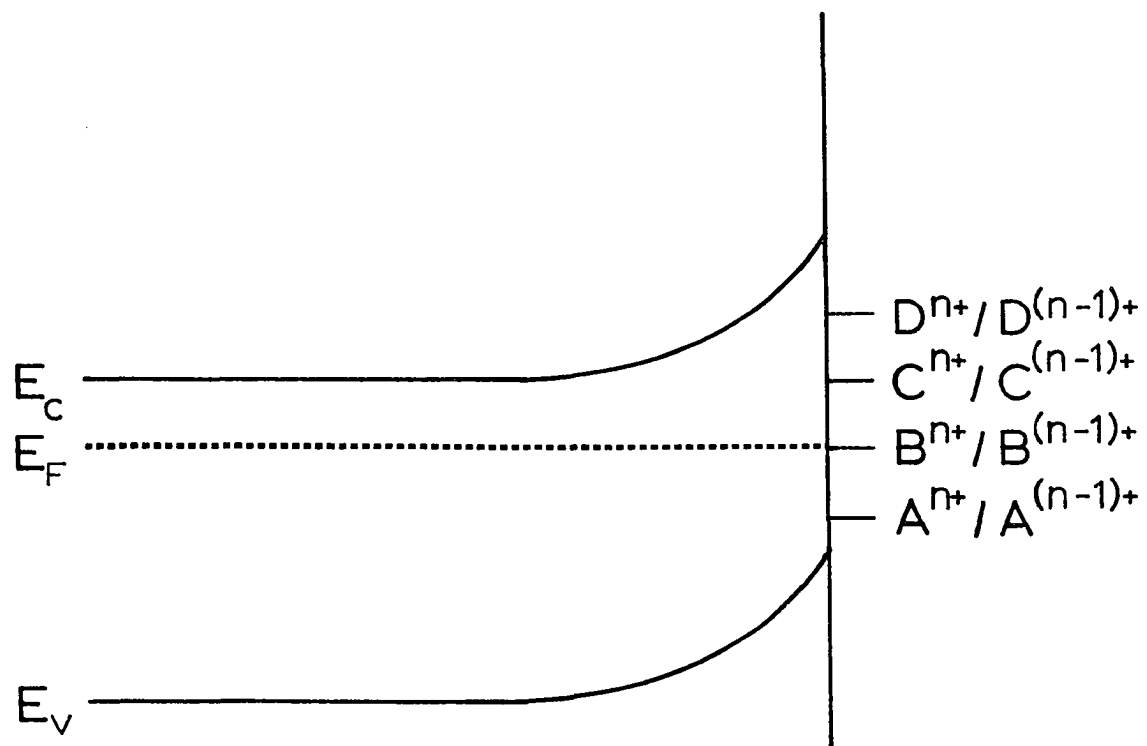


Figure 4-9. Simplified energy level diagram relating the Fermi level of the semiconductor to the electrochemical potential of various redox couples. The semiconductor is in equilibrium with the $B^{n+} / B^{(n-1)+}$ redox couple

energy level of the oxidized ion is different from that of the reduced ion.

The "standard redox potential" E° of a redox couple is defined for the reaction



(where R and O are reduced and oxidized species) by the Nernst equation

$$E = E^\circ + \frac{RT}{nF} \ln \frac{[O]^{\nu_O}}{[R]^{\nu_R}} \quad [4-62]$$

where F is the Faraday constant (96,489 C/mole). The potential E of the redox couple is dependent upon the relative concentration of species in solution, while E° assumes equal species concentrations (for $\nu_O + \nu_R$). The redox potentials are tabulated in handbooks, and expected energy levels of ions in solution may be readily obtained. By preparing a band diagram including the semiconductor along with the thermodynamic energy level for the redox couple, one can observe by inspection whether it is thermodynamically favorable to transfer electrons to or from the semiconductor. The hydrogen couple H_2/H^+ has been chosen as the universal reference potential with its corresponding Fermi energy chosen as an arbitrary zero.

If one describes the properties of the solution via an energy level description rather than a chemical potential description, the properties of the semiconductor and solution can be more lucidly related. The energy level description of ions in solution is complicated by the effect of the polar solvent surrounding the ions. The solvent dipoles are highly mobile and readily polarized by introduction of the ions into solution. An equilibrium polarization may be defined, with consideration given to the effects of thermal fluctuations. The probability of the energy level being at a particular energy E is best described by a Gaussian distribution. The probability of electron transfer between an electrode and an ion in solution will depend on the energy level of the ion at the instant of transfer. Figure 4-10 shows the accepted model for energy levels in solution. Energy is shown on the ordinate while the probability of finding the energy level of an ion at a particular energy is plotted on the abscissa. Thus, E_{OX} is indicated as the most probable energy level for an oxidizing agent representing the condition where the polar medium is at its equilibrium polarization. The Gaussian function shows the probability of finding the energy level at another energy due to thermal fluctuations of the solvent dipoles. An analogous description exists for E_{RED} . The energy E_{REDOX}° is defined by $E_{REDOX}^{\circ} = \frac{1}{2}(E_{OX} + E_{RED})$. The

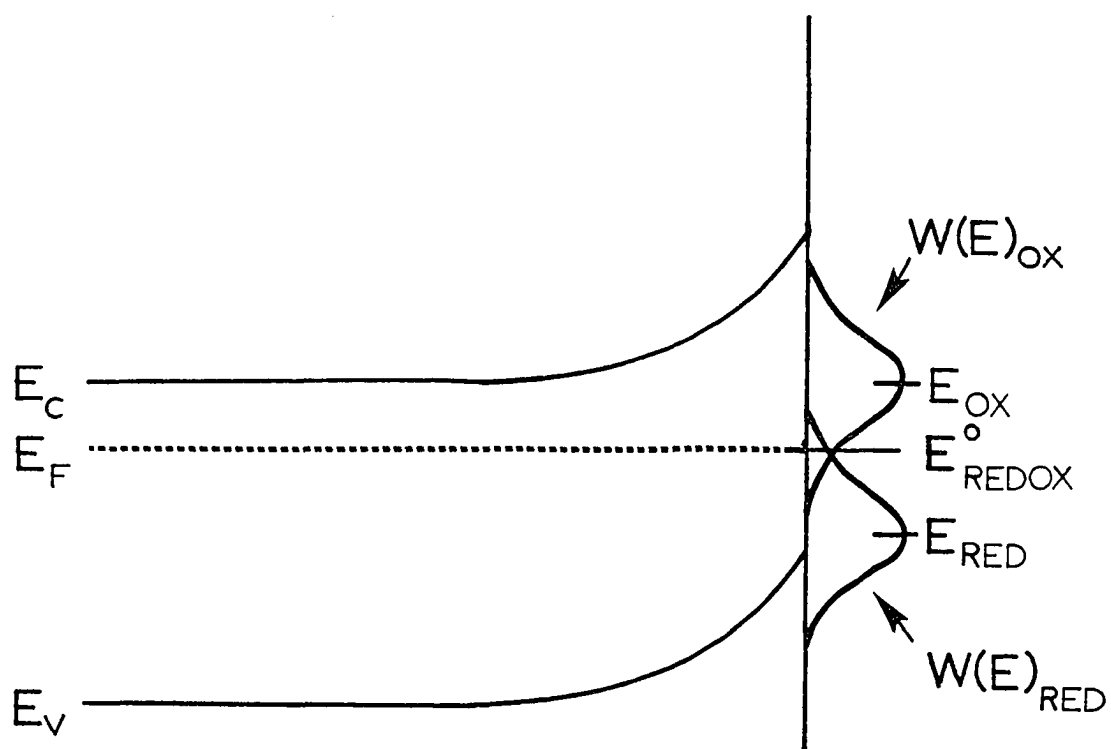


Figure 4-10. Energy level diagram of a semiconductor/redox system at equilibrium. The probability distributions and energy levels for both the oxidizing agent and reducing agent in solution are shown

probability function for an energy level having energy E is given by

$$W(E) = (4\pi\lambda kT)^{-\frac{1}{2}} \exp[-(E_t - E)^2 / 4\lambda kT] \quad [4-63]$$

where the preexponential factor is a normalizing constant which makes the integrated probability unity. The quantity E_t is the mean energy of the surface state (either E_{OX} or E_{RED}) and λ is the "reorganization energy." The reorganization energy λ is most simply given by (141)

$$\lambda = \left(\frac{q^2}{8\pi\epsilon_0 a} \right) (K_{op}^{-1} - K_s^{-1}) \quad [4-64]$$

where a is the ionic radius, K_{op} and K_s the optical and static dielectric constants of the medium, respectively, and ϵ_0 is the permittivity of free space. A typical value of λ for an ion of $\sim 3\text{\AA}$ radius dissolved in water is 1 eV. The relationship between the reorganization energy and the mean energies of the energy level distributions turns out to be

$$E_{OX} - E_{RED} = 2\lambda \quad [4-65]$$

assuming that the value of λ is the same for both species. If equilibrium is reached by an electrode in solution, the Fermi level of the electrode, E_F , will move to the energy E_{REDOX} of the redox couple via electron exchange. At

equilibrium

$$E_{\text{REDOX}} = E_{\text{F}} \quad [4-66]$$

and if the redox species are present in equal concentrations

$$E_{\text{REDOX}}^{\circ} = \frac{1}{2}(E_{\text{OX}} + E_{\text{RED}}) \quad [4-67]$$

Equation [4-67] is considered to be always valid, while [4-66] is only valid at equilibrium.

The Double Layer at the Solid/Liquid Interface

Three distinct double layers appear at the solid/liquid interface, as shown in Figure 4-11. The first region is the semiconductor space charge region, whose width is defined by (for a depletion region)

$$W_{\text{d}} = \left[\frac{2\epsilon\epsilon_0(V - V_{\text{fb}})}{qN_{\text{d}}} \right]^{\frac{1}{2}} \quad [4-68]$$

where ϵ and ϵ_0 are the permittivities of the semiconductor and free space, respectively, and V and V_{fb} represent the applied potential and flatband potential. The doping density of the semiconductor is N_{d} . The second region is a Helmholtz region existing between the semiconductor and the "outer Helmholtz plane" (the locus of centers of the solvated ions residing nearest the semiconductor surface). The third region is the Gouy-Chapman region which extends from the

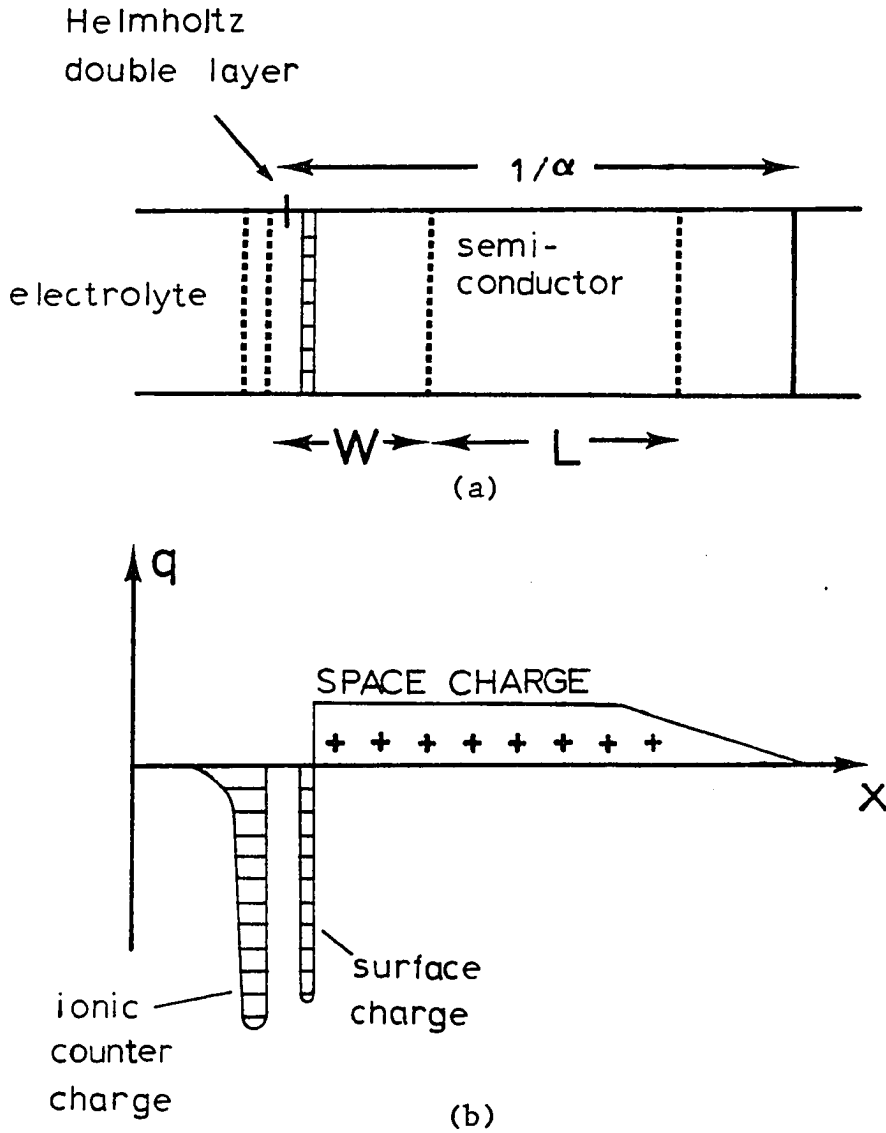


Figure 4-11. The electrolyte-semiconductor interface
 (a) Schematic diagram of the semiconductor/
 electrolyte interface depicting the double
 layer structure, absorption length $1/d$, space
 charge region W , and diffusion length L . (b)
 Location of charge corresponding to (a)

outer Helmholtz plane into the bulk of the solution and is defined by the presence of an excess of ions of one sign. For high redox couple concentrations, this region blends into the Helmholtz region and is typically ignored.

Charge storage in the various space charge regions or planes relates to electrical capacitance, each double layer having an associated capacitance. For a parallel plate capacitor,

$$C = \frac{dQ}{dV} = \frac{AK\epsilon_0}{d} \quad [4-69]$$

where dQ/dV is the differential charge per unit potential, A is the area, and d is the distance between separated charges being stored. In addition to capacitive impedance, resistive impedance to current flow is also present, particularly in the space charge region of the solid.

Charge Transfer

When an electrode is placed in a redox couple containing electrolyte solution, electrons are injected into the electrode by the reducing agent and extracted from the electrode by the oxidizing agent. Equilibrium is reached when the two rates are equal and there is no net current flow. The current in each direction across the interface at equilibrium is called the "exchange current." If an overvoltage is applied,

the electrode potential shifts and a net current flow results. The net electron transfer rate is proportional to the number of ions available for electron transfer at the surface, the number of occupied (unoccupied) states in the solid, and the probability that the energy level in solution has fluctuated to the energy level of the appropriate state in the solid as given by equation [4-63].

$$W(E) = (4\pi kT)^{\frac{1}{2}} \exp[-(E_{\text{t}} - E)^2 / 4\lambda kT]. \quad [4-70]$$

The simplest model dictates that

$$J(E) \propto \int_{\text{RED}} dW(E) \quad [4-71]$$

or

$$J(E) \propto C_{\text{OX}} dW(E) \quad [4-72]$$

where d represents the distance from the surface which will effect a unit probability of transfer (any ion beyond d will be nonreactive). $J(E)$ is the contribution to the current by ions at energy E . Complications arise for this model due to adsorption of species on the surface. For an adsorbed species, the energy levels differ significantly from the energy levels of the species in solution, and the corresponding value of λ is lower than the value for the ion in solution.

The rate equations which describe charge-transfer are similar to the equations already presented for bulk recombination, and particularly for surface state recombination, with

the noted exception that the "surface state" in question corresponds to the fluctuating energy level of an ion in solution, where only a single carrier will undergo the transfer isoenergetically.

The rate of capture of conduction band electrons at the surface can be expressed as

$$\frac{dn_t}{dt} = \sigma_n v_{th} [n_s (N_t - n_t) - n_1 n_t] \quad [4-73]$$

where n_s is the density of electrons per unit volume in the conduction band at the surface, n_t is the density of electrons per unit area in the "surface state", N_t is the total density of "surface states", n_1 is a temperature dependent constant determined by applying the condition that at equilibrium $dn_s/dt = 0$. The average thermal velocity of a conduction band electron is given by $v_{th} = \sqrt{3kT/m^*}$ and σ_n represents the electron capture cross-section of the "surface state." Equation [4-73] represents the sum of two terms: the first, a cathodic process by which an electron is captured by the "surface state"; the second, the anodic process whereby an electron returns to the conduction band.

The net rate of hole exchange with a "surface state" is determined similarly by

$$\frac{dp_t}{dt} = \sigma_p v_{th} [p_s n_t - p_1 p_t] \quad [4-74]$$

where n_t represents the density of holes per unit volume in the "surface state", σ_p is the hole capture cross-section, p_1 is a temperature dependent constant determined from equilibrium conditions, and n_t is the density of electrons per unit volume in the "surface state." The first term represents the anodic process (the rate at which holes are captured), and the second the cathodic process (the rate at which holes are returned to the conduction band).

If charge transfer at the surface is determined to be rate-limiting rather than chemical or ionic processes occurring in solution, the "surface states" can now represent the energy levels of the redox couple. The voltage dependence of the charge transfer now rests on n_s and p_s , which are given by

$$n_s = n_b \exp(-qV_s/kT) \quad [4-75]$$

and

$$p_s = p_b \exp(qV_s/kT) \quad [4-76]$$

where n_b and p_b are the bulk densities of charge carriers and V_s represents the extent of band bending. The parameters n_t and $N_t - n_t$ represent the density of ions in solution at the interface. The density of occupied and unoccupied states is not dependent upon applied voltage, and, therefore, n_t and $N_t - n_t$ are constant. The p_s and n_s vary with applied voltage,

as dictated by equations [4-75] and [4-76].

The Tafel equation (developed in 1905) which determines the relationship between current and overvoltage for a general electrode reaction is

$$\eta = a + b \log i \quad [4-77]$$

In order to determine the Tafel relationships for both of the semiconductor bands, it is first assumed that no net current flows through the system at equilibrium.

$$J = \frac{qdn_t}{dt} = \frac{qdp_t}{dt} = 0 \quad [4-78]$$

Therefore, for the conduction band,

$$N_t - n_t = \frac{n_l n_t}{n_s} \quad [4-79]$$

Defining $n_s = n_{s0}$ at equilibrium, one has the following general relationship

$$J = \frac{qdn_t}{dt} = q\sigma_n v_{th} n_l n_t \left[\left(\frac{n_s}{n_{s0}} \right)^{-1} \right]. \quad [4-80]$$

Furthermore,

$$\frac{n_s}{n_{s0}} = \frac{n_b \exp(-qV_s/kT)}{n_b \exp(-qV_{s0}/kT)} = \exp(-\eta_{sc} q/kT) \quad [4-81]$$

where $\eta_{sc} = V_s - V_{s0}$, V_{s0} being the surface barrier at equilibrium. Therefore,

$$J_c = (J_o)_c [\exp(-\eta_{sc} q/kT) - 1] \quad [4-82]$$

where

$$(J_o)_c = q\sigma_n v_{th} n_1 n_t \quad [4-83]$$

Analogously, for the valence band

$$J_v = (J_o)_v [\exp(+\eta_{sc} q/kT) - 1] \quad [4-84]$$

where

$$(J_o)_v = q\sigma_p v_{th} p_1 p_t \quad [4-85]$$

Values of $(J_o)_c$ or $(J_o)_v$ are extremely small for E°_{REDOX} situated in the bandgap such that the energy levels of the redox couple do not overlap strongly with the band edges. For semiconductors whose bandgap is of a width which makes them ideal for absorption of the solar spectrum, most often one band is active, and stray currents due to surface flaws, tunneling, or corrosion far outweigh J_o . Therefore, the concept of overvoltage η_{sc} loses its importance because the correct voltage at equilibrium, V_{so} , is not measurable. The measurable quantity V_s , however, leads to the following current-voltage relationships for the conduction and valence bands of an n-type semiconductor.

$$J_c = J_1 \exp(-qV_s/kT) - J_2 \quad [4-86]$$

$$J_v = J_2 \exp(+qV_s/kT) = J_c \quad [4-87]$$

where J_1 and J_2 are coefficients for cathodic (anodic) current in the conduction (valence) band, and J_a and J_c represent the anodic (cathodic) current in the conduction (valence) band.

Various models for the determination of J_1 , J_2 , J_a and J_c have been devised, and quantitative expressions for current flow across the interface have been developed utilizing the fluctuating energy level model. The Marcus-Hale model (142) and Gerischer model (143,144) are two of the best known for calculation of the required constants.

Two-step charge transfer processes via surface states are also under consideration. The charge carrier is first captured from the semiconductor band by the surface state and then undergoes transfer to solution. If the two-step process is energetically favorable, capture by the surface state could be the rate limiting process. Extensive literature exists describing isoenergetic charge transfer (145-148) and charge transfer via surface states (149,150).

PEC Photovoltaic Cells

In Figure 4-12 is shown a photovoltaic PEC with the optimum bandgap energy for absorption of the solar spectrum, 1.4 eV. Wide bandgap semiconductors absorb fewer photons from the solar spectrum, and narrow bandgap semiconductors

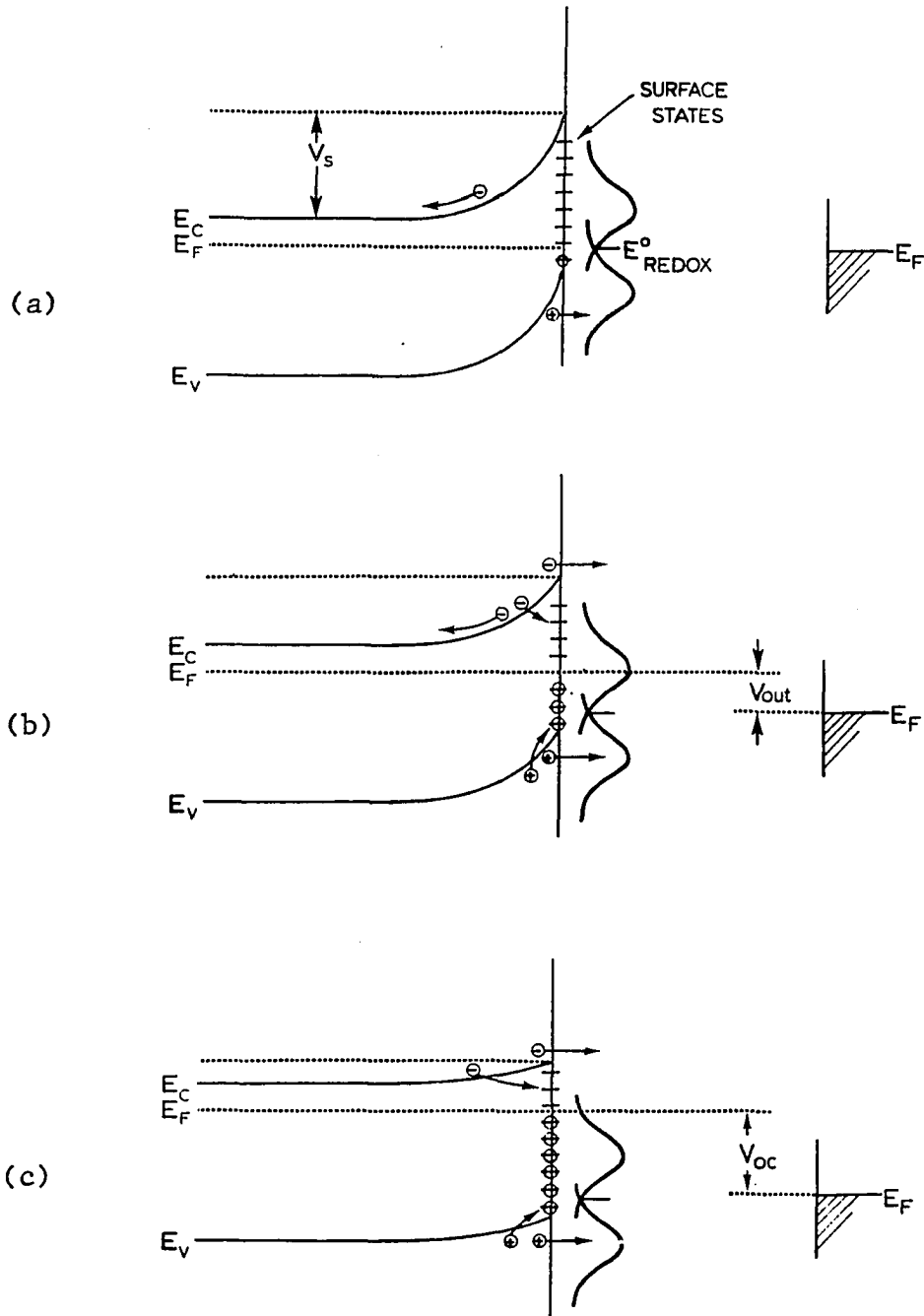


Figure 4-12. PEC photovoltaic cell under various operating conditions (a) Dark or short circuit; (b) Maximum power output; (c) Open circuit

waste much of the absorbed energy as heat. The narrow band-gap semiconductors also produce low photovoltages, undesirable in light of the fact that high power output ($v \times I$) defines high efficiency. A typical redox couple reorganization energy, λ , of ~ 1 eV is shown, whereby the distribution functions for the redox couple extend into the band regions. By choosing a redox couple whose E_{REDOX}° lies slightly above the valence band edge, the largest photopotentials may be obtained. The value of E_{REDOX}° cannot be below the valence band edge, however, because the reducing agent must be able to efficiently capture photogenerated holes.

No overvoltages are assumed at the metal counterelectrode for Figure 4-12 (a-c), and therefore $E_{\text{REDOX}}^{\circ} = E_{\text{F}}$ for the metal. For the semiconductor at equilibrium in the dark, $E_{\text{REDOX}}^{\circ} = E_{\text{F}}$ of the semiconductor, Figure 4-12a illustrates the PEC under equilibrium conditions in the dark. Very few of the surface states are occupied, and small equilibrium currents flow for both valence and conduction band. Figure 4-12a also illustrates the effect of illuminated operation under short circuit conditions. The photogenerated electron-hole pairs are separated by the potential gradient, as shown by the arrows. The holes move to the surface and oxidize the reduced form of the redox couple in solution, while the electrons are driven through the external circuit to the

counterelectrode, where reduction takes place. Because there is no voltage drop across the external circuit, no power is derived from the cell.

Figure 4-12b shows the illuminated PEC under open circuit conditions. Electron-hole pairs are no longer driven apart by the diminished potential gradient, and the E_F of the semiconductor moves up in energy with respect to E_{REDOX}° . The open circuit voltage V_{oc} is the measured difference in Fermi energy between the semiconductor and the metal counterelectrode. The open circuit photovoltage obtainable from the system is less than the bandgap due to three losses: the residual potential V_g , the energy difference between the bulk conduction band and the Fermi energy, and the separation of E_{REDOX}° from the valence band edge. Both electrons and holes are either lost to the solution through the semiconductor surface or recombine through the surface states, many of which are filled by the raising of the Fermi energy. Once again, no power is produced, for no current flows.

Figure 4-12c shows the PEC under optimum power conversion conditions, i.e., with the $I \times V$ product maximized. This is accomplished by adjusting the load. Under illumination, the surface barrier is lowered and a current flows due to efficient separation of electron-hole pairs. A nonzero potential is developed with current flowing. Losses of

efficiency are due to electrons flowing through the interface into the solution and recombination via the surface states. Ideally, these losses are a minimum.

A-C Techniques

By using a-c measurement techniques, some of the more important characteristics of a PEC may be determined. As previously defined, the differential capacity is

$$C = dQ/dV = K\epsilon_0 A/D \quad [4-88]$$

where dQ is the amount of charge stored upon altering the voltage by dV . In this equation, A is the area, K the dielectric constant, d the thickness of the insulating layer (parallel plate capacitor model), and ϵ_0 is the permittivity of free space. The three important capacitances associated with the PEC are to be considered here: the Helmholtz capacity, the space charge layer capacity, and the capacity of surface states

$$C_H = dQ/dV_H \quad [4-89]$$

$$C_{SC} = dQ_{sc}/dV_s \quad [4-90]$$

$$C_{SS} = dQ_{ss}/dV_s \quad [4-91]$$

where V_H represents the potential difference across the Helmholtz region and V_s represents the potential difference due

to band bending. The combination of above capacitances is such that

$$C^{-1} = (G_{SC} + C_{SS})^{-1} + C_H^{-1}, \quad [4-92]$$

i.e., C_H acts as a capacitor in series with the parallel combination of C_{SC} and C_{SS} . The entire PEC may be described in terms of an "equivalent" circuit consisting of an array of resistors and capacitors arranged to give the same impedance as the PEC itself. Two examples of equivalent circuits are shown in Figure 4-13. The simplest, Figure 4-13a, is a linear RC combination. A more realistic equivalent circuit is shown in Figure 4-13b which includes the impedance due to surface states.

The physical measurement of the impedance, in order to determine the capacity, is done with a capacity bridge, a lock in amplifier, or some other form of phase sensitive detection equipment. Assuming initially that the capacity being measured is the space charge capacity C_{SC} , the relationship between C_{SC} and V_s may be obtained from the solution of Poisson's equation, which after a bit of manipulation leads to

$$\begin{aligned} C_{SC}^{-2} &= \left[\frac{2}{qN_{sc}K\epsilon_o A^2} \right] \left(V_s - \frac{kT}{q} \right) \\ &= \left[\frac{2}{qN_{sc}K\epsilon_o A^2} \right] \left(V_m - V_{fb} - \frac{kT}{q} \right) \end{aligned} \quad [4.93]$$

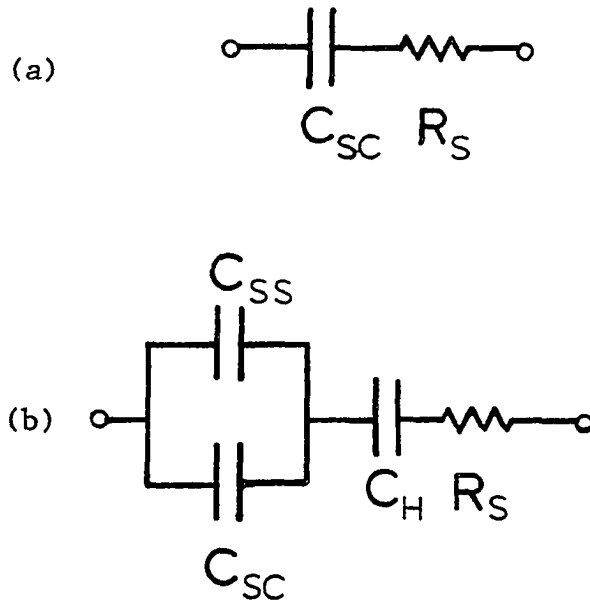


Figure 4-13. PEC equivalent circuits

(a) Linear RC combination utilizing space charge capacitance and series resistance of semiconductor and electrolyte.

(b) RC combination utilizing space charge, Helmholtz layer, and surface state capacitances along with series resistance of semiconductor and electrolyte

The space charge capacity is measured as a function of the applied potential under depletion conditions yielding an intercept of V_{fb} (the flatband potential) and a slope proportional to the density of charge in the space charge region N_{sc} . The flatband potential is determined by extrapolation, and the factor kT/q is often ignored, being small and within the range of experimental uncertainty. The plot described here is known as a Mott-Shottky plot.

Simple Mott-Shottky (M-S) plots are quite often observed, but deviations from linearity in an M-S plot can be attributed to certain effects. If double layers other than the space charge region contribute to the capacity of the system in an appreciable manner, the value of V_{fb} will be shifted. For example, C_H is typically large compared to C_{SC} . If, however, C_{SC} is made high by heavy doping (high N_d , thin space charge region), the value of V_{fb} will shift by an amount $(K\epsilon_0 q N_{sc} / 2C_H)$. Changes in the slope of the M-S plot and consequent changes in apparent N_{sc} will arise from changes in N_{sc} with time or distance from the surface. These changes may be due to the trapping of charges in the space charge region, and manifested by frequency dependent capacities. Interpretation of these deviations can lead to better equivalent circuit models and, hence, better knowledge of the physical processes underlying operation of the PEC.

I-V Characteristics

The measurement of current-voltage characteristics of a PEC is accomplished using cyclic voltammetry techniques. A three electrode system is typically used to perform this operation (Figure 4-14) with the aid of potentiostatic control (151). Through potentiostatic control, the applied potential can be programmed as a function of time, and the resultant current is measured. Cyclic voltammetry involves programming such that $dV/dt = \pm K$, i.e., the voltage sweep is triangular. This technique has become a highly sophisticated tool in metal electrochemistry, revealing the characteristics of solution species. With a semiconductor in solution, less information pertaining to the solution is obtained. In a metal electrode, free movement of the Fermi energy as a function of applied potential permits knowledge of the relative energies and concentrations of redox couples in solution. However, in a semiconductor, the band edges determine reactions with the redox species, and they remain fixed in energy with respect to the redox potential regardless of the applied potential. Therefore, information about the extent of band bending, the thickness of the space charge region, and the overall efficiency of the PEC may be determined. The current-voltage (I-V) characteristics for a typical PEC under illumination is shown in Figure 4-15. Curves for both dark and

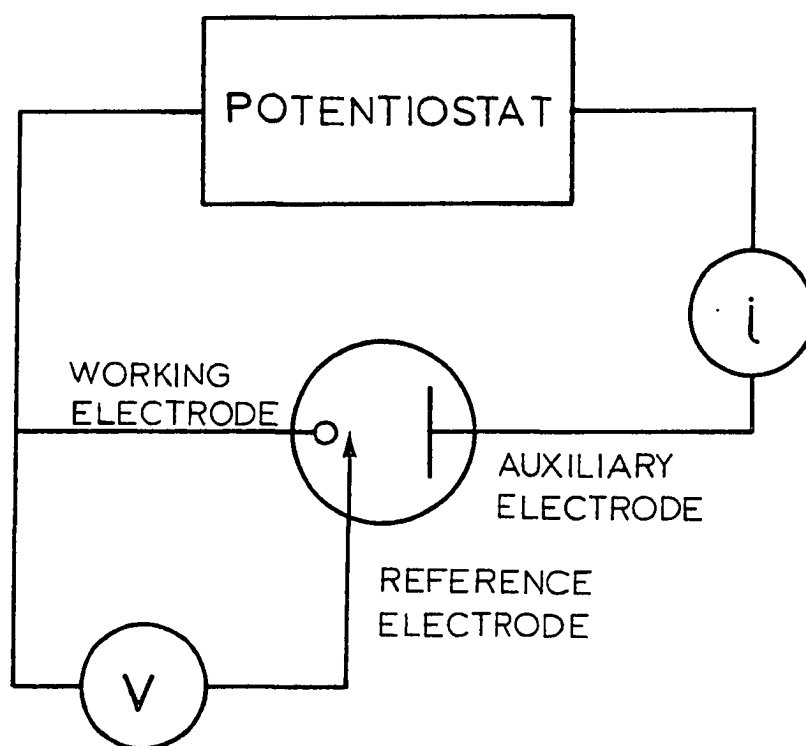


Figure 4-14. Three electrode cell under potentiostatic operating conditions

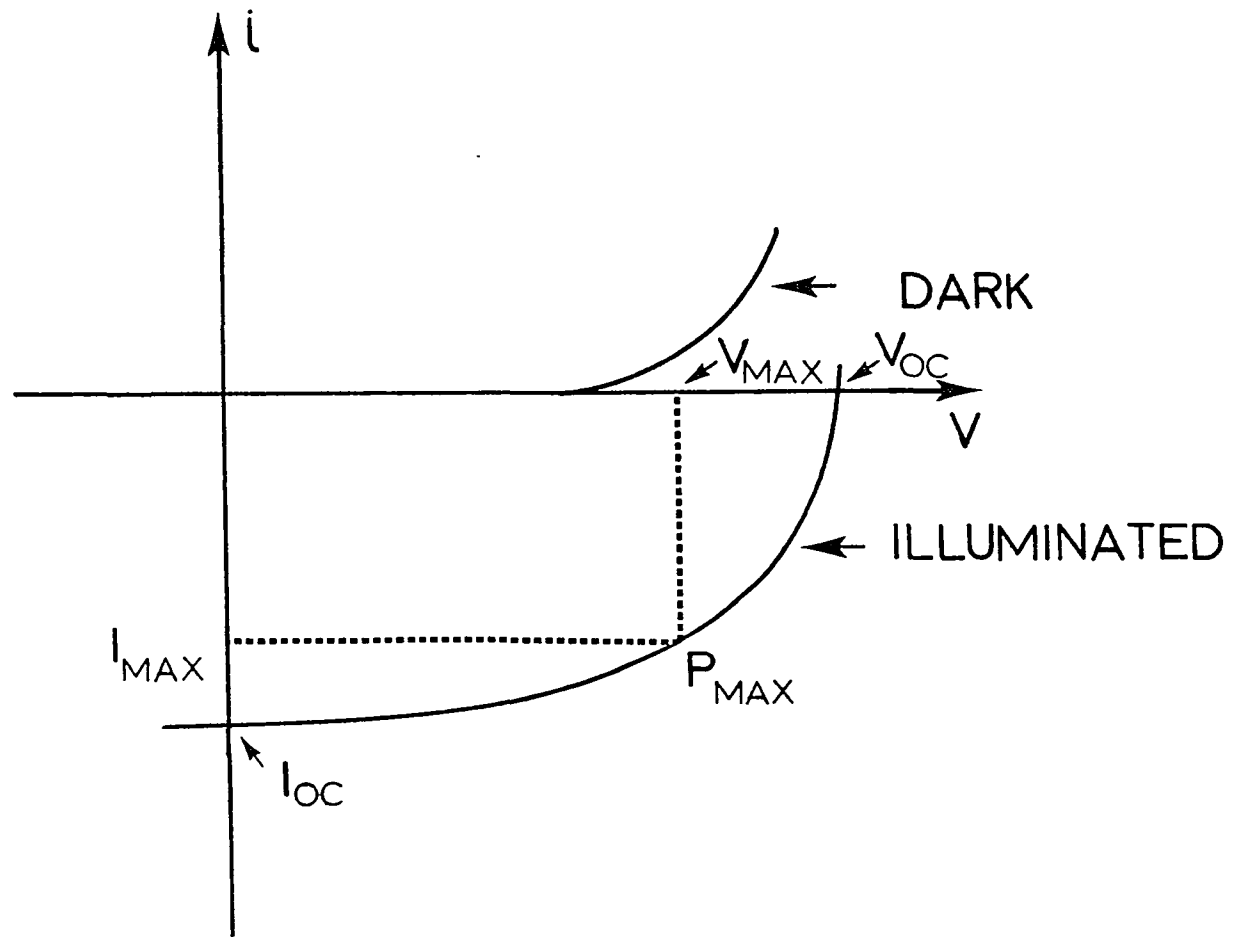


Figure 4-15. Current-voltage curves for PEC photovoltaic cell under dark and illuminated conditions

illuminated conditions are presented. Quantities to be noted are the open circuit voltage, V_{oc} , the short circuit current, I_{sc} , the voltage for maximum power, I_{max} , the maximum power point P_{MAX} . A relative figure of merit for solar cells is called the "fill factor" which relates P_{MAX} to I_{sc} and V_{oc} by

$$f = \frac{I_{max} V_{max}}{I_{sc} V_{oc}} \quad [4-94]$$

and gives a relative measure of the "rectangularity" of the I-V curve. The solar efficiency n is defined as the ratio of P_{max} to incident solar power

$$n = \frac{f I_{sc} V_{oc}}{P_{SOLAR}} = \frac{I_{max} V_{max}}{P_{SOLAR}} \quad [4-95]$$

Typical values for systems of interest are $V_{oc} = 0.1-0.6V$, $I_{sc} = 1-10 \text{ mA cm}^{-2}$, $f = 0.5-0.8$ and $n = 5-15\%$.

An equivalent circuit model for the PEC may be devised with the cell represented as a constant current source shunted by a nonlinear junction device (diode) (152). The circuit (Figure 4-15a) gives rise to the expression

$$I = I_s - I_o \left[e^{\frac{-qV}{AkT}} - 1 \right] \quad [4-96]$$

where I_s is the light generated current, I_o is the reverse saturation current of the diode, V is the output voltage, and A is a constant (153) whose value ranges from 1-2. From this relationship, $I_{sc} = I_s$ when $V = 0$ and

$$V_{oc} = \frac{AkT}{q} \ln \left[\left(\frac{I_s}{I_o} \right) + 1 \right]. \quad [4-97]$$

A more accurate form of this model (Figure 4-15b) involves the inclusion of a shunt resistance R_{SH} and a series resistance R_S to the circuit. Equation [4-86] then becomes

$$I = I_s - I_o \left[e^{\frac{-qV}{AkT}} - 1 \right] + \frac{V - IR_S}{R_{SH}}. \quad [4-98]$$

The value of R_{SH} can be determined by the slope of the I-V curve at the current axis, and the value of R_S is derived from the slope at the voltage axis. For cells which have high efficiencies, the last term will drop out and equation [4-96] will be obtained.

PEC Transient Studies

Transient techniques for the study of charge carrier kinetics in solar cells have evolved from experiments designed to determine carrier mobilities in n- or p-doped semiconductor materials. Haynes and Shockley (154) were the first to measure the mobilities of holes and electrons injected into n-type and p-type germanium, respectively. In the latter experiment, a current pulse was applied to one end of a semiconductor rod and the injected charge carriers detected as they swept to the other end of the rod by an applied electric field which produced a constant low current

through the sample. Measurement of the current as a function of the detection point also provided an estimate of the effective minority carrier lifetime, which depends upon the true minority carrier lifetime, the surface recombination velocity, and the dimensions of the sample.

The first photoconductive transient technique was developed by Stevenson and Keyes in 1951 (155). In this experiment, a rod shaped sample of p- or n-doped semiconductor was illuminated by a short pulse of light, and the decay of photogenerated carriers was measured via the change in sample conductance. Constant low current was applied, as in the Haynes and Shockley experiment. This was developed into a standard measurement technique for minority carrier lifetime determination by the Institute of Radio Engineers, currently the Institute of Electrical and Electronics Engineers (IEEE).

Several transient methods for the study of minority carrier lifetimes in p-n junction devices, including heterojunction and homojunction solar cells, have been devised. The most important of these include open circuit voltage decay (156), photoconductivity decay (157), light generated photovoltaic decay (158,159), and open circuit to short circuit switching (160,161). With many of these techniques available, the advantages of any one technique is difficult to judge. Dhariwal and Vasu (162) have presented a common

mathematical formulation applicable to all of these techniques, along with a discussion of the merits of each technique with respect to given operating conditions.

Photoelectrochemical cells have mainly been studied using steady state or long term measurements. Ideally, however, one would like to study kinetic factors, particularly the rates of fundamental chemical reactions occurring at the electrode/electrolyte interface. These reactions occur on timescales ranging from the subnanosecond to the microsecond regime, dictating the use of transient methods. At present, very few experiments have been performed, and the information derived from these experiments has been mainly qualitative.

The most recent work of Richardson et al. (163,164) involved the perturbation of a PEC from equilibrium (dark) conditions in a "laser coulostatic" experiment. In electrochemical terms, a "coulostatic" experiment is defined as one in which an "instantaneous" (much faster than the system decay time) quantity of charge is injected into an electrochemical cell electronically. The cell is then open-circuited, and the decay of the potential back to equilibrium is observed, typically through the use of a high impedance ($\sim 10^{11} \Omega$) differential amplifier whose output is coupled to a fast oscilloscope. The assumption underlying the coulostatic experiment is that only nonfaradaic current flows, i.e., the cell can be

modeled as a linear RC circuit. The capacitor is first charged, and then the discharge is observed. The "laser coulometric" experiment differs from a coulometric experiment only in that the charge injection is a result of pulsed laser excitation. The rationale behind this experiment is based on the fact that the resolution of the observed temporal decay is no longer limited by the cell $R_c C_c$ time constant. The cell resistance R_c remains the same, but now the cell capacitance C_c is modified by the input capacitance of the measurement electronic and cable capacitances. The new time constant, $R_c C_m$, is now on the order of a few nanoseconds, whereas $R_c C_c$ is typically three orders of magnitude higher.

Most of the work done by Richardson et al. utilized CdS electrodes in aqueous sulfide and polysulfide solutions. Earlier work was performed using n-TiO₂ electrodes in 1.0 M KNO₃ aqueous solution (165). In all cases, a four-electrode cell (working electrode, reference electrode, counter electrode, and quasi-reference electrode) was used. A PARC model 147A polarograph provided potentiostatic control. A Molelectron UV1000/DL200 nitrogen pumped dye laser was used as an excitation source. The potentiostat was first adjusted to bring the working electrode to the desired potential. A master timer then disconnected the cell from the potentiostat ~ 30 μ sec prior to triggering the laser pulse. The time scale

of the cell potential decay (dark) was typically 10^{-1} - 10^0 seconds, thereby allowing the cell to remain at the preset potential as photoexcitation occurs.

Several prominent trends were noted in this work. The wavelength dependence of the photoresponse for CdS and TiO_2 electrodes was found to be very similar for transient photopotential measurements as for d.c. photocurrent measurements. It was found that the CdS electrode photoresponse would begin to saturate for laser power densities in excess of 200 W/cm^2 using superbandgap illumination. Subbandgap illumination, on the other hand, produced a linear photoresponse up through extremely high excitation power densities. The measurement of transient photopotential peaks as a function of cell potential showed that the maximum potential excursion was always approximately equal to the flat-band potential. At potentials negative of the flat-band potential, an excitation pulse-width limited (~ 20 nsec) response was observed.

Risetimes of the transient potentials were not always found to be instrument-limited, but in many circumstances exhibited an initial fast response followed by a slower rise to the peak. The magnitude of this two-component rise behavior was seen to be dependent upon laser power, laser power density, and excitation wavelength. The initial rapid photopotential rise was thought to arise from generation of

electron-hole pairs, while the second, slower rise was attributed to the readjustment of the semiconductor and solution Fermi levels occurring during the initial stages of charge transfer.

Transient photopotential decay exhibited a $t^{-2/3}$ dependence for TiO_2 on a microsecond timescale. A very poor fit to $t^{-2/3}$ dependence was found for CdS. The original intent here was to model the decay curves based on electron-hole separation and recombination, photoinduced oxidation, dark reduction, and expansion and relaxation of the space charge layer. The last factor was compared to that of theoretical predictions for diffuse double layer relaxation at a planar metal electrode, where a $t^{-2/3}$ dependence is readily observed (166).

The rates of luminescence decay in CdS electrodes was also studied by Richardson et al. to complement the laser coulometric experiments. One observed trend was that the luminescence decay time depended upon electrode potential for low laser powers. Biexponential decay extending from 10 to 150 nanoseconds was seen. Bandgap illumination (515 nm) produced a decay which was ~ 2.5 times longer than that produced by suprabandgap illumination (406 nm). The longer luminescence time for 515 nm illumination was thought to be due to the optical depth exceeding that of the space charge

layer. Electron-hole pairs formed in the bulk are not subject to the potential gradient, which rapidly separates carriers produced in the space charge region.

Time resolved photocurrent, photopotential, and photoluminescence studies for CdS and CdSe single crystal PECs have been carried out by Harzion et al. (167,168). A two electrode cell (working electrode, counterelectrode) was used in conjunction with 0.2M S, 1M Na₂S, 4M NaOH electrolyte. For photopotential measurements, a high impedance (10 MΩ) FET probe was used. Photocurrent transients were measured using an inductively coupled current probe, with small load resistors placed across the cell electrodes. A spark-gap lamp served as a white light source for the electrical measurements (10 nanosecond FWHM), while the second and third harmonic outputs of an Nd³⁺/glass laser (6 picosecond FWHM) were used for luminescence measurements. The semiconductor samples were generally pretreated previous to an experiment by either mechanical polishing or chemical etching. Some samples were also tested as received.

A pronounced effect of surface pretreatment was reflected in the photocurrent transients. A sample which was first mechanically polished, then chemically etched, exhibited a higher photocurrent peak, larger charge per pulse, and shorter decay times. Simple exponential decay of the photo-

current was observed when using small load resistors. The measured decay time, τ , of the photocurrent exhibited a linear dependence on R_L for $R_L < 100\Omega$. This showed that the decay is a function of a combined cell/external circuit RC time constant. The simple electronic circuit model of the PEC shown in Figure 4-16 can be used to explain the temporal response of the cell. In this model, the semiconductor-electrolyte interface is represented by a capacitor C in parallel with a shunt resistance R_{in} . The remaining resistance in the circuit, R_{out} , consists of the sum of the series cell resistance R_s and the external load resistance, R_L . It is assumed that a current source injects a delta function current pulse into the system. The time variation of the current in the external circuit is given by

$$I_{out} = \frac{\Delta Q}{I_{out} C} \exp(-t/\tau) \quad [4-99]$$

where ΔQ is the charge injected by the source into the capacitor. The decay time τ is given by $\tau = (R_L + R_s)C$ for $R_{out} \ll R_{in}$ and $\tau = R_{in}C$ for $R_{out} \gg R_{in}$. If $R_{out} \ll R_{in}$, a graph of τ vs. R_L should be linear (observed) with slope C and intercept $R_s C$. If $R_{out} \gg R_{in}$, τ is independent of R_L and R_{in} may be determined from the limiting value of τ . The effect of chemical etching as evaluated by this technique was seen to lower R_s without greatly affecting the interfacial capacitance

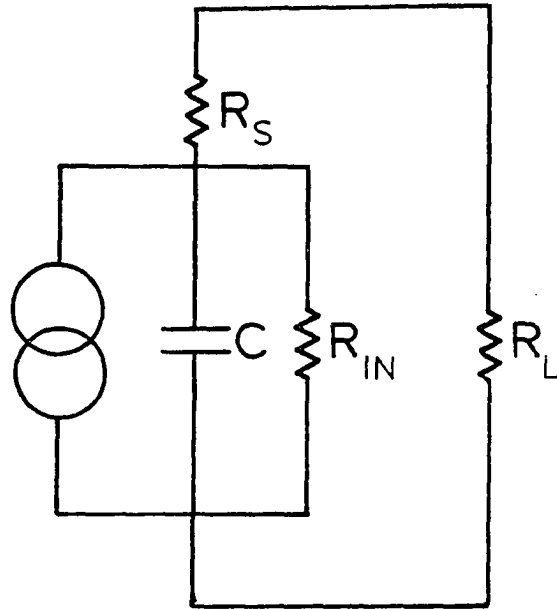


Figure 4-16. Equivalent circuit depicting double layer capacitance, shunt and series resistances

C. This ohmic effect shows that the transport rates for charge through a mechanically damaged surface (polished) are lower. However, the circuit model fails in that it cannot account for the lower charge per pulse and lower photopotentials which are resultant upon high recombination rates in the damaged layer.

Laser coulostatic measurements were also performed in an attempt to match the theoretical predictions ascribed by Gottesfeld and Feldberg (169). Neither etched nor polished samples could be fit to theoretical predictions, but the decay of polished samples was seen to be much more rapid than that of etched samples. Excitation pulse intensities 4-10 times larger were required to obtain the same peak photopotentials from the polished samples as from the etched ones. Mechanically polished CdS samples showed a slow component to the photopotential rise, which disappeared after etching. The slow rise could also be quenched by simultaneous continuous illumination with either suprabandgap or subbandgap light. These effects are indicative of trapping occurring in the damaged layer.

Luminescence studies showed decay times which were very sensitive to the surface pretreatment. Prior to any surface treatment, both CdS and CdSe exhibited luminescence decay times shorter than the laser excitation width, i.e., <10 psec.

Mechanical polishing produced decay times of ~ 50 psec, and chemical etching produced much longer biexponential decays with $\tau_1 \sim 400$ psec and $\tau_2 \sim 8$ nsec (CdSe). The observed rates of emission show evidence for accelerated recombination rates in damaged surfaces.

Nonpotentiostated current transients were observed in the work of Kawai, Tributsch and Sakata (170). The PEC under study was n-MoSe₂ in contact with an electrolyte containing 1 M KI. In this work, a 50 Ω resistor was used as a load between the working electrode and platinum counterelectrode and the photocurrent signal was displayed on a Tektronix 7902 oscilloscope employing a 50 Ω input. Adjustment of the working electrode potential prior to illumination was accomplished by attaching a battery between the electrodes. A Molectron UV22 nitrogen laser was used to pump a Molectron DL14 dye laser which produced a 7 nsec pulse at 580 nanometers using Rhodamine 6G as the laser dye.

The time resolved photocurrent response in this investigation showed two distinct portions. First, a rapid response was seen to be excitation pulsewidth limited. This initial peak was in turn followed by a second, less intense peak which decayed very slowly. It was hypothesized that the first peak was due to charge generation and separation followed by rapid recombination, and the second peak was due to

charge transfer to the electrolyte.

At present, no specific experimental technique has allowed the design of a universal model describing the kinetics of a photoelectrochemical cell. This, in part, is due to the complexity of the PEC system. The lack of ability to observe individually any of the several processes occurring simultaneously hampers easy interpretation. Also, at least two schools of thought exist regarding theoretical models for PECs. Electronic analogues have been presented utilizing resistors and capacitors to duplicate the dynamics of the cell, and in many cases the important aspects of the physical nature of the cell itself has been neglected. Under certain experimental conditions, the R and C parameters describing the cell can be assumed constant, but this appears to be the exception rather than the rule. The physical kinetic interpretation, on the other hand, has provided more qualitative information than the electronic interpretation. Perhaps a merging of the two approaches can help to provide a picture of the underlying cell dynamics in the near future.

CHAPTER V. SAMPLE PREPARATION AND TECHNIQUES
FOR OBSERVING PHOTOCURRENT TRANSIENTS

Semiconductor/Redox Couple

Photocurrent transient studies were conducted using either n-WSe₂ or n-MoSe₂ photoanodes in contact with aqueous electrolyte solutions containing I⁻/I₃⁻ or Fe²⁺/Fe³⁺ redox couples. The WSe₂ and MoSe₂ (transition metal dichalcogenide) semiconductors are attractive for use in photovoltaic PEC's because of their small bandgaps and resistance to photocorrosion.

Polar semiconductors such as CdS, GaAs or GaP are found to be unstable in aqueous solution under illumination. Photoexcitation can result in the promotion of a bonding electron from a site on the surface of the crystal, thereby activating the weakened bond toward reaction with electrolyte species, resulting in the subsequent destruction of the bond. Typically a p → s phototransition occurs (e.g., in n-CdS, n-CdSe) which liberates the anion in molecular form as an anodic deposit, thereby decreasing the energy conversion efficiency. The careful selection of a redox couple which promotes rapid charge transfer (due to favorable thermodynamic or kinetic effects) will somewhat quench the decomposition reaction.

Another technique for preventing surface decomposition involves surface modification of the semiconductor via intercalation or overcoating.

The obvious drawbacks associated with the use of polar semiconductors led to the initiation of a search for new semiconductor types for solar cell applications. Ideally, molecular semiconductors which undergo electronic transitions between nonbonding d orbitals of the metal component should be stable. This search led to the transition metal dichalcogenides, specifically those exhibiting maximum d-d splittings which yield absorptive transitions on the order of 1.5 eV. The first semiconductors of this type to be studied were WS_2 and MoS_2 (171). Following this, the characteristics of n- $MoSe_2$ (172,173) and n- WSe_2 (174) photoelectrodes in Fe^{2+}/Fe^{3+} and I^-/I_3^- redox couple-containing electrolytes were studied. Information concerning the solid state properties of $MoSe_2$ and WSe_2 is still incomplete, and detailed band structure calculations have not been done. However, much is qualitatively understood about these materials.

Both $MoSe_2$ and WSe_2 exhibit a quasi-two dimensional structure in their pure crystalline form, whereby X-M-X sandwiches (X \equiv chalcogenide, M \equiv transition metal) are loosely bound to the next sandwich layer by van der Waals forces (Figure 5-1). Modification of the stacking of the

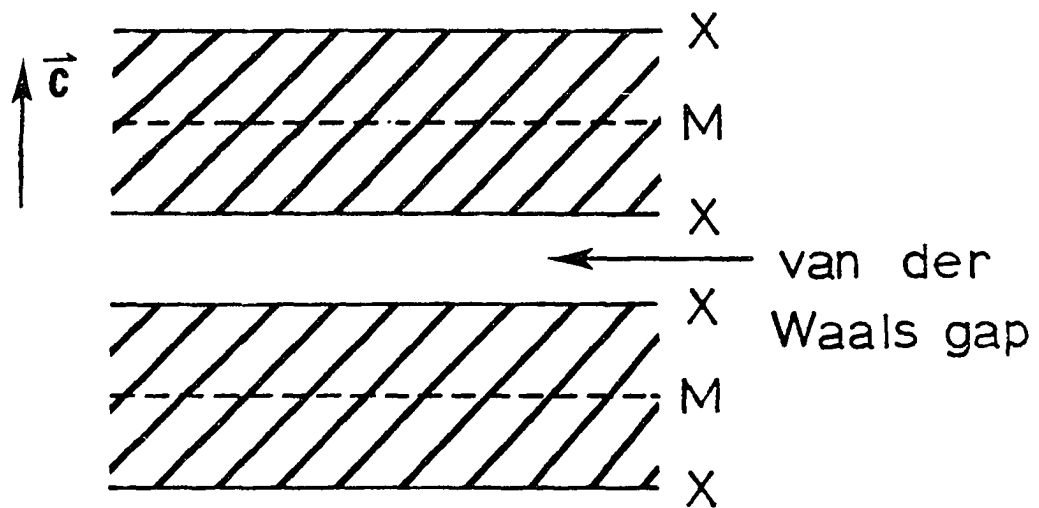


Figure 5-1. General form of layered transition metal dichalcogenide compounds illustrating "sandwich" structure

layers occurs through periodic insertion of stacking faults. Stacking faults are two-dimensional defects manifested by an irregularity in the stacking sequence of an atomic plane. One would expect that the stacking faults should be randomly distributed, but instead there is a marked tendency towards an orderly arrangement of the stacking faults, leading to long period structures which are called polytypes. As compared to a more common unit cell, two unit cell dimensions are equal, while the third dimension, usually along the \vec{c} -axis, varies from about 10 Å in small period polytypes to over 1000 Å in some of the longer period polytypes. The coordination of the chalcogenide atoms about the metal atoms in MoSe_2 and WSe_2 depends upon the specific polytypic form in which the crystal exists. Crystals of MoSe_2 and WSe_2 are not naturally occurring (as MoS_2 and WS_2 are) and must be prepared. Synthetic MoSe_2 occurs in either the 2H or 3R modification, while WSe_2 is always 2H. The 2H modification, as shown in Figure 5-2, occurs with two sandwich layers per unit cell stacked in hexagonal symmetry in AbA/BaB sequence in the $[11\bar{2}0]$ section (A,B \equiv chalcogen atoms; a,b \equiv transition metal atoms; / \equiv van der Waals gap). The chalcogen atoms are found in close-packed hexagonal layers, while the transition metal atoms exhibit sixfold prismatic coordination (Figures 5-3 and 5-4); the corresponding space group is $P6_3/mmc-D_{6h}^4$. 2H poly-

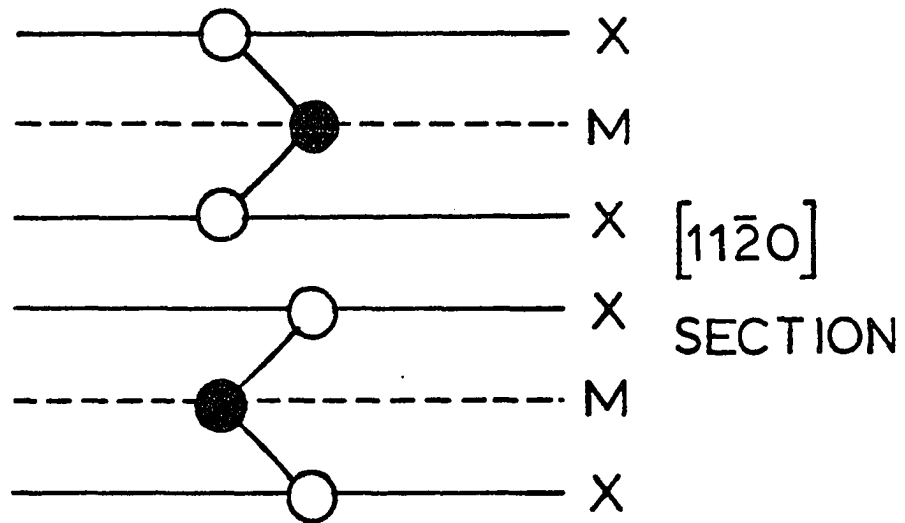


Figure 5-2. Relative positions of metal and chalcogene atoms in MoSe₂ and WSe₂ ([11 $\bar{2}$ 0] section)

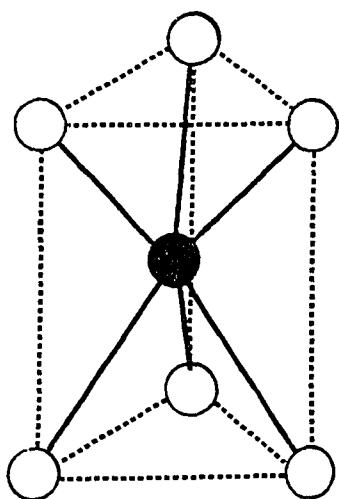
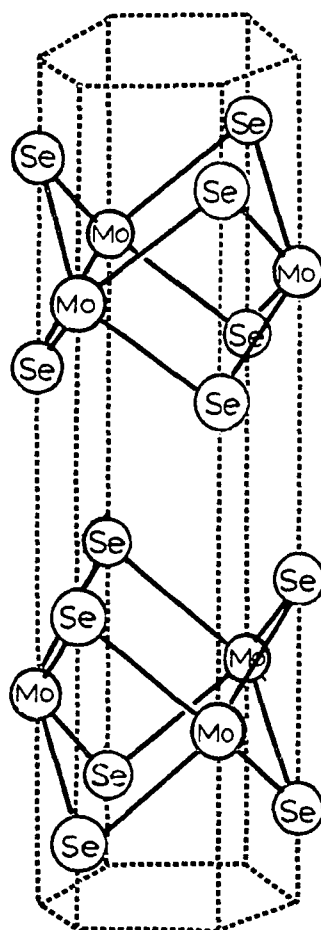


Figure 5-3. Trigonal prismatic coordination of chalcogene atoms about metal atoms (AbA)



2H - MoSe₂

Figure 5-4. Unit cell structure of 2H polytype MoSe₂

type MoSe_2 and WSe_2 crystals have the following unit cell dimensions:

	<u>a(Å)</u>	<u>c(Å)</u>	<u>c/a</u>
MoSe_2	3.288	12.920	3.924
WSe_2	3.286	12.976	3.952

The 3R modification (not of interest to this work; none of the crystals used exhibited 3R polytypism) has 3 layers per unit cell in rhombohedral symmetry, possessing an AbA/BcB/CaC sequence in the $[11\bar{2}0]$ section with the chalcogenide atoms exhibiting octahedral coordination about the transition metal atom.

In both modifications, the metal and chalcogen atoms are tightly bound by covalent links within the layers; weak van der Waals interactions couple adjacent sheets of chalcogen atoms. The surface perpendicular to the \vec{c} -axis is commonly called the "van der Waals surface."

The bonding scheme for these semiconductors requires hybridization of molecular orbitals. Each chalcogen atom places a lone pair of electrons in the van der Waals region, thereby requiring that each metal atom supply four electrons to fill the bonding orbitals. Any additional electrons (WSe_2 and MoSe_2 supply two each) must enter the nonbonding orbitals, which may accommodate up to six electrons. These nonbonding

orbitals arise largely from hybridization of the metal d and p states. The five d-orbitals and three p-orbitals combine to give hybrid orbitals ψ_1 , largely of d_z^2 character; ψ_2 , largely of $d_{x^2-y^2}$ and p_z character; and ψ_3 , largely of d_{xy} , p_x , p_y character (Figure 5-5). In the case of trigonal prismatic coordination, ψ_1 yields poor metal-metal overlap, and ψ_2 and ψ_3 are degenerate. Shown in Figure 5-6 are the simplified energy band diagrams for MoSe_2 and WSe_2 corresponding to this scheme. The bandgap energies assigned for direct interband transitions are 1.531 eV (175) and 1.622 eV (176) for MoSe_2 and WSe_2 , respectively. Corresponding indirect bandgaps have been determined to be ~ 1.09 eV for MoSe_2 and ~ 1.20 eV for WSe_2 (177,178).

Experimental results published to date indicate that the semiconductor-electrolyte interfacial chemistry is similar for MoSe_2 and WSe_2 . The most distinct difference between the two compounds is the higher open circuit voltage exhibited by WSe_2 , which is a result of larger equilibrium band-bending in the dark. For n- MoSe_2 and n- WSe_2 samples having similar donor densities ($N_D = 2 \times 10^{17} \text{ cm}^{-3}$), the conduction band edges lie at -0.30V and -0.44V vs SCE, respectively (179). When utilizing the I^-/I_3^- redox couple with $E^\circ_{\text{redox}} = 0.29\text{V}$, the maximum possible PEC photovoltages are $\sim 0.59\text{V}$ (n- MoSe_2) and $\sim 0.73\text{V}$ (n- WSe_2).

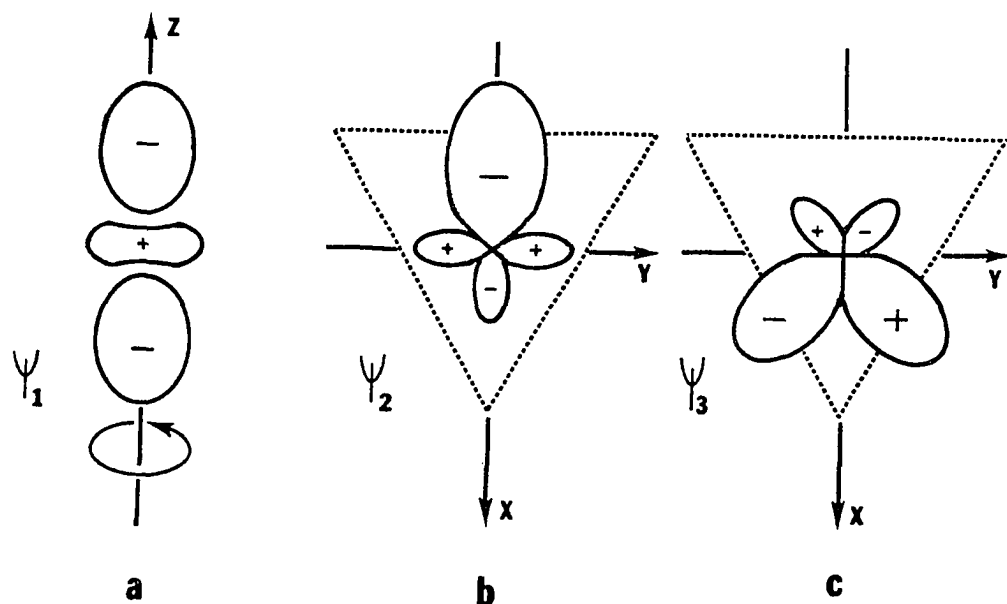


Figure 5-5. Shape and orientation of nonbonding orbitals for MX_2 layered compounds exhibiting trigonal prismatic coordination. Orbital ψ_1 is largely d_{z^2} in character, while orbitals ψ_2 and ψ_3 are combinations of $(d_{x^2-y^2}, p_x, p_y)$ and (d_{xy}, p_x, p_y) , respectively. Orbitals ψ_2 and ψ_3 are degenerate

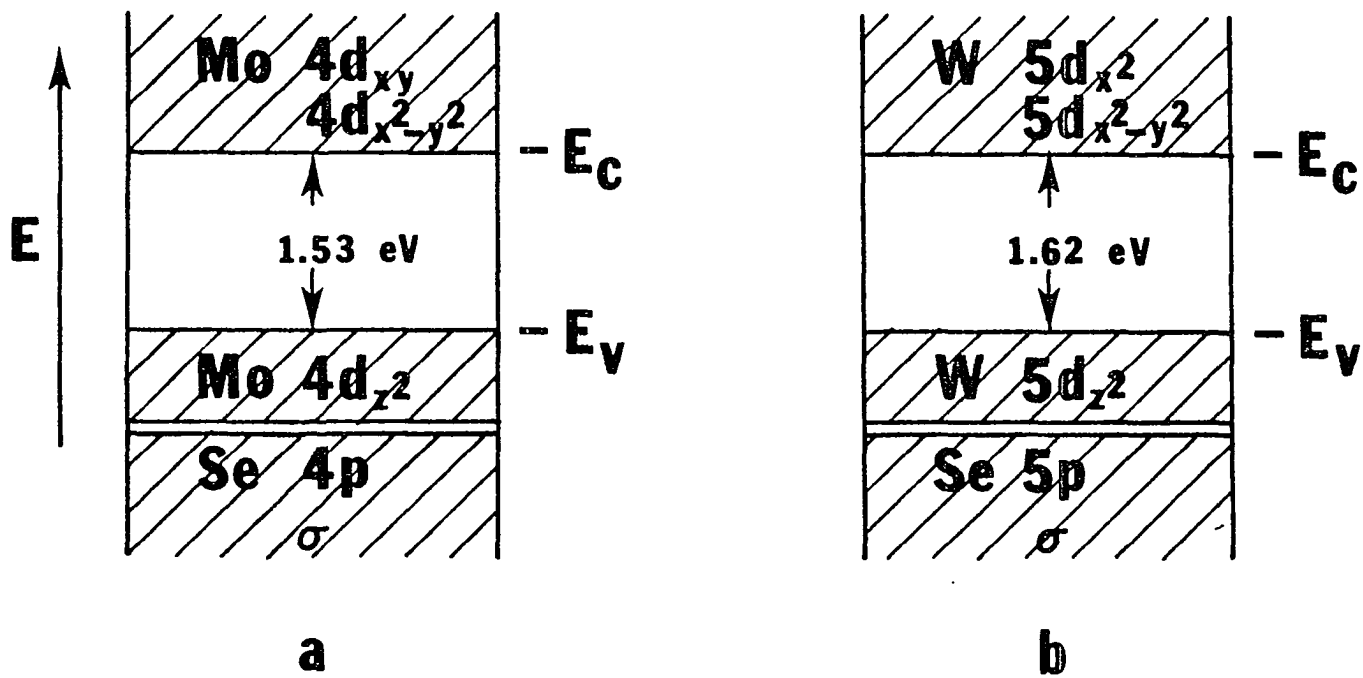


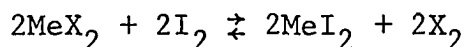
Figure 5-6. Simplified energy band diagram for a) MoSe₂ and b) WSe₂, showing specific orbitals involved in electronic transitions

Tributsch et al. (180) studied the photopotential output dependence upon redox couple electrochemical potential for n-MoSe₂ and n-WSe₂ photoanode PECs. For redox couples with electrochemical potentials slightly more positive than flat-band potential, linear increases in photopotential were seen, as theoretically from $U_{\text{MAX}} = U_{\text{FB}} - U_{\text{REDOX}}$. For redox couples which were greater than 0.3 volts positive of flat-band potential, the photopotential was seen to approach a limiting value. The I⁻/I₃⁻ couple proved to be the only exception to this scheme and produced the largest photopotential of all redox couples under investigation. In addition, I⁻ added to redox electrolytes with redox potentials more positive than that of I⁻/I₃⁻ was seen to shift the redox potential in a negative direction. It was suggested that the existence of surface states within the bandgap stabilized the Fermi level of the electrodes for more positive redox potentials. The adsorption of I⁻ and I₃⁻ onto Pt surfaces has been studied (181), and I⁻ is thought to adsorb strongly onto semiconductor surfaces (182). This reaction of I⁻ with the semiconductor surface apparently counteracts the effect of surface states, thereby making the electrode behave close to ideal.

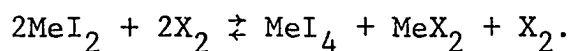
Sample Preparation

Single crystals of n-MoSe₂ and n-WSe₂ are most readily prepared by vapor transport. First, a polycrystalline charge of the transition metal dichalcogenide is formed by heating a stoichiometric mixture of the elements in vacuo. The charge is then volatilized as a chemically intermediate phase at a high temperature T₁ (reaction temperature). The intermediate phase then diffuses or convects to a region of lower temperature T₂ (growth temperature). Here, the chemical intermediate decomposes, and the dichalcogenide appears in single crystal form.

In the growth of dichalcogenides by halogen vapor transport, it is believed that the chemically intermediate phase is a halogen vapor and the reaction



is responsible for transport. At the growth temperature, association of the dihalide with X₂ to form the tetrahalide occurs, depositing the dichalcogenide according to



The tetrahalide then cycles to the reaction end of the system, where it reacts with more dichalcogenide, the process

continuing until all the charge is transported to the growth region.

Preparation of the single crystal samples was done by Gary Kline, Duane Canfield, and Kam Keung-Kam, all with the physics department at Iowa State University. Details of the vapor transport technique used for crystal growth are as follows: Stoichiometric amounts (total charge of approximately 30 grams) of tungsten (99.98%) or molybdenum (99.9%) powder and selenium (99.999%) shot were initially transferred to a flame-outgassed quartz ampoule under dry nitrogen. The diameter and length of the ampoule were 49 mm. and 30 cm., respectively. The ampoule was evacuated to a pressure of $<10^{-5}$ torr, sealed, and placed in a tube furnace. The tube furnace temperature was raised in 50°C increments from room temperature to a final temperature of 950°C, which was maintained constant for one week, after which time glittery microcrystals of compound were seen to occupy the ampoule. The microcrystals were then transferred to a second flame-outgassed quartz ampoule under dry nitrogen. This ampoule was first evacuated to a pressure of $<10^{-5}$ torr and then sealed under a pressure of 400 torr of chlorine. The vapor phase transport reaction was allowed to take place for two weeks in a multizone furnace. The furnace was operated with a temperature gradient of 1°C/cm, with reaction and growth

temperatures of 920°C and 900°C, respectively. Most of the crystals thus obtained possessed macroscopic defects such as stacking faults, edge dislocations and screw dislocations. X-ray powder diffraction patterns of arbitrarily selected single crystals of MoSe_2 and WSe_2 established all as being 2H polytype. The crystals were determined to be n-type by the sign of their Hall coefficients (183) and the direction of photocurrent when operating in a PEC.

Crystals were mounted "as is" if the desired surface was present. Improvement of the surface quality prior to mounting could be achieved by lifting off layers of the crystal using Scotch tape. Several repetitions of this simple procedure at times produced good quality surfaces free of major visible defects under microscopic examination. The crystals were initially cleaned by immersion in 2 M HCl (30 seconds), followed by thorough rinsing with triply distilled water. This was followed by rinsing with 1-1-1 trichloroethane, acetone, methanol, and triply distilled water once again.

The crystals were mounted by forming an ohmic contact between a clean van der Waals face of the crystal and a machined brass mount. The mounts consisted of 1/4" long sections of brass rod, threaded at the rear (8-32) for electrical contact and machined to fit inside of 8 mm glass tubing. Two types of ohmic contacts were prepared. In-

initially, a small drop of highly conductive silver paint was applied between the semiconductor and the mounting surface. The silver paint was then allowed to dry in air or vacuum. More reliable ohmic contacts were prepared by soldering the crystals to the mount with indium using an ultrasonic soldering gun in an argon atmosphere.

The brass mounts were set into short lengths of 8 mm OD pyrex glass tubing or 1/2 inch OD teflon supports. Epoxy (Ton Seal or Bipax BA-2126) was used to cover the junction between the crystal and mount, as shown in Figure 5-7, leaving only a portion of the desired working surface exposed. The epoxy also bonded the mounted crystal to the glass or teflon support. Both of the epoxy resins used exhibited resistance to chemical attack over a period of months.

Electrochemical Cell

The electrochemical cell used in this work is depicted in Figure 5-8. The cell body was first prepared of nylon, but glass-filled teflon was later used as the nylon tended to absorb species from solution. The cell was 2 inches in diameter and 2 1/4 inches long. A 1/8 inch thick quartz optical flat was fitted into the front of the cell. Chemically inert Viton O-rings (Parker) were used to seal the optical flat and the sample holder. Six 6-32 stainless :

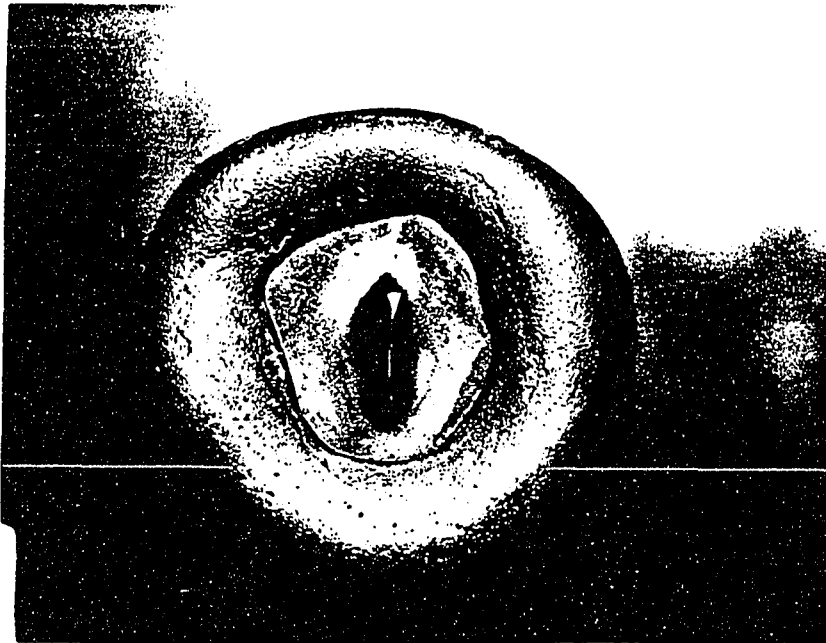


Figure 5-7. Typical sample face with epoxy mounted crystal. An edge mounted (only sites \perp to \vec{c} axis exposed) sample is shown

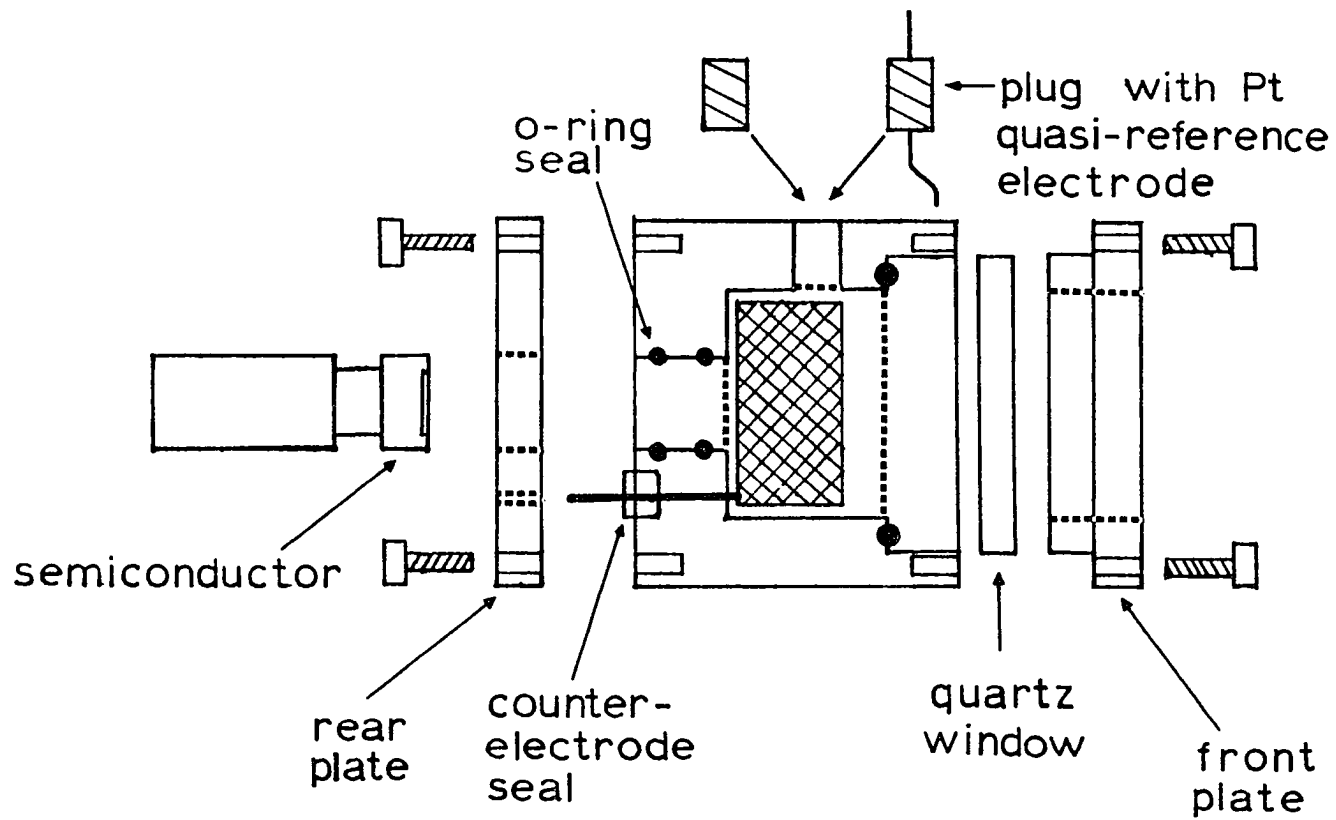


Figure 5-8. Exploded cross-sectional view of photoelectrochemical cell (PEC)

steel socket head cap screws held the window retaining ring in place and served to seal the O-ring against the window. At the rear of the cell, a glass-filled teflon plate was used to seal the counter electrode electrical lead in position. Six more cap screws attached the rear plate. The counter electrode consisted of a platinum wire spot welded to a cylinder of platinum gauze. The counter electrode was designed to be concentric with the sample to ensure symmetrical current flow, while being of large surface area to counteract concentration polarization effects. A sample positioner was used which places the sample 0.48 cm away from the window. Consistent positioning of the sample helped to avoid complications due to the variation of solution absorption with respect to thickness of the solution layer. When used in a 2-electrode configuration, a 1/4-20 threaded nylon plug was inserted into the top of the cell. In the 3-electrode configuration, a plug fitted with a thin platinum wire was inserted into the top of the cell. When in use, the end of the platinum wire was positioned ~ 1 mm from the semiconductor face and served as a quasi-reference electrode. The cell held approximately 20 ml of electrolyte solution.

Electrolyte

The electrolyte was prepared with analytical reagent grade chemicals without further purification, using triply distilled water which was first distilled from a 5 mM KMnO_4 and 33 mM NaOH solution to oxidize any organic molecules in the water. Two redox couples were used in the aqueous electrolyte solutions. The redox couple I^-/I_3^- was prepared using reagent grade KI (Baker) and twice sublimed I_2 (Baker). The redox couple $\text{Fe}^{2+}/\text{Fe}^{3+}$ was prepared using ferrous ammonium sulfate ($\text{Fe}(\text{NH}_4)_2(\text{SO}_4)_2 \cdot 6\text{H}_2\text{O}$; Baker) and ferric ammonium sulfate ($\text{Fe}(\text{NH}_4)(\text{SO}_4)_2 \cdot 12\text{H}_2\text{O}$; Mallinckrodt). In some instances, KCl (Fisher) was used as a supporting electrolyte. The cell was designed to hold ~20 ml of electrolyte solution.

Experimental Apparatus

The experimental set-up used for photoexcitation and subsequent signal detection is shown in Figure 5-9. The flashlamp-pumped transverse-flow dye laser used for this study is documented in detail in Chapters I-III of this work. Nanosecond excitation pulses were obtained by operating the laser in a nonmodelocked configuration and utilizing the Pockels cell electrooptic switch as a simple "light gate."

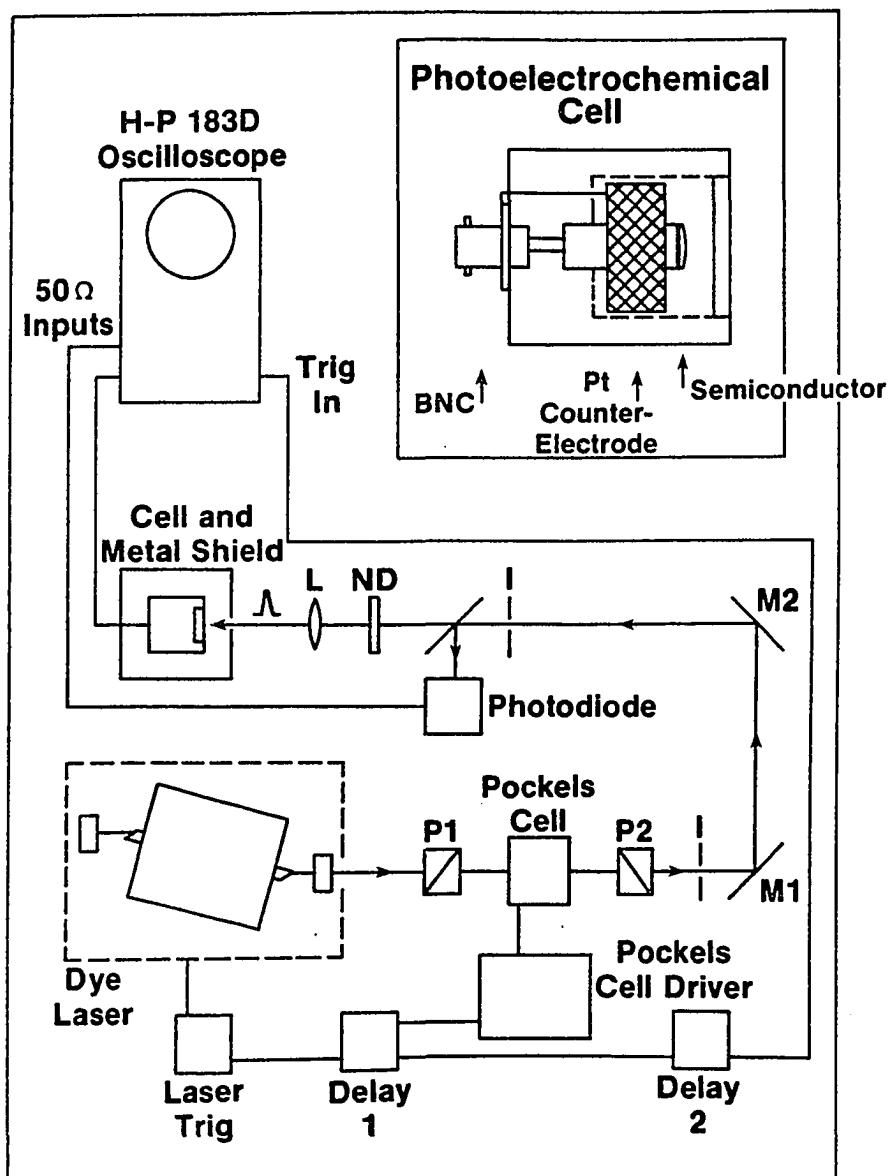


Figure 5-9. Schematic of experimental apparatus showing excitation source (transverse-flow flashlamp-pumped dye laser), cell and Faraday cage, and detection equipment (H-P 183D oscilloscope)

A triggering source adjustable from 0.7-200 Hz was used to initiate laser operation and subsequent signal detection. Data collection (photographic recording of traces) was facilitated by operating the laser at 0.7 Hz throughout the experiments. The trigger signal was simultaneously sent to the EG&G Ortec TM-27 thyatron driver module and to an EG&G Ortec 416A gate and delay generator. The gate and delay generator in turn triggered one channel of an EG&G Ortec 924 quad discriminator, which supplied the required 5 nsec FWHM -0.7V signal to the EG&G Ortec HV100/N Pockels cell driver module. Operation of the Pockels cell was thus synchronized with the peak intensity of the microsecond output from the dye laser. A 5 ns FWHM pulse at 607 nm was produced in this fashion, with the remainder of the microsecond output being rejected and steered into a beam stop where it was absorbed. The nanosecond pulse was then spatially filtered using an iris, steered by two mirrors, and spatially filtered by a second iris.

A glass slide beamsplitter angled at 45° to the beam axis was used to select off a small portion of the laser pulse and send it to a Hewlett-Packard 4220 p-i-n photodiode. The photodiode detector was operated in a low impedance (fast response) configuration. Appropriate neutral density filters were placed before the photodiode to ensure

linear operation. The beamsplitter/photodiode combination was used to measure the pulse energies via oscilloscope monitoring of peak photovoltaic signal. The pulse energy monitoring system was calibrated using another laser system consisting of a Molectron DL 200 dye laser pumped by a Molectron UV 14 N₂ laser. The N₂ laser pumped dye laser was operated at 25 Hz. Laser output was passed through the beamsplitter, and the photovoltaic response of the photodiode was noted while monitoring the laser output passed by the beamsplitter with a calibrated Scientech 361 power meter.

Prior to reaching the PEC, the dye laser pulse was attenuated with one or several Schott neutral density filters. The neutral density filters were calibrated singly and in groups (as used) using a Perkin-Elmer Model 320 UV-visible spectrometer. The range of pulse energies used for excitation extended from 4-4000 nj per pulse.

A 1 meter focusing lens was used to vary the area of photoexcitation at the semiconductor surface. Four spot sizes (at the semiconductor surface) were used during the experiments: 0.107 cm², 0.042 cm², 0.015 cm², and 0.0038 cm². The spot sizes were accurately measured using Polaroid film (Type 667, ASA 3000), exposed by the highly attenuated laser pulse. Corresponding measurements of the semiconductor surface areas were also performed by cutting and weigh-

ing enlarged photographs of the samples.

Modified female BNC case mount connectors (Berkley Nucleonics) were used to electrically contact the PEC. The connectors have a threaded brass stud (8-32) mounted on the front for direct connection to the cell. The counterelectrode was connected by clipping onto a flange mounted on the connector. The BNC connector, in position, is schematically depicted in the insert of Figure 5-9.

The PEC was enclosed in a steel box which was completely sealed during experiments, with the exception of a 1/4" orifice in the front for admitting the laser pulse. A small removable metal panel next to the orifice facilitated sample alignment. A single BNC connector mounted at the rear of the box was used to output the transient signal to the oscilloscope. A short length of RG 59/U coaxial cable located in the box was used to connect to the PEC. An RG 59/U coaxial cable also provided the interconnection between the box and the oscilloscope. The cable was shielded by covering with ground braid, which was anchored to the BNC connectors at both ends. By using the steel box and shielding the cable, RF noise generated by the laser was kept to a minimum. Prior to using this shielding scheme, the RF noise pickup completely obscured the photocurrent signal.

A Hewlett-Packard 183D oscilloscope mainframe outfitted

with an 1830A dual channel vertical amplifier and 1840A timebase was used for signal detection. The 1830A vertical amplifier employs 50Ω inputs, 10 mV/division maximum sensitivity, and offers a 250 MHz bandwidth. The 1840A timebase has a minimum sweep of 10 ns/division. The timebase was externally triggered to allow synchronization of the oscilloscope sweep with the arrival time of the photocurrent transient. A NIM module featuring a double pulse mode with adjustable time duration between pulses (up to 1 ms) was constructed to trigger the oscilloscope. The first trigger pulse was used to display the transient signal, while the second, which appeared long after the transient had decayed, was used to establish a reference of zero volts. Through the use of this double triggering technique, both signals could be viewed on the oscilloscope screen simultaneously.

Oscilloscope traces of the photocurrent transients were recorded photographically using a Tektronix C-27 oscilloscope camera outfitted with a mounting bracket for the Hewlett-Packard oscilloscope. The shutter was set to bulb mode, and a remote shutter switch was used. Polaroid type 667 ASA 3000 film was used throughout. The oscilloscope trace photographs were later rephotographed using a 35 mm camera equipped with a 1:3 macro lens and a 4.0 diopter enlarging ring. The 35 mm film (Kodak TP 135-36 Tek Pan 2415 ESTAR-AH Base) was used to

make enlarged ($8\frac{1}{2} \times 11$) prints of the traces, thereby facilitating data treatment.

Current-voltage (i-V) curves were taken for each sample used in the photocurrent transient studies to provide a qualitative indication of sample conditions. A Pine instrument company RDE2 potentiostat was used to adjust the potential of the semiconductor while monitoring photocurrent output. The three electrode configuration of the PEC was used, with the Pt wire electrode placed near the semiconductor, thereby operating as a quasi-reference electrode. A sweep rate of 1 volt/min was used, and all scans were repeated twice to check for hysteresis. Both illuminated and dark i-V curves were recorded. Illumination was provided by a Spectra-Physics 155 He-Ne laser (632.8 nm). A Metrologic 60-530 Laser Radiometer was used to measure the average power of the laser output, which was 0.72 mW, unattenuated. The laser beam was spatially filtered by a pinhole aperture and defocused using a 15 cm lens such that the exposed semiconductor surface was nearly filled. Measurement of the beam spot size at the crystal face allowed the calculation of excitation power densities.

A Hewlett-Packard 4815A RF Vector Impedance Meter was used to determine the RC characteristics of the assembled

PECs. Impedance magnitude (z) and phase angle (θ) were read directly from the instrument, from which R and C are readily determined assuming a linear RC Model for the cell.

CHAPTER VI. PHOTOCURRENT TRANSIENTS IN

MoSe₂ AND WSe₂

Transient Decays

A representative example of the observed photocurrent decays is shown in Figure 6-1. The photocurrent transients exhibit three distinct regions which appear in unique combination for each transient. First, an excitation pulsewidth limited rise is always observed. This initial excursion at times is followed by a more slowly rising portion culminating at the peak photopotential, which in turn decays back to zero. The form of the decay initially appears to be exponential and possibly reflects the RC time constant of the system. However, one must keep in mind the nature of the PEC. The resistance and capacitance of the solution does not vary appreciably during pulsing, due to the invariance of the relative concentrations of the redox species during the short time period of each transient. The semiconductor sample, on the other hand, experiences large changes in minority carrier population (conductivity) and consequential charging of the space charge and Helmholtz region, i.e., variations in R and C which depend upon illumination level, surface homogeneity, and the nature of the semiconductor-electrolyte interface. It is quite obvious that a simple linear RC circuit model produces only a single exponential decay. Ideally, the system

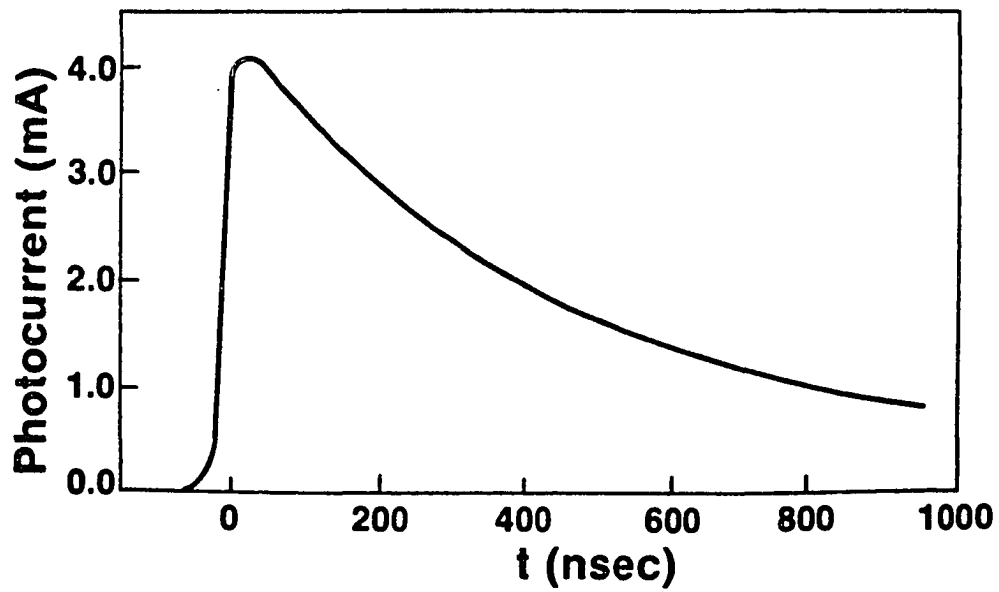


Figure 6-1. Photocurrent transient for sample with high surface quality (WSe_2 #50-4) in 5.0 M KI/ 10^{-2} M I_2 containing electrolyte. Incident pulse energy 46.2 nanojoules

could be best treated by abandoning the RC model and constructing a model for which the spatial distributions of charge carriers are known for all times. Realistically, a model employing features of both treatments may be used as an approximation.

Careful observation of the decay portion of the transients shows them to be, in fact, nonexponential. Shown in Figure 6-2 is a plot of the natural logarithm of a photocurrent decay (normalized to the peak) with respect to time. Two linear portions are pronounced in this figure, pointing to the possibility of a biexponential decay. Before viewing the decays as biexponential, other decay types were first tested for goodness of fit.

The current-time response associated with semi-infinite linear diffusion of electroactive species to a planar electrode may be determined from the solution of the linear differential equation

$$\frac{\partial [\text{RED}(x,t)]}{\partial t} = D_{\text{RED}} \frac{\partial^2 [\text{RED}(x,t)]}{\partial x^2} \quad [6-1]$$

where $\text{RED}(x,t)$ is the concentration profile of reduced species as a function of distance x from the interface, and D_{RED} is the diffusion coefficient associated with the reduced species. The solution to this differential equation yields the Cottrell equation

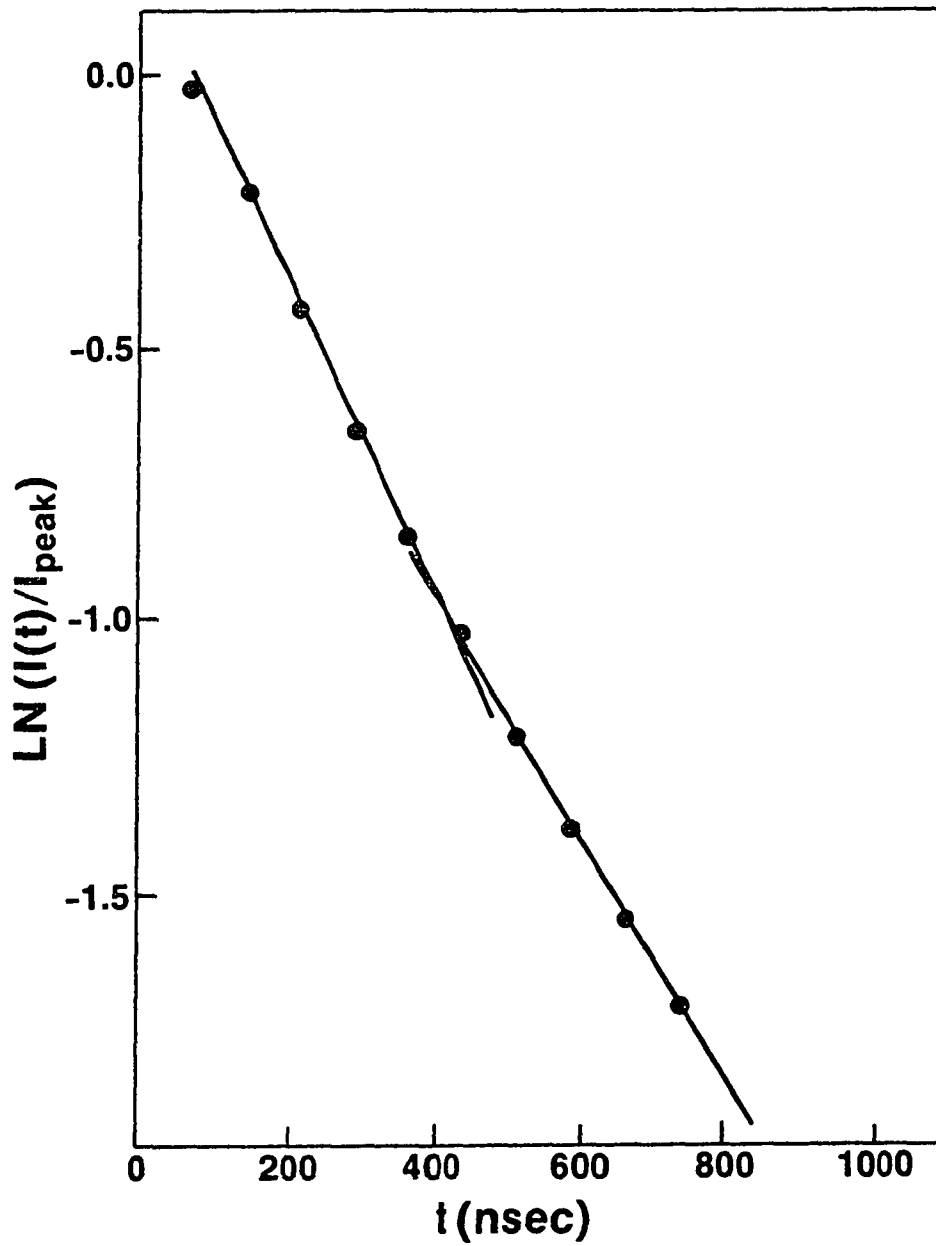


Figure 6-2. Sample of natural logarithm of photocurrent (normalized to peak photocurrent) as a function of time to time for sample WSe_2 #50-4 in I^-/I_3^-

$$i(t) = \frac{nFAD_{RED}^{\frac{1}{2}} [RED^*]}{\pi^{\frac{1}{2}} t^{\frac{1}{2}}} \quad [6-2]$$

which shows that the effect of depleting the electroactive species near the surface of the electrode is characterized by a $t^{\frac{1}{2}}$ dependence. In this equation, n is the charge on the redox species, F is the Faraday constant, A is the electrode cross-sectional area, and $[RED^*]$ is the bulk concentration of reduced species. None of our transients obey a $t^{\frac{1}{2}}$ decay, thereby eliminating concentration polarization as a dominant feature.

Open circuit decays corresponding to photo-charge injection (164, 165) have been observed to follow a $t^{-2/3}$ dependence as theoretically predicted by Feldberg and by Feldberg and Gottesfeld (166, 169). None of the observed decays obey this scheme. Therefore, expansion and contraction of the space charge layer, in analogy with that suggested in the work of Richardson, Perone et al. (165), cannot be applied here. One important point to note, however, is that the sum of two (or more) exponential decays under the right circumstances may appear to approximately follow a $t^{-2/3}$ dependence. The cited authors may have fallen prey to this dilemma for their later work (164) shows a fit which is inferior to the one previously determined.

Other general decay functions were tested without conclusive results. Therefore, it was decided to pursue the

trend towards biexponential decay. The first experiment from which data were treated involved the observation of photocurrent transients as a function of incident laser pulse energy and spot size at the crystal face. For this study, sample WSe_2 #50-4 was used in either I^-/I_3^- or $\text{Fe}^{2+}/\text{Fe}^{3+}$ containing electrolytes. All of the resultant data showed behavior more complex than single exponential. The rising portions of the transients, whose durations were not significant in comparison to those of the decays, were initially ignored to simplify the mathematical treatment. Referring again to Figure 6-2, it is evident that a potential problem exists which makes proper interpretation more difficult. That is, in some cases the slopes are very similar. A biexponential decay of the type

$$I(t) = I_1 e^{-t/\tau_1} + I_2 e^{-t/\tau_2} \quad [6-3]$$

is easily interpreted only if $\tau_1 \ll \tau_2$. If such is the case, the linear portion at long times may be treated as being entirely due to the second decay. From the determination of τ_2 , I_2 and subsequently I_1 and τ_1 may be found. Initial treatment of the decay curves under discussion was performed using this simple technique. Better values were then obtained using a gradient-search least squares technique applicable to general nonlinear functions (184). The only drawback of this technique is the convergence rate, which is slower than for other more sophisticated techniques (such as

a χ^2 parabolic extrapolation technique utilizing matrix inversion). In the gradient search method, all of the coefficients a_j in the equation

$$y = a_1 e^{-x/a_2} + a_3 e^{-x/a_4} \quad [6-4]$$

are incremented simultaneously with relative magnitudes adjusted such that the resultant direction of travel in parameter space is along the gradient (or direction of maximum variation) of χ^2 , where chi-squared (χ^2) represents a (weighted) sum of the squares of the deviations of the data points from the calculated values.

The gradient is followed until the minimum of χ^2 is straddled. A parabolic extrapolation is then performed to find the minimum χ^2 value, and a new iteration is initiated. The gradient search program, along with other programs applicable to this study, were run on a 16-bit Texas Instruments TI99/4A desktop minicomputer utilizing BASIC computer language.

Current Voltage Curves

Not all semiconductor samples studied were amenable to this type of treatment. Samples exhibiting various surface quality were examined. Surfaces exhibiting a high degree of perfection (as shown in Figure 5-1) were easily separable from

those possessing imperfections by monitoring current-voltage curves taken under dark and CW illuminated conditions.

Figure 6-3 illustrates the different i - V curves obtained for four samples. All samples were in $5.0 \text{ M I}^-/10^{-2} \text{ M I}_2$ solutions, and illumination was by a He-Ne laser operating at 632.8 nm (1.87 mW/cm^2). Samples a and b are WSe_2 #50-4 and MoSe_2 #33-2, respectively. Both of these samples clearly exhibit high photopotentials and photocurrents in conjunction with low dark currents, characteristic of semiconductors with high quality surfaces. Sample c is WSe_2 #50-1, which is mounted such that only edges (\parallel to \vec{c} axis) are exposed to the solution. Very low photovoltage and photocurrent are seen, along with an extremely large dark current. The high cathodic dark current is due to the very small amount of band bending present at edge sites. A small negative applied potential readily flattens the bands, causing majority carriers (electrons) to reduce species in solution. Sample d is MoSe_2 #2, which has only the van der Waals face exposed to the solution. Very low dark current is seen. However, the photocurrent under illuminated conditions is very low. Band bending is normal for this sample, but high recombination rates provide a shunted pathway for the disposal of photogenerated charge other than through charge transfer. Losses are high, and the corresponding fill factor and efficiency are low. The surface of MoSe_2 #2 under close inspection is seen to be concave

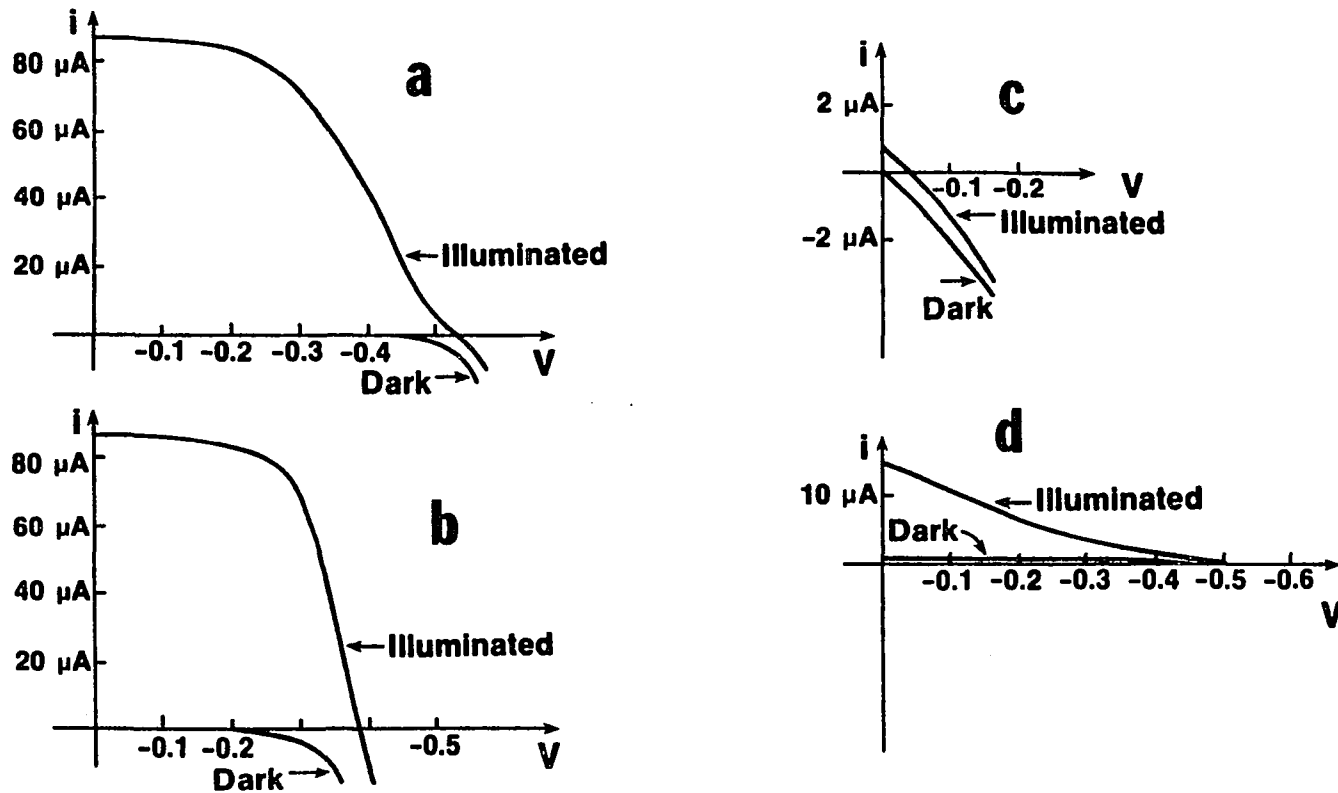


Figure 6-3. Current voltage curves for various semiconductor samples under dark conditions and CW illumination at 632.8 nanometers ($1.87\text{mW}/\text{cm}^2$). All samples in $5.0\text{ M KI}/10^{-2}\text{ M I}_2$ a) WSe_2 #50-4. b) MoSe_2 #33-2. c) WSe_2 #50-1 (edge mount). d) MoSe_2 #2 (concave surface)

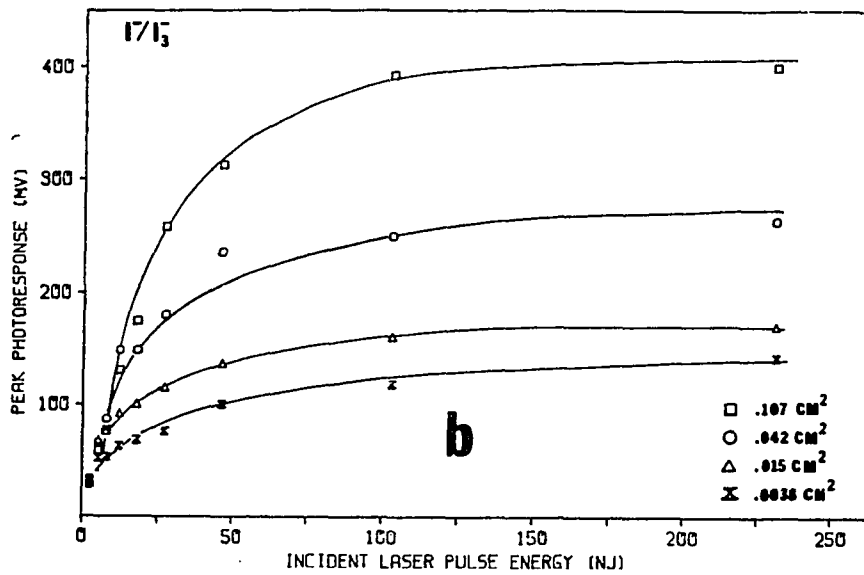
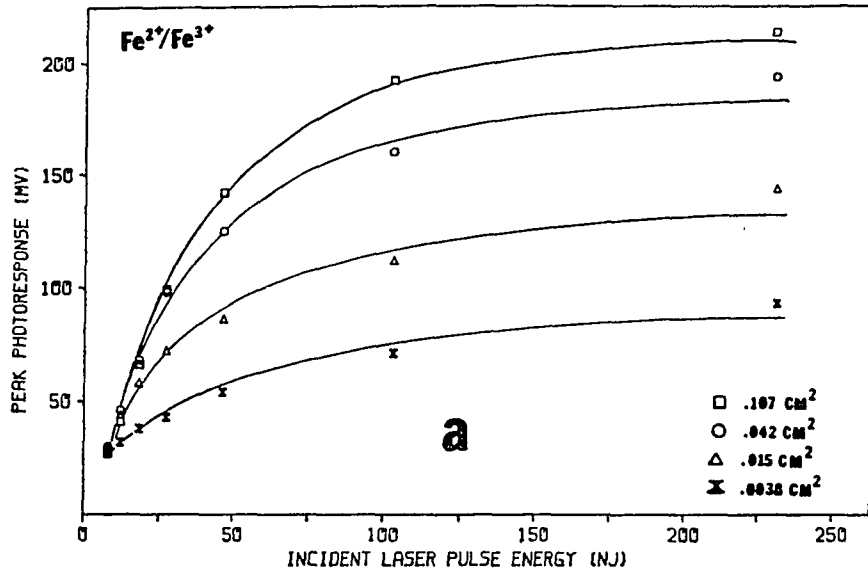
rather than flat, leading one to believe that a high proportion of edge sites exists on the crystal surface.

Peak Photoresponse

Peak photocurrent was determined as a function of laser pulse energy and laser spot size at the crystal surface. Incident pulse energies ranged from 2-250 nanojoules, and the four spot sizes used were of cross sectional areas $.107 \text{ cm}^2$, $.042 \text{ cm}^2$, $.015 \text{ cm}^2$, and $.0038 \text{ cm}^2$. The largest spot size would typically nearly fill the area of the semiconductor exposed to the solution. The focused spots were used to study the effects of increasing power densities. In a CW experiment, it is observed that the short circuit photocurrent is linearly dependent upon the incident photon flux, while the open circuit photopotential is logarithmically dependent on the photon flux. The photocurrent transients obtained in this study are observed under conditions which are much closer to short circuit than to open circuit conditions, but the photoexcursions which are observed on the oscilloscope are, of course, photovoltage transients. It is assumed that the photocurrent is directly proportional to the photovoltage (via the load resistance, i.e., the oscilloscope). The term "photocurrent" is used here because a substantial current due to charge transfer into the solution occurs. The peak photo-

response vs. incident laser pulse intensity is shown in Figure 6-4a for WSe_2 #50-4 in $\text{Fe}^{2+}/\text{Fe}^{3+}$ containing solution and in Figure 6-4b for I^-/I_3^- containing solution. Note the different scales for the two figures. The PEC utilizing I^-/I_3^- clearly produces the better photoresponse. Smaller peak photoresponse is seen using $\text{Fe}^{2+}/\text{Fe}^{3+}$ under similar conditions. The chemical potential of the $\text{Fe}^{2+}/\text{Fe}^{3+}$ couple is more positive than that of I^-/I_3^- , however, and therefore one would expect to see the opposite effect. However, as stated in the previous chapter, only the I^-/I_3^- couple shows evidence that the degree of band bending is linear with respect to redox potential (185). The I^-/I_3^- couple is by far the most efficient redox couple, a fact which may be rationalized as follows. Surface states due to imperfections are appreciably present on all crystals, including those of the highest quality. The I^-/I_3^- couple tends to counter these states by perturbing them (via adsorption) such that they are no longer accessible. Either the timescale required for the capture of photo-produced charge becomes longer than that pertinent to the experiment, or the states are shifted, becoming energetically inaccessible. The $\text{Fe}^{2+}/\text{Fe}^{3+}$ couple appears to be separated from the semiconductor by at least a monolayer of solvent molecules. Surface states due to imperfections remain unperturbed and, therefore, can fill on the timescale of the experiment, effectively pinning the Fermi level of the

Figure 6-4. Peak photoresponse as a function of incident laser pulse energy for WSe_2 #50-4 in a) $\text{Fe}^{2+}/\text{Fe}^{3+}$ redox couple containing solution, and b) I^-/I_3^- redox couple containing solution



semiconductor and limiting band movement.

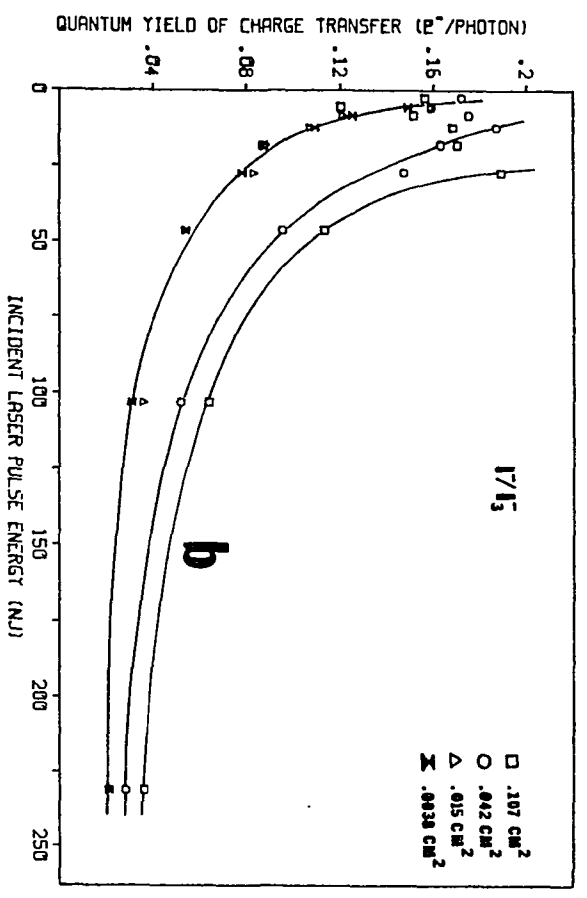
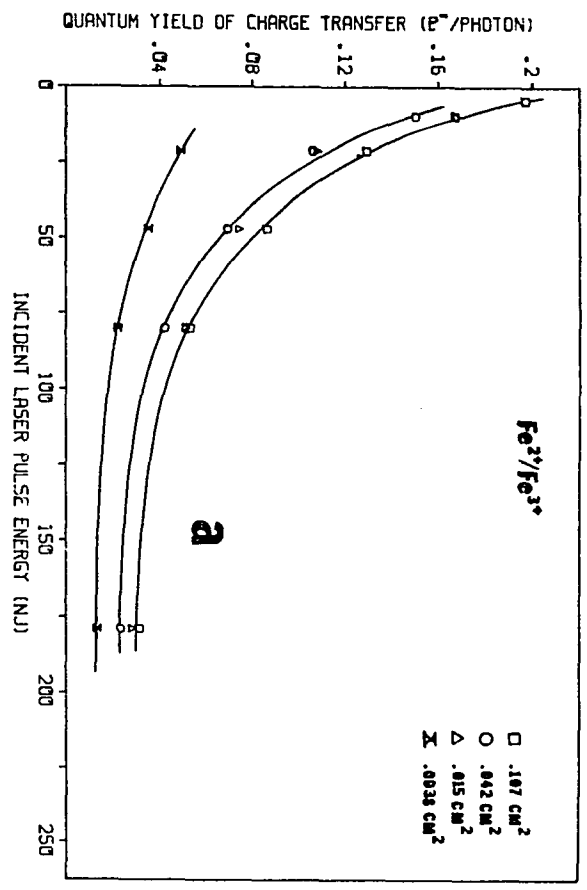
The smaller spot sizes which in turn correspond to higher power densities clearly produce lower photopotential responses. As the power density is increased, the density of photoproduced charge increases. When the photogenerated charge is separated by the space charge field, losses due to recombination may be enhanced. Due to the high optical absorption coefficient ($\alpha \sim 10^5 \text{ cm}^{-1}$) for WSe_2 , $\sim 80\%$ of the photogenerated charge is produced within 200 nanometers of the crystal surface, well within the space charge region. Separation of electrons and holes via migration should take place in < 1 nanosecond. Edge luminescence intensities displaying a quadratic dependence upon excitation intensity and having decay times (major component of decay) of ≈ 400 picoseconds have been observed for PECs employing CdS and CdSe electrodes in sulfide and polysulfide electrolytes (168). Assuming that the initial recombination rate is charge carrier density-dependent, the quadratic photopotential variation is reasonable. One final point is that the peak photoresponse does in fact exhibit a logarithmic dependence upon the excitation energy.

Charge Transfer Quantum Yield

Quantum yields of charge transfer were calculated based on integrated photocurrents versus number of photons imping-

ing upon the PEC. Integrations were performed by cutting and weighing photoreproductions of the traces and referencing them against a standard (copy of the oscilloscope screen). Corrections for solution absorption were employed, as in the peak photoresponse calculations. Corrections were not made for reflection at the semiconductor surface. The resultant plots for WSe_2 #50-4 with $\text{Fe}^{2+}/\text{Fe}^{3+}$ and I^-/I_3^- redox couples are shown in Figures 6-5a and 6-5b, respectively. Quantum yields appear to be comparable for both redox couples with the I^-/I_3^- couple showing a distinct trend toward higher quantum yields at low excitation energies. The low values obtained for the quantum yields overall reflect the extent of recombination induced by high illumination levels. For excitation energies greater than 50 nanojoules, it appears that the redox couple has a very small effect, which would indeed be the case if much of the recombination occurs slightly into the depletion region and not at the surface. At lower excitation energies, more of the photogenerated charge separates, and effects of the redox couple become evident. The I^-/I_3^- couple, through suppression of surface states which could lead to either recombination or surface photodegradation, facilitates a higher quantum yield of charge transfer. Once again, the effects of enhanced recombination for smaller spot sizes is self-evident.

Figure 6-5. Quantum yield of charge transfer as a function of incident laser pulse energy for WSe₂ #50-4 in a) Fe²⁺/Fe³⁺ redox couple containing solution and b) I⁻/I₃⁻ redox couple containing solution

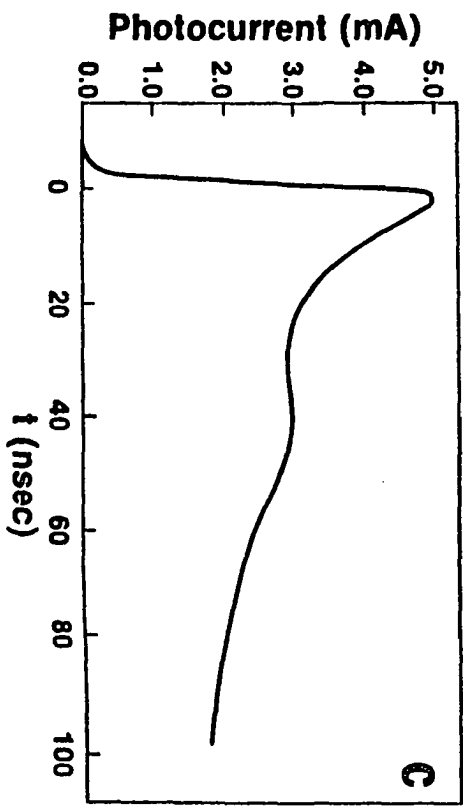
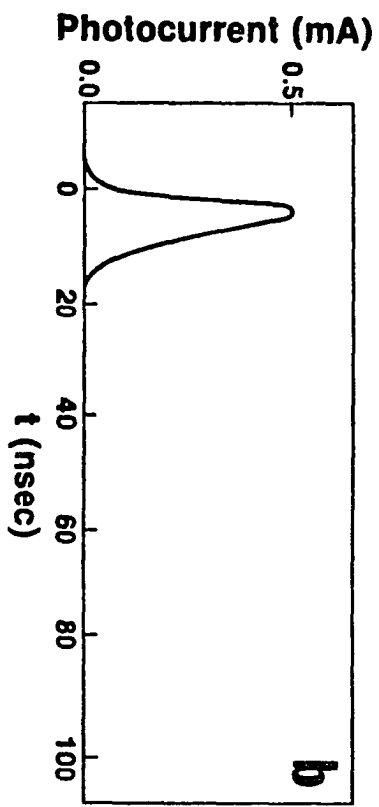
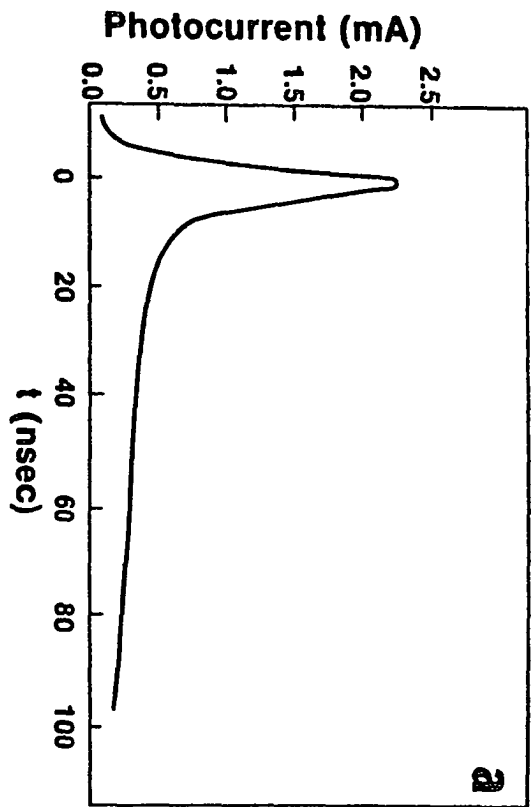


Surface Imperfections

The technique for analyzing the biexponential character of the photocurrent transient decays has already been discussed. Samples exhibiting a high degree of surface perfection produce a biexponential decay regardless of redox couple used. Other semiconductor samples of poor quality (as determined by current-voltage curves and/or visual inspection) tend to show lower peak photocurrents and two distinctly separate decay regions. Figure 6-6 depicts three of these decays, each of which exhibits unique behavior. The semiconductors were immersed in 5.0 M KI/0.2 M I_2 . The i-V curves for the first two traces may be seen in Figure 6-3. The transient response of sample $MoSe_2$ #2, which exhibited the surface concavity, is depicted in Figure 6-6a. Incident pulse energy is 179 nanojoules. In Figure 6-6b, the photocurrent transient for edge-mounted sample WSe_2 #50-1 (illumination \perp to \vec{c} -axis) is seen. Incident pulse energy is 2470 nanojoules. Figure 6-6c shows the photocurrent transient of WSe_2 #50-3, which has visible steps on the surface. Incident pulse energy is once again 2470 nanojoules. Figures 6-6a and 6-6b both show evidence of a photoexcitation pulsewidth-limited risetime. In Figure 6-6b, edge site recombination dominates because only edge sites exist. The low peak photocurrent (in spite of the high excitation energy) suggests that

Figure 6-6. Photocurrent transients for samples showing low efficiencies

- a) MoSe_2 #2; incident pulse energy 103 nanojoules; $5.0 \text{ M KI}/10^{-2} \text{ M I}_2$.
- b) WSe_2 #50-1 (edge mounted sample, illumination) \perp to c-axis); incident pulse energy 2470 nanojoules; $5.0 \text{ M KI}/10^{-2} \text{ M I}_2$.
- c) WSe_2 #50-3 (visible steps on surface); incident pulse energy 2470 nanojoules; $5.0 \text{ M I}^-/10^{-2} \text{ M I}_2$



a very small amount of band-bending is present at the junction. The quantum yield of charge transfer corresponding to this sample is $<10^{-3}$. Similar behavior seen in Figure 6-6a can be attributed to the same mechanism. In addition, however, a more slowly decaying tail is seen. Charge which is not trapped at a recombination site may undergo charge transfer, and, therefore, the tail either reflects the rate of normal charge transfer or possibly the lifetime of traps which are in thermal equilibrium with the bands, existing on the semiconductor surface. Figure 6-6c shows a transient response very similar to the type seen by Kawai et al. (170) in that it exhibits two peaks. Their explanation for the two peaks attributes the first peak to charge separation and recombination, and the second to charge transfer. The evidence presented here shows that the sample used for their study was in very poor condition. However, one characteristic which is always observed in common with their work is not the presence of the second peak (extremely high excitation energies in combination with poor surface quality must be obtained to observe this), but rather the small dip in photocurrent ~ 20 nanoseconds after the start of photoexcitation. Because the dip is observed regardless of excitation energy or redox couple, it is most likely attributable to a time dependent property inherent to the semiconductor. At present, not enough information is available to explain this phenomenon.

Calculated Biexponential Decays

A representative sample of the computer fitted biexponential decay is shown with experimental data points in Figure 6-7. All of the data from the previous study utilizing WSe₂ #50-4 in I⁻/I₃⁻ and Fe²⁺/Fe³⁺ were fitted to help determine a model for the decay based on observed trends in decay times. Figures 6-8a and 6-8b show calculated values of τ_1 and τ_{2N} ($\tau_1 < \tau_2$), respectively, for WSe₂ #50-4 in I⁻/I₃⁻ containing solution, while Figures 6-9a and 6-9b show calculated values of τ_1 and τ_2 ($\tau_1 < \tau_2$), respectively, for WSe₂ #50-4 in Fe²⁺/Fe³⁺ containing solution.

Note that some trends are observable, but a lot of scatter exists in the calculated data. With the exception of the shorter decay time (τ_1) for Fe²⁺/Fe³⁺ use, all of the decay times increase gradually with increasing excitation energy. The Fe²⁺/Fe³⁺ decay time τ_1 increases and then decreases for excitation energies $\gtrsim 50$ nanojoules. Also, while the τ_1 decay times appear comparable for both redox couples, the τ_2 decay times corresponding to Fe²⁺/Fe³⁺ use are longer than τ_2 values for I⁻/I₃⁻ use (particularly at low excitation energies).

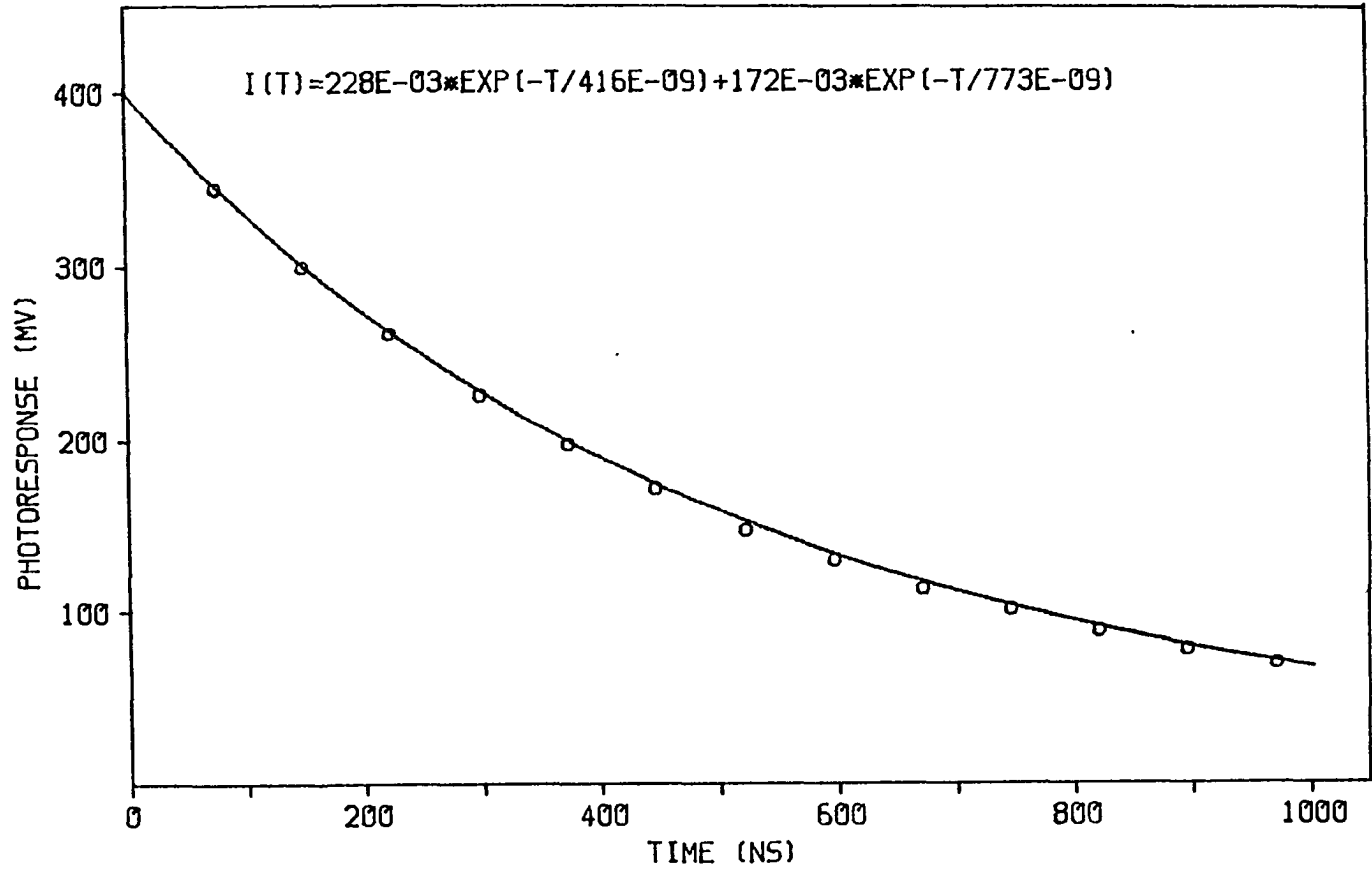


Figure 6-7. Sample of computer fitted biexponential transient decay

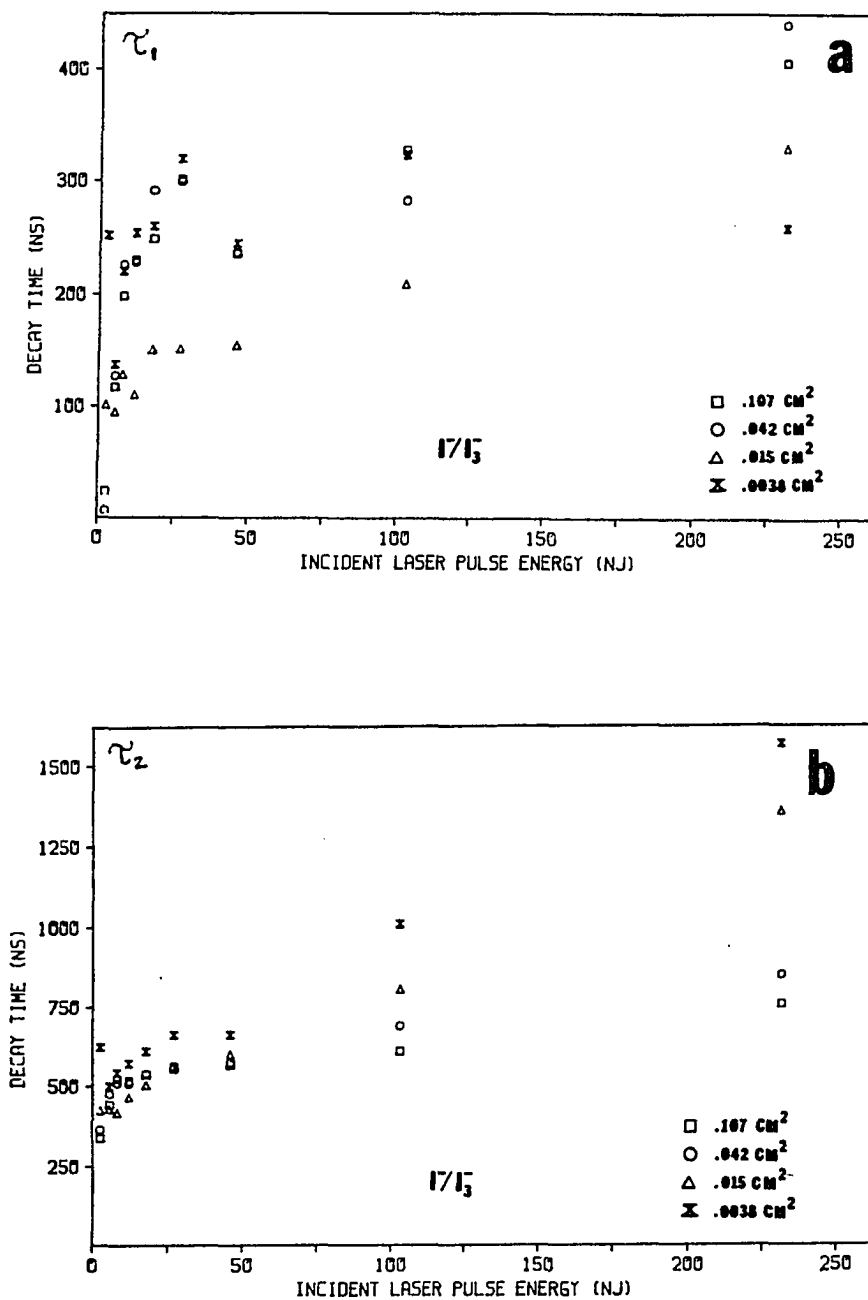


Figure 6-8. Calculated decay time constants for WSe_2 #50-4 in I^-/I_3^- containing solution as a function of incident pulse energy.
 a) τ_1 . b) τ_2

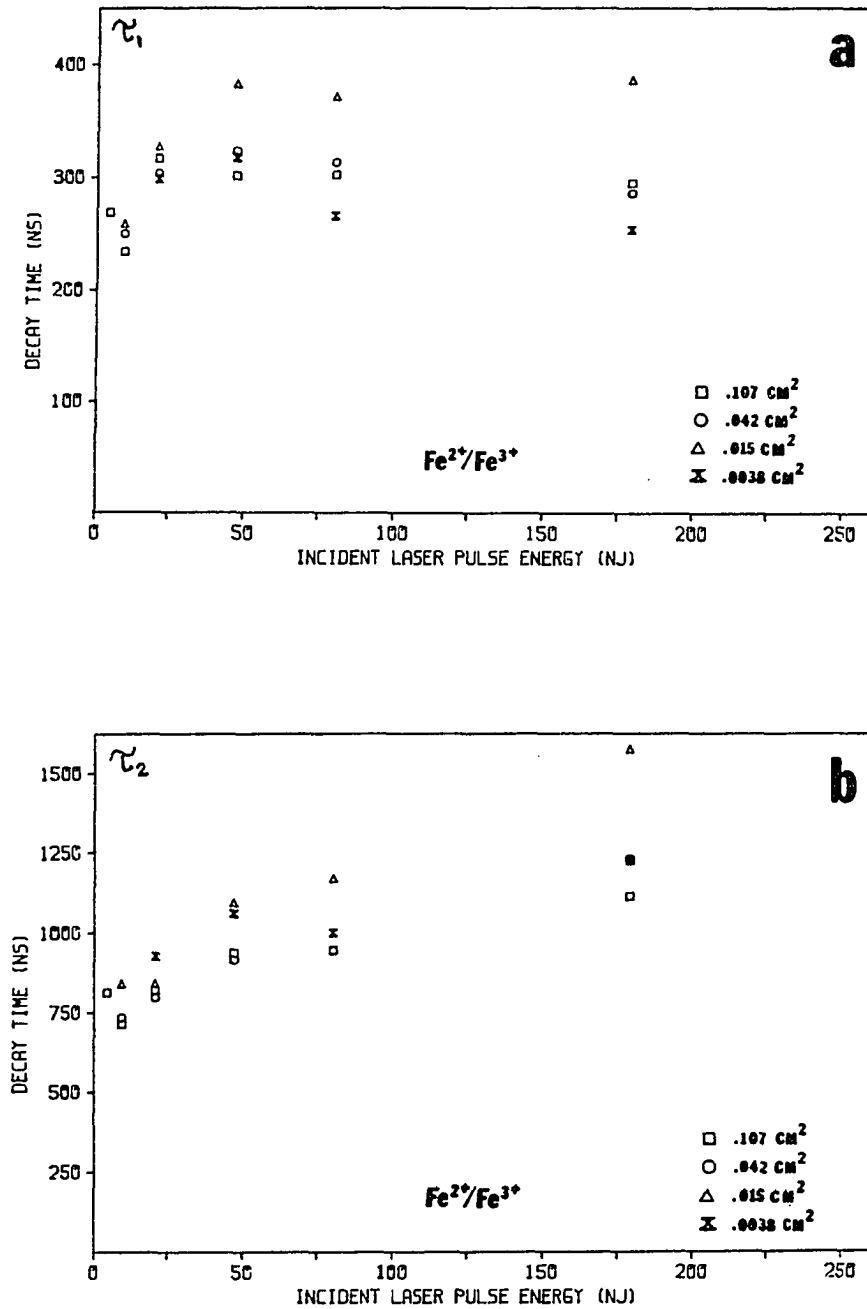


Figure 6-9. Calculated decay time constants for WSe₂ #50-4 in Fe²⁺/Fe³⁺ containing solution as a function of incident pulse energy. a) τ_1 . b) τ_2

PEC Model

Several models for the current-voltage characteristics of PEC operation under CW illumination exist in the literature (145, 146, 148, 186, 188). Of the transient studies thus far documented, no models which fit the experimental data have been presented. However, a recent theoretical model has been developed by R. H. Wilson (189). In this simple model which combines kinetic and electronic effects, recombination losses and charge transfer of photogenerated carriers are assumed to obey first order kinetics. Trapping effects are treated similarly. Figure 6-10 illustrates the phenomenological equivalent circuit which applies. The two capacitors C_S and C_H are representative of the space charge and Helmholtz regions, respectively, while the resistances R_i and R_c represent the internal resistance (of the semiconductor and solution) and the added cell load resistance. The rate constants k_S and k_H represent the rates of disposal of photogenerated minority carriers (holes, in this case).

Photogenerated holes may either undergo charge transfer and contribute to k_H or recombine with an electron to contribute to k_S (recombination is equivalent to charge movement opposite to the field dictated direction; the energy acquired by the charge carrier is lost within the cell, not in the external circuit).

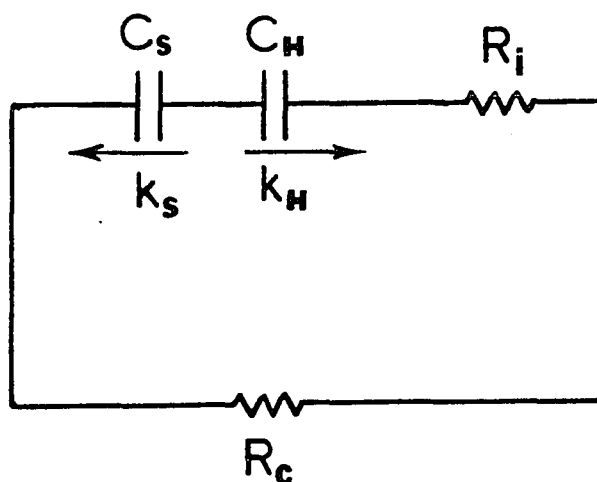


Figure 6-10. Circuit model for photocurrent transient analysis. Capacitors C_S and C_H represent the space charge layer and Helmholtz layer capacitances, respectively. Resistances R_i and R_c represent internal (PEC) resistance and external (circuit) resistances. Kinetic constants k_H and k_S represent charge transfer and recombination, respectively

An impulse of light, assumed to be delta-like such that no deconvolution need be performed, impinges upon the PEC, charging C_S with an initial amount of charge Q_{S0} . The Helmholtz region capacitance is uncharged by the illumination. The overall resistance is defined by

$$R = R_c + R_i, \quad [6-5]$$

and the capacitance and decay rate defined by

$$\frac{1}{C} = \frac{1}{C_S} + \frac{1}{C_H} \quad [6-6]$$

and

$$k = k_S + k_H. \quad [6-7]$$

Initial and final conditions are represented by

$$Q_{S0} \neq 0; \quad Q_{H0} = 0; \quad Q_{S\infty} = Q_{H\infty} = 0, \quad [6-8]$$

where $\frac{Q_{S0}}{q}$ represents the incident number of photons multiplied by the quantum efficiency. If the movement of charge through the capacitors is viewed as a perturbation upon normal discharge, the following obtains.

$$\frac{dQ_S}{dt} = -i - k_S (Q_S - Q_H) \quad [6-9]$$

$$\frac{dQ_H}{dt} = -i + k_H (Q_S - Q_H) \quad [6-10]$$

$$\frac{Q_S}{C_S} + \frac{Q_H}{C_H} = iR \quad [6-11]$$

If $k_H = k_S = 0$, the eventual fate of the circuit would be that C_S would discharge until C_H obtained an equal and opposite charge, at which time current flow would cease leaving trapped charge on each capacitor. With $k_H \neq 0$ and $k_S \neq 0$, the solution of [6-9] and [6-10], subject to the proper boundary conditions, produces the following expression for the time-dependent current $i(t)$.

$$i(t) = Q_{SO} \left[\frac{\frac{k_S - k_H}{RC_S} e^{-kt} + \frac{\frac{k_H - \frac{1}{R^2 C C_S}}{RC}}{k - \frac{1}{RC}} e^{-t/RC}}{k - \frac{1}{RC}} \right] \quad [6-12]$$

The general form of equation [6-12] is a biexponential of the form

$$y = a_1 e^{-t/\tau_1} \pm a_2 e^{-t/\tau_2}. \quad [6-13]$$

For $t = 0$, equation [6-12] reduces to

$$i(0) = \frac{Q_{SO}}{RC_S}, \quad [6-14]$$

as expected. Values for a_1 , τ_1 , a_2 , τ_2 and Q_{SO} may be expressed in terms of measurable quantities. The resistance R_i of the cell, as determined by a vector impedance measurement, is $\sim 10\Omega$. Therefore, $R \approx 60\Omega$, inclusive of the oscilloscope input. Calculation of the desired quantities follows

simply.

$$C_S = \frac{Q_{SO}}{R(a_1 + a_2)} ; \quad C_H = \frac{CC_S}{C_S - C} \quad [6-15]$$

$$C = \frac{\tau_1}{R} ; \quad k = \frac{1}{\tau_2} \quad [6-16]$$

$$k_H = RC \left[\frac{\bar{a}_1}{QS_0} (k - 1/RC) + \frac{1}{R^2 CC_S} \right] \quad [6-17]$$

$$k_S = RC_S \left[\frac{\bar{a}_2}{QS_0} (k - 1/RC) + \frac{k_H}{RC_H} \right] \quad [6-18]$$

Calculated values of k_H , k_S , C_H and C_S show a great deal of scatter when plotted as a function of excitation energy, so that only general trends may be discussed at this point. The values calculated for the space charge layer capacitance, C_S , are comparable for both the I^-/I_3^- and Fe^{2+}/Fe^{3+} couples, as expected. For excitation energies of <50 nanojoules, a linear increase in capacitance is observed with excitation energy, starting at ~ 6 nanofarads and increasing to ~ 12 nanofarads. (A vector impedance measurement performed on this particular PEC yielded a value of $C_S = 6.6$ nanofarads under a small perturbation of ~ 15 millivolts.) For excitation energies up to 250 nanojoules, no further increase in C_S is noted. The characteristic changes observed in the space charge capacitance are readily understood in terms of the width of the depletion region, which is proportional to $V_S^{1/2}$, with V_S

being the amount of band bending present. As noted previously, V_S decreases with increasing pulse energy (see Figure 6-4) until a saturation point is reached. As V_S decreases, so correspondingly does the width W of the depletion region. Since capacitance is inversely proportional to the width (distance between "plates") of the space charge region, it rises with the increasing perturbation from equilibrium and stops changing as the amount of band bending becomes independent of excitation energy. As a function of increasing spot size, C_S is observed to always decrease. This is once again reasonable, for the amount of band movement is observed to be less for the smaller spots due to increased recombination during photoexcitation.

Values of the calculated Helmholtz layer capacitance, C_H , are observed to be very similar to those of C_S , which is not generally expected. The differences in thickness of the space charge and Helmholtz regions, approximately 2000 \AA vs. 3 \AA , respectively, should produce Helmholtz region capacitances which are ~ 2 orders of magnitude larger. The discrepancy noted here is not well understood and may in fact be a real phenomenon of the system. The values for C_S are typically about twice the values for C as determined from the decay constant RC values. If the Helmholtz capacitance is to be, as expected, about two orders of magnitude larger than the space charge capacitance, C_S should assume values

only 1-2% larger than values for C. Large errors in the assumed R value could account for the discrepancy. However, this is unlikely because most of R comes from the solution resistance (which is constant due to high redox concentration) and the input resistance of the oscilloscope. Dependence of C_H on spot size shows C_H to increase with increasing spot size, the opposite effect from that observed with C_S . This is reasonable because the thickness of the Helmholtz region should not vary during the course of the transient, and therefore the capacitance in the Helmholtz region should increase with increasing cross-sectional illumination area.

Calculated values of k_H slowly decrease with increasing illumination intensities. This means that the rate of charge transfer decreases with higher perturbations from equilibrium. At ~ 10 nj excitation energy values for use of the I^-/I_3^- couple and Fe^{2+}/Fe^{3+} couple are $1.39 \times 10^6 \text{ sec}^{-1}$ and $1.01 \times 10^6 \text{ sec}^{-1}$, respectively. At ~ 100 nj excitation energy, k_H values have decreased to $1.03 \times 10^6 \text{ sec}^{-1}$ and $.728 \times 10^6 \text{ sec}^{-1}$. The I^-/I_3^- couple demonstrates a rate of charge transfer which is approximately 35% higher than that for Fe^{2+}/Fe^{3+} , evidencing the rapid transfer of charge via adsorbed triiodide.

Values of k_S are also seen to decrease with increasing pulse energy, i.e., recombination rates decrease. At the lowest excitation energies, the I^-/I_3^- couple appears to be

inducing higher recombination rates than the $\text{Fe}^{2+}/\text{Fe}^{3+}$ couple. At ~ 250 nanojoule excitation energy, the k_S values for both redox couples are low and comparable in magnitude. Values of k_S also increase with decreasing spot size.

Rising portions of the photocurrent transients were initially ignored to facilitate the use of a simple model. However, risetimes are totally inconsequential (laser excitation pulsewidth limited) only for the largest spot size, and even then finite risetimes appear for the lowest excitation energies. The general rule is that risetime increases with decreasing spot size, and that for a fixed spot size, the risetime decreases with increasing excitation energy. Attempts to fit risetimes to a diffusion-controlled model failed. It may be noted, however, that the slow rise to peak photoresponse is always preceded by an excitation-limited rapid rise portion of finite amplitude.

This exact type of behavior may be fitted to the Wilson model for the case where $k_S < k_H$, $k_H \sim 10^6 \text{ sec}^{-1}$, and $C_S \sim C_H$ (as seen for the treated data). The slowly rising portion becomes more and more prominent as the RC time constant becomes longer. This does not correlate directly with the results thus far determined, but treatment of each data set inclusive of the risetimes could produce interesting results.

Variation of PEC Load Resistance

Variation of the load resistance at the rear of the cell produces radically different decays for a fixed level of photoexcitation. The effect of the RC time constant is always seen to be dominant. The PEC external resistance was calculated as the parallel combination of resistance added to the cell plus the oscilloscope input. For external resistances of $>50\Omega$, a $1\text{ M}\Omega$ input vertical amplifier was used (Tektronix 7704 oscilloscope). At $1\text{ M}\Omega$, decay of a multiexponential character is evident (a log plot produces linear plus sharply curved portions). This multiexponential character appears at resistances as low as $10\text{ k}\Omega$, and then disappears below that value. The multiple exponential is probably indicative of multiple pathways for the decay of photogenerated charge other than charge transfer. The peak photopotentials observed for the PEC used (sample MoSe_2 #33-2 in $5.0\text{ M KI}/10^{-2}\text{ M I}_2$ containing electrolyte; pulse energy 231 nanojoules) were all $\sim 250\text{ mV}$ for load resistances in the range of $50\Omega - 1\text{ M}\Omega$. In the presence of the highest load resistances, the semiconductor is held near the flatband potential for a relatively long time, thereby prompting recombination through any levels that are available.

For the purpose of observing the variation in decay time and quantum yield of charge transfer with respect to added

resistance, it is simplest to treat the decays as single exponential. All of the decay times were therefore calculated using linear regression. Correlation coefficients for $R_L < 10 \text{ k}\Omega$ were greater than 0.99, with the higher resistances offering a slightly poorer fit. Figure 6-11a shows a log-log plot of decay time versus load resistance over the range $1\Omega - 100 \text{ M}\Omega$, while Figure 6-11b shows a plot of decay time versus load resistance for $1\Omega - 50\Omega$. The circuit displayed in Figure 6-11b can be readily used to describe the variation of decay times. In this circuit, R_L represents the added load resistance, R_S represents the PEC series resistance contribution, while R_{in} represents the "internal shunt resistance" of the PEC. The capacitor is representative of the space charge layer capacitance (the Helmholtz layer capacitance is assumed to be much greater than space charge region capacitance). The two circles represent a current impulse source which provides for ideal instantaneous charging of C. The decay time of the circuit discharge is represented by

$$\tau = RC = \left[\frac{1}{R_{IN}} + \frac{1}{R_{OUT}} \right]^{-1} C, \quad [6-19]$$

where R_{IN} represents an "internal shunt" resistance, and R_{OUT} represents the resistance combining the load resistance R_L and the internal series resistance of the cell R_S .

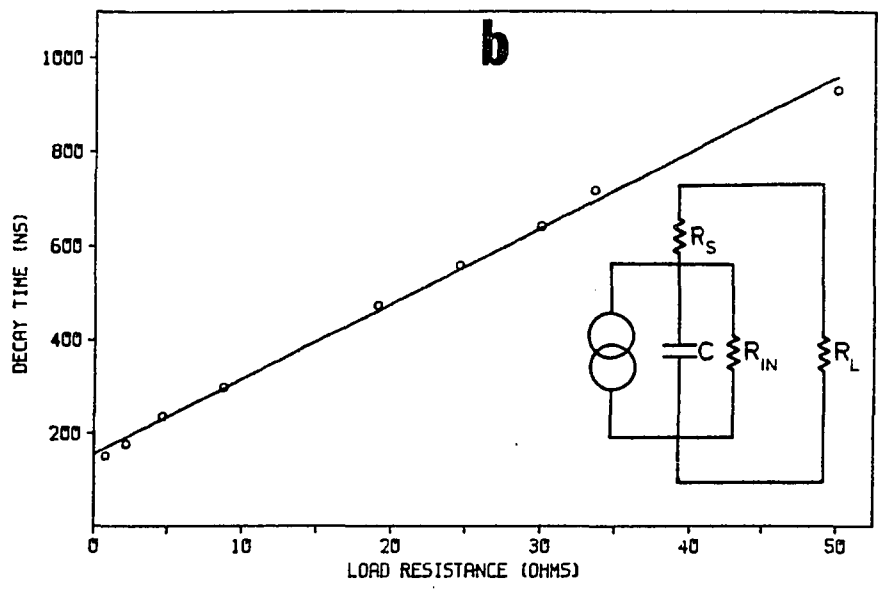
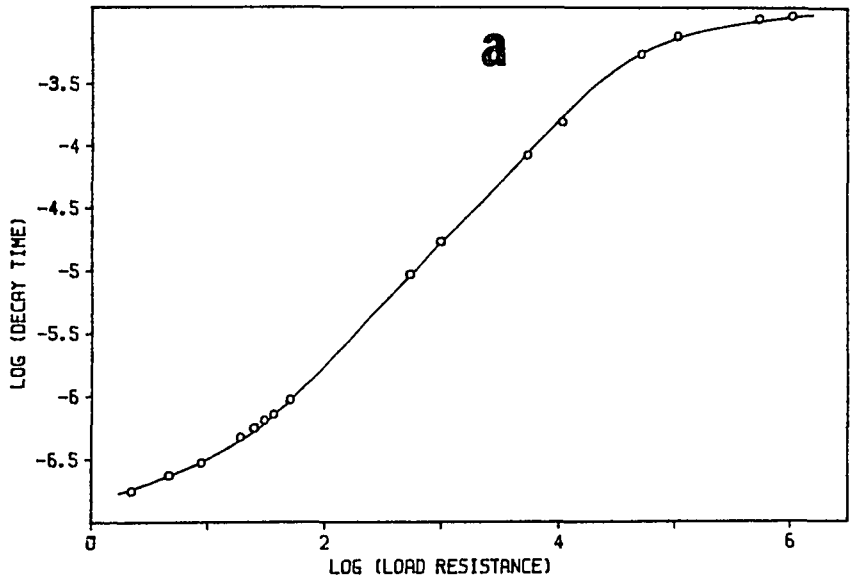
$$R_{OUT} = R_S + R_L \quad [6-20]$$

Figure 6-11. Photocurrent transient decay time constants as a function of load resistance.

a) $\log \tau$ (transient decay time constant) as a function of $\log R_L$ (load resistance). MoSe_2 #33-2 in $5.0 \text{ M KI}/10^{-2} \text{ M I}_2$. Incident pulse energy 231 nanojoules. $1\Omega < R_L < 1 \text{ M}\Omega$.

b) τ (transient decay time constant) as a function of load resistance R_L . MoSe_2 #33-2 in $5.0 \text{ M KI}/10^{-2} \text{ M I}_2$. Incident pulse energy 231 nanojoules. $1\Omega < R_L < 50\Omega$. Insert-equivalent circuit for determination of R_S ,

R_{IN} , C



For the condition $R_L \gg R_{IN}$, $\tau = R_L C$ and for $R_L \ll R_{IN}$, $\tau = R_{OUT} C = (R_L + R_S) C$. Therefore, if $\tau = (R_L + R_S) C$, a plot of τ versus R_S should be linear, with a concomitant slope of C and intercept $R_S C$, which determines R_S .

As seen in Figure 6-11b, a linear relationship does indeed exist, yielding values of $R_S = 10.2 \Omega$ and $C = 15.9 \times 10^{-9}$ F. By using the values of τ and R_L corresponding to the two largest values of R_L in combination with equation [6-19], it is determined that $R_{IN} \approx 70 \times 10^3 \Omega$. Values for τ precise to within $\pm 5\%$ may be found by again using equation [6-19] with the derived values of R_S , R_{IN} , and C .

Photogenerated carriers which do not pass through the external circuit (R_{OUT}) are obviously lost due to recombination. The calculated value of R_{IN} represents the "resistance" of the cell to recombination effects. Through the calculation of quantum yields of charge transfer, the effect of R_{IN} may be further elucidated. Figure 6-12a shows how R_L affects the quantum yield of charge transfer. Noting that the respective currents through R_{IN} and R_{OUT} may be represented by

$$i_{IN} = \frac{V_{MAX}}{R_{IN}} e^{-t/RC} \quad [6-21]$$

and

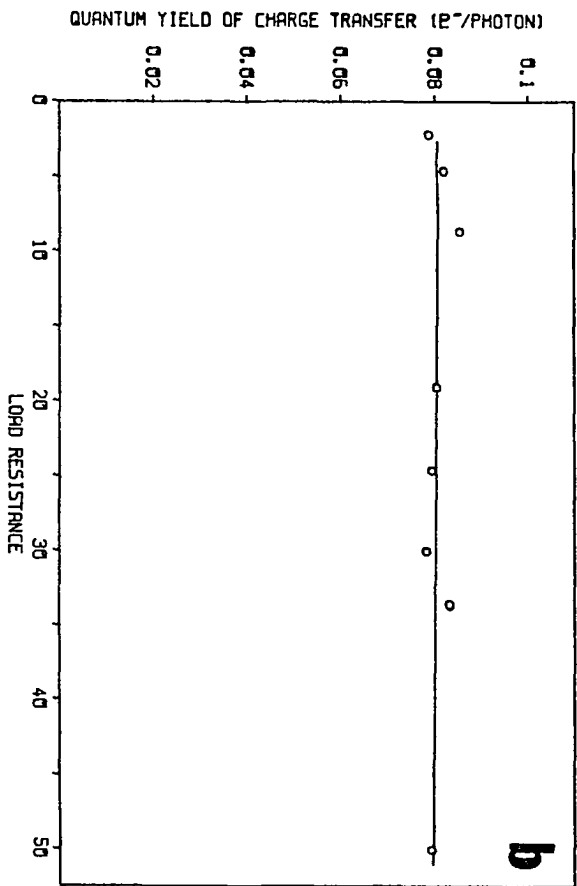
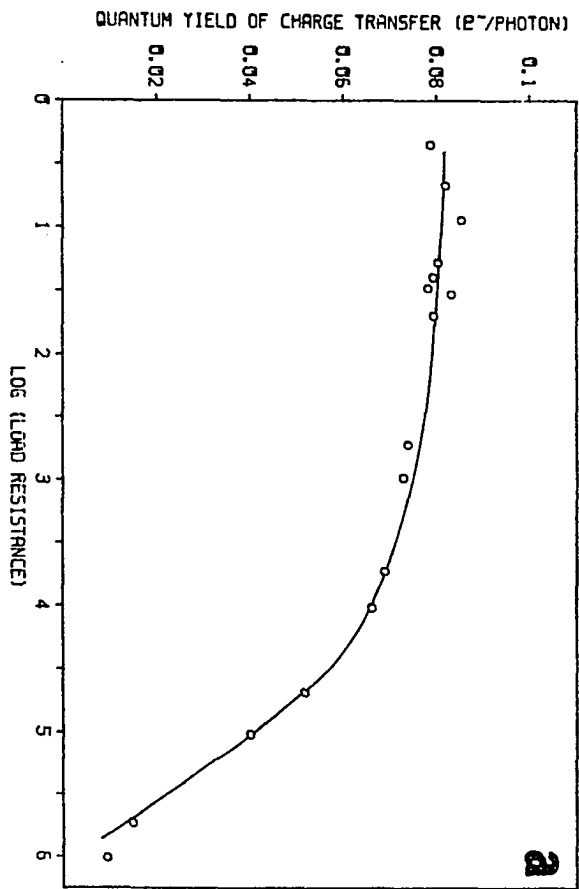
$$i_{OUT} = \frac{V_{MAX}}{R_S + R_L} e^{-t/RC}, \quad [6-22]$$

one sees that the relative amount of charge passing through

Figure 6-12. Quantum yields of charge transfer

a) Quantum yield of charge transfer as a function of $\log R_L$ (load resistance).

MoSe₂ #33-2 in 5.0 M KI/10⁻² M I₂. Incident pulse energy 231 nanojoules. b) Quantum yield of charge transfer as a function of R_L for $R_L < 50\Omega$



R_{OUT} compared to that initially photoproduced can be determined to be

$$\Sigma(R_{OUT}) = \frac{Q(R_{OUT})}{Q(C)} = \frac{R_L + R_S}{R_L + R_S + R_{IN}} \quad [6-23]$$

Assuming that the best quantum yield available ($R_{OUT} \sim R_S$) is $\sim 8\%$ (as seen in Figure 6-12a), other values of quantum yield may be found by multiplying the maximum quantum yield by $\Sigma(R_{OUT})$, yielding values with a precision of $\pm 10\%$.

The maximum quantum yield attainable in this experiment is limited by recombination prior to the decay, i.e., during the photogeneration stage. Recombination losses after photoexcitation are dependent upon the length of time the bands are held near flatband potential. As the load resistance increases to large values, losses become greater. As $R_L \rightarrow \infty$, the maximum decay time τ_∞ is approached asymptotically. It appears that $\tau_\infty \sim 10^{-3}$ seconds, which probably reflects a maximum "average" trap lifetime (average because the distribution of trapping levels is not known).

All of the aforementioned has been presented under the assumption that only nonfaradaic current flow takes place. However, the limitations of this model via the presence of faradaic current flow is evidenced in several ways. First, the character of the decays was approximated by a single exponential, which is contrary to a varying extent to the true nature of the decays. Also, a vector impedance meter

measurement performed on this particular PEC yielded values of $R_S = 6.1\Omega$ and $C = 12.3 \times 10^{-9}$ F. Finally, CW measurements reveal that current does indeed flow through the external circuit, obviously pointing to faradaic current flow. Therefore, it appears that, in the case of pulsed excitation, both faradaic and nonfaradaic contributions must be accounted for, strictly speaking.

Variation of Redox Couple Concentration

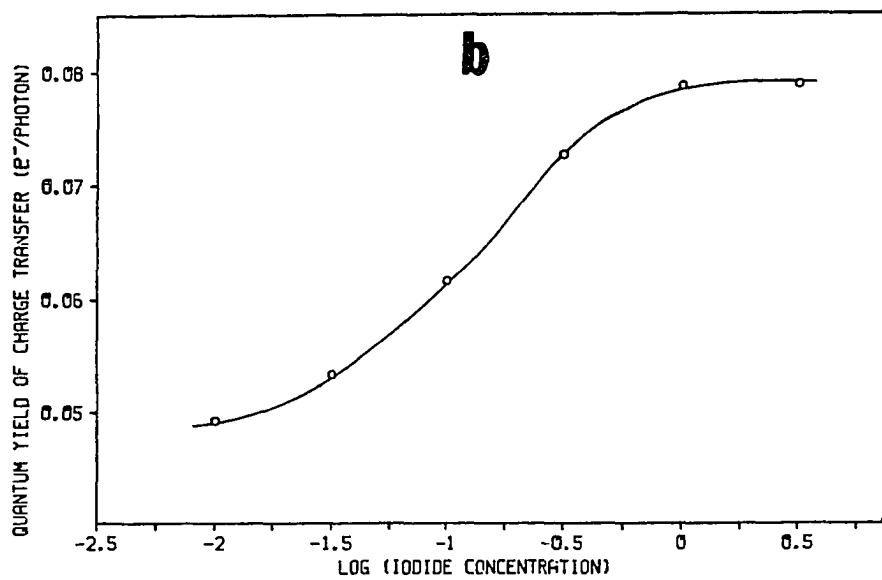
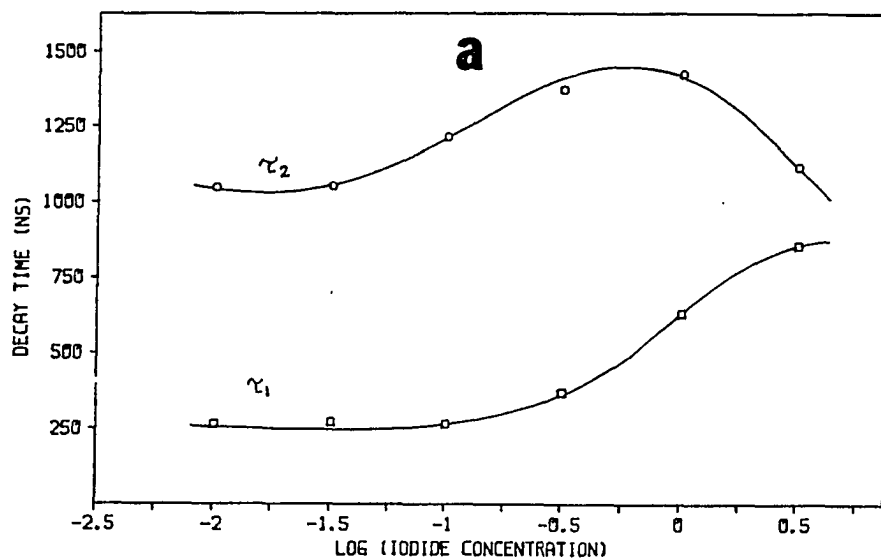
An attempt to model decay times and quantum yields of charge transfer as a function of I^-/I_3^- redox couple concentration resulted in incomplete results due to some contamination of the sample encountered during the experiment. Nonetheless, some qualitative information may be obtained. Semiconductor sample $MoSe_2$ #33-2 was used in the PEC for this experiment. The amounts of KI/I_2 were varied from 0.01 M $KI/3.16 \times 10^{-5}$ M I_2 to 3.16 M $KI/10^{-2}$ M I_2 , while keeping the ionic strength at a constant value of 3.16 by adding KCl to the solution. The added KCl acted as a supporting electrolyte to eliminate migration effects from the solution. The proportion of KI/I_2 was kept constant to assure that the semiconductor Fermi level maintained the same energy for each solution. Evidence of this stability was found in the maximum photoexcursion after excitation, which proved to be ~ 160 millivolts for all of the solutions. Dual exponential decays

were seen for all solutions, with the biexponential approaching what appeared to be a single exponential as the redox couple concentration was increased. However, one must note that in the limit of a single exponential, two sources may be contributing, but with similar time constants by coincidence. Figure 6-13a shows the decay times corresponding to each part of the biexponential. Note that the abscissa is in units of $\log [I^-]$ and that the value of $\log [I_3^-]$ (triiodide concentration) is simply related by $\log [I_3^-] = \log [I^-] - 2.5$. If one looks at these decays in accordance with the Wilson model assuming $R = 60\Omega$, several observations can be made. First, the RC time constant (τ_1) does not change with concentration until $\log [I^-] > -1$. At this point the capacitance starts to rise sharply. Calculations show that both the space charge and Helmholtz layers are affected, with the capacitance in the space charge region increasing more rapidly. The value for C at $\log [I^-] = 0.5$ is 14.57 nanofarads. Modification of the interface by adsorption appears to prompt this effect. Meanwhile, the value of k, ($1/\tau_2$), corresponding to charge transfer plus recombination rates, appears to show a minimum. No explanation is offered for this at the present time.

The plot of quantum yield of charge transfer versus $\log [I^-]$ is shown in Figure 6-13b. The points corresponding to the

Figure 6-13. Effects of variation of triiodide concentration

a) Decay time constants τ_1 and τ_2 as a function of variation of iodide (triiodide) concentration. MoSe_2 #33-2. Pulse energy 80.1 nanojoules. Ionic strength held constant at 3.16 with KCl. b) Quantum yield of charge transfer as a function of variation of iodide (triiodide) concentration



lowest iodide/triiodide concentrations are speculative, but the saturation of quantum yield seen at high concentrations is real and tends to parallel the isotherm for triiodide adsorption on a WSe_2 photoanode, as recently determined by chronocoulometry experiments (190).

CHAPTER VII. DISCUSSION

Laser induced photocurrent transients for PECs employing n-MoSe₂ and n-WSe₂ semiconductor photoanodes in I⁻/I₃⁻ and Fe²⁺/Fe³⁺ redox couple containing aqueous electrolytes have been studied in order to achieve a better understanding of the dynamics of charge carrier generation, recombination, and transfer across the semiconductor-solution junction. A model which encompasses both faradaic and nonfaradaic charge transfer has been applied to the data with promising results. MoSe₂ and WSe₂ samples showed similar behavior. Different cell dynamics were observed for different redox couples. The transient studies exhibited strong correlation with studied performed under continuous illumination conditions.

The surface quality of MoSe₂ and WSe₂ single crystals was readily detectable from the form of the observed photocurrent transients. The types of transients observed ranged from excitation pulsewidth limited with very low peak photocurrent for an edge-mounted sample, to much longer biexponential decay with high peak photocurrent for a sample relatively free of surface defects. Samples containing a high proportion of edge sites on the van der Waals surface showed a combination of the two decay behaviors.

For a given redox couple, WSe₂ produced the largest phototransients. For a given semiconductor sample of good

quality, the I^-/I_3^- couple was more efficient than the Fe^{2+}/Fe^{3+} couple due to a higher degree of band bending in the dark as a result of triiodide adsorption onto the solid surface. Peak photoresponse versus laser pulse energy showed a saturation effect due to band flattening at high intensities. Quantum yields of charge transfer ranged from $\sim 4\%$ (pulse energy ~ 250 nanojoules) to $\sim 20\%$ (pulse energy ~ 4 nanojoules), showing that high illumination intensities produce the highest recombination losses. Due to the similar timescale of the decays irrespective of quantum yield, it may be concluded that the highest losses are due to recombination within the space charge layer of the crystal, and furthermore that these losses occur during the process of photoexcitation. Variation of quantum yields of charge transfer triiodide concentration showed a nonlinear effect, thereby supporting the adsorption of triiodide onto the semiconductor surface.

Variation of the load resistance of the PEC under constant illumination conditions can be used to determine values of R and C corresponding to a simple linear RC circuit model. For a WSe_2 sample in $5.0 \text{ M KI}/10^{-2} \text{ M I}_2$, values of $R = 10.2 \Omega$ and $C = 15.9 \times 10^{-9} \text{ F}$ were found, which were similar to values determined using vector impedance measurements. The value of a "shunt" resistance was also determined, which relates to the propensity of this particular PEC toward recombination losses. As short circuit conditions were approached, a limiting value

of the decay constant (τ_{sc}) of ~ 160 nanoseconds was seen. Correspondingly, an upper limit of the open circuit decay constant (τ_{oc}) of $\sim 10^{-3}$ seconds was seen. However, τ_{oc} was obtained without further variation while high but finite resistances were used. This value of τ_{oc} , therefore, appears to be a measure of the maximum length of time free charges can reside in the semiconductor, independently of the solution properties, and most likely attributable to "slow" traps within the semiconductor.

The lengthening of observed transient decays with the addition of load resistance to the PEC points toward domination of the transients by the external RC constant. The non-exponential character of the transients, however, lends credence to a model which includes faradaic current flow. A model employing both kinetic and electronic factors devised by Wilson (189) produces reasonable values for charge transfer rates as well as electrical component values. Further investigation of the utility of this model should be conducted. Some problems encountered in data acquisition for this work have limited somewhat the application of the Wilson model. The first improvement to be made would involve the laser system itself.

Single nanosecond pulse selection was achieved by creating a 5 nanosecond "window" of the flashlamp-pumped dye laser microsecond output using a Pockels cell with a 700:1 rejection

ratio. Because of the nonlinear response of the PEC to perturbation by an impulse of light, very low levels of non-rejected light outside of the window may slightly alter the transient decays. The use of either a nitrogen pumped dye laser or a modelocked cavity-dumped argon ion pumped dye laser as an excitation source should rectify this situation. Another improvement would involve the digital recording of data instead of recording data photographically, as was done in this study. Maintenance of the digitally recorded data on a floppy disk or other storage device would facilitate rapid interpretation utilizing either the aforementioned gradient search program or another more sophisticated program to simultaneously fit all parameters in the equation describing the transient.

A capability for more accurate interpretation of the transients would also facilitate modification of the Wilson model. All parameters have thus far been determined in terms of first order kinetic rate constants and RC time constants. However, it has been shown that the values of R , C_H , C_S , k_S , k_H , and Q_{S0} are not constants of the system but are affected by the extent of the perturbation of the cell from equilibrium in a complex way. The concept of a capacitance is only approximate in the first place, for in the space charge region a continuous distribution of charge is found rather than parallel sheets of charge of opposite polarity. Surface

state capacitances, furthermore, determine the amount of charge of either polarity stored in a single sheet. In order to improve the model, work needs to be done in computer simulation of the PEC transient response. By following the distribution of charge in the system with respect to time, a better knowledge of the dynamics of the system could be attained.

Further Work

Peak photoresponse as a function of laser intensity was seen to saturate prior to attaining the value of the flatband potential, evidencing that during the photogeneration of charge carriers, the majority of recombination takes place either through the direct edge emission of radiation, or through the two-step process encountered via a recombination center. The concurrent monitoring of emission intensity and photoresponse should further elucidate the proportion of losses due to each event. Picosecond photoexcitation will be necessary due to the rapid migration of charge. Experiments should be done using a range of load resistances extending operating conditions of the PEC from open circuit to short circuit. The importance of concentration polarization effects for various redox couples may also be studied by illuminating the cell with a square pulse of light of variable duration.

Observation of the variation of transient response of the PEC to excitation of different wavelengths could add insight to the cell dynamics also. Repetition of the experiments in this work using lower excitation energies would also be warranted, but techniques for signal averaging or amplification without distorting the signal are a must. The use of lower excitation energies would place the mode of operation of the PEC much nearer to normal (solar insolation) operating conditions.

BIBLIOGRAPHY

1. Bradley, D. J. in "Ultrashort Light Pulses", 1st ed.; Shapiro, S. L., Ed.; Springer-Verlag: New York, 1976; Vol. 18, Chapter 2.
2. Moreau, G. A.; Sizer, T. Opt. Comm. 1982, 41, 47.
3. Shank, C. V.; Fork, R. L.; Yen, R.; Stolen, R. H. Appl. Phys. Lett. 1982, 40, 761.
4. Siegman, A. E.; Kuizena, D. J. Opto-Electronics 1974, 6, 43.
5. Hargrove, L. E.; Fork, R. L.; Pollack, M. M. Appl. Phys. Lett. 1964, 5, 4.
6. Mocker, H. W.; Collins, R. J. Appl. Phys. Lett. 1965, 7, 270.
7. Demaria, A. J.; Stetser, D. A.; Heynau, J. Appl. Phys. Lett. 1966, 8, 174.
8. Demaria, A. J.; Farrar, C. M.; Danielson, G. E. Appl. Phys. Lett. 1966, 8, 22.
9. Didomenico, M.; Marcos, H. M.; Geusic, J. E.; Smith, R. E. Appl. Phys. Lett. 1966, 8, 180.
10. Sorokin, P. P.; Lankard, J. R. IBM J. Res. Develop. 1966, 10, 162.
11. Glenn, W. H.; Brienza, J. J.; Demaria, A. J. Appl. Phys. Lett. 1968, 12, 52.
12. Schmidt, W.; Schafer, F. P. Z. Naturforsch. 1968, 26A, 558.
13. Schmidt, W.; Schafer, R. P. Z. Naturforsch. 1967, 22A, 1563.
14. Sorokin, P. P.; Lankard, J. R.; Moruzzi, U. L.; Hammond, E. C. J. Chem. Phys. 1968, 48, 4726.
15. ILC Bulletin 1524, 1976, Sunnyvale, California.
16. Marling, J. B.; Gregg, D. W.; Wood, L. Appl. Phys. Lett. 1970, 17, 527.

17. Keller, R. A. IEEE J. Quant. Electron. 1970, QE-6, 411.
18. Soffer, B. H.; MacFarland, B. B. Appl. Phys. Lett. 1967, 10, 266.
19. Walther, G.; Hall, J. L. Appl. Phys. Lett. 1970, 17, 239.
20. Bloom, A. J. J. Opt. Soc. Amer. 1974, 64, 447.
21. Hodgkinson, I. J.; Vukusic, J. I. Appl. Opt. 1970, 17, 1944.
22. Holtom, G.; Tesche, O. IEEE J. Quant. Electron. 1974, QE-10, 577.
23. Strome, F. C., Jr.; Webb, J. P. Appl. Opt. 1971, 10, 1348.
24. Jasny, J.; Jethwa, J.; Schafer, F. P. Opt. Comm. 1978, 27, 426.
25. Kato, D.; Sato, T. Opt. Comm. 1974, 5, 134.
26. Danielmeyer, H. G., in "Lasers", 1st ed.; Levine, A. K.; Demaria, A. J., Eds.; Marcel Dekker: New York, 1976; Vol. 4, Chapter 1.
27. Demaria, A. J.; Glenn, W. H., Jr.; Brienza, M.; Mack, M. E. Proc. IEEE 1969, 57, 2.
28. Arthurs, E. G.; Bradley, D. J.; Roddie, A. G. Appl. Phys. Lett. 1971, 19, 480.
29. O'Neill, F. Opt. Comm. 1972, 6, 360.
30. Ippen, E. P.; Shank, C. V.; Dienes, A. Appl. Phys. Lett. 1972, 21, 348.
31. Miyazoe, Y.; Maeda, M. IEEE J. Quant. Electron. 1971, QE-7, 36.
32. Lin, C. IEEE J. Quant. Electron. 1975, QE-11, 602.
33. Statz, H.; Demars, G., in "Quantum Electronics, A Symposium", Townes, C. H., Ed.; Columbia University Press: New York, 1960.
34. Dunsmuir, R. J. Elec. Contr. 1961, 10, 453.

35. Siegman, A. E. "An Introduction to Lasers and Masers", 1st ed.; McGraw-Hill: New York, 1971; Chapter 10.
36. Yariv, A. "Quantum Electronics", 2nd ed.; John Wiley & Sons: New York, 1975; Chapter 11.4.
37. Smith, P. W.; Duguay, M. A.; Ippen, E. P., in "Progress in Quantum Electronics", 1st ed.; Sanders, J. H.; Stenholm, S., Eds.; Pergamon: Oxford, 1975; Vol. 3, Chapter 2.
38. Snitzer, E.; Young, C. G., in "Lasers", 1st ed.; Levine, A. K., Ed.; Marcel Dekker: New York, 1968; Volume 2, Chapter 2.
39. Fleck, J. A., Jr. J. Appl. Phys. 1968, 39, 3318.
40. Fleck, J. A., Jr. Phys. Rev. B 1969, 1, 84.
41. Letokhov, V. S. Sov. Phys. JETP 1969, 28, 569.
42. Kryukov, P. G., Letokhov, V. S. IEEE J. Quant. Electron. 1972, QE-8, 766.
43. von der Linde, D. IEEE J. Quant. Electron. 1972, QE-8, 328.
44. Glenn, W. H. IEEE J. Quant. Electron. 1975, QE-11, 8.
45. Arthurs, E. G.; Bradley, D. J.; Roddie, A. G. Appl. Phys. Lett. 1973, 23, 88.
46. Mialocq, J. C.; Boyd, A. W.; Jaraudias, J.; Sutton, J. Chem. Phys. Lett. 1976, 37, 236.
47. Letokhov, V. S. Sov. Phys. JETP 1969, 26, 562.
48. Haus, H. A. J. Appl. Phys. 1975, 46, 3049.
49. New, G. H. C. Opt. Comm. 1972, 6, 188.
50. New, G. H. C. IEEE J. Quant. Electron. 1974, QE-10, 115.
51. Haus, H. A. IEEE J. Quant. Electron. 1975, QE-11, 736.
52. Haus, H. A. IEEE J. Quant. Electron. 1975, QE-11, 323.
53. Ausschnitt, C. P. IEEE J. Quant. Electron. 1974, QE-13, 321.

54. Bradley, D. J.; Higgins, J. F.; Key, M. H.; Majumdar, S. Opto-Electron. 1969, 1, 62.
55. Pinnekamp, F.; Himmel, G.; Bergstedt, K. Opt. Comm. 1974, 11, 225.
56. Jethwa, J.; Schafer, F. P. Appl. Phys. 1974, 4, 299.
57. Loth, C.; Meyer, Y. H. Appl. Opt. 1973, 12, 123.
58. Jethwa, J.; Schafer, F. P.; Jasny, J. IEEE J. Quant. Electron. 1978, QE-14, 119.
59. Boiteaux, M.; DeWitte, O. Appl. Opt. 1970, 9, 514.
60. Morey, W. W.; Glenn, W. H. IEEE J. Quant. Electron. 1976, QE-12, 311.
61. Friedman, H. W.; Morton, R. G. Appl. Opt. 1976, 15, 1494.
62. Laser Focus Buyer's Guide, 1979, Newton, Massachusetts.
63. Negran, T. J.; Glass, A. M. Appl. Opt. 1978, 17, 2812.
64. Schmidt, W.; Schafer, F. P. Phys. Lett. 1968, 26A, 558.
65. Bradley, D. J.; O'Neill, F. Opt. and Quant. Elec. 1969, 1, 69.
66. Gassman, M. H.; Weber, H. Opt. and Quant. Elec. 1971, 3.
67. Furumoto, H. W.; Ceccon, H. L. Appl. Opt. 1969, 8, 1613.
68. Pappelardo, R.; Samelson, H.; Lempicki, A. J. Appl. Phys. 1972, 43, 3776.
69. Snavely, B. B.; Schafer, F. P. Phys. Lett. 1969, 28A, 728.
70. Snavely, B. B. Proc. IEEE 1969, 37, 1374.
71. Hirth, A.; Vollrath, K.; Fouassier, J. P. Opt. Comm. 1973, 9, 139.
72. Evtuhov, V.; Neeland, J. K. Appl. Opt. 1967, 6, 437.
73. Gusinow, M. A. J. IEEE Quant. Electron. 1975, QE-11, 929.

74. Hecht, E.; Zajac, A. "Optics", 1st ed.; Addison-Wesley: Reading Mass., 1974; Chapter 4.3.
75. Mack, M. E. Soc. Photo-Opt. Instr. Eng. 1975, 69, 35.
76. Gavronskaya, E. A.; Groznyi, A. V.; Staselko, D. I.; Strigun, V. L. Opt. Spectrosc. 1977, 42, 213.
77. Drake, J. M.; Morse, R. I. Opt. Comm. 1974, 12, 132.
78. Melles Groit Optics Guide, 1975, Irvine, California.
79. Marling, J. B.; Gregg, D. W.; Thomas, S. J. J. IEEE Quant. Electron. 1970, QE-6, 570.
80. Hirth, A.; Faure, J.; Lougnot, D. Opt. Comm. 1973, 8, 318.
81. Loth, C.; Gacoin, P. Opt. Comm. 1975, 15, 179.
82. Weber, J. Opt. Comm. 1973, 7, 420.
83. Rosenthal, I. Opt. Comm. 1978, 24, 164.
84. Weber, J. Phys. Lett. 1971, 37A, 179.
85. Dempster, D. N.; Morrow, T.; Quinn, M. F. J. Photochem. 1973, 2, 343.
86. Malley, M. M.; Morou, G. Opt. Comm. 1974, 10, 323.
87. Falkenstein, W.; Penzkofer, A.; Kaiser, W. Opt. Comm. 1978, 27, 151.
88. Ricard, D.; Lowdermilk, W. H.; Ducuing, J. Chem. Phys. Lett. 1972, 16, 617.
89. Dolan, G.; Goldschmidt, D. Chem. Phys. Lett. 1976, 39, 320.
90. ILC Technical Bulletin No. 5, Sunnyvale, California.
91. Jolzrichter, J. F.; Schawlow, A. L. Annals of N.Y. Acad. of Sciences 1970, 168, 703.
92. Markiewicz, J. P.; Emmet, J. L. IEEE J. Quant. Elec. 1966, QE-2, 707.
93. Frungel, F. B. A. "High Speed Pulse Technology", 1st ed.; Academic Press: New York, 1965; Volume I, Chapter B.

94. Frungel, F. B. A. "High Speed Pulse Technology";, 1st ed.; Academic Press: New York, 1965, Volume III, Chapter B.
95. Stephens, R. L.; Hug, W. F. Laser Focus 1972, 8(7), 38.
96. ILC Technology F-Series Catalog, Sunnyvale, California.
97. Mroczkowski, J. A.; Milburn, R. H. Rev. Sci. Instrum. 1977, 48, 1555.
98. Ornstein, M. H.; Derr, V. E. Appl. Opt. 1974, 13, 2100.
99. Marotta, A.; Arguello, C. A. J. Phys. E.: Sci. Instrum. 1976, 9, 478.
100. Chu, S.; Smith, R. W. Opt. Comm. 1979, 28, 221.
101. Yee, T. K.; Fan, B.; Gustafson, T. K. Appl. Opt. 1979, 18, 1131.
102. Goldstein, R. Laser Focus 1968, 4, 21.
103. Steinmetz, L. L.; Pouliot, T. W.; Johnson, B. C. Appl. Opt. 1973, 12, 1468.
104. Hecht, E.; Zajac, A. "Optics", 1st ed.; Addison-Wesley: Reading, Mass., 1974; Chapter 8.4.
105. Scott, J. C.; Palmer, A. W. J. Phys. E.: Sci. Instrum. 1978, 11, 901.
106. Higgens; Key; Majumdar. Opt. and Quant. Electro. 1968, 1, 62.
107. Davis, S. J.; Murray, J. E.; Downs, D. C.; Lowdermilk, W. W. Appl. Opt. 1978, 17, 3184.
108. Hyer, R. C.; Sutphin, H. D.; Winn, K. R. Rev. Sci. Instrum. 1975, 46, 1333.
109. Bradley, D. J.; Liddey, B.; Roddie, A. G.; Sibbett, W.; Sleat, W. E. Opt. Comm. 1971, 3, 426.
110. Arthurs, E. G.; Bradley, D. J.; Roddie, A. G. Appl. Phys. Lett. 1972, 20, 125.
111. Rautian, S. G. Sov. Phys. Uspekhi 1958, 66, 245.
112. van de Hulst, H. C.; Reesinck, J. J. M. J. Astrophys. 1947, 106, 121.

113. Bradley, D. J.; Liddy, B.; Sleat, W. E. Opt. Comm. 1971, 2, 391.
114. Demaria, A. J., in "Progress in Optics", 1st ed.; Wolf, E., Ed.; North Holland Publishing: Amsterdam, 1971; Vol. IX, Chapter 2.
115. Ippen, E. P.; Shank, C. V., in "Ultrashort Light Pulses", 1st ed.; Shapiro, S. L., Ed.; Springer-Verlag: New York, 1976; Vol. 18, Chapter 3.
116. Dienes, A.; Ippen, E. P.; Shank, E. V. Appl. Phys. Lett. 1971, 19, 258.
117. Weber, H. P.; Danielmeyer, H. G. Phys. Rev. A 1970, 2, 2074.
118. Pike, H. A.; Hercher, M. J. Appl. Phys. 1970, 41, 4562.
119. Lill, E.; Schneider, S.; Dorr, F. Opt. Comm. 1977, 20, 223.
120. Mialocq, J. C.; Goujon, P. Opt. Comm. 1978, 24, 255.
121. Harris, L. A.; Wilson, R. H. Ann. Rev. Mater. Sci. 1978, 8, 99.
122. Tomkiewicz, M.; Fay, H. Appl. Phys. 1979, 18, 1.
123. Bruce, J. A.; Murahashi, T.; Wrighton, M. S. J. Phys. Chem. 1982, 86, 1552.
124. Gerischer, H. Surf. Sci. 1969, 18, 97.
125. Gerrard, W. A. J. Electroanal. Chem. 1978, 86, 421.
126. Nozik, A. J. 2nd International Conference on Photochemical Conversion and Storage of Solar Energy, Cambridge, England, August 1978.
127. Heller, A.; Parkinson, B. A.; Miller, B. In "Proceedings of the 13th IEEE Photovoltaic Spec Conference"; IEEE: New York, 1979.
128. Heller, A.; Miller, B.; Lewerenz, H. J.; Bachmann, K. J. J. Am. Chem. Soc. 1980, 102, 6555.

129. Kronig, R.; Penney, W. G. Proc. Roy. Soc. London 1931, A130, 499.
130. Bloch, F. Z. Physik. 1928, 52, 555.
131. Panhove, J. I. "Optical Processes in Semiconductors", 1st ed.; Prentice-Hall, Inc.: New Jersey, 1971; chapter 4.
132. Bardeen, J.; Blatt, F. J.; Hall, L. H. In "The Proceedings of the Atlantic City Photoconductivity Conference, 1954"; John Wiley & Sons: New York, 1956; chapter II-C.
133. Sze, S. M. "Physics of Semiconductor Devices", 3rd ed.; John Wiley & Sons: New York, 1981; chapter 1.
134. Van Roosbroeck, W.; Shockley, W. Phys. Rev. 1954, 94, 1558.
135. Sah, C. T.; Noyce, R. N.; Shockley, W. Proc. IRE 1957, 45, 1228.
136. Hall, R. N. Phys. Rev. 1952, 87, 387.
137. Shockley, W.; Read, W. T. Phys. Rev. 1952, 87, 835.
138. Many, A.; Goldstein, Y.; Grover, N. B. "Semiconductor Surfaces", 1st ed.; John Wiley & Sons: New York, 1965; chapter 7.
139. Runyan, W. R. "Semiconductor Measurement and Instrumentation"; McGraw-Hill: New York, 1975; chapter 3.
140. Morrison, S. R. "Electrochemistry at Semiconductor and Oxidized Metal Electrodes"; Plenum Press: New York, 1980; chapter 1.
141. Marcus, R. A. J. Chem. Phys. 1956, 24, 966.
142. Marcus, R. A. J. Chem. Phys. 1965, 43, 679.
143. Gerischer, H. Z. Phys. Chem. N. F. 1960, 26, 223.
144. Gerischer, H. Z. Phys. Chem. N. F. 1961, 27, 48.
145. Wilson, R. H. J. Appl. Phys. 1977, 48, 4292.

146. Russ, H. J. Electrochem. Soc. 1978, 125, 937.
147. Lemasson, P.; Etcheberry, A.; Gautron, J. Electrochimica Acta 1982, 27, 607.
148. Alberty, N. J.; Bartlett, P. N.; Hamnett, A.; Dare-Edwards, M. P. J. Electrochem. Soc. 1981, 128, 1493.
149. Chazalviel, J. N. J. Electrochem. Soc. 1982, 129, 963.
150. Rajeshwar, K. J. Electrochem. Soc. 1982, 129, 1004.
151. Von Fraunhofer, J. A.; Banks, C. H. "Potentiostat and its Applications"; Butterworth & Co.: London, 1972.
152. Prince, M. B. J. Appl. Phys. 1955, 26, 534.
153. Sah, C.; Noyce, R. N.; Shockley, W. Proc. IRE 1957, 45, 1228.
154. Haynes, J. R.; Shockley, W. Phys. Rev. 1950, 81, 835.
155. Stevenson, D. T.; Keyes, R. J. J. Appl. Phys. 1955, 26, 190.
156. Lederhandler, S. R.; Giacoletto, L. J. Proc. IRE 1955, 43, 477.
157. Reynolds, J. H.; Meulenber, A., Jr. J. Appl. Phys. 1974, 45, 2582.
158. Mahan, J. E.; Ekstedt, J. W.; Frank, R. I.; Kaplow, R. IEEE Trans. Electron. Dev. 1979, ED-26, 733.
159. Dhariwal, S. R.; Vasu, N. K. IEEE-ED Letts. 1981, 2, 53.
160. Dhariwal, S. R.; Vasu, N.; Gardre, R. Electron. Letts. 1979, 15, 456.
161. Dhariwal, S. R. IEEE Proc. 1980, 127i, 20.
162. Dhariwal, S. R.; Vasu, N. K. Solid State Elec. 1981, 24, 915.

163. Richardson, J. H.; Perone, S. P.; Monaco, S. B.; Steinmetz, L. L.; Harrar, J. E. In "Photoelectrochemistry: Fundamental Processes and Measurement Techniques"; The Electrochemical Society: New York, 1982.
164. Richardson, J. H.; Perone, S. P.; Deutscher, S. B. J. Phys. Chem. 1981, 85, 341.
165. Perone, S. P.; Richardson, J. H.; Deutscher, S. B.; Rosenthal, J.; Ziemer, J. N. J. Electrochem. Soc. 1980, 127, 2580.
166. Feldberg, S. W. J. Phys. Chem. 1970, 74, 87.
167. Harzion, Z.; Croitow, N.; Gottesfeld, S. J. Electrochem. Soc. 1981, 128, 551.
168. Harzion, Z.; Huppert, D.; Croitow, N.; Gottesfeld, S. J. Electrochem. Soc. submitted for publication.
169. Gottesfeld, S.; Feldberg, S. W. J. Electroanal. Chem. submitted for publication.
170. Kawai, T.; Tributsch, H.; Sakata, T. Chem. Phys. Lett. 1980, 69, 336.
171. Tributsch, H. Ber. Bunsenges. Physik. Chem. 1977, 81, 361.
172. Tributsch, H. Ber. Bunsenges. Physik. Chem. 1978, 82, 169.
173. Tributsch, H. Electrochem. Soc. 1978, 125, 1086.
174. Gobrecht, J.; Gerischer, H.; Tributsch, H. Ber. Bunsenges. Physik. Chem. 1978, 82, 1331.
175. Goldberg, A. M.; Beal, A. R.; Levy, F. A.; Davis, E. A. Phil. Mag. 1975, 32, 367.
176. Frindt, R. F. J. Phys. Chem. Sol. 1963, 24, 1107.
177. Kautek, W.; Gerischer, H.; Tributsch, H. J. Electrochem. Soc. 1980, 127, 2471.
178. Kam, K. K.; Parkinson, B. A. J. Phys. Chem. 1982, 86, 463.

179. Fan, F. F.; Bard, A. J. J. Electrochem. Soc. 1981, 128, 945.
180. Tributsch, H.; Gerischer, H.; Clemen, C.; Bucher, E. Ber. Bunsenges. Phys. Chem. 1979, 83, 655.
181. Llopis, J.; Fernandez-Braige, J.; Perez Gernandez, M. Electrochim. Acta. 1959, 1, 130.
182. Meyer, E.; Gerischer, H. Z. Phys. Chem. N. F. 1971, 74, 302.
183. Kam, K. K. Ph.D. dissertation, Iowa State University, Ames, Iowa, 1982.
184. Bevington, P. R. "Data Reduction and Error Analysis for the Physical Sciences"; McGraw-Hill: New York, 1969; Chapter 11.
185. Tributsch, H. Solar Energy Mat. 1970, 1, 257.
186. Bruchenstein, S.; Miller, B. J. Electrochem. Soc. 1982, 129, 2029.
187. McCann, J. F.; Haneman, D. J. Electrochem. Soc. 1982, 129, 1135.
188. Alberty, W. J.; Bartlett, P. N. J. Electrochem. Soc. 1983, 130, 1699.
189. Wilson, R. H., presented at the U.S./Japan Photoelectrochemistry Meeting, San Diego, March 1983.
190. Turner, J. A.; Parkinson, B. A. J. Electroanal. Chem., in press.

ACKNOWLEDGMENTS

I would like to dedicate this thesis to Mal Iles, a talented individual and good friend whose life was unexpectedly cut short in his 28th year.

I wish to extend special thanks to Dr. Walter Struve for his guidance, encouragement, and support throughout my graduate training.

I also wish to extend special thanks to Dr. Bruce Parkinson for his many helpful suggestions concerning the PEC project.

Thank you to those who assisted on the PEC project: Rich Pineault, Phil Anfinrud, and Dave Hart.

Thank you to others of my research group for their support and friendship: Bob Crackel and Jack Hedstrom.

Finally, a special note of thanks goes out to Betsy for helping to keep me sane during the final stages of this work. Thank you for your love and understanding.